THE APPLICATION OF AN INDUCTION MOTOR THERMAL MODEL TO MOTOR PROTECTION AND OTHER FUNCTIONS

Thesis submitted in accordance with the requirements of the University of Liverpool for the degree of

Doctor in Philosophy

by

David Roberts

September, 1986.

ACKNOWLEDGEMENTS

The author is grateful to Professor J.D. Parsons for providing the facilities of the Electrical Engineering Department for this research.

The author is beholden to his research supervisor, Mr D.R. Turner, for his invaluable advice, guidance and encouragement during the research and in the writing of the thesis.

The author's thanks are also extended to Dr. P.H. Mellor for his useful comments and help during the research.

The author very much appreciates the assistance and support given by GEC Small Machines p.l.c., Blackheath, particularly Mr. D.F. Warne, Mr. I. Williams, Mr. I. Fradley, Mr. D. Smith and all the staff who helped during the time the author spent at Blackheath.

The author acknowledges with gratitude the assistance rendered by the technical staff of the department, in particular Messrs. K. Mealor and A. Edwards.

Finally, the author would like to thank the SERC for co-sponsoring this project with GEC Small Machines p.l.c..

ABSTRACT

Accurate protection of induction motors relies upon the thermal tracking ability of the model incorporated in the motor protection relay. Future protection devices will rely upon the adoption of more comprehensive thermal models which are able to predict accurately the motor temperatures in areas where failure due to thermal overload is likely to occur.

A bulk component thermal model is applied to a motor protection application to assess whether an accurate protection device, based upon the real time computation of the model on a simple microprocessor, might be feasible. The performance of the model for three different machines is illustrated by comparing measured and simulated temperatures during varying load conditions. Tests carried out in real time using a simple microprocessor system indicate that a protection device is feasible though possible problems which might be encountered in it s implementation are identified.

The model is modified to allow for the more onerous heating conditions that arise when an induction motor is being operated from an unbalanced three phase supply. A digital sampling scheme is developed to calculate the sequence components of the motor inputs for use in computing the unbalanced motor losses. The so called 'unbalanced model' is tested against measurements taken on two of the motors when operating under varying conditions of supply unbalance and load.

The thermal model is also applied in a thermal duty cycle calculation system which calculates motor temperatures from the output power rather than the input current. This package may be used by a manufacturer to help size motors to particular customer's requirements, and two case studies are presented to illustrate the package operation. This second use of the thermal model might help foster the manufacturer's co-operation in the compilation of the model data.

CONTENTS

CHAPTER 1. INTRODUCTION.

In recent years there has been a shift in the design of electric motors aimed at reducing their cost for a given output. This has been accomplished, in part, by reducing the size, hence material content, of each motor unit at the expense of their margin of tolerance to thermal overloads [1]. The competitive market for small and medium sized, squirrel cage induction motors has meant that they have borne the brunt of this cost cutting and as such, now operate nearer their ultimate thermal limits than ever before. Industry's demand for these smaller, cheaper motors seems to indicate that this trend will continue.

In general the motor components which are most likely to fail as a result of thermal overload are the stator and rotor windings. To ensure a satisfactory motor lifetime, the stator winding temperature must remain within its designated insulation class limits whilst, for squirrel cage rotors, the rotor winding material must retain sufficient physical strength to withstand the centrifugal forces generated at rated speed. In the light of the trend towards these smaller motors, the devices used to protect the windings of these motors from overheating now require greater sensitivity than they have previously.

The need for improvements in motor protection relays was demonstrated in a survey of some 9000 motor failures in Britain, Finland and the USA conducted in 1977 [2]. The major causes of motor failure were identified as follows:

Overload	30%
Single phasing	14%
Insulation aging	10%
Moisture, oil, grease, dust	19%
Bearing failure	13%
Rotor failure	5%
Others	9%

Analysis of this information reveals that approximately 50% of the failures resulted directly from overheating which could have been prevented by an effective protection device. The alarming fact is that all the motors polled did indeed have a thermal protection device fitted.

In response to the evident need for better protection new, more sophisticated devices have emerged to take the place of the solderpot and bimetal strip relays which were once prominent. These new devices fall into two categories - those which monitor the motor winding temperatures by direct measurement and those which seek to model the winding temperatures from information on the motor supply conditions.

The former emerged along with thermometers such as thermistors which were small enough to be embedded in the windings of motors. However, such devices were, and still are, restricted to motors which have had these temperature sensors implanted in the windings during manufacture.

It is the devices in the latter category which constitute the vast majority of the induction motor protection devices used. These devices

rely upon some algorithm by which the motor temperatures may be determined or implied from input supply conditions. The most common is the solid state overload relay [3,4]. Like the bimetal strip devices before them, the solid state overload relays protect on the basis of an inverse time characteristic. This means high current overloads cause quick disconnection whilst lower overloads are tolerated for longer. More complicated devices use electronics in conjunction with resistor/capacitor networks in order to create heating and cooling characteristics which model those of induction motors in general. One such device, the Sprecher and Schuh CET 3 [5], simulates motor heating by a two node resistor capacitor network, representing the thermal capacitances of the winding and iron, and the heat transfer between them and to the surroundings. Though the model is crude, such a device represents a significant step forward in motor protection as it monitors the motor temperature under all conditions, not just overload, giving it an inherent memory of the recent thermal history of the motor. Should an overload occur, the 'tripping characteristic' is adjusted automatically. This ensures that the motor is sufficiently protected should it already be hot when an overload occurs.

Recently, microprocessor protection devices have begun to appear on the market [6-10]. These are notable, not for their advances in thermal simulations, but for the additional protective and control functions that they offer. The devices reviewed protected either on the basis of inverse time overload curves, direct thermometer measurement or digital simulation of one or two node resistor/capacitor networks.

One of the most recent microprocessor based devices, the Westinghouse IQ 2000 [8], improves on other direct measurement devices by providing protection against rotor over-temperatures. The occurrence of rotor failures whilst starting high inertia loads were reported by Eliasen [11] and although rotor failures are low on the list of causes of motor failure, at five percent they still represent a significant number of machines. The Westinghouse device [8] incorporates a digital simulation of a single node resistor/capacitor network, representing heat flow from the rotor under transient conditions, to provide an estimate of the rotor temperature with respect to the directly measured stator winding temperature. The input to the single node model is weighted to account for the additional rotor losses which occur when the motor is operating from an unbalanced three phase supply. Most other contemporary devices [3,7,9] simply set an allowable percentage overload above which the relay is tripped. However, the gradual heating which can occur with only moderate degrees of unbalance, particularly in motors of deep cage construction, is just the sort of effect to which the smaller motors produced now will be vulnerable.

The need still remains for a protection device which is more sensitive to the effects that cause overheating in small and medium induction motors but does not rely upon direct temperature measurement and therefore can be retrofitted to motors already in service.

The success of any thermal overload relay depends heavily upon the algorithm, model or physical phenomenon used to predict the motor temperatures. The 1977 poll shows that the devices used then were inadequate. Since then, the relay manufacturers have turned to more

complicated models which represent the motor winding temperature as the sum of two exponentials of different time constants - the two node analogue or digital models. This represents the first approximation to the true solution which is an infinite series of exponentials as the winding temperature rise depends ultimately on the temperature rise in each miniscule element of the motor [20].

In thermal models in general, approximations are made to the true solution by dividing the motor into distinct components which can be modelled individually before being joined to each of their neighbours. The solution at any point in the motor is then given by the sum of a number of exponentials equal to the number of components.

In the extreme instances this leads to finite difference or finite element models which define a large number of elements and hence equations [12,13]. Simpler models split the motor into larger, more distinct elements; these are known as bulk component or lumped parameter thermal models [14-23].

One such bulk component model was developed by Mellor [16] in his work which was primarily concerned with the efficiency of parallel machine drives. The ten component model was used to calculate the stator winding 'hot spot' temperature for use in analysing the aging of the motors in the parallel drive. It was shown that the model could accurately predict these temperatures, under transient load conditions, for a 5.5 kW Totally Enclosed Fan Cooled (TEFC) induction motor and further, that the solution of the model was simple enough to be programmed on an eight bit microprocessor with only modest requirements for computation time

and memory. Mellor speculated that the model might be solved in real time and used, in a simple microprocessor based device, for induction motor protection. The feasibility of such a device is the subject of this thesis.

The ten component model of Mellor was retained in its basic form, though a number of minor alterations and corrections to the model equations were performed.

A major alteration was made by introducing temperature dependence into the calculations of the motor losses which provide the inputs to the thermal model [15]. The decision to include temperature dependence also influenced the choice of tests required to find the electrical equivalent circuit parameters as the method employed by Mellor was no longer suitable. Ultimately, however, this led to more accurate thermal tracking of the motor temperatures. A detailed description of the lumped parameter thermal model along with its solution is given in Chapter 2.

Mellor's work was repeated and extended by applying the amended model to another two 4 pole induction motors in the small to medium sized TEFC category in order to establish whether or not the model was generally applicable. One of these motors was of the same size as that previously tested by Mellor, though from a different manufacturer, whilst the other was much larger being rated at 75 kW.

The respective models were tested under balanced supply conditions, by subjecting the motor to time varying loads. During the tests, the motor temperatures were measured by platinum resistance

thermometers placed in areas of interest around the machine geometry. Subsequent comparisons with predicted data showed that the thermal model was able to accurately track the motor temperatures, both above and below rated load, for each of the motors.

Once the accuracy and general applicability of the model had been established using these predictions performed on a mainframe computer, it remained to be proved that a similar performance could be achieved in real time, by computing the model on a microprocessor. The thermal model was programmed into a prototyping system based upon an Intel 8085 microprocessor and was provided with the model data for one of the 5.5 kW motors which was subsequently subjected to another time varying load test. During this test the prototyping system performed the dual role of predicting the motor temperatures in real time, from measurements of the motor input conditions and also a data logging role recording the measured and predicted temperatures. The graphical comparisons between the measured and predicted temperatures from each of the varying load tests are presented in Chapter 4 whilst the development of the prototyping system hardware and software is dealt with in Chapter 3.

To enhance the thermal models eligibility for motor protection applications, it was adapted to include the effects which can cause overheating when a motor is being operated from an unbalanced three phase supply. These effects have been noted by several authors [24-28] and cannot be ignored particularly when considering the protection of the present generation of smaller motors. Positive and negative sequence currents were used to calculate the additional heating effects during

unbalanced operation whilst the spatial concentration of the stator copper losses, in the phase carrying the greatest current, required the remodelling of the balanced model stator endwinding component.

The unbalanced model is presented in Chapter 5, which also includes the details of a digital sequence current measuring system, developed using the prototyping system of Chapter 3 and used to provide the sequence current information required for the computation of the model, in a form compatible with the microprocessor model of Chapter 3. To test the model, time varying load tests were conducted under unbalanced supply conditions, though only for the two smaller motors; supply difficulties made such tests upon the larger motor impractical.

Results are presented in Chapter 5 which show that the unbalanced model successfully tracks the temperatures of the hottest endwinding and, as such, is capable of providing more effective protection, under these conditions, than has hitherto been available.

Finally, in Chapter 6, another application of the thermal model of direct interest to the manufacturers of induction motors is discussed. This involved the development of an interactive system designed to compute the motor temperature profile during a given duty cycle and used to assess the suitability of the motor before resorting to expensive on-line tests.

British Standards [29] demand that motor manufacturers apply a duty cycle rating to each of their motors to denote the applications for which the motor is considered suitable. Normally, the choice of a motor

for a particular application would be made as a result of discussions between the manufacturer's applications department and the customer. It was considered that this choice might be aided by a software package which could predict the maximum temperature rise of the manufacturer's motors for a wide range of duty cycles; including those which might not be accurately represented by the British Standard ratings. Such a system was developed based upon the existing balanced thermal model.

Additional features were built into the model, which was now required to estimate the motor temperatures from the motor output conditions, as opposed to the input conditions used previously. These features included motor lifetime calculations, based upon the insulation lifetime analysis of Dakin [30], to give a further criterion on which the choice of a motor could be made, and also included an analysis of the starting and braking losses which become important for duties involving the starting and stopping of high inertia loads. Two fictional case studies are presented, at the end of Chapter 6, to illustrate the features of the duty cycle calculation package.

CHAPTER 2. THE INDUCTION MOTOR THERMAL MODEL

2.1 INTRODUCTION.

The bulk component thermal model developed by Mellor [16] was chosen for the proposed motor protection application for its simplicity and compactness and for the fact that it had already been proven, under transient conditions, to give accurate predictions of the stator winding 'hot spot' temperature for a small TEFC induction motor.

The model was retained in its basic form which consisted of ten components.

1. The frame.
2. The stator back iron.
3. The stator teeth.
4. The stator slot winding.
5. The stator endwinding.
6. The airgap.
7. The endcap air.
8. The rotor winding.
9. The rotor iron.
10. The shaft.

Each of the components is modelled by a node representing the components mean temperature from which heat flows, via thermal resistances, to each of the neighbouring components. Any heat generation in the component is assumed to be concentrated at the node and is repres-

ented by a current source using the thermal/electric circuit analogy. Heat storage in the component is represented by a capacitance which is also added at the node. Details of the models for conduction and convection and their application to each of the ten bulk components are given in sections 2.2 to 2.4. A small portion of radiation is included in the frame to ambient thermal resistance which is measured experimentally. Throughout the rest of the model however, internal radiation is assumed negligible in comparison with the other forms of heat transfer at the normal operating temperatures [22]. Further attention is given to the calculation of the frame/core contact resistance, as the experimental curves [31], referenced by Mellor, were found to be plotted over an insufficient pressure range for two of the three motors investigated.

A number of modifications were made to the method of calculating the thermal generators originally postulated by Mellor. Firstly, locked rotor and no-load tests were used to find the equivalent circuit parameters in preference to the graphical method adopted by Mellor. The latter determined the parameters from the results of a load test during which the motor losses were calculated from real and reactive input power measurements and power output estimations. This method was not retained for two reasons; one, because the errors involved in estimating the motor losses and also in determining parameters from the relatively small changes in reactive power which occurred over the range of the load test, made it difficult to obtain consistent results; and two, because it did not lend itself to the the second modificat ion - the temperature dependence of the thermal generators. The modelling of the motor losses is covered in section 2.4.

The networks of thermal resistances, capacitances and generators, created to model each of the ten bulk components, are joined together to form the complete fifteen node model of figure 2.16. A mathematical equation which represents the transient model is established by applying a heat balance equation to each of the fifteen nodes; this equation is later simplified by eliminating the equations for the nodes with no thermal capacitance. Eigenvalue and eigenvector theory is applied to uncouple the equations which can then be solved using a discrete approximation.

The thermal model parameters, derived for each of the three motors used in this work using the principles and equations identified in this Chapter, are presented in Appendix B; their performance under transient load conditions is studied in Chapter 4. In Chapter 5, changes found necessary to allow the application of the thermal model under unbalanced supply conditions are detailed. The necessary alterations were, however, accomplished without major disturbance to the structure and solution of the balanced model presented here.

2.2 THERMAL MODELS FOR CONDUCTION AND CONVECTION.

2.2.1 CONDUCTIVE HEAT TRANSFER.

Heat flow in the solid components of the induction motor thermal model is by conduction. In a cylindrical element (figure 2.1) this heat is transferred in three dimensions; radially, axially and circumferentially though the circumferential heat flow in the cylindrical elements of an induction motor can normally be neglected without serious error [22].

Assuming that the heat flow in the radial and axial planes are independent, allows the use of one dimensional equations to model the conduction. Further assuming that the mean temperatures in either of these directions are the same, allows the networks developed from the one dimensional conductive heat transfer equations to be superimposed resulting in the two dimensional model shown in figure 2.4.

The one dimensional conductive heat transfer equation which describes the radial temperature distribution is given by,

$$\frac{\partial^2 T}{\partial r^2} + \frac{1}{r}\cdot\frac{\partial T}{\partial r} + \frac{g}{k} = 0 \qquad (2.1)$$

g = heat generated per unit volume (W/m^3)

k = thermal conductivity in the radial direction ($W/m°C$)

The general solution for the mean temperature in terms of the radial boundary conditions ($T=T_1$ at $r=r_1$ and $T=T_2$ at $r=r_2$) is derived in Appendix A as,

$$T_m = T_2\cdot\left[\frac{r_2^2}{(r_2^2-r_1^2)} - \frac{1}{2\ln(r_2/r_1)}\right] + T_1\cdot\left[\frac{1}{2\ln(r_2/r_1)} - \frac{r_1^2}{(r_2^2-r_1^2)}\right] + \frac{g.(r_1^2+r_2^2)}{8k} - \frac{g.(r_2^2-r_1^2)}{8k.(\ln(r_2/r_1))} \qquad (2.2)$$

The particular solution for the case of zero internal heat generation can be modelled by the two resistor network shown in figure 2.2. The

mean temperature T_m can be expressed in terms of the boundary temperatures and thermal resistances as,

$$T_m = T_1 \cdot \frac{R_2}{R_1+R_2} + T_2 \cdot \frac{R_1}{R_1+R_2} \qquad (2.3)$$

Comparing the coefficients of T_1 and T_2 in equation 2.3 and those from equation 2.2 with g=0, defines the thermal resistances R_1 and R_2 as,

$$R_1 = \frac{1}{4\pi kL}\left[\frac{2r_2^2\ln(r_2/r_1)}{r_2^2-r_1^2} - 1\right] \qquad (2.4)$$

$$R_2 = \frac{1}{4\pi kL}\left[1 - \frac{2r_1^2\ln(r_2/r_1)}{r_2^2-r_1^2}\right] \qquad (2.5)$$

For the general case $g \neq 0$, Perez and Kassakian [22] proposed a 'T' network with an additional resistance R_m added at the central node of figure 2.2 to give the thermal equivalent circuit of figure 2.3. The model should be generally applicable under any boundary conditions, so to find the expression for R_m it is convenient to let $T_1=T_2=0$:

$$T_m = G.\left(R_m + \frac{R_1.R_2}{R_1+R_2}\right) \qquad (2.6)$$

G = Total heat generated in the component (W)

The mean temperature, T_m, is also given for these same boundary conditions from equation 2.2 as,

$$T_m = \frac{g.(r_2^2+r_1^2)}{8k} - \frac{g.(r_2^2-r_1^2)}{8k(\ln(r_2/r_1))} \qquad (2.7)$$

equating equation 2.7 with 2.6 gives,

$$R_m = \frac{-1}{8\pi kL(r_2^2-r_1^2)} \left[r_1^2+r_2^2 - \frac{4r_1^2r_2^2\ln(r_2/r_1)}{r_2^2-r_1^2} \right] \qquad (2.8)$$

As R_m is negative, the mean temperature T_m is lower than the central network temperature, denoted in figure 2.3 as T'_m.

The axial heat flow by conduction is described by the parabolic equation below,

$$\frac{\partial^2 T}{\partial l^2} + \frac{g}{k} = 0 \qquad (2.9)$$

The general solution of this parabolic equation, with the boundary conditions ($T=T_3$ at $l=0$, and $T=T_4$ at $l=L$) shown in figure 2.1, is also derived in Appendix A as,

$$T_m = \frac{T_3+T_4}{2} + \frac{g.L^2}{12k} \qquad (2.10)$$

As the asymmetries caused by the external cooling fan are ignored, then the axial temperatures can be assumed to be parabolically distributed about a radial plane through the axial centre of the stator core. This assumption permits the simplification of equation 2.10 as now $T_3=T_4$. Later, this same assumption is adopted generally so that only half the machine need be modelled.

A resistance, R_3, may now be defined as the resistance to heat flow from the axial mean temperature to each of its boundaries by substituting,

$$g = G/(\pi(r_2^2-r_1^2)L) \tag{2.11}$$

in equation 2.10 to give,

$$R_3 = L/(12\pi(r_2^2-r_1^2)k) \tag{2.12}$$

If it is assumed that the mean temperatures in the radial and axial directions are the same then this resistance, R_3, may be added to the circuit of figure 2.3 to give the two dimensional thermal equivalent circuit.

In order that this be applied to transient conditions a component representing the thermal capacitance of the bulk component is added at the mean temperature node such that the heat stored in the component is equal to the product of the thermal capacitance C and the mean temperature T_m. C is given by,

$$C = \rho.c_p.V \tag{2.13}$$

where,

ρ = density of component material (Kg/m^3)

c_p = Specific heat capacity of component material ($J/Kg°C$)

V = Component volume (m^3)

For the cylindrical component of figure 2.1,

$$C = \rho.c_p.\pi(r_2^2-r_2^2)L \tag{2.14}$$

In the equivalent thermal network, the thermal capacitance is represented by a capacitor at the mean temperature node. The total internal heat generation, G, is represented by a current source which is also added at the mean temperature node. Introducing the thermal resistance to axial heat flow, the thermal capacitance and the total internal heat generation to the 'T' network of figure 2.3, results in the complete transient model of a cylindrical component shown in figure 2.4. This model can be applied directly to those components which can be modelled by such a cylindrical structure - the stator back iron, the stator teeth, the rotor iron and rotor winding components. The stator slot winding, endwinding and shaft components are modelled by a special case of the cylindrical structure as their inside radius, r_1, is zero so that they form cylindrical rods.

Considering the particular solution of the radial heat flow equation with $T_1=T_2=0$ (equation 2.7), the mean temperature as r_1 tends to zero is given by,

$$\lim_{r_1 \to 0} T_m = \frac{g.r_2^2}{8k} \qquad (2.15)$$

Thus making the substitution for g from equation 2.11, the resistance to heat flow from the component mean temperature to the radial boundary is given by equation 2.16.

$$R_1 = 1/(8\pi kL) \qquad (2.16)$$

The thermal resistance to heat flow in the axial direction can easily be determined by setting r_1 to zero in equation 2.12 to give,

$$R_3 = L/(12\pi k) \qquad (2.17)$$

The model for conductive heat transfer in a cylindrical rod structure is thus shown by figure 2.5.

2.2.2 CONVECTIVE HEAT TRANSFER.

The heat transfer from the solid components to the internal air in the enclosed motor, and from the enclosure to the ambient air, is by convection. When the motor is stationary, assuming that there is no external cooling apparatus, the heat transfer is by free convection. Under running conditions, the motor's external fan causes forced convection which improves the motor cooling.

Convective heat transfer between the solid boundary temperature T_1 and the cooling medium's free stream temperature T_m is modelled by a single resistance, R_c, which can have one of two values depending upon whether the motor is running or is stationary. R_c is defined as

$$R_c = \frac{1}{h_c A} \qquad (2.18)$$

Where,

h_c = convective heat transfer coefficient ($W/°Cm^2$)

A = Area of contact surface (m^2)

The convective heat transfer coefficient h_c is a function of the physical properties of the cooling fluid and the nature of the solid boundary.

The coefficients for heat transfer to the internal cooling air were calculated from the results of several authors [32-36], all of whom were referenced by Mellor [16], whose works were based on geometries similar to those found in electrical machines.

The convective heat transfer coefficients for the air gap are found from work by Taylor [33] on heat transfer between smooth rotating cylinder and the experimental results of Gazley [34] which suggest a 10% increase in the coefficients of Taylor, to account for the additional fluid disturbances caused by stator slotting. It is assumed that the axial air flow in the air gap, hence the heat transfer, is negligible in comparison with that in the radial direction and, as such, is ignored.

Taylor gives the convective heat transfer coefficient, h_c, as:

$$h_c = \frac{N_u . K}{l_g} \qquad (2.19)$$

The values of the Nusselt number, N_u, to be used in equation (2.19), are defined by the following conditions:

$$N_u = 2.0 \quad \text{for } N_{ta} \leq 41 \qquad (2.20)$$

$$N_u = 0.212\ N_{ta}^{0.63} . N_{pa}^{0.27} \quad \text{for } 41 < N_{ta} < 100 \qquad (2.21)$$

Where the Taylor and Prandtl numbers, N_{ta} and N_{pr}, can be found from,

$$N_{ta} = \frac{\rho . \omega l_g}{\mu} . \left(\frac{l_g}{r}\right)^{0.5} \qquad (2.22)$$

$$N_{pr} = \frac{c_p . \mu}{k} \qquad (2.23)$$

k = Thermal conductivity of air ($W/m^{2\circ}C$)

l_g = Air gap (m)

ρ = Density of air (Kg/m^3)

ω = Angular rotor velocity (rads/s)

r = Air gap log mean radius (m)

c_p = Specific heat capacity at constant pressure ($J/Kg.^\circ C$)

Gazley's improvements suggest,

$$N_u = 2.2 \quad \text{for } N_{ta} \leq 41 \qquad (2.24)$$

$$N_u = 0.23\ N_{ta}^{0.63} . N_{pa}^{0.27} \quad \text{for } 41 < N_{ta} < 100 \qquad (2.25)$$

The critical value of 41 for N_{ta} represents physically the transition from laminar to turbulent flow in the airgap air.

Generally, for small air gap machines, including the motors modelled during this work, the Taylor number will lie between 41 and 100 and equation 2.25 is applicable. For the stationary condition (N_{ta}=0) slotting has no effect and equation 2.20 is used.

The value of the convective heat transfer coefficient associated with the endcap air is determined from experimental work by Luke [35] on the

dissipation of heat from endwindings by forced ventilation which, in a rotating motor would be provided by the rotor endring fins. For small cooling air velocities (<7.5 m/s) the results of Luke can be approximated by equation 2.26

$$h_c = 15.5(0.39v + 1) \tag{2.26}$$

For cooling velocities greater than this, h_c may be found directly from Luke's experimental curve.

The cooling air velocity (v) is a function of the rotor angular velocity (ω), the log mean radius of the endring fins (r_m) and the effectiveness with which the fins fan the internal air (η). This effectiveness relates the rotor angular velocity to the resulting radial air velocity in accordance with equation 2.27.

$$v = r_m.\omega.\eta \tag{2.27}$$

$$r_m = \frac{(r_2-r_1)}{\ln(r_2/r_1)} \tag{2.28}$$

r_2 = rotor endring fin outer radius (m)

r_1 = rotor endring fin inner radius (m)

As no additional data relating to the radial air velocity could be found, η was assumed to be 0.5, the value adopted previously by Mellor. The angular velocity is assumed to be constant at the motor's synchronous speed. For the stationary condition, v is zero and the convective heat transfer is given simply from equation 2.26 by,

$$h_c = 15.5 \text{ W/m}^2\text{°C}$$

These same coefficients are applied to each of the other surfaces in contact with the endcap air.

A further set of coefficients was necessary to model the heat transfer to the rotor cooling holes, present in one of the motors tested. The stationary coefficient was assumed to be equal to that for the endcap air (15.5 $\text{W/m}^2\text{°C}$). The rotational coefficient was found from a theoretical analysis of the heat transfer in a cylindrical pipe rotating about a parallel axis by Mori and Nakayama [36]. Their results give the convective heat transfer coefficient in terms of the Nusselt number, which in turn is expressed as a function of the Reynolds and Rayleigh numbers of this system.

$$h_c = \frac{N_u.k}{2a} \tag{2.29}$$

$$N_u = \frac{48}{11} 0.19(Re.Ra)^{0.2} \tag{2.30}$$

$$Re = \frac{2a.v.\rho}{\mu} \tag{2.31}$$

$$Ra = \frac{N_{pr}.R.\omega^2.\Delta\theta.\beta.\rho^2.a^4}{\mu^4} \tag{2.32}$$

Re = Reynolds number

Ra = Rayleigh number

a = pipe radius (m)

R = pipe rotation radius (m)

ΔT = axial temperature gradient (°C)

v = airflow velocity along pipe (m/s)

β = coefficient for the volumetric expansion of air ($°C^{-1}$)

Because of the lack of experimental results for such a geometry, values for ΔT and v were assumed. It was considered that their values would be small resulting in a rotating heat transfer coefficient of the order of 20% greater than the stationary coefficient.

The physical properties of air used to calculate these convective heat transfer coefficients are temperature dependent; a conservative air temperature of 80°C is assumed throughout.

In creating the thermal equivalent circuits for the airgap and endcap air it was assumed that the thermal capacitance of these elements was negligible in comparison with their solid neighbours. Ignoring the thermal capacitance of these components in this way allowed them to be eliminated, along with the secondary nodes introduced by the two dimensional, cylindrical heat conduction equivalent circuit developed in the previous section, to produce a more compact but no less accurate solution.

The final set of convective heat transfer coefficients which must be found, are those which model the heat flow between the frame and the ambient air. These coefficients were not found explicitly, rather the frame to ambient thermal resistances were found directly from exper-

imental tests upon each of the motors. For the rotating motor, this resistance was found from the results of a test in which the motor was run on no-load until thermal equilibrium was obtained. Readings of the central frame temperature T_f, and the ambient air temperature, T_a, were recorded and the resistance calculated from,

$$R_{cr} = \frac{T_f - T_a}{q_r} \tag{2.33}$$

In the above equation q_r is the heat loss at steady state that occurs within the frame of the induction motor; the windage of the external fan which acts outside this boundary is not included. It is assumed that the friction and windage of the motor, found from a separate test, is split evenly between internal friction and windage and bearing friction, and the windage of the cooling fan which acts outside the frame boundary.

The resistance for the stationary condition is found similarly from a locked rotor test. In this test all the measured power input to the motor is dissipated as heat within the frame;

$$R_{cs} = \frac{T_f - T_a}{q_s} \tag{2.34}$$

In each of these cases all the heat generated inside the motor is assumed to be transferred to the ambient by convection. However, any heat conducted along the motor shaft to the load or through the feet to the bedplate is also included in the calculation as is a component of heat transfer by radiation from the frame to the surroundings.

Equation 2.36 was obtained by private correspondence with Staff at GEC Small Machines Ltd.

2.2.3 A MODEL FOR THERMAL CONTACT RESISTANCE.

Due to its position on the main heat flow path from the stator winding to the ambient air, the stator core/frame interface thermal resistance requires careful consideration. It cannot be assumed that a thermal short circuit exists between the frame and the stator back iron due to the roughness of the surfaces which tends to hold the metals apart; the actual metal to metal contact is normally small with most of the contact area being composed of air pockets. The heat flow across the interface can be modelled by a single thermal contact resistance, R_c, where,

$$R_c = \frac{1}{h.A} \qquad (2.35)$$

h = thermal contact coefficient ($W/m^2{}^\circ C$)

A = apparent contact area (m^2)

The thermal contact coefficient, h, is a function of the pressure which is created when the frame is shrunk onto the core during manufacture and the roughness of the surfaces in contact. This pressure may be estimated, using the manufacturer's design drawings and the physical properties of the core and frame materials, from equation 2.36.

$$\frac{bP.(b^2+c^2}{E_a\ c^2-b^2} + \mu_a) + \frac{bP.(a^2+b^2}{E_s\ b^2-a^2} - \mu_s) = \delta \qquad (2.36)$$

Where,

P = contact pressure (N/m^2)

a = half the stator bore (m)

b = radius of the core frame interface (m)

c = frame barrel diameter (m)

μ_a = Poissons ratio for the frame material

E_a = elastic modulus of the frame (N/m^2)

μ_s = Poissons ratio for the core material

E_s = elastic modulus of the core (N/m^2)

δ = outer core radius - inner frame radius (m)

For low contact pressures, the contact resistance can be found directly from the experimental curves of Brunot and Buckland [31], which plots the contact resistance against contact pressure for aluminium shims sandwiched between two laminated magnetic steel blocks. The curves, however, only extend to pressures of 200 psi (1.38×10^6 N/m^2) which were far below the calculated contact pressures, at least for two of the motors modelled. It proved possible to extrapolate the relevant curve by applying a semi-empirical equation, presented by Shlykov and Ganin [37], to the experimental points of Brunot.

Shlykov and Ganin had compared the predictions of their equation with experimental data on the contact resistance between various metals with different surface finishes with good results. The equation is given below.

$$\frac{1}{R_c} = \frac{2\lambda_m}{ha_1+ha_2} + \frac{2.1+N.\lambda_M.10^4}{3\sigma_B s} \qquad (2.37)$$

where,

R_c = thermal contact resistance

λ_m = thermal conductivity of air

λ_M = thermal conductivity of the metal

s = nominal contact area

σ_B = ultimate strength of the less plastic metal

ha_1, ha_2 = average surface microroughness of the materials in contact.

For contacts between dissimilar metals,

$$\lambda_m = \frac{2\lambda_{m1} \cdot \lambda_{m2}}{\lambda_{m1} + \lambda_{m2}} \qquad (2.38)$$

λ_{m1} = thermal conductivity of metal 1

λ_{m2} = thermal conductivity of metal 2

The extrapolated curve of Brunot, for pressures up to 2000 psi (15×10^6 N/m^2) is presented in figure 2.19. The calculated values of the contact pressures and the corresponding contact coefficients are presented in table 2.1; the values for the Brook Crompton Parkinson motor were not available for the reasons given in Chapter 4. Also presented in Chapter 4, is an experimental method for calculating this contact resistance which casts doubt upon the accuracy of the coefficients shown here.

2.3 DETAILED DESCRIPTION OF MODEL COMPONENTS.

There follows, in this section, a detailed description of each of the bulk components outlining the assumptions and simplifications made in

applying the models for conduction and convection developed in the previous section. The resulting thermal equivalent circuits and equations for the circuit elements may be found in figures 2.6 to 2.15.

2.3.1 THE FRAME.

The frame component includes both the ribbed cooling structure which, in the case of the machines studied in this work, was shrunk onto the stator core, and the endcaps which were bolted onto each end of the ribbed structure. The whole structure was assumed to be at a uniform temperature and was modelled by a two resistance network - the frame to ambient resistance, found from experiment, and the frame to stator core contact resistance. The thermal capacitance was estimated from the masses and thermal properties of the frame and endcaps.

2.3.2 THE STATOR BACK IRON.

The stator back iron component consisted of the stator lamination pack minus the teeth which were modelled separately. The model developed in section 2.2, for conductive heat flow in a cylinder, applies directly to this component. The radial and axial conductivities differ as the interlamination electrical insulation also acts to limit the axial heat flow. In the radial direction a stacking factor is introduced to account for the proportion of the core occupied by the lamination insulation; the axial conductivity can be found from data published in the GE Heat Transfer Data Book [32].

2.3.3 THE STATOR TEETH.

The stator teeth component makes up the remainder of the stator lamination pack and is modelled in the same way as the stator back iron though it is assumed to be a closed cylinder with a radial cross section equal to the actual tooth cross section.

2.3.4 THE SLOT WINDING

The array of conductors, insulation and varnish which make up the stator winding are modelled as a solid cylindrical rod thus facilitating the use of the model for such a structure developed in section 2.2.1. In determining the axial and radial conductivities it is assumed that only the copper conductors transfer heat axially along the slot, in the radial direction the rod is modelled as a homogeneous solid with a conductivity a factor F times greater than that of the varnish alone. As a 100% slot fill is assumed, the radius of the rod is chosen to give a cross section equivalent to that of a slot. The slot liner is modelled separately as a polyamide strip of a thickness consistent with 415 V, class F insulation systems.

2.3.5 THE ENDWINDING.

The endwinding is modelled as a homogeneous toroid structure representing the circumferential mesh of conductors and insulation, with legs which represent the short cylindrical extensions of the stator slot winding. If the external toroid radius, R, was not given explicitly by the manufacturers design drawings, then it was estimated as the mean

radius of the stator slots about the radial centre of the motor. The internal toroid radius, r_2, can then be found from the estimated toroid mass, determined by subtracting the mass of the copper contained in the slot section and 'legs' from the total mass of copper in the complete winding. This radius is increased by 50% to allow for the addition of varnish and insulation.

Both the toroid and the 'legs' are modelled as cylindrical rods in a similar manner to the stator slot winding. For the toroid section the rod length is taken as the toroid's mean circumference. It is assumed that heat is generated uniformly throughout the component and thus is split between the toroid and 'leg' sections in the ratio of their volumes. Furthermore, it is assumed that the mean temperature in each section is the same and that the radial heat flow consists only of heat generated in that particular section. In the application of a thermal model to motor protection, the endwinding 'hot spot' temperature becomes more important than the mean. Thus, to give the hot spot, rather than the mean temperature at this node, the endwinding thermal resistances are multiplied by a factor w, defined as the ratio of the temperature difference between the endwinding hot spot and surface temperatures divided by the difference between the mean and surface temperatures. If the radial temperature distribution is assumed to be parabolic with the maximum temperature at the radial centre, then w will be equal to 1.5. In order that the heat balance equation should remain unchanged, the thermal capacitance to be added at this node, must be divided by this factor w.

2.3.6 THE AIRGAP

The thermal resistances between the air gap and the solid components which form its boundaries, were calculated from the convective heat transfer coefficients developed in section 2.2.2 and the estimated contact areas of the solids.

2.3.7 THE ENDCAP AIR

Again the thermal resistances between this component and its solid neighbours were calculated from the convective heat transfer coefficients of section 2.2.2 and the respective contact areas. The area afforded by the smooth endwinding 'toroid with legs' was increased by 50% to allow for the surface irregularities and the greater area which was available in the flatter structure of the true endwinding. The thermal capacitance of both the endcap air and the airgap was assumed to be negligible in comparison with their solid neighbours

2.3.8 THE ROTOR WINDING

The rotor winding was modelled as continuous aluminium cylinder with a volume equal to that of the cage bars; the end-disc with its fins and studs was modelled by a disc with a surface area equivalent to that of actual end-disc and was joined to the main cylindrical structure at each end. Approximating the rotor winding structure in this way allows the cylindrical heat conduction model of section 2.3 to be used.

2.3.9 THE ROTOR IRON

For this component the cylindrical heat conduction model can be applied directly though if axial cooling holes are present the thermal resistances must be increased in proportion to the reduction in cross sectional area. The radial and axial thermal conductivities are assumed to be those already found for the stator laminations.

2.3.10 THE SHAFT.

The shaft model is a special case of the cylindrical rod model in that it has no internal heat generation. It is, however, assumed that the resistance to heat flow from the radial boundaries to the component mean temperature is equivalent to that derived for the internally generated heat flowing in the opposite direction. A good thermal contact was assumed to exist between the shaft and bearings so that the ends of the shaft would be at the frame temperature. As there was only a small contact area with the endcap air any heat transfer between these components was neglected.

2.4 THERMAL GENERATORS.

The complete bulk component model, shown in figure 2.16, is created by joining each of the component models to each of its neighbouring models. In addition to the thermal resistances and capacitances, thermal generators, shown as current sources, must also be defined to model the motor heat losses which provide the model inputs.

The derivation of the thermal generators and the assumptions used in distributing the generators between the model nodes are presented here.

2.4.1 CALCULATION OF THE MOTOR LOSSES

With respect to the application of the thermal model to motor protection the thermal generators must be determined as functions of easily measurable quantities such as the motor input current and voltage. A convenient way to represent the motor losses in terms of these quantities is to use an induction motor electrical equivalent circuit. A particularly convenient form of equivalent circuit is shown in figure 2.20; a parameter c is included to allow the transfer of the stator quantities R_1 and X_1 to the rotor side of the magnetizing branch [38]. The components of the equivalent circuit may easily be found from conventional no-load and locked rotor tests though care must be taken to account for the effects of the high rotor current frequency during the locked rotor tests. The parameters thus calculated model the copper and iron losses plus a component of windage and friction which represents the portion of this loss which occurs within the motor frame. Any additional, or stray, losses which might occur under normal operating conditions are ignored. This assumption was supported by experimental tests, reported in Chapter 4, performed to compare the measured and calculated losses.

Referring to figure 2.20, the total machine losses per phase are given from the equivalent circuit by,

$$P_L = \frac{V_1^2}{cR_m} + (I_2/c)^2 \cdot cRsc \qquad (2.39)$$

$(I_2/c)^2$ can be found in terms of the measurable quantities V_1 and I_1 by consideration of the reactive power in the circuit and the vector diagram relating I_m, (I_2/c) and I_1 to the input voltage, shown in figure 2.21. Assuming that I_m is purely reactive ($cX_m << cR_m$) then,

$$(I_2/c)^2 = (I_1\cos\theta)^2 + (I_1\sin\theta - I_m)^2 \tag{2.40}$$

and furthermore,

$$I_m = V_1/cX_m \tag{2.41}$$

Expanding equation 2.40 and substituting for I_m from equation 2.41 gives,

$$(I_2/c)^2 = I_1^2 - 2V_1I_1\sin\theta/cX_m + V_1^2/cX_m^2 \tag{2.42}$$

The term $V_1I_1\sin\theta$ is the reactive power per phase, Q, which, from inspection of the equivalent circuit can be expressed as,

$$Q = V_1^2/cX_m + (I_2/c)^2 cX_{sc} \tag{2.43}$$

Substituting this into equation 2.42 and gathering terms of $(I_2/c)^2$ yields $(I_2/c)^2$ as a function of I_1 and V_1.

$$(I_2/c)^2 = \frac{cX_m . I_1^2}{(cX_m + 2cX_{sc})} - \frac{V_1^2}{cX_m(cX_m + 2cX_{sc})} \tag{2.44}$$

The total power loss per phase can thus be expressed as,

$$P_L = \frac{V_1^2}{cR_m} - \frac{cR_{sc}.V_1^2}{cX_m(cX_m+2cX_{sc})} + \frac{cX_m.cR_{sc}.I_1^2}{(cX_m+2cX_{sc})} \qquad (2.45)$$

This must be split into three components - the stator copper loss, given explicitly by equation 2.46, the rotor copper loss, given by equation 2.47, with the iron loss (equation 2.48) making up the remainder.

$$P_{SC} = I_1^2.R_1 \qquad (2.46)$$

$$P_{RC} = \frac{cX_m.c^2R_2.I_1^2}{cX_m+2cX_{sc}} - \frac{c^2R_2.V_1^2}{cX_m(cX_m+2cX_{sc})} \qquad (2.47)$$

$$P_I = \frac{V_1^2}{cR_m} - \frac{R_1.V_1^2}{cX_m(cX_m+2cX_{sc})} - \frac{(2cX_{sc}-(c-1).cX_m).R_1.I_1^2}{cX_m+2cX_{sc}} \qquad (2.48)$$

The iron loss component also includes the mechanical losses of friction and windage within the frame of the motor; the losses due to the external cooling fan are excluded as they do not contribute to the internal heating of the motor.

2.4.2 DISTRIBUTION OF THE MOTOR LOSSES

The stator copper losses, P_{SC}, are split between the slot end endwinding sections in the ratio of their respective mass. A factor, f, is derived from the manufacturers design data and is the ratio of the mass of the copper in the slot section divided by the total winding mass. Thus the slot and endwinding copper losses, P_{sw} and P_{ew} respectively, are given by,

$$P_{sw} = f.P_{SC} \tag{2.49}$$

$$P_{ew} = (1-f).P_{SC} \tag{2.50}$$

The iron loss and internal friction and windage losses, given by equation 2.48, are distributed evenly between the stator and rotor. Though it is likely that the iron losses, which form by far the largest component of these losses, will be concentrated mainly in the stator, no reliable information exists to indicate precisely what the percentage split might be. Tests performed on the smaller motors to produce such information, failed to give conclusive results, thus, as the friction and windage is concentrated around the rotor, the 50:50 distribution, used originally by Mellor, was retained. For ease, the loss distribution is assumed to be independent of the motor slip.

As physically the rotor iron loss will be concentrated around the rotor periphery, then this loss is introduced at the rotor winding node which, due to model approximations, occupies this area (equation 2.52). The stator iron loss is introduced solely at the stator teeth node (equation 2.51):

$$P_{st} = 0.5\ P_I \tag{2.51}$$

$$P_{rw} = P_{RC} + 0.5\ P_I \tag{2.52}$$

2.4.3 TEMPERATURE DEPENDENCE.

One of the features of the induction motor copper losses is their

dependence on the conductor temperature; for a given current the total losses can vary by up to 50% between a cold and hot motor. Referring to the piecewise solution of the thermal model, presented in the following section, temperature dependence may be implemented by adjusting the stator and rotor winding resistances R_1 and R_2, using equations 2.53 and 2.54 below, at every time step.

$$R_1 = (1+\alpha_{cu}T_S).R_{10} \tag{2.53}$$

$$R_2 = (1+\alpha_{al}T_R).R_{20} \tag{2.54}$$

R_{10} = stator winding resistance at 0°C (Ω)

R_{20} = referred rotor resistance at 0°C (Ω)

α_{cu} = temperature coefficient of resistance of stator winding material ($°C^{-1}$)

α_{al} = temperature coefficient of resistance of rotor winding material ($°C^{-1}$)

T_s = mean stator winding temperature (°C)

T_r = mean rotor winding temperature (°C)

The mean stator winding temperature must be calculated from the model estimations of the slot and endwinding temperatures, T_{sw} and T_{ew} respectively, using equation 2.55. The factor f is that previously defined in section 2.4.2.

$$T_S = f.T_{sw} + (1-f).T_{ew} \tag{2.55}$$

Though some error might be expected as T_{ew} is in fact the hot spot rather than the mean endwinding temperature, this error is assumed to have a negligible effect upon the final loss calculation.

2.5 THE MODEL SOLUTION.

The complete thermal model consists of the network of resistances, capacitances and thermal generators shown in figure 2.16. The model has fifteen nodes in total, ten of these are the mean temperature nodes of each bulk component; of the remaining five, four are the secondary nodes of the cylindrical conduction model of section 2.2.1, the remaining node forms the junction between the stator teeth, iron and slot winding components. The inter-node resistances that model convective heat transfer will have one of two values depending upon whether or not the motor is rotating or not.

Mathematically, the model can be described by a set of fifteen heat balance equations, one for each node. These may be presented in matrix notation by equation 2.56.

$$[C][dT] = [Y][T] + [G] \tag{2.56}$$

where,

[C] = 15x15 matrix of thermal capacitance

[Y] = 15x15 matrix of thermal admittances

[G] = 15x1 matrix of thermal generators

[T] = 15x1 matrix of nodal temperatures

[dT] = 15x1 matrix of the time derivative of the nodal temperatures.

The matrix of thermal admittances [Y] has two possible values $[Y_r]$ and $[Y_s]$ depending upon whether the motor is rotating or stationary, thus, two sets of equations of the form of equation 2.56 are required. The format of the [C] and [Y] matrices are shown in figures 2.17 and 2.18. The values of the matrix parameters, for each of the motors modelled, are presented in Appendix B.

It can be noted from the thermal model, figure 2.16, and from the [C] matrix in figure 2.18, that there are seven nodes with no thermal capacitance associated with them. These include the endcap air and airgap nodes. These nodes are of little interest in the motor protection application and can be removed mathematically by Gaussian elimination [39]. The resulting eight node representation is no less accurate, yet the computation time and memory required to store and compute the model have both been cut. Further, the removal of these nodes allows a non-zero determinant to be found for the diagonal [C] matrix which can then be inverted and equation 2.56, now of order eight, can be rewritten as,

$$[dT] = [Y'][T] + [C]^{-1}[G] \tag{2.57}$$

where,

$$[Y'] = [C]^{-1}[Y] \tag{2.58}$$

The equations are coupled - that is, each row equation involves all eight unknowns. Eigenvalue and eigenvector techniques [40] are used to express [T] in terms of an arbitrary vector [Z] and then to uncouple the equations.

Eight distinct eigenvalues λ_i and their associated eigenvectors $[X_i]$ can be found for [Y'] from the characteristic equation (equation 2.59) and equation 2.60 respectively.

$$\text{Det } ([Y']-\lambda[I]) = 0 \tag{2.59}$$

$$[Y'][X] = \lambda_i[X_i] \tag{2.60}$$

$[X_i]$ is the column eigenvector associated with the eigenvalue λ_i.

The eigenvalues and eigenvectors of the matrix [Y'], were found using numerical library routines [48] available on the mainframe computer.

As there exist eight distinct eigenvalues, then each of the eight eigenvectors are linearly independent; as such, the vector [T] may be expressed as a linear combination of the eigenvectors.

$$[T] = Z_1[X_1] + Z_2[X_2] + \ldots \quad Z_8[X_8] \tag{2.61}$$

In matrix form,

$$[T] = [X][Z] \tag{2.62}$$

[Z] is a scalar function made up of the variables Z_1 to Z_8.

[X] is the 8x8 matrix of eigenvectors made up of each of the column eigenvectors $[X_1]$ to $[X_8]$

Substituting for [T] in equation 2.57 and dividing through by [X] gives,

$$[dZ] = [X]^{-1}[Y'][X][Z] + [X]^{-1}[C]^{-1}[G] \tag{2.63}$$

The product $[X][Y'][X]^{-1}$ can be shown, from equation 2.60, to be equivalent to an eight by eight diagonal matrix of eigenvalues, therefore, by performing this substitution, the system can be described by a set of eight simultaneous equations of the form,

$$dZ_i = \lambda_i Z_i + u_i \tag{2.64}$$

u_i is the product of the i^{th} row calculation between the 8x8 matrix resulting from the multiplication of $[X]^{-1}[C]^{-1}$ and the generator matrix $[G]$.

Each row is now a function of one variable and appears in the familiar state variable form, still in terms of $[Z]$. The solution of this equation in the time domain for a given set of inputs $[G(t)]$ and initial conditions $[Z(0)]$ is well known and is,

$$Z_i = e^{\lambda_i t} Z_i(0) + e^{\lambda_i t} \int_0^t e^{-\lambda_i \tau} u_i(\tau)\, d\tau \tag{2.65}$$

In matrix form,

$$[Z(t)] = [e^{\lambda t}][Z(0)] + [e^{\lambda t}] \int_0^t [e^{-\lambda \tau}][X]^{-1}[C]^{-1}[G(\tau)]\, d\tau \tag{2.66}$$

Resubstituting for $[T]$ from equation 2.65 gives a particular solution to equation 2.33 as;

$$[T(t)] = [X][e^{\lambda t}][X]^{-1}[T(0)] + [X][e^{\lambda t}] \int_0^t [e^{-\lambda \tau}][X]^{-1}[C]^{-1}[G(\tau)]\, d\tau \tag{2.67}$$

A stepwise approximation to the above equation is made by assuming that the input, generator matrix, $[G(\tau)]$, remains constant over a time

period Δt considered to be small in comparison with the overall system time constants.

Integrating between the general limits of $(n-1)\Delta t$ and $n\Delta t$, gives rise to a solution in which the temperatures during the n^{th} time period $[T_{n\Delta t}]$ are expressed as a function of the temperatures during the previous $(n-1)^{th}$ time period $[T_{((n-1)\Delta t)}]$ plus a function of the n^{th} time period inputs $[G_{n\Delta t}]$.

$$[T_{n\Delta t}] = [X][e^{\lambda\Delta t}][X]^{-1}[T_{(n-1)\Delta t}] + [X][(e^{\lambda\Delta t}-1)/\lambda][X]^{-1}[C]^{-1}[G_{n\Delta t}] \quad (2.68)$$

Expressed alternatively,

$$[T_{n\Delta t}] = [D_1][T_{(n-1)\Delta t}] + [D_2][G_{n\Delta t}] \quad (2.69)$$

where,

$[D_1], [D_2]$ are constant matrices once Δt has been chosen.

Again two such equations exist, one for a rotating and another for a stationary machine,

$[D_1]=[D_{1r}]$, $[D_2]=[D_{2r}]$ for a running machine.

$[D_1]=[D_{1s}]$, $[D_2]=[D_{2s}]$ for a stationary machine.

The solution is exact for a stationary unsupplied machine ($[G]=0$) or for constant input conditions when the motor input voltage and current (hence $[G]$) do not vary with time. For other conditions it is assumed that the motor input current and voltage remain constant over the small time interval Δt.

The model can be solved in real time by measurement of the motor line current and voltage, enabling the calculation of the generator matrix $[G_{n\Delta t}]$ which is assumed to be valid over the interval Δt. The temperatures $[T_{n\Delta t}]$ are then calculated by simple matrix multiplication and addition from equation 2.69.

This solution gives the temperature rise at the model nodes with reference to the ambient conditions. If the absolute temperatures are required then the ambient temperature must be added as an offset.

The prediction of temperatures at some time in the future, defined by Δt, based upon the most recent measurements of the supply conditions, is a characteristic of the model solution. Normally, Δt would be chosen to be small so that the assumption that the generator matrix, $[G_{n\Delta t}]$, remains constant over this interval does not lead to large errors in the temperature predictions should the supply or load conditions change. In the application of the thermal model to motor protection, using data matrices, $[D_1]$ and $[D_2]$, formulated for a extended time step, Δt, of five minutes say, in addition to the small time step matrices used in the real time solution, would present the useful function of forecasting potential overtemperature conditions far enough in advance to enable possible corrective action to be taken in order to prevent that condition arising.

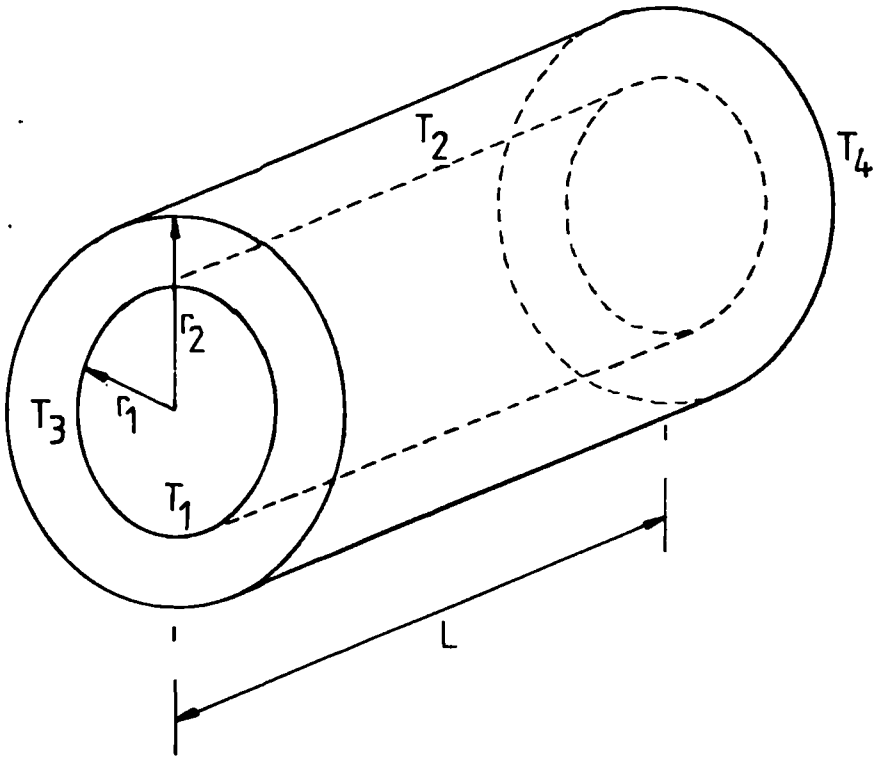

Figure 2·1 Two Dimensional Cylindrical Element

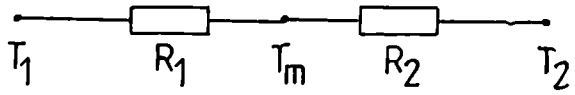

Figure 2·2 Zero Generation Model

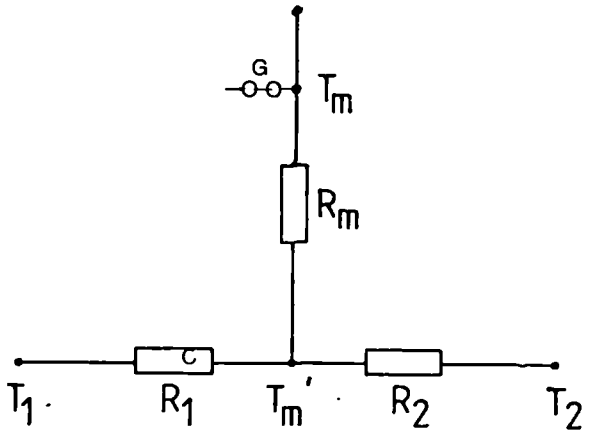

Figure 2·3 Radial Conduction Equivalent Circuit

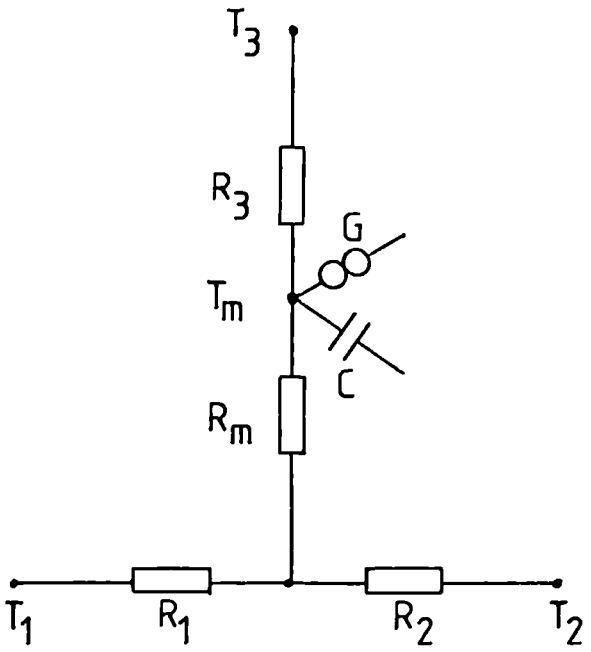

Figure 2·4 Two Dimensional Equivalent Circuit for Cylinder

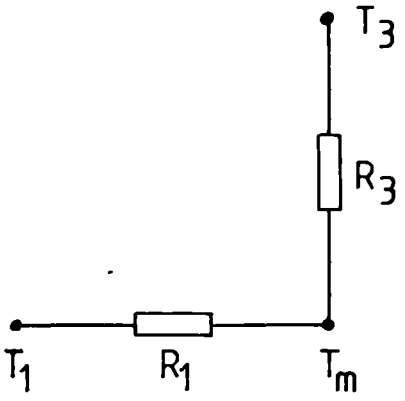

Figure 2·5 Model for Cylindrical Rod

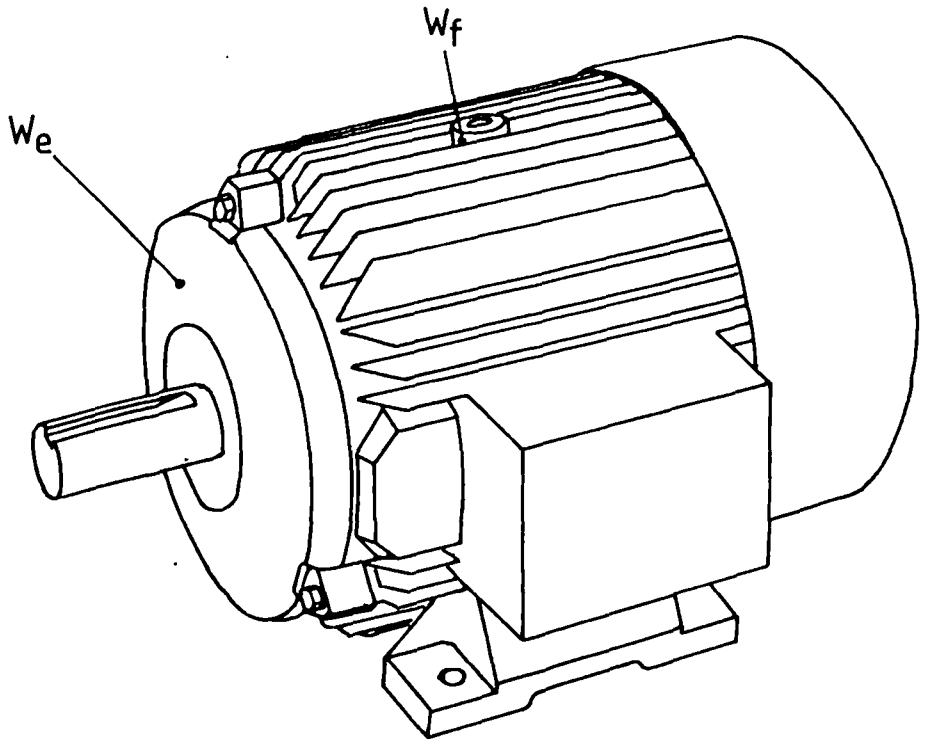

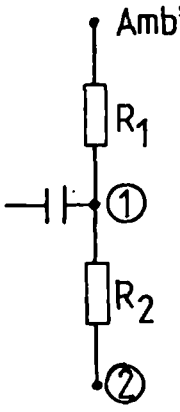

R_1 = Measured directly

$$R_2 = \frac{1}{h \pi L r}$$

$$C_1 = W_e C_e + \frac{1}{2} W_f C_f$$

	BCP 5.5KW	GEC 5.5KW	GEC 75KW
L = Stator length (m)	.1207	.1143	.280
r = Stator radius (m)	.1016	.1016	.200
Y_{1r} = Rotating frame-ambient thermal admittance (W/°C)	13.0	17.0	58.5
Y_{1s} = Stationary frame ambient thermal admittance (W/°C)	2.35	2.60	11.7
w_e = Mass of endcaps (kg)	3.97	.85	8.5
w_f = Mass of frame (Kg)	4.20	4.536	100.0
c_e = Endcap specific heat (J/Kg°C)	502.0	963.0	963.0
c_f = Frame specific heat (J/Kg°C)	896.0	963.0	963.0
h = Frame/core contact coefficient ($W/m^2°C$)	275.0	1500.0	887.0

Figure 2·6 Frame

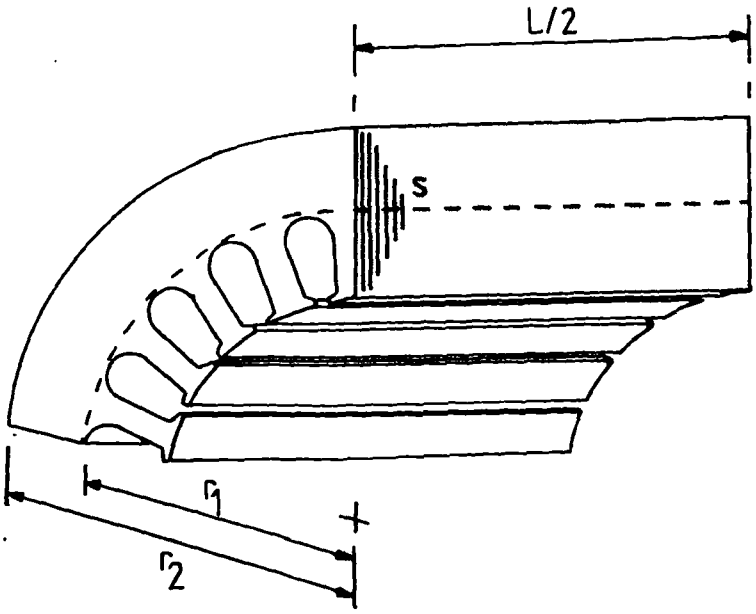

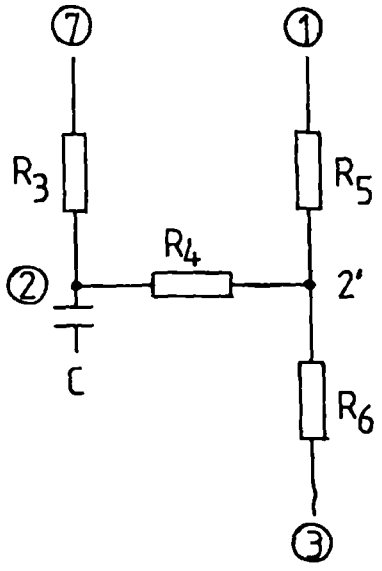

$$R_3 = \frac{L}{6\pi k_a (r_2^2 - r_1^2)}$$

$$R_4 = \frac{-1}{4\pi k_r L s (r_2^2 - r_1^2)} \left[r_1^2 + r_2^2 - \frac{4 r_1^2 r_2^2 \ln(r_2/r_1)}{(r_2^2 - r_1^2)} \right]$$

$$R_5 = \frac{1}{2\pi k_r L s} \left[1 - \frac{2 r_1^2 \ln(r_2/r_1)}{(r_2^2 - r_1^2)} \right]$$

$$R_6 = \frac{1}{2\pi k_r L s} \left[\frac{2 r_2^2 \ln(r_2/r_1)}{(r_2^2 - r_1^2)} - 1 \right]$$

$$C_2 = \frac{c \rho \pi L s (r_2^2 - r_1^2)}{2}$$

	BCP 5.5KW	GEC 5.5KW	GEC 75KW
L = Stator length (m)	.1207	.1143	.280
r_1 = Inner radius (m)	.0828	.0822	.164
r_2 = Outer radius (m)	.1016	.1016	.200
s = Stacking factor	.97	.97	.97
K_r = Radial conductivity (W/m°C)	45.2	45.2	45.2
K_a = Axial conductivity (W/m°C)	1.97	1.97	1.97
c = Steel specific heat (J/Kg°C)	502.0	502.0	502.0
ρ = Steel density (Kg/m^3)	7850.0	7850.0	7850.0

Figure 2·7 Stator Iron

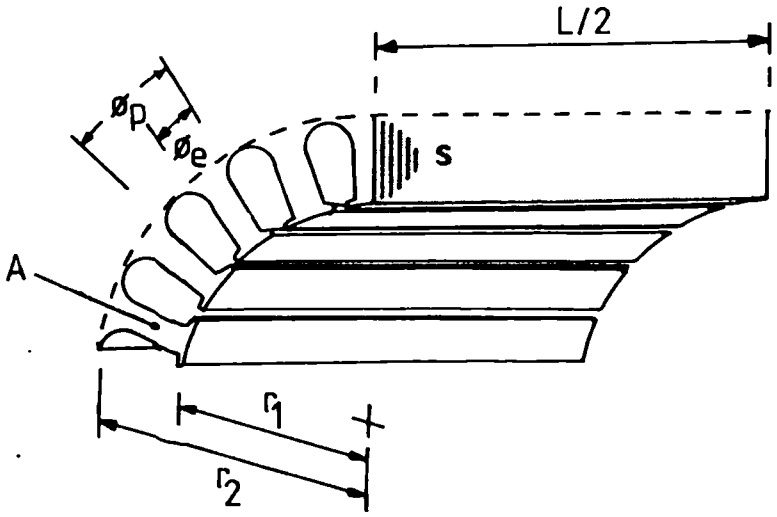

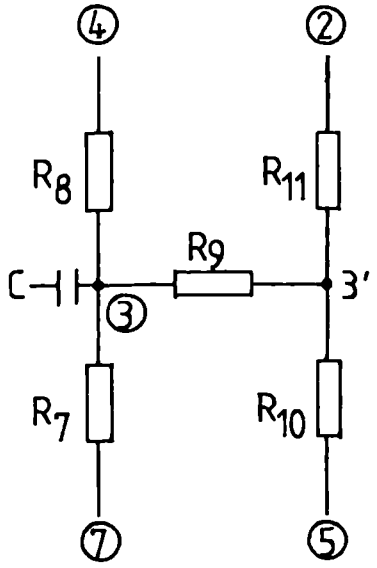

$$R_7 = \frac{L\phi_p}{6\pi k_a \phi_e (r_2^2 - r_1^2)}$$

$$R_8 = \frac{\pi\phi_e (r_2^2 - r_1^2)}{k_r L s \phi_p (r_2 - r_1)^2 n^2}$$

$$R_9 = \frac{-\phi_p}{4\pi k_r L s \phi_e (r_2^2 - r_1^2)} \left[r_1^2 + r_2^2 - \frac{4 r_1^2 r_2^2 \ln(r_2/r_1)}{(r_2^2 - r_1^2)} \right]$$

$$R_{10} = \frac{\phi_p}{2\pi k_r L s \phi_e} \left[\frac{2 r_2^2 \ln(r_2/r_1)}{(r_2^2 - r_1^2)} - 1 \right]$$

$$R_{11} = \frac{\phi_p}{2\pi k_r L s \phi_e} \left[1 - \frac{2 r_1^2 \ln(r_2/r_1)}{(r_2^2 - r_1^2)} \right]$$

$$C_3 = \frac{c\rho\pi L s \phi_e (r_2^2 - r_1^2)}{2\phi_p}$$

	BCP 5.5KW	GEC 5.5KW	GEC 75KW
L = Stator length (m)	.1207	.1143	.280
r_1 = Inner radius (m)	.0635	.0635	.1325
r_2 = Outer radius (m)	.0828	.0822	.164
s = Stacking factor	.97	.97	.97
K_r = Radial conductivity (W/m°C)	45.2	45.2	45.2
K_a = Axial conductivity (W/m°C)	1.97	1.97	1.97
ϕ_p = Tooth pitch (°)	10.0	10.0	7.5
ϕ_e = Equivalent tooth arc (°)	5.6	6.7	4.0
c = Steel specific heat (J/Kg°C)	502.0	502.0	502.0
ρ = Steel density (Kg/m^3)	7850.0	7850.0	7850.0
n = Number of teeth	36.0	36.0	48.0

Figure 2-8 Stator Teeth

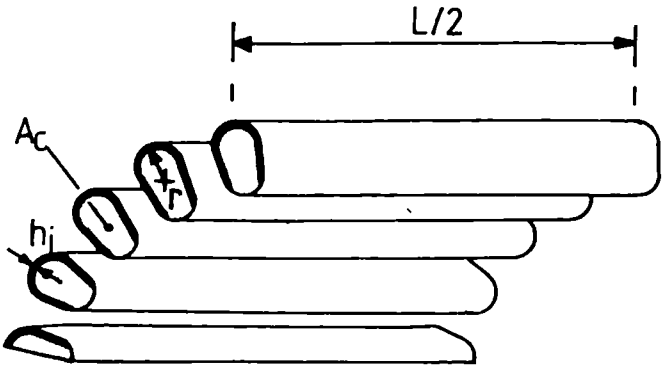

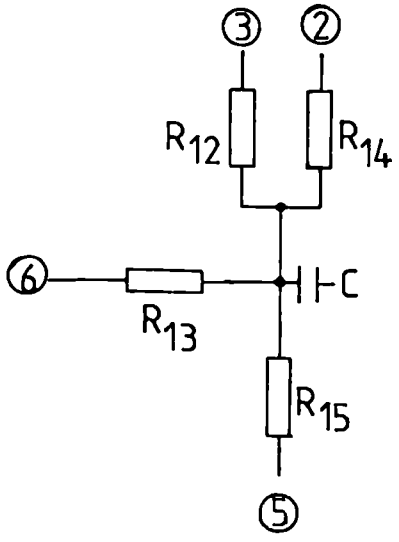

$$R_{12} = \frac{2h_i}{\pi k_i L r n} + \frac{1}{2\pi k_v L F n}$$

$$R_{13} = \frac{L}{6 k_c A_c n}$$

$$R_{14} = \frac{4h_i}{\pi k_i L r n} + \frac{1}{\pi k_v L F n}$$

$$R_{15} = \frac{1}{\pi k_v L F n}$$

$$C_4 = \frac{c \rho A_c L n}{2}$$

	BCP 5.5KW	GEC 5.5KW	GEC 75KW
L = Stator length (m)	.1207	.1143	.280
r = Equivalent winding radius (m)	.005	.00368	.0067
h_i = Insulation thickness (m)	.0005	.00033	.00033
A_c = Cross section of copper in slot (m^2)	.424 E-04	.425 E-04	.142 E-03
K_i = Slot liner conductivity (W/m°c)	.30	.30	.30
K_v = Varnish conductivity (W/m°c)	.40	.40	.40
F = Radial conductivity factor	2.5	2.5	2.5
K_c = Copper conductivity (W/m°c)	385.2	385.2	385.2
c = Copper specific heat (J/Kg°C)	383.2	383.2	383.2
ρ = Copper density (Kg/m^3)	8954.0	8954.0	8954.0
n = Number of slots	36.0	36.0	48.0

Figure 2·9 Stator Winding

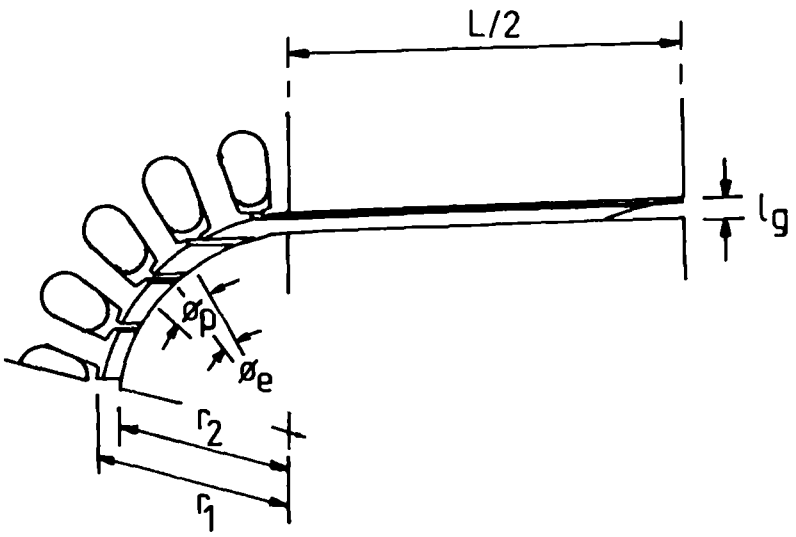

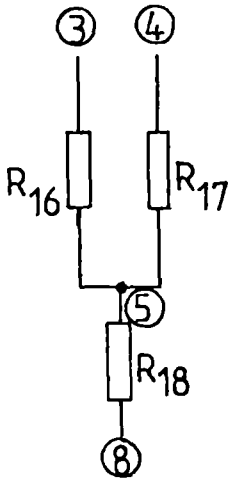

$$R_{16} = \frac{\phi_p}{\phi_e \pi r_1 h_{2s}(h_{2r})L}$$

$$R_{17} = \frac{\phi_p}{(\phi_p - \phi_e)\pi r_1 h_{2s}(h_{2r})L}$$

$$R_{18} = \frac{1}{\pi r_2 L h_{2s}(h_{2r})}$$

	BCP 5.5KW	GEC 5.5KW	GEC 75KW
L = Stator length (m)	.1207	.1143	.280
r_1 = Stator inner radius (m)	.0635	.0635	.1336
r_2 = Rotor radius (m)	.0625	.0632	.1325
ϕ_p = Tooth pitch (°)	10.0	10.0	7.5
ϕ_e = Equivalent tooth arc (°)	5.6	6.7	4.0
h_{2r} = Rotating airgap heat transfer coefficient ($W/m^2°C$)	67.9	219.2	102.8
h_{2s} = Stationary airgap heat transfer coefficient ($W/m^2°C$)	61.8	199.3	55.25

Figure 2·10 Air Gap

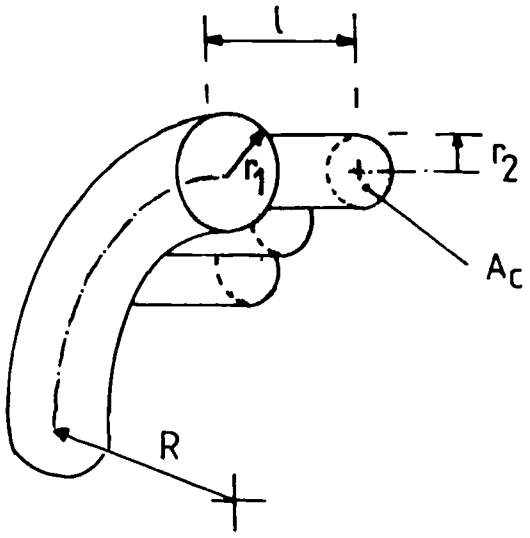

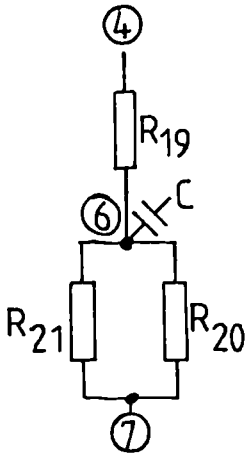

$$R_{19} = \frac{l_w}{n A_c k_c}$$

$$R_{20} = \frac{w}{16\pi^2 R F k_v}$$

$$R_{21} = \frac{w r_1^2}{8\pi r_2^2 L F k_v n}$$

$$C_6 = \frac{\rho_c C A_c n (1-\alpha)}{w} \frac{LT}{2}$$

	BCP 5.5KW	GEC 5.5KW	GEC 75KW
R = Endwinding toroid radius (m)	.079	.073	.148
r_1 = endwinding cross-section radius (m)	.012	.013	.0259
r_2 = Stator winding effective radius (m)	.005	.00368	.0067
l = Slot winding overhang (m)	.034	.025	.033
A_c = Cross section of copper in slot (m^2)	.424 E-04	.425 E-04	.142 E-03
K_v = Varnish conductivity (W/m°c)	.40	.40	.40
F = Radial conductivity factor	2.5	2.5	2.5
K_c = Copper conductivity (W/m°c)	385.2	385.2	385.2
c = Copper specific heat (J/Kg°C)	383.2	383.2	383.2
ρ = Copper density (Kg/m^3)	8954.0	8954.0	8954.0
n = Number of slots	36.0	36.0	48.0
w = Surface-hot spot:surface-mean temperature ratio	1.5	1.5	1.5
α = Slot: $^{\text{total}}_{\text{winding}}$ volume ratio	.389	.388	.465
L_T = Effective stator winding length (m)	.3103	.2946	.602

Figure 2·11 Endwinding

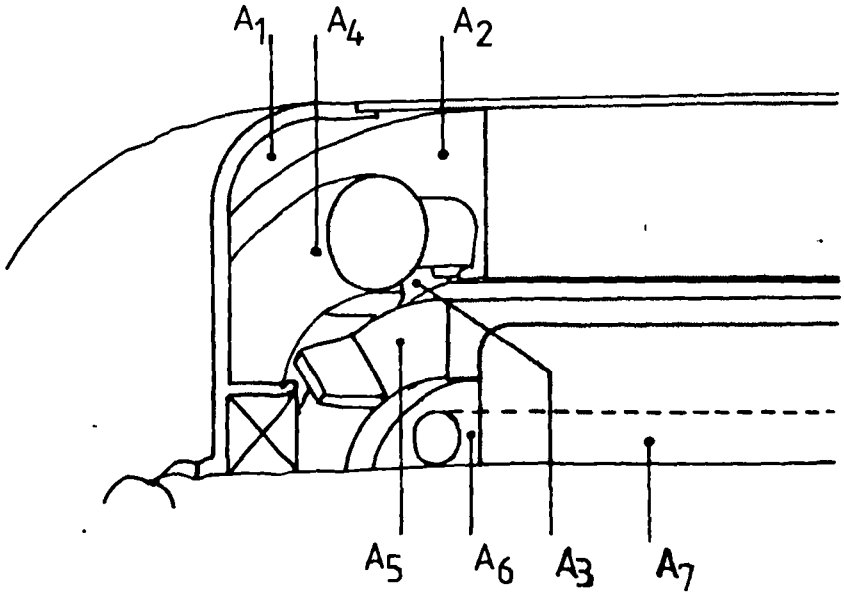

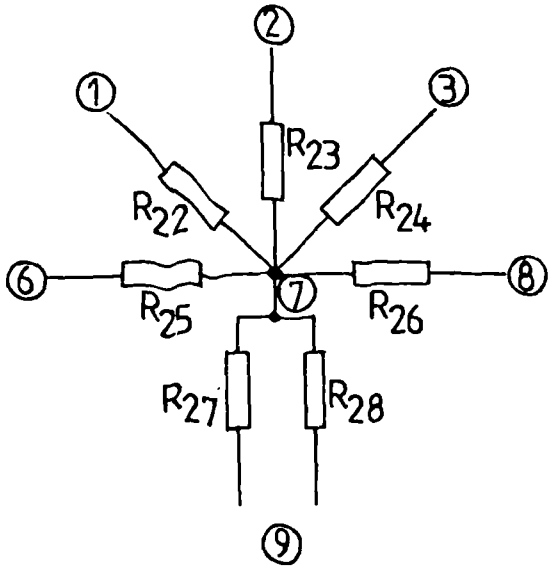

$$R_{22} = \frac{1}{h_{3s}(h_{3r})A_1}$$

$$R_{23} = \frac{1}{h_{3s}(h_{3r})A_2}$$

$$R_{24} = \frac{1}{h_{3s}(h_{3r})A_3}$$

$$R_{25} = \frac{1}{h_{3s}(h_{3r})A_4}$$

$$R_{26} = \frac{1}{h_{3s}(h_{3r})A_5}$$

$$R_{27} = \frac{1}{h_{3s}(h_{3r})A_6}$$

$$R_{28} = \frac{1}{h_{4s}(h_{4r})A_7}$$

	BCP 5.5KW	GEC 5.5KW	GEC 75KW
A_1 = Contact area of endcap (m^2)	.067	.107	.299
A_2 = Contact area of stator iron (m^2)	.0109	.0112	.0412
A_3 = Contact area of stator teeth (m^2)	.0049	.0057	.01453
A_4 = Contact area of endwinding (m^2)	.0759	.0744	.315
A_5 = Contact area of rotor fan and end-discs (m^2)	.0216	.0229	.1179
A_6 = Contact area of rotor iron (m^2)	.0044	.00864	.0448
A_7 = Contact area of rotor cooling hole (m^2)	.012	0.0	0.0
h_{3r} = Rotating endcap heat transfer coefficient ($W/m^{2\circ}C$)	38.9	38.6	65.1
h_{3s} = Stationary endcap heat transfer coefficient ($W/m^{2\circ}C$)	15.5	15.5	15.5
h_{4r} = Rotating rotor cooling hole coefficient ($W/m^{2\circ}C$)	18.8	0.0	0.0
h_{4s} = Stationary rotor cooling hole coefficient ($W/m^{2\circ}C$)	15.5	0.0	0.0

Figure 2·12 Endcap Air

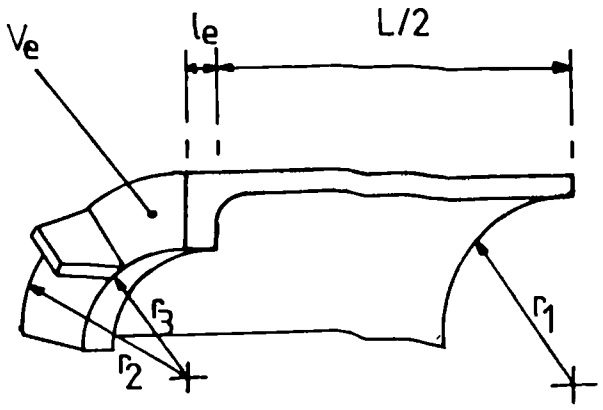

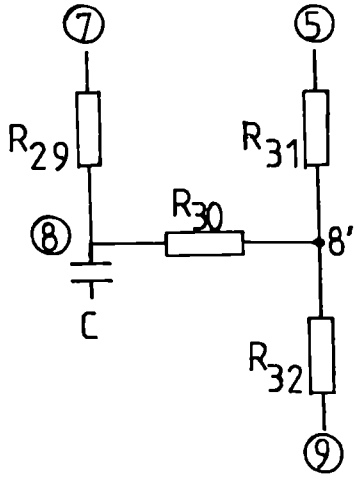

$$R_{29} = \frac{L}{6\pi k_a (r_2^2 - r_1^2)} + \frac{l_e}{\pi k_a (r_2^2 - r_3^2)}$$

$$R_{30} = \frac{-1}{4\pi k_a L (r_2^2 - r_1^2)} \left[r_1^2 + r_2^2 - \frac{4 r_1^2 r_2^2 \ln(r_2/r_1)}{(r_2^2 - r_1^2)} \right]$$

$$R_{31} = \frac{1}{2\pi k_a L} \left[1 - \frac{2 r_1^2 \ln(r_2/r_1)}{(r_2^2 - r_1^2)} \right]$$

$$R_{32} = \frac{1}{2\pi k_a L} \left[\frac{2 r_2^2 \ln(r_2/r_1)}{(r_2^2 - r_1^2)} - 1 \right]$$

$$C_8 = c_a \rho_a \left[\frac{\pi L (r_2^2 - r_1^2)}{2} + V_e \right]$$

L = Rotor length (m)

r_2 = Rotor radius (m)

r_1 = Equivalent rotor winding radius (m)

r_3 = Enddisc inner radius (m)

V_e = Volume of end-disc and fan (m)

l_e = End-disc width (m)

k_a = Aluminium conductivity (W/m°C)

ρ_a = Aluminium density (Kg/m^3)

c_a = Aluminium specific heat (J/Kg°C)

BCP 5.5KW	GEC 5.5KW	GEC 75KW
.1207	.1143	.280
.0625	.0631	.1325
.0576	.0581	.1277
.0381	.0348	.0561
.84 E-04	.104 E-03	.122 E-02
.0095	.0119	.027
204.0	211.0	211.0
2707.0	2707.0	2707.0
896.0	896.0	896.0

Figure 2·13 Rotor Winding

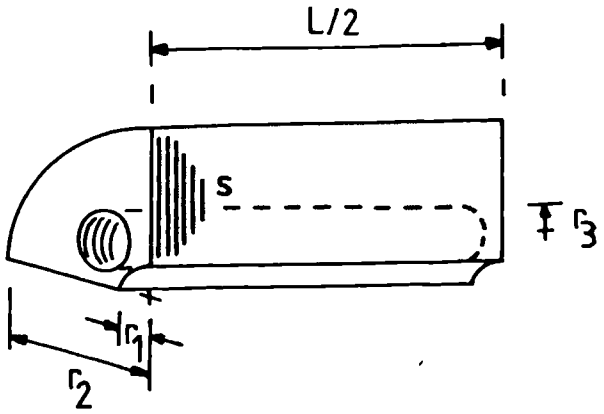

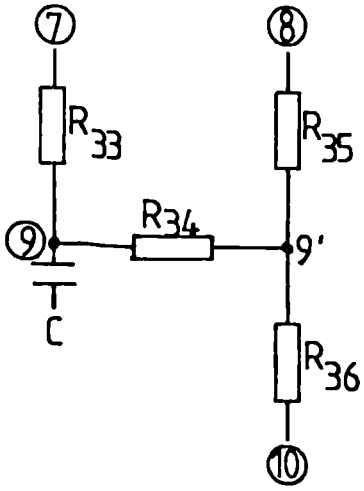

$$R_{33} = \frac{L}{6\pi k_a (r_2^2 - r_1^2 - n r_3^2)}$$

$$R_{34} = \frac{-1}{4\pi k_r L s (r_2^2 - r_1^2 - n r_3^2)} \left[r_1^2 + r_2^2 - \frac{4 r_1^2 r_2^2 \ln(r_2/r_1)}{(r_2^2 - r_1^2)} \right]$$

$$R_{35} = \frac{(r_2^2 - r_1^2)}{2\pi k_r L s (r_2^2 - r_1^2 - n r_3^2)} \left[1 - \frac{2 r_1^2 \ln(r_2/r_1)}{(r_2^2 - r_1^2)} \right]$$

$$R_{36} = \frac{(r_2^2 - r_1^2)}{2\pi k_r L s (r_2^2 - r_1^2 - n r_3^2)} \left[\frac{2 \ln(r_2/r_1) r_2^2}{(r_2^2 - r_1^2)} - 1 \right]$$

$$C_9 = \frac{c \rho \pi L s (r_2^2 - r_1^2 - n r_3^2)}{2}$$

	BCP 5.5KW	GEC 5.5KW	GEC 75KW
L = Rotor length (m)	.1207	.1143	.280
r_1 = Inner radius (m)	.0222	.025	.045
r_2 = Outer radius (m)	.0576	.0581	.1277
r_3 = Cooling hole radius (m)	.00635	0.0	0.0
s = Stacking factor	.97	.97	.97
K_r = Radial conductivity (W/m°C)	45.2	45.2	45.2
K_a = Axial conductivity (W/m°C)	1.97	1.97	1.97
c = Steel specific heat (J/Kg°C)	502.0	502.0	502.0
ρ = Steel density (Kg/m^3)	7850.0	7850.0	7850.0
n = Number of cooling holes	5.0	0.0	0.0

Figure 2·14 Rotor Iron

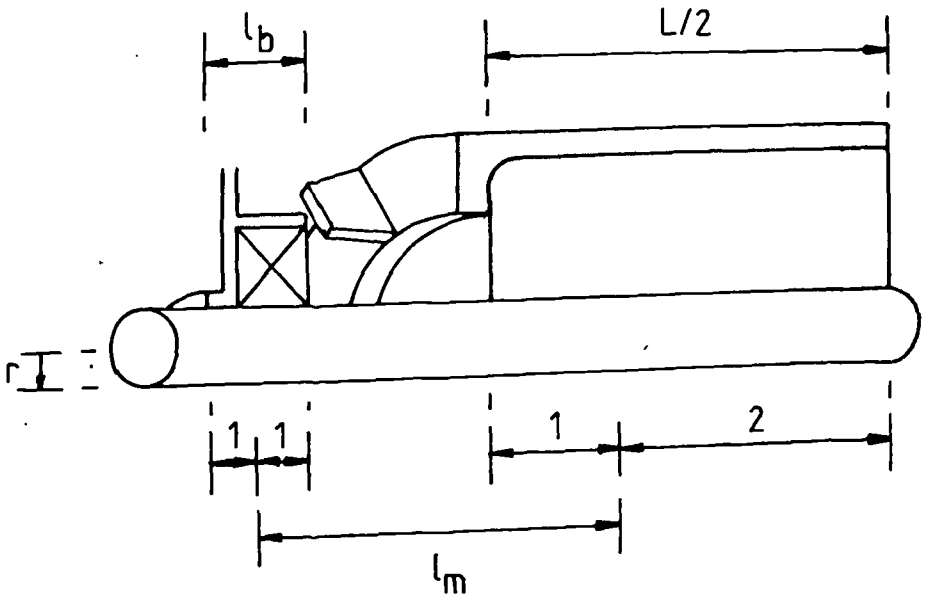

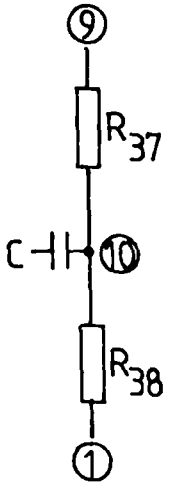

$$R_{37} = \frac{1}{2\pi k_s L} + \frac{l_m}{2\pi k_s r^2}$$

$$R_{38} = \frac{1}{4\pi k_s l_b} + \frac{l_m}{2\pi k_s r^2}$$

$$C_{10} = \rho c \pi r^2 \left(l_m + \frac{1}{2} l_b + \frac{1}{6} L\right)$$

	BCP 5.5KW	GEC 5.5KW	GEC 75KW
L = Rotor length (m)	.1207	.1143	.280
l_b = Bearing housing length (m)	.0254	.01845	.02825
l_m = Length between bearing centre and rotor mean (m)	.0931	.11295	.239
r = Shaft radius (m)	.0222	.025	.044
k = Steel conductivity (W/m°C)	41.3	41.3	41.3
c = Steel specific heat (J/Kg°C)	502.0	502.0	502.0
ρ = Steel density (Kg/m^3)	7850.0	7850.0	7850.0

Figure 2·15 Shaft

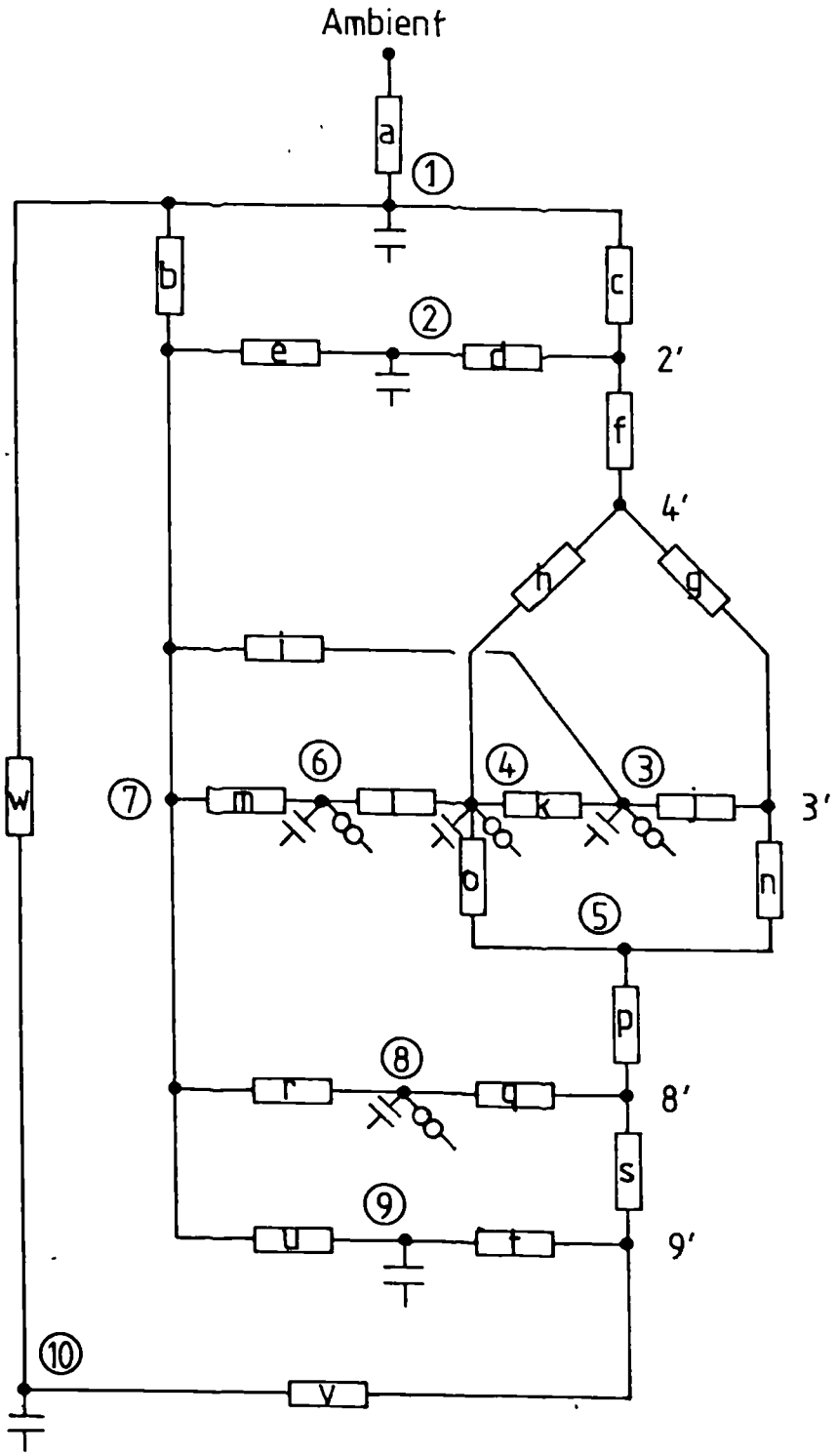

Figure 2·16 Induction Motor Thermal Equivalent Circuit

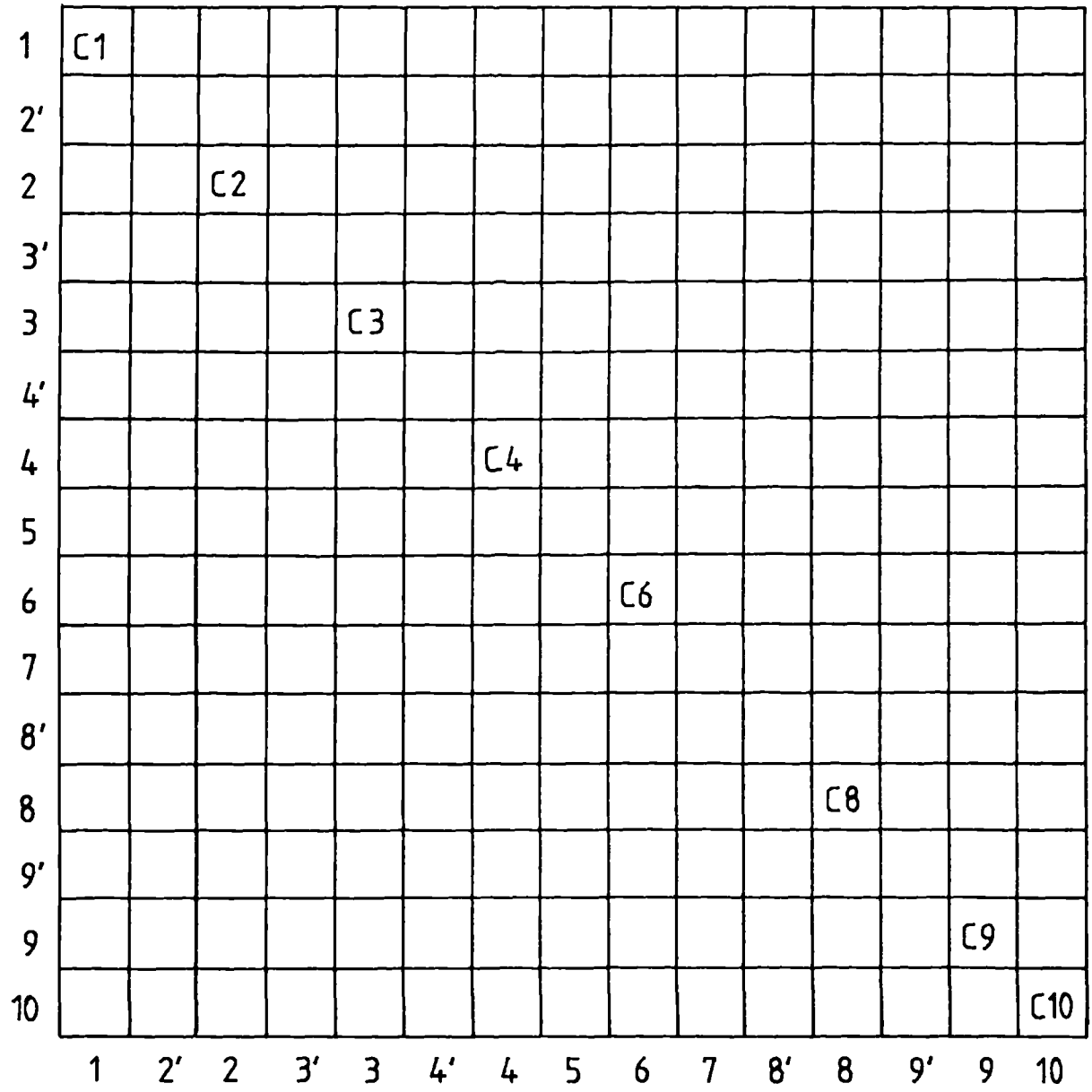

Figure 2·17 Thermal Capacitance Matrix

	1	2'	2	3'	3	4'	4	5	6	7	8'	8	9'	9	10
1	X_1	Y_c								Y_b					Y_w
2'	Y_c	$X_{2'}$	Y_d			Y_f									
2		Y_d	X_2							Y_e					
3'				$X_{3'}$	Y_j	Y_g		Y_n							
3				Y_j	X_3		Y_k			Y_i					
4'		Y_f		Y_g		$X_{4'}$	Y_h								
4					Y_k	Y_h	X_4	Y_o	Y_l						
5				Y_n			Y_o	X_5			Y_p				
6							Y_l		X_6	Y_m					
7	Y_b		Y_e		Y_i				Y_m	X_7		Y_r		Y_u	
8'								Y_p			$X_{8'}$	Y_q	Y_s		
8										Y_r	Y_q	X_8			
9'											Y_s		$X_{9'}$	Y_t	Y_v
9										Y_u			Y_t	X_9	
10	Y_w												Y_v		X_{10}

$X_n = -$ (Sum of Admittances in Row n)

Figure 2·18 Thermal Admittance Matrix

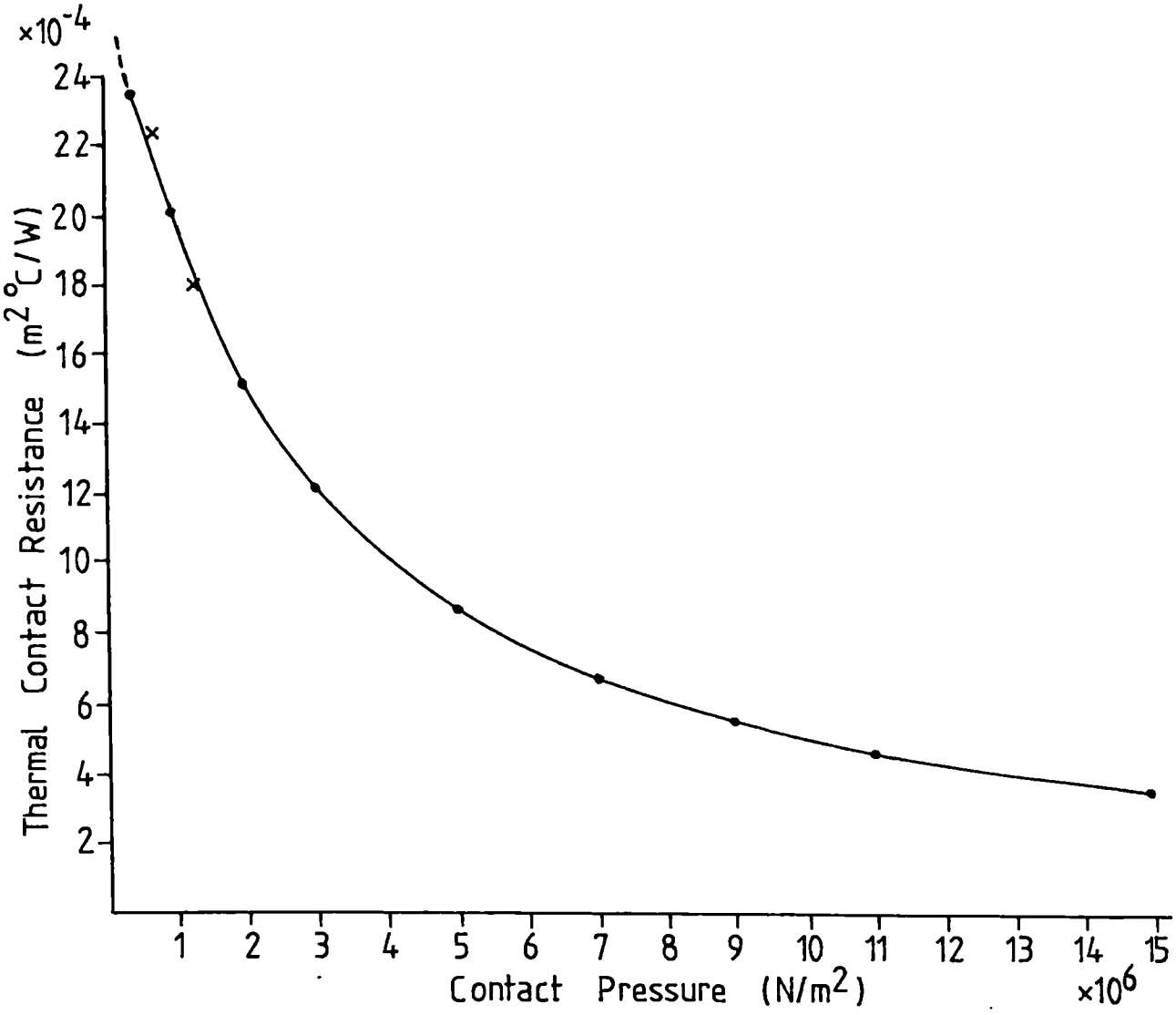

× Brunot's experimental points

• Best fit with Shlykov's equation

Figure 2·19 Extrapolated Contact Resistance Curve

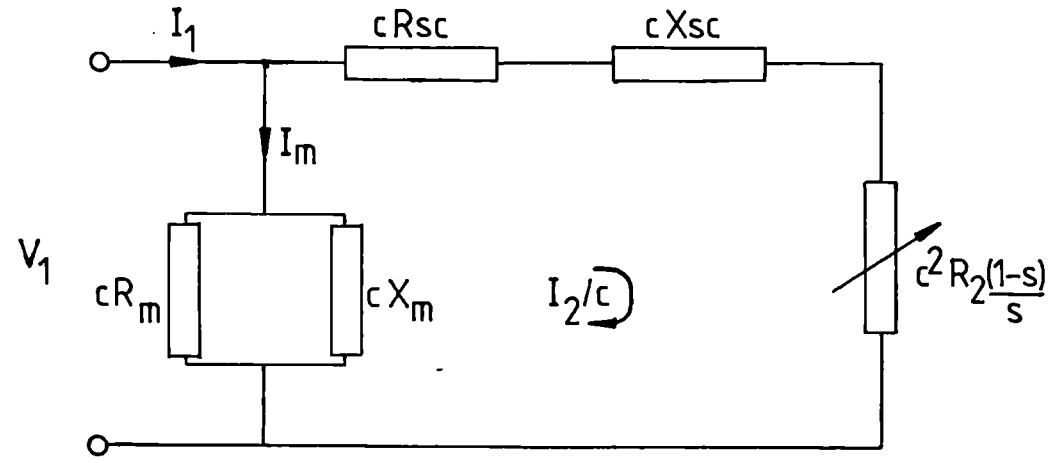

$$cRsc = cR_1 + c^2R_2$$

$$cXsc = cX_1 + c^2X_2$$

$$c \approx 1 + \frac{X_1}{cX_m}$$

Figure 2·20 Induction Motor Electrical Equivalent Circuit

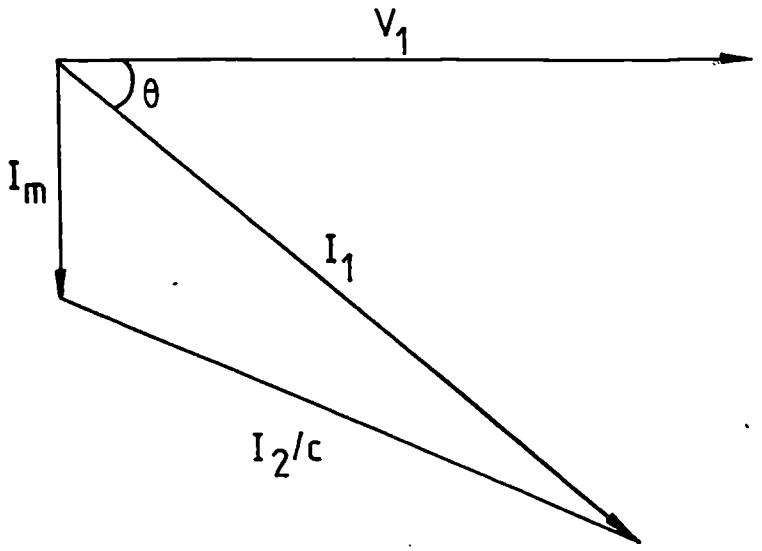

Figure 2·21 Equivalent Circuit Phasor Diagram

CHAPTER 3. THE ON-LINE PREDICTOR AND DATA LOGGER.

3.1 INTRODUCTION.

This Chapter deals with the development of a prototyping system which was used to gather data upon the motor supply conditions and temperatures during varying load tests performed on each of the motors. The data was later made available to the mainframe computer where it was used in the thermal model calculations and in the production of the comparisons between measured and simulated temperatures shown, and discussed, in Chapter 4.

The prototyping system, which incorporated an Intel 8085A microprocessor, was also used in the development of the on-line predictor which computed the thermal model in real time and, as such, formed the basis of the study into the feasibility of using the thermal model in a motor protection device. It was not the intention during this work to produce a working prototype so the prototyping system, whilst it contained all the elements which would be required in a working device, also contained additional elements of hardware and software used in the data logging function and other duties. The specific elements required in a commercial device, incorporating the other protective functions, commonly found in contemporary devices, are identified more explicitly in the final section of this chapter.

The choice of an 8085A microprocessor for the thermal predictor, was simply a matter of availability and the accessibility of suitable

software development equipment [42], though it is worth noting that this same processor was used in the other contemporary, microprocessor based devices identified in Chapter 1 [7-10].

To meet the requirement of computational accuracy using this eight bit microprocessor, all the model arithmetic was performed correct to sixteen binary digits. In this respect, it might have seemed more sensible to have chosen a sixteen bit microprocessor, such as an Intel 8088; however, the attractions of such a sixteen bit system are somewhat offset by the high cost in comparison with modern eight bit systems. It is considered that in a commercial device, unless the difference in costs between sixteen and eight bit systems fall and so long as sufficient accuracy is possible, it is likely that a processor similar to the Intel 8085 would be adopted. The subject of the accuracy, or resolution, of the microprocessor thermal model calculations is discussed in detail, with the support of some experimental findings in section 3.4.

3.2 THE PROTOTYPING SYSTEM.

A schematic of the prototyping system used to perform the on line thermal predictions and data logging duties is shown in figure 3.1. The system was developed to perform the data logging duties required to provide data for the mainframe computer which could then be used to compute the thermal model and subsequently, to provide a comparison between the measured and simulated temperatures. In addition to this duty, the prototyping system was also programmed with the thermal model which was computed in real time in the same way as would be required from a working protection device. The real time simulated temperatures

and measured data were recorded and transferred to the mainframe computer which, in this instance, acted in a purely passive role to convert the transferred data into the graphical comparisons shown in the next Chapter.

The system was based upon an Intel 8085A microprocessor which was itself housed in an SDK 85 development kit [43]. This provided all the 8085 hardware support required to make a working computer system - memory, input/output ports, a programmable timer, and a hexadecimal keypad with a six digit, seven segment display. To supplement the 512 bytes of Random Access Memory (RAM) available in the kit, an additional one kilobyte was added externally. Four kilobytes of Read Only Memory (ROM) were also added to simplify the software development. This memory was eventually used to hold the thermal predictor and data logging software as well as the thermal model data.

3.2.1 TEMPERATURE MEASUREMENTS.

Platinum resistance thermometers were chosen to measure the motor temperatures to compare with the predicted data produced by the thermal model. Despite their relatively large size, their ease of use made them preferable to devices, such as thermocouples, that require a cold junction; the difference in thermal time constants between the two devices were considered negligible with respect to those of the induction motor.

The prototyping system accommodated up to ten thermometers which were wired in series and supplied from a constant current source. Each thermometer was individually addressed and could be accessed via semi-

conductor switches, the digitized thermometer output becoming available to the SDK 85 system bus after a time governed by the analogue to digital conversion time. Four wire thermometers were used to ensure that the digital representation of the temperatures did not include any voltage drops that might have occurred in the current carrying conductors.

The hardware was set up to measure temperatures in the range 0°C to 255°C with a resolution of 1°C. Generally, only eight of the ten available thermometers were used in any one test, the other two positions were occupied by high stability resistances, representing 0°C and 255°C respectively, so that the system calibration could be checked throughout the tests.

A comparison was made between temperatures measured using this system and those measured by thermocouples which had been left in situation in the 75kW motor, following tests performed previously by the manufacturer. At one location, on the frame, a thermocouple and a platinum resistance thermometer were mounted in close enough proximity to assume that they were measuring the same temperature. The agreements, shown for thermal steady state conditions during no load and locked rotor tests on the motor in table 3.1, are good and support the choice of the easier to use resistance thermometers.

In order to provide a sensible reference against which the thermal model performance could be compared, the thermometers were located at points considered to approximate to the mean temperatures of the accessible model elements; these are shown in figure 3.2. For the stator back iron and teeth this involved drilling holes to a depth which would align

the thermometers with the radial centre of the element, at an axial position which corresponded to the mean of a parabola, symmetric about the axial centre of the motor. Generally, the axial thermal asymmetry, due to the cooling fan at the non drive end of the motor, was ignored though if thermometers were available, drive end and non drive end temperatures were measured and the average taken. The holes that were drilled were kept as small as possible to prevent excessive disturbance to the original motor heat flow.

Stator slot winding temperatures were measured by inserting thermometers into convenient spaces where the array of winding conductors met the slot liner (figure 3.3). Generally two thermometers were employed, one at at each axial end; the circumferential location was governed solely by the availability of suitable spaces. It was found from the results of the manufacturers full load heat run test on the 75 kW motor, that the position normally occupied by the drive end slot winding thermometer, gave the best approximation (within 5%) to the component's mean temperature calculated from the average of 24 thermocouple readings.

The nearest suitable locations to the endwinding hot spot temperature, presumed to be in the radial centre of the array of conductors modelled by the toroid in endwinding model of Chapter 2, were provided by irregularities at the endwinding surface between which the thermometer probes could be inserted. As well as providing a better approximation to the endwinding hot spot, this also provided a better mechanical and thermal contact than could be achieved by merely strapping the thermometer to the endwinding surface. Again, examination

of the manufacturers heat run results, revealed that the temperatures, at similar positions to those occupied by the resistance thermometers on the drive end endwinding, were within 5% of the hottest recorded endwinding temperature though it could not be proved that this was the true hot spot temperature.

Thermal cement was employed throughout to ensure a good thermal contact between the thermometer and it s surroundings.

	PLAT. RES. THERM.	THERMOCOUPLE
NO-LOAD	35	35.1
LOCKED ROTOR	79	78.4

Table 3.1. Comparison of thermocouple and platinum resistance thermometer measurements in °C.

3.2.2 SUPPLY MONITORING

A digital measurement of the motor input current (RMS) in one phase was implemented using a true RMS to DC converter. Any imbalance between the line currents was assumed to be small: this was generally found to be the case for the tests, using the balanced three phase laboratory supply, in which this current monitoring circuit was used. The circuit was scaled to give a resolution of 0.06A for the small motors, and 0.6A for the 75 kW motor, considered to be more than adequate for this application. This circuit was later superceded by the sequence current measuring system described in Chapter 5.

For simplicity, throughout the model testing, the motor supply voltage was assumed to remain constant and was entered, as a constant, with the other thermal model data.

3.2.3 DATA RECORDING.

The final peripheral associated with the prototyping system was a paper tape punch which was used to provide a permanent copy of the data recorded during the tests. It also provided the medium of data transfer to the University's mainframe computer. Data was recorded on the paper tape at one minute intervals. During the balanced supply tests, this data consisted either of the line current and the ten thermometer readings, or these items plus the eight microprocessor predicted temperatures, depending on whether the thermal predictor software had been invoked or not. During the unbalanced supply tests the results of the sequence current measuring system, consisting of all three line currents and the sequence currents, were recorded in addition to the thermometer temperatures.

A more detailed description of the prototyping system, including circuit diagrams, is given in Appendix C.

3.3 THERMAL PREDICTOR SOFTWARE.

The matrix calculations required of the microprocessor in performing the model solution are described by equation 2.69 derived in the previous chapter.

$$[T_{n\Delta t}] = [D_1].[T_{(n-1)\Delta t}] + [D_2].[G_{n\Delta t}]$$

The product $[D_2].[G_{n\Delta t}]$ represents the temperature rise of each node caused by the input of heat from the motor losses, over a time period of Δt, whilst the product of $[D_1]$ and the previous time step matrix, $[T_{(n-1)\Delta t}]$, gives the nodal temperature change due to heat transfer between the model nodes over the same period. The sum of the products gives the new temperature matrix, $[T_{n\Delta t}]$, valid from the beginning of the next time step.

To ensure that the approximation that the motor losses remain constant over the time period Δt remains valid, this time step must be chosen to be short in relation to the overall motor time constants. On the other hand, Δt must be long enough to allow the processor sufficient time to accomplish the thermal computations and other duties required of it, be they data logging duties, as here, or possibly other protection functions in a protection device, without overlapping into the next cycle. In accordance with these criteria, a time step of one second was chosen.

To implement the one second cycle time, the software was run under the control of a real time clock which was stored in the prototyping system memory and was constantly updated by interrupts from the system's programmable timer/counter. The timer was programmed to give a square wave of 5ms duration - the nearest convenient divisor of one second to the maximum count capability of 5.33ms- and connected to the RST 7.5 interrupt pin of the 8085A processor.

The structure of the on-line predictor software is best illustrated by the timing diagram and flowcharts of figure 3.4. After initialisation, measurements of the motor temperatures and the input current are

recorded; the former are superfluous to the real time solution, apart from the ambient measurement, but are recorded to give a comparison with the real time predicted temperatures. The input line current is squared upon input and used to indicate whether the stationary or rotating equations apply: zero current is used to indicate that the motor is de-energized and is in a stationary cooling condition. It should be noted that under these conditions the thermal generator calculations are omitted and the time required for the model computations will be less than the 200ms shown in figure 3.4 as this is based upon the rotating model solution. The time remaining after the calculations are complete is spent either in an idle state, waiting for the beginning of the next cycle, or in punching the measured and predicted data onto paper tape, depending upon where within the one minute punching cycle the programme is operating.

In a protection application, this time could be spent implementing the other protection functions identified in section 3.5 of this Chapter and possibly performing the prediction function which is a characteristic of the model solution. The second computation would take less time than the first as the generator matrix would not need re-calculating, thus leaving more than half the one second cycle time to perform any additional duties.

The introduction of the sequence current measurements and the additional calculations associated with the unbalanced model (Chapter 5) will also add to the computation time. However, even with these extra calculations, the complete model execution time, including the prediction cycle, should not exceed 600 ms.

The choice of the number of bits used for storage and calculation of the model constants and variables, has a pronounced effect upon the thermal model performance. A sixteen bit word length was adopted as it provided a greatly enhanced resolution in comparison with eight bits, but did not pose the additional software complications which would have resulted from the use of a twenty four bit word length. The consequences of this choice are the subject of the next section.

In addition to the nodal temperature rises, given by the thermal calculations, the true nodal temperatures, found by the addition of the ambient, are required both for use in the computation of the temperature weightings to be applied to the thermal generators and, in this application, to allow a direct comparison between the measured and predicted temperatures. In the on-line predictor, use was made of the ambient temperatures recorded as part of the data logging duties; though, in a commercial device, the expected average ambient temperature could be programmed as a model constant.

More details of the thermal model software can be found in Appendix D.

3.4 THERMAL MODEL RESOLUTION.

Anticipating the results of the first on-line predictor varying load test, presented graphically as predicted and measured temperatures versus time in the next Chapter (figures 4.16-4.20), the predictions appear to fail after the first 2 hours of a $2\frac{1}{2}$ hour stationary cooling period. This phenomenon was confirmed in a separate test when the

motor was heated, by running on load, then allowed to cool with the on-line predictor still running, figure 4.21. The post test analysis revealed that the problem was due to the resolution of the thermal calculations; the temperature change over the one second cycle time was too small to be registered as a change in the least significant bit of the sixteen bit representation of the nodal temperatures, hence, the predicted temperatures remain constant while those measured continue to fall.

This effect was apparent only during stationary cooling as the more gradual temperature changes resulting from the longer thermal time constants make the resolution critical. The problem was therefore remedied by substituting constant matrices formulated for a time step of 60 seconds in the place of the original one second matrices with some success (figures 4.22 and 4.23-4.27). While the presumption that this effect would only occur during stationary cooling was supported, to some extent, by the experimental findings, later analysis has revealed that this is not necessarily so and that the thermal model resolution is a potentially more serious problem.

An indication of the errors involved in using different word sizes in the model calculations was obtained by computing the full load steady state endwinding temperature on the mainframe computer correct to 32 bits, then constricting the resolution of the solution to word sizes between eight and twenty four bits and comparing the results. Graphs of percentage error, when compared with the 32 bit solution, versus the number of bits used to represent the model temperatures, were plotted for one of the 5.5 kW motors and for the 75 kW motor. They are shown in figures 3.5 and 3.6 respectively.

The graphs show the importance of an adequate model resolution; eight bits are completely inadequate, whilst sixteen bits give a 5.7% error for the 5.5 kW motor but a 17.9% error for the larger motor. A twenty four bit word length gives an error of less than 0.03% in both cases.

The curves, shown by the dashed lines, represent the results for an extended time step of two seconds. They show the benefits, with respect to the model resolution, that can be gained by this action; increasing the time step by a factor of two leads to an approximately proportionate reduction in the error at sixteen bits. However, these benefits must be weighed against the increased error in the stepwise solution that would occur during gradual load changes, and the possibility of missing short duration input line transients.

It would appear that, in order to ensure an accurate model solution which can be generally applied to induction motors up to 75 kW, a twenty four bit word length might be necessary. There is no reason, in principle, why such a solution could not be implemented on an 8085A microprocessor system, using similar methods to those adopted for sixteen bits. The solution would, however, take longer, and require more memory than the present sixteen bit implementation. The extra time could be relatively easily recovered by upgrading the 8085A system clock to 5 MHz (the maximum clock rating for this particular processor), as the present system operates from the 3.2 MHz clock provided on the SDK 85.

3.5 A MOTOR PROTECTION DEVICE.

The results recorded during the on-line predictor tests indicate

that the thermal model is indeed suitable for use in a microprocessor based device, providing that some account is taken of the resolution of the thermal calculations, particularly for larger motors.

A suggested minimum system configuration for implementing such a protection device is shown in figure 3.7. The system shown includes an allowance of extra Read Only Memory which might be required to implement a twenty four bit solution; the present sixteen bit solution, including the data logging software plus an allowance for the sequence current measurements, occupies 2.5 kilobytes of ROM and 0.5 kilobytes of RAM, the thermal model data occupies less than 0.3 kilobytes of ROM. Also shown is a keypad and display for communication with the user, this does not preclude any alternative mechanism to perform this task should it be deemed more suitable.

The data, including an extra set of matrices which could be used for the 'future prediction' function, could be stored in a ROM device separate from the main body of software. In this way the greatest disadvantage of the thermal predictor, that is the need for detailed thermal model data valid only for one design of motor, might be overcome by building up a library of these ROM devices which could be easily interchanged, depending upon the application.

The peripheral equipment would be governed largely by the functions to be performed in addition to thermal overload protection. Those commonly found in the more comprehensive contemporary protection relays include protection against single phasing, phase unbalance, phase sequence, stall, underload, earth fault and bearing overtemperature

though the later is conditional upon the availability of motor bearing thermometers.

Protection against single phasing is provided invariably by monitoring the line currents. Should a phase be lost then the overload trip curves, or other 'time to trip' mechanisms, are bypassed and the protection relays are tripped immediately.

Phase unbalance protection is normally provided on the basis of an allowable percentage line current unbalance, the exception being the Westinghouse device [8] which incorporates sequence current measurements as a means of predicting the motor heating conditions. Protection against an incorrect phase sequence, is designed to ensure correct running after installation or supply maintenance, as such, measurements are based on the line voltages 'upstream' of the protection relays.

Stall and underload conditions are indicated by the input line currents, the underload function being provided for the protection of motors cooled by the conveyed medium, and, in some instances, for the protection of the load. A stalled motor is represented by the input current exceeding a preset threshold. This threshold will also be exceeded during starting so to prevent the inevitable nuisance trips, an allowable locked rotor, or acceleration, time can be set which overrides the stall function until acceleration is complete. The Westinghouse device is again the exception as it provides for rotor protection during starting by a single node digital model of heat flow from the rotor. Earth faults are normally monitored by an earth leakage transformer.

A device based upon the thermal predictor developed in this Chapter, could protect only against thermal overload, stall and underload[1], and even these only under balanced supply conditions. Incorporating the sequence current measuring system of Chapter 5 would also encompass phase unbalance and single phasing. Should it be thought necessary, the supply phase sequence could be monitored by multiplexing the scaled phase voltages, on the supply side of the motor relays, onto the sequence current measuring equipment; a phase sequence opposite to that expected would be indicated by a negative sequence voltage of greater magnitude than that of the positive. It is also worth noting that a phase sequence reversal occurring during normal running would appear as a large, almost purely negative sequence current thus almost certainly causing a motor trip to occur within one second.

As the thermal model would track the motor temperatures up to, and after the trip, it could thus be used to give an sensible indication of when the motor had cooled down sufficiently to withstand a restart; a function implemented in most current devices by an enforced time delay.

Thus, in addition to providing the additional function of future temperature predictions, there is no reason why a device based on the real time solution of the unbalanced model should not also incorporate the additional protective functions offered by contemporary devices.

[1] An underload condition arises when the motor input current, which varies according to the load, falls below a preset value thus indicating a possible load fault (broken coupling etc).

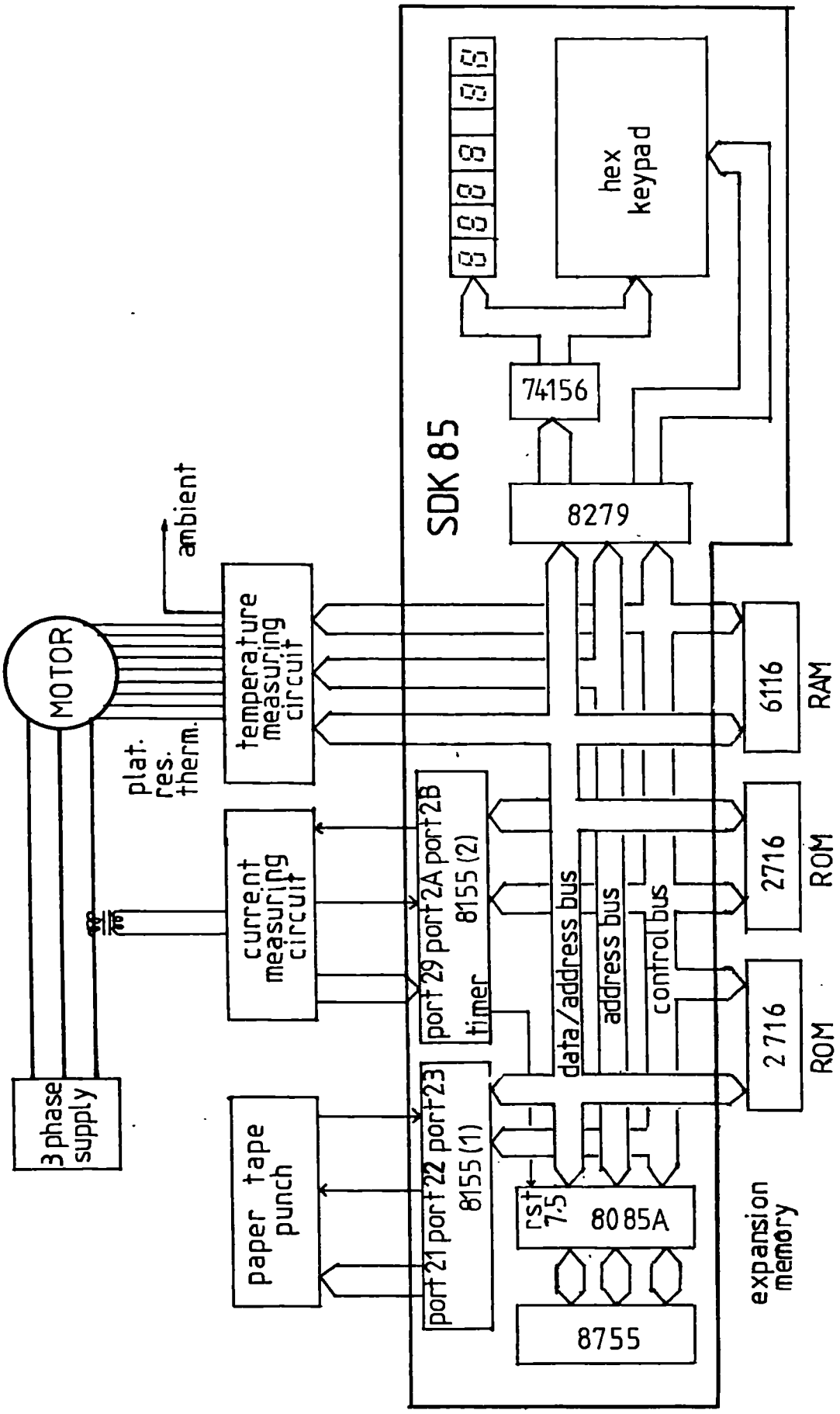

Figure 3·1 Prototyping System Schematic

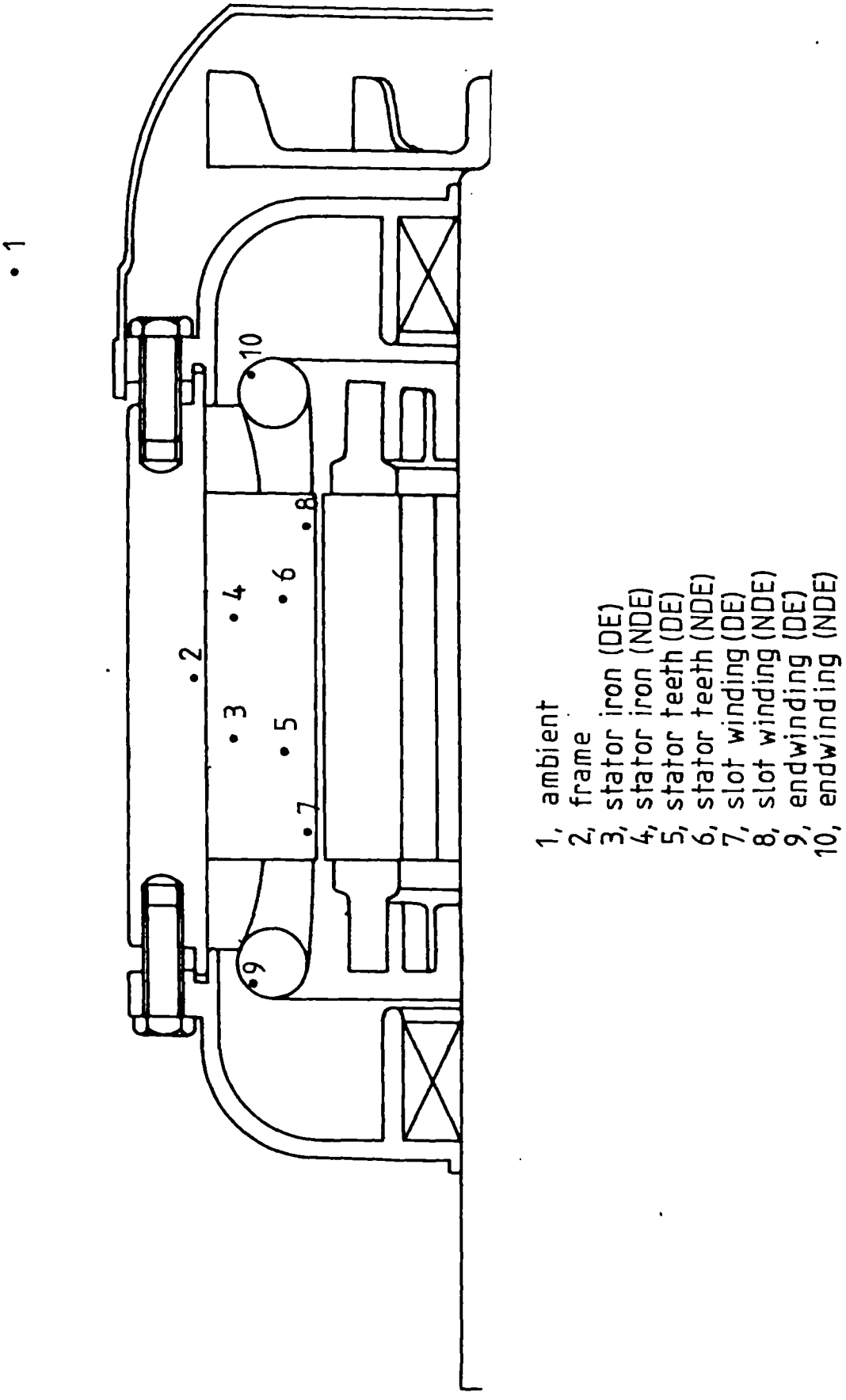

Figure 3·2 Thermometer Positions

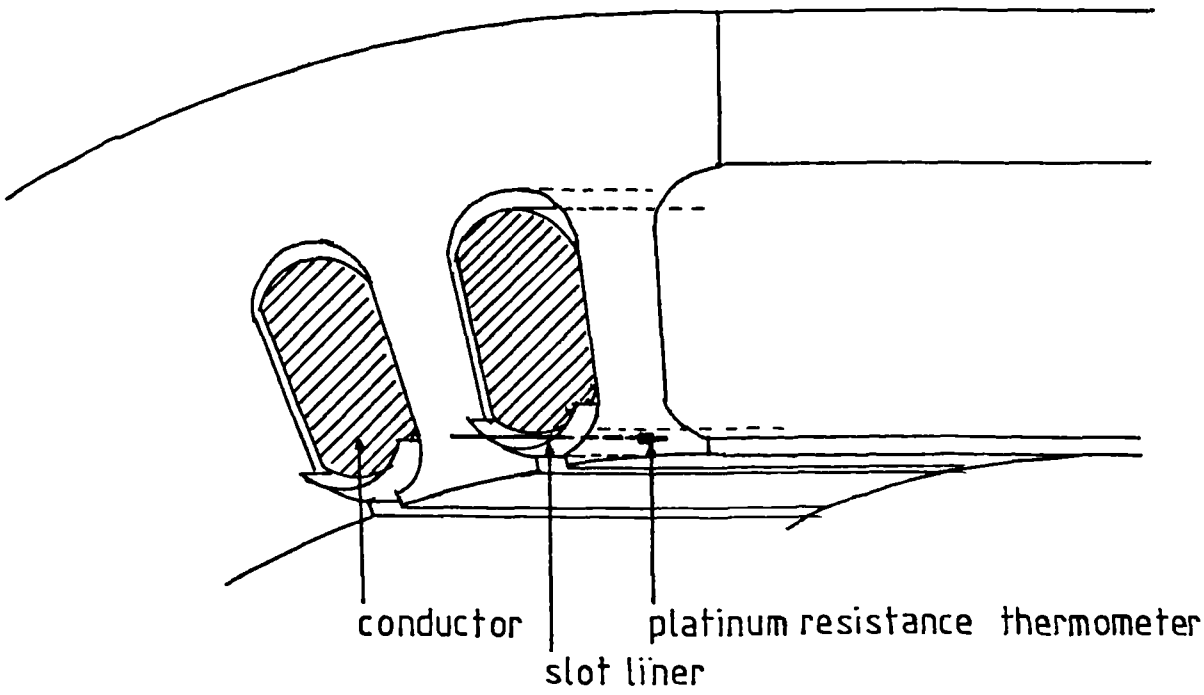

Figure 3·3 Slot Winding Thermometer Position

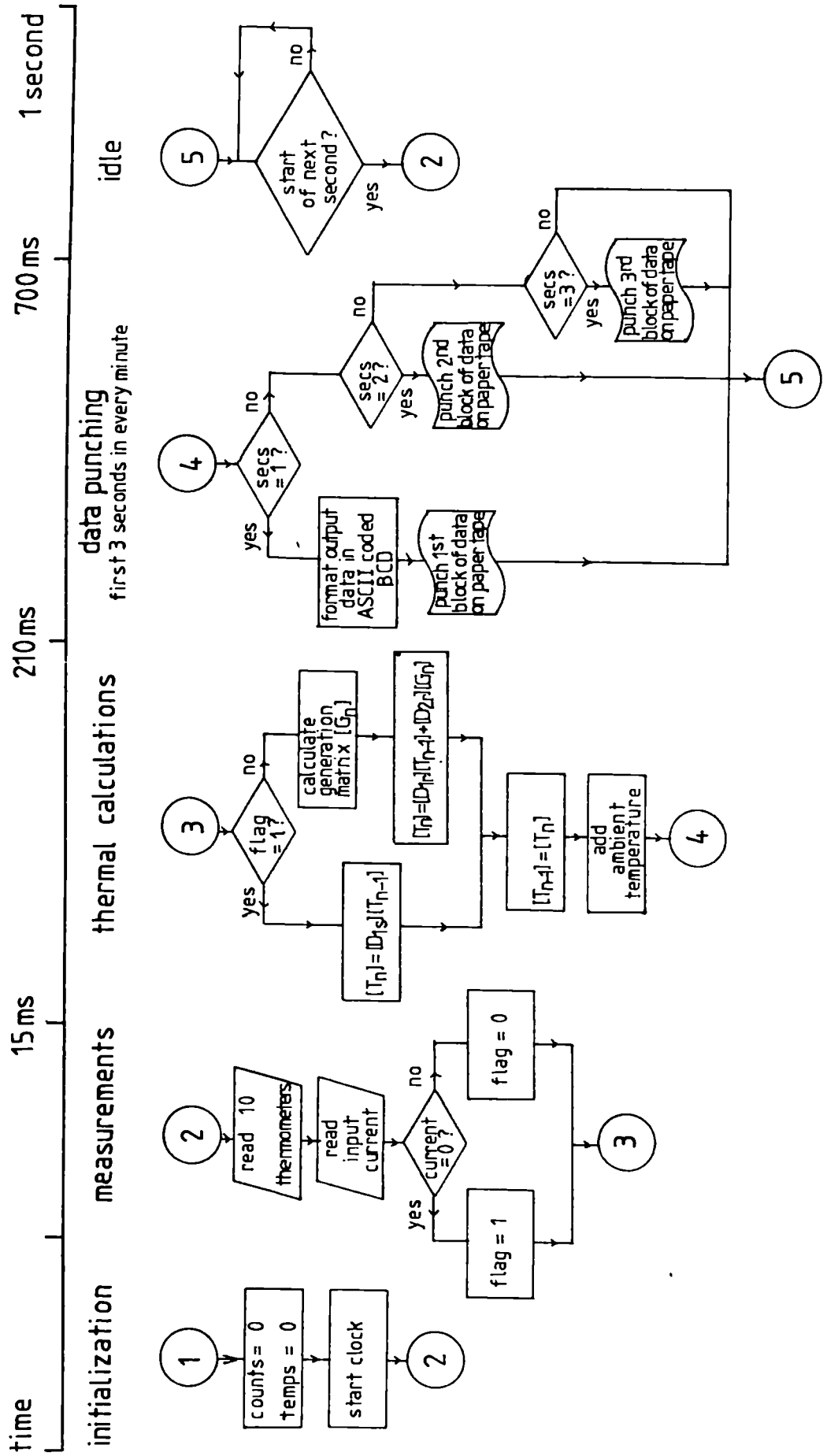

Figure 3·4 Structure of On-line Predictor Software

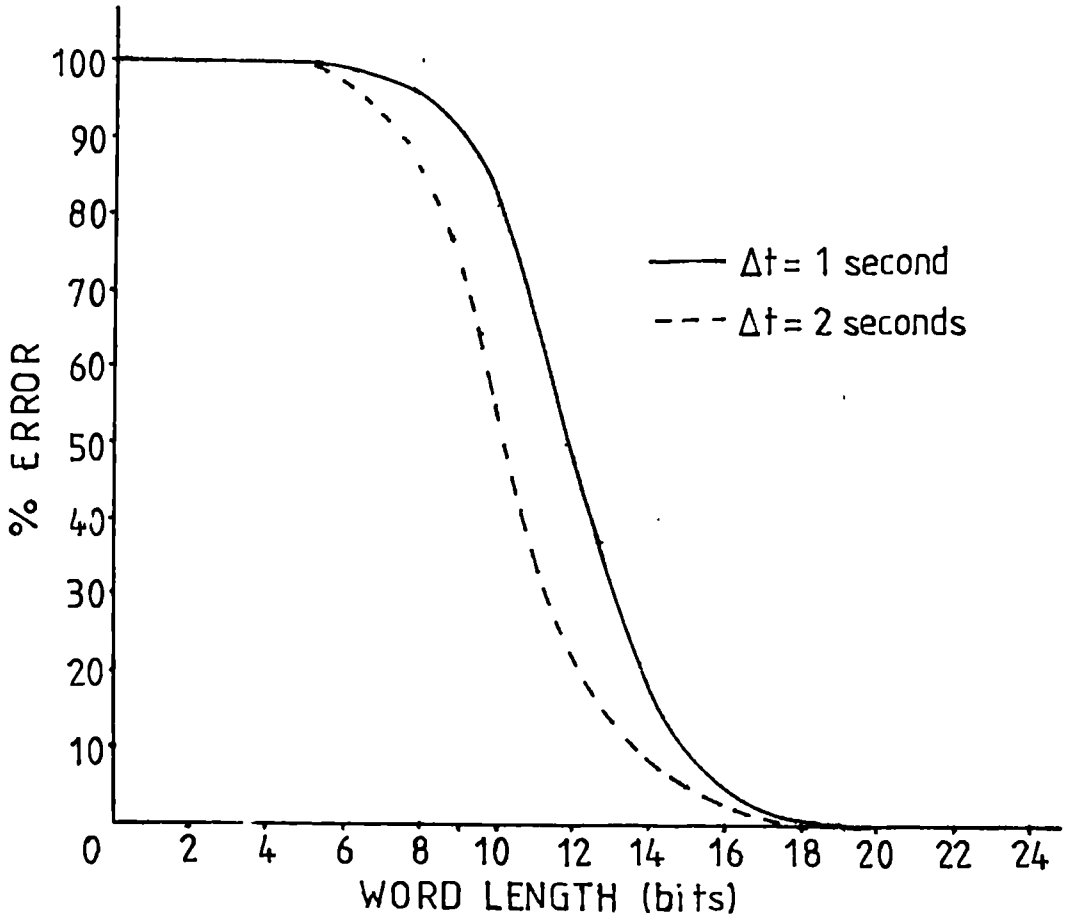

Figure 3·5 Percentage Error in Thermal Calculations for GEC 5·5 kW

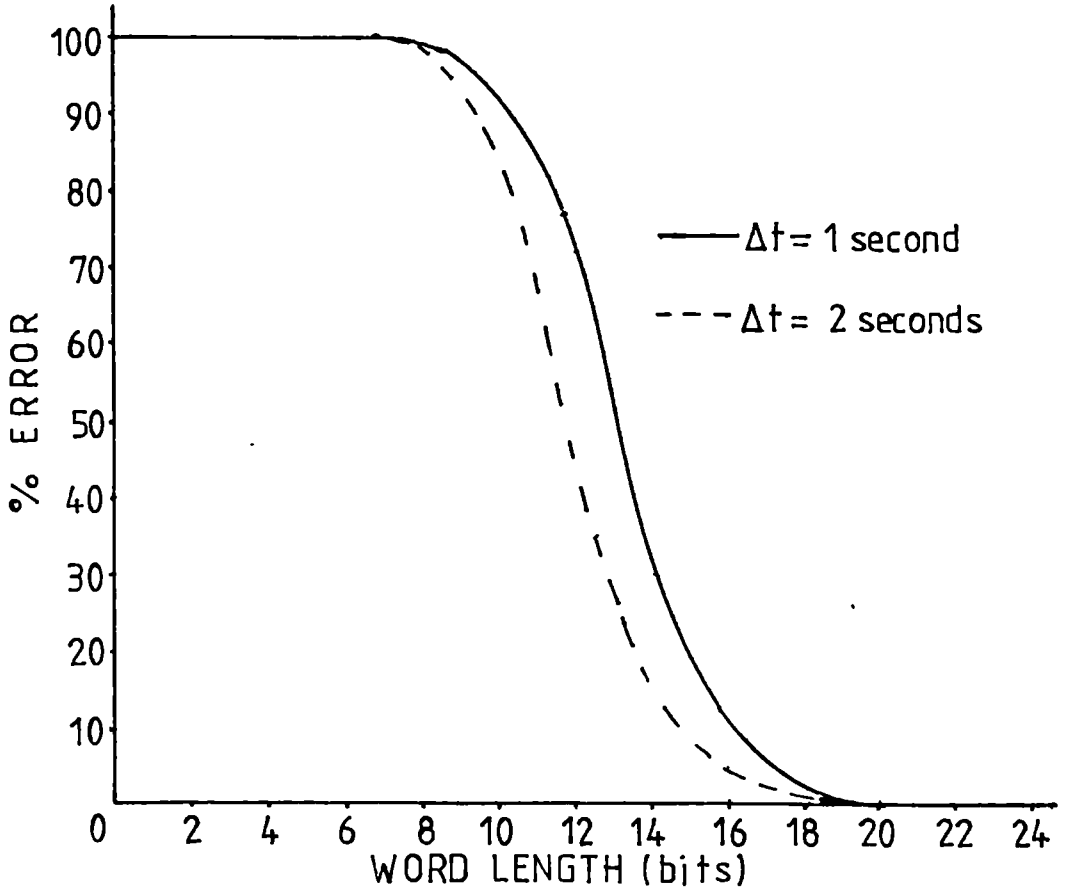

Figure 3·6 Percentage Error in Thermal Calculations for GEC 75 kW

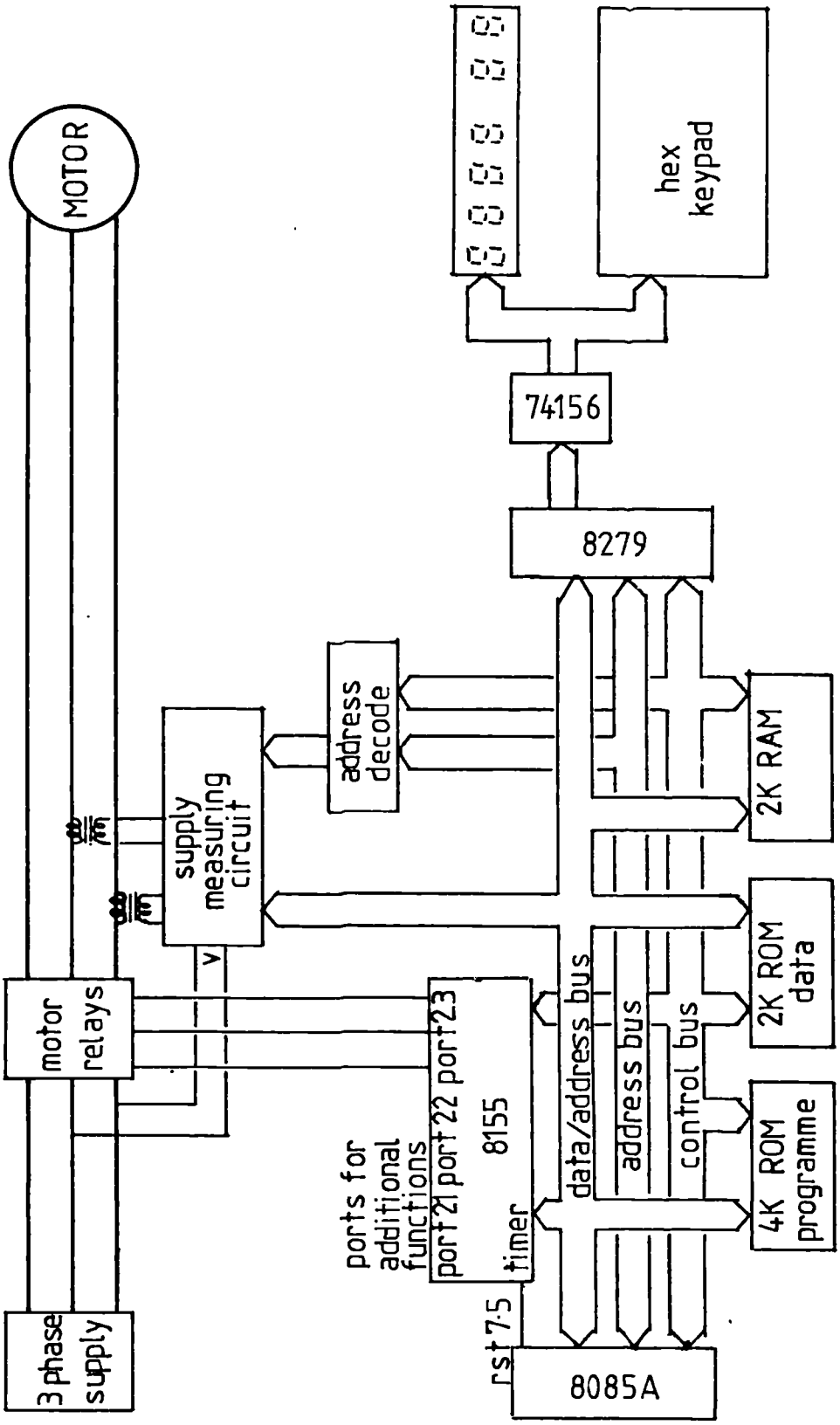

Figure 3-7 Minimum System for Protection Device

CHAPTER 4. THERMAL MODEL TESTING AND RESULTS.

4.1 INTRODUCTION

Three four pole, totally enclosed fan cooled (TEFC) induction motors were modelled and tested to assess the general applicability of the thermal model to motors in this small to medium motor category. Two of the motors were rated at 5.5 kW though, being from different manufacturers, the differences in their design warranted quite separate thermal models. The third motor was rated at 75 kW and thus represented the larger motors in the small to medium category. Because of the supply and load requirements, the tests on this motor were performed at GEC Small Machines, Blackheath. The smaller motors were tested in the laboratory at Liverpool University. Details of each motor, of particular relevance to the testing and subsequent thermal modelling, are presented in the next section.

Locked rotor and no-load tests, performed on each of the motors, served the dual purposes of estimating the stationary and rotating frame to ambient thermal resistances and also determining the electrical equivalent circuit parameters. Accounting for the frequency dependence of the rotor quantities calculated from the locked rotor tests, resulted in equivalent circuit parameters which were shown to accurately predict the induction motor losses.

Having established the accuracy of the thermal generator calculations, the ultimate appraisal of the thermal model performance under

transient conditions, was provided by conducting tests, on each motor, in which the motor load was randomly varied. Measurements of the motor temperatures and input line current were recorded, at intervals of one minute, throughout the tests, which typically lasted between 6 and 9 hours, using the prototyping system described in Chapter 3. The measured temperatures were used to create graphical comparisons with the thermal model temperatures, simulated later on the mainframe computer using the recorded line currents. The graphics packages [49] available to the mainframe computer were also used to create graphical comparisons between the temperatures simulated in real time by the microprocessor, and those recorded simultaneously in the on-line predictor tests mentioned previously in Chapter 3. Both the mainframe and microprocessor predictions are presented at the end of this Chapter along with a discussion of thermal model performance for each of the motors.

Although rotor temperatures were not measured during the varying load tests, an indication of the accuracy of the model rotor temperature predictions was obtained from the results recorded during a steady state load test performed by the manufacturer on the 75 kW motor, in which thermocouples were connected to the rotor via sliprings; the same test results were used in Chapter 3 to assess the validity of the platinum resistance temperature measurements.

4.2 THE INDUCTION MOTORS.

There follows, in this section, a brief description of the three induction motors modelled and tested during this work, outlining the

features of each which were of particular relevance to the thermal modelling. The nameplate details of each motor can be found in table 4.1.

Each of the motors had an aluminium frame which had been shrunk onto the stator core pack during manufacture. However, previous to the work associated with this thesis commencing, the core of the Brook Crompton Parkinson (BCP) 5.5 kW motor had been pushed out from its frame to facilitate the drilling of the holes that would subsequently be used to hold the back iron and teeth resistance thermometers. The subsequent refitting left only a fraction of the contact pressure initially established during manufacture, thus increasing the thermal contact resistance across the frame/core interface. As the contact pressure could not be established, this resistance was determined experimentally (section 4.4).

Disregarding the dimensions, the stator core, stator and rotor winding and shaft assemblies were similar for all three motors. In fact the only major difference in physical construction was the presence of rotor cooling holes in the rotor laminations of the BCP 5.5 kW machine.

Each motor had class F insulation so a common insulation system, consistent with that defined by GEC for class F motors, was assumed. This system consisted of strips of Nomex, a polyamide based insulator, for the phase separators and slot liners, and an Isophalic Alkyd varnish for the impregnated stator winding.

The stator winding is modelled by a homogenious combination of conductor and insulator, the fact that the 75 kW motor has a double layer winding while those of the smaller motors are single layer winding is ignored in the balanced model. For the unbalanced model, however, it is recognized that the inter-phase thermal resistance will be reduced by the greater inter-phase surface area afforded by the double layer winding. Each motor had an aluminium squirrel cage rotor winding, however, the degree with which these were affected by the frequency of the rotor currents differed enormously. The frequency dependence was estimated from the theoretical results of Swann and Salmon [41], and indicated that, whilst the BCP 5.5 kW motor exhibited hardly any frequency dependence, the rotor winding resistance of the GEC 75 kW motor increased by a factor of 3 between it s 0 Hz value and it s value at 50 Hz.

4.3 THE LOCKED ROTOR AND NO-LOAD TESTS.

The locked rotor and no-load tests served the dual purpose of finding the electrical equivalent circuit parameters and calculating the stationary and rotating frame to ambient thermal resistances; the test results for each of the motors are shown in table 4.2.

During the no-load test the motor was run at rated voltage, mechanically uncoupled from it s load, until it reached thermal equilibrium. At this point readings of power input, line voltage and line current were recorded along with the frame and ambient temperatures. Before either the electrical equivalent circuit parameters, cR_m and cX_m, or the rotating frame to ambient thermal resistance could be calculated, the windage

This assumption was tested by measurement on one of the 5.5 kW motors (GEC). The external fan losses were measured by determining the difference between the no-load losses with and without the external fan. The value obtained was 40 W and the total windage and friction, measured by an excitation test, was 75 W (table 4.2).

losses of the external fan had to be deducted from the measured input power as this does not contribute to the motor heating within the frame. It was assumed that this loss would be half the combined friction and windage losses for the motor at rated speed. The friction and windage was determined separately from an excitation test [50] in which the motor input power was plotted against the supply voltage squared, from rated to 15% of rated voltage. The curve could then be extrapolated back onto the zero voltage axis to give the friction and windage.

The parameters can thus be found, assuming a delta connected stator winding from;

$$cR_m = \frac{3V_l^2}{(P_i - 0.5P_{fw})} \tag{4.1}$$

$$cX_m = \frac{3V_l^2}{(3V_l^2 I_l^2 - P_i^2)^{0.5}} \tag{4.2}$$

where,

V_l = supply line voltage (V)

P_i = measured input power from no-load test (W)

P_{fw} = friction and windage from excitation test (W)

The frame to ambient thermal resistance for a rotating motor, R_r, can now be calculated from,

$$R_r = \frac{T_f - T_a}{(P_i - 0.5P_{fw})} \tag{4.3}$$

T_f = frame temperature

T_a = ambient temperature

Since the thermal model assumes axial symmetry, and thus only half the motor is modelled, the numerical value for the frame to ambient resistance used in the final model is twice that given by equation 4.3.

One of the reasons that the no-load and locked rotor tests were chosen in preference to the load test method of Mellor [16] is that they enable the winding temperatures to be noted at the time of taking the readings which aids the determination of the parameters to be used in the temperature dependent solution. Unlike the no-load tests, which were found to give consistent readings from switch on to steady state, the locked rotor results changed as the motor heated up. For this reason, it was considered sensible to record the input power, line voltage and line current for the locked rotor test immediately upon switch on. In this way all the winding temperatures can be assumed to be at ambient temperature, provided sufficient time has been allowed for the motor to cool down after any previous tests, without serious error. The motor is left to reach steady state before the reading are retaken to calculate the stationary frame to ambient thermal resistance.

Referring to the electrical equivalent circuit shown in figure 2.20, the parameters, cR_{sc} and cX_{sc} are found from equations 4.4 and 4.5 respectively.

$$cR_{sc} = \frac{P_i/3 - V_l^2/cR_m}{(I_2/c)^2} \qquad (4.4)$$

$$cX_{sc} = \frac{Q_i/3 - V_1^2/cX_m}{(I_2/c)^2} \qquad (4.5)$$

where,

Q_i = reactive power supplied to the motor (VAR)

The stator winding resistance R_1 was found from a standard DC resistance test. The value thus obtained was increased by 10% to allow for the skin effect in the stator conductors at 50 Hz and extrapolated to to it s 0°C value, R_{10}, by applying equation 4.6
The 10% value being an empirical factor.

$$R_{10} = \frac{R_1(T)}{(1 + \alpha T)} \qquad (4.6)$$

where,

T = stator winding temperature (°C)

α = temperature coefficient of resistance for the stator winding material ($°C^{-1}$)

The rotor winding components of cR_{sc} and cX_{sc} (c^2R_2 and c^2X_2) can be found from,

$$c^2R_2 = cR_{sc} - cR_1 \qquad (4.7)$$

$$c^2X_2 = cX_{sc} - cX_1 \qquad (4.8)$$

where cX_1 is given by,

$$cX_1 = \frac{cR_1}{cR_{sc}} . cX_{sc} \qquad (4.9)$$

Swann's results apply to the bar section of the cage. However, for the purposes of this work they are assumed to apply to the whole winding. This is likely to cause little error in R_2 but possibly greater error in X_2. Tests on the GEC 5.5 and 75 kW motors confirmed that this assumption produced reasonable results.

Depending upon the rotor winding construction, in particular the depth of the conductors, the rotor parameters may or may not be noticeably frequency dependent. The frequency dependence must be allowed for in translating the locked rotor parameters, at supply frequency, to their equivalents during normal operation where the frequency drops to near 0 Hz. The ratio of the 50 Hz parameters to their 0 Hz, or DC, equivalents is related to the rotor winding depth b, divided by the skin depth, d, of the rotor conductor at 50 Hz in a theoretical analysis by Swann and Salmon [41]. Having determined (b/d) from the manufacturers design data and the physical properties of the rotor conductor, the ratios $R_2(50\ Hz)/R_2(0\ Hz)$ and $X_2(50\ Hz)/X_2(0\ Hz)$ can be read directly from Swann's theoretical curve. The correction factors for each of the motors are listed in table 4.3

Proof of the validity of this correction process was gained by comparing the corrected locked rotor rotor parameters with those determined from a separation of loss analysis , at full load, for the GEC 5.5 kW and 75 kW motors. The comparison shows good agreement between the two methods (table 4.4). The final electrical equivalent circuit parameters for each of the motors are shown in table 4.5

The final evidence that the equivalent circuit could be used to give accurate indications of the motor losses was gained by plotting the predicted losses against those found by subtracting the recorded motor input and output powers for varying loads - figure 4.1. The motor output power was calculated from the readings of a load cell connected to the swinging arm dynamometer load, and stroboscopic slip measurements. Because of the rather ill-conditioned nature of the loss calcu-

lations every care was taken to ensure the accuracy of the power output measurements considered to be most susceptible to experimental errors; this included performing separate tests to deduce the dynamometer windage loss which would not be reflected in the load cell measurements [44]. The stator winding temperatures used in the calculation of the theoretical points of figure 4.1 were found from the platinum resistance thermometers situated in the slot and endwinding sections. The rotor winding temperatures were estimated in relation to the stator winding temperatures to be the values typically obtained in the thermal simulations under these conditions.

4.4 THE FRAME/CORE THERMAL CONTACT RESISTANCE.

The model for this resistance has previously been described in Chapter 2 where the *semi-empirical equation of Shlykov and Ganin [37]* was used in the extrapolation of Brunot's experimental curve [31] for contact pressures more commonly expected from the shrink fitting process. The estimated contact resistance was read directly from the curve once the contact pressure had been established. For the BCP 5.5 kW motor, which had had it s frame removed and refitted, there was no way of estimating the the resulting contact pressure, except that it was small; a fact indicated by the ease with which the refit had been accomplished. A test was undertaken therefore, which aimed to give an experimental estimate of this resistance for this motor. The test was repeated for the GEC 5.5 kW motor so that a comparison with the theoretical results given in Chapter 2 could be made.

The rotor was removed and the shaft holes remaining after the endcaps had been replaced were covered. Resistance thermometers were mounted on the endwinding surface, in the stator core, in the frame and in the endcap air. For the GEC 5.5 kW motor the core and frame thermometers were in their estimated component mean temperature positions (Chapter 3). For the BCP 5.5 kW machine, however, an addition hole drilled just into the core, near the frame thermometer position, was adjudged to be more suitable for the core temperature measurement. In both cases the endcap air thermometers were suspended a few centimetres below the endwinding conductors. The stator winding coils were wired in parallel and supplied with a DC current until thermal equilibrium was reached.

An estimate of the percentage of the heat input that passes through the frame/core interface under steady state conditions, was found by first considering the heat loss from the endwinding to the endcap air - this being the alternative heat flow path from the stator winding.

The experiments of Luke [35], reported in Chapter 2, give the convective heat transfer coefficient from an unventilated endwinding as 15.5 $W/m^2{}^\circ C$. Multiplying this by the estimated endwinding surface area gives a thermal admittance along this path, Y_e, which can be used in the calculation of the heat loss q_{ec}.

$$q_{ec} = (T_{ew} - T_{ec}).Y_e \qquad (4.10)$$

The remainder of the heat input to the windings is assumed to pass through the frame/core thermal contact resistance which can thus be calculated from,

$$R_c = \frac{T_c - T_f}{q_c} \tag{4.11}$$

Finally, the equivalent contact coefficient, h, can be found from equation 4.7.

$$h = \frac{1}{R_c . A} \tag{4.12}$$

Where,

A = Area of frame/core interface.

The contact coefficients estimated in this way are given in table 4.6. Also shown is the theoretical coefficient for the GEC 5.5kW motor, obtained from the extrapolated curve of Brunot and Buckland for the purpose of comparison with the experimental value.

As can be seen, the difference between the coefficients for the two motors is substantial. Further analysis shows that whilst the full load, steady state temperature drop for the GEC motor, using the experimental results, would be of the order of 3°C, that for the BCP motor would be of the order of 21°C. These expected temperature drops are substantiated, to some degree, by the measured core and frame temperatures

recorded for full load operation during the varying load tests described later.

Another important observation from table 4.6 is the large discrepancy between the measured and theoretical values of h for the GEC 5.5 kW motor. This casts a certain amount of doubt upon the validity of the extrapolated curve, used in the theoretical estimations, which must be looked at more closely. The estimation of the thermal contact pressure is critically dependent upon the difference between the outer core radius and the inner frame radius which can vary substantially over the range of allowed manufacturing tolerances; for the GEC 5.5 kW motor the calculated contact pressure increases by a factor of 4 between the 'slackest' and 'tightest' tolerances. Another important factor which alters the frame/core resistance is the surface finish, or microroughness, of the materials in contact. Comparing the constant term of Shlykov's equation with the numerical equivalent gained by fitting the equation to Brunot's curve, gives an estimation of the microroughness of the lamination/aluminium interface in Brunot's experiment as 149.5 μm. The possibility that the core and frame surfaces of the GEC 5.5 kW motor were smoother than this cannot be discounted though no data exists to support or refute this possibility. Table 4.7 demonstrates the effect that both these variables have upon the contact coefficient and the resulting effects upon the estimated full load, steady state temperature drop across the frame/core interface. Values for the coefficients are shown for microroughnesses of 149.5 μm and 75 μm at contact pressures representing the tightest, slackest and zero-tolerance fits for the GEC 5.5 kW motor. However, even the tightest fit, assuming a microroughness of 75μm, gives a coefficient of 1250 $W/m^2°C$, which is still smaller than the measured

value of 1497.7 $W/m^2°C$; in fact, the microroughness required to achieve the measured value of contact coefficient, assuming the 'zero-tolerance' value of contact pressure, was estimated to be 44.3μm. While this represents a very smooth core in relation to that used in Brunot's experiments, it is still a factor of 2 greater than the roughest material tested by Shlykov.

In formulating the thermal model, the measured values of frame/core contact coefficient were used in preference to the theoretical values. As no such measurements were made on the 75 kW motor during the tests performed at GEC Small Machines, there was no other option than to adopt the theoretical value. Whilst it is recognised that this value is subject to the same uncertainties that have been identified for the smaller motors, no justification could be found for changing it; actually, the correlation between the measured and simulated core and frame temperatures indicate that the adopted value is of the right order.

4.5 BALANCED MODEL PERFORMANCE - COMPUTER PREDICTIONS.

The induction motors were subjected to tests in which the load on the motor was varied randomly for periods between 6 and 9 hours. All the tests included long periods of stationary cooling and short periods of overload. During the tests, the prototyping system was used as a data logger, automatically recording the motor temperatures and input line current on paper tape at one minute intervals.

After the tests had been completed, the recorded data was transferred to the mainframe computer where the measured line currents were

input into a programme which performed the thermal model calculations. The constant matrices used in this solution were formulated using a time step, Δt, of 60 seconds, to correspond with the data recording interval. This allowed the thermal model output to be correlated directly with the measured temperatures.

As the change in the supply voltage was typically observed to be less than 1% over the duration of the tests, it was considered appropriate to enter the average value as a model constant rather than recording it with the input current. The ambient temperature was also observed to remain approximately constant though, to ensure compatibility between the simulated and measured temperature comparisons, the values recorded by the data logger were used in the model solution. The results of the tests for each of the motors are presented graphically in figures 4.2 to 4.15.

A discussion of the approximation of the resistance thermometer measurements to the component mean temperatures has been given in Chapter 3 where it was estimated, for the 75 kW motor, that the error for the stator winding temperature measurements was of the order of 5%. In the following discussions, errors of this order will also be assumed to apply to the stator winding measurements for the smaller motors. The drive end endwinding temperature, being the hottest, was used exclusively in comparisons with the simulated endwinding hot spot temperatures.

4.5.1 THE BCP 5.5 KW MOTOR.

The results of the varying load tests performed upon this motor are shown in figures 4.2 to 4.7.

This was the original motor that was modelled and tested by Mellor. The changes performed upon the model in the course of this work have served to improve the performance of the model in tracking the motor temperatures.

The large temperature drop between the stator back iron and the frame, over 20°C at one point, is immediately evident when comparing figures 4.2 and 4.3. As noted previously this is due to the particularly small frame/core contact pressure which existed for this motor.

Assuming that any change in speed has a negligible effect upon the frame to ambient thermal resistance and further that there is no shift in the frame temperature distribution which might alter the relationship between the frame measurement and the frame mean temperature, then the measured frame temperature should give an indication of the motor losses. Using this calorimetric effect to compare with the simulated losses, which at steady state are proportional to the simulated frame temperatures, seems to indicate that the modelled losses are slightly too high. However this is not reflected in the winding temperature simulations which show excellent agreement.

The frame temperature rise upon switching off the machine was noted for all three motors. It is caused by the rapid redistribution of

heat as both the heat generating losses and forced ventilation are removed at the same time. The model being transient in nature also simulates this time delay of the heat flux as it finds its way to the model boundary and models this effect well.

Figure 4.7 is included to demonstrate how including temperature dependence in the thermal generator calculations improves the model performance; in this figure the generators were calculated from winding resistances calculated for fixed temperatures of 60°C and 80°C respectively - the measured values are common with those of figure 4.6. Whilst the results for the non temperature dependent simulation are not bad, the improvement in the integrity of the thermal tracking in the temperature dependent simulation of figure 4.6 should be noted.

4.5.2 THE GEC 75 KW MOTOR.

Although the tests upon this motor were performed at GEC Small Machines, Blackheath, it still proved possible to incorporate the prototyping system to record the input line current and temperatures during the tests in the same way as for the other motors. The graphical comparisons with these temperatures and those subsequently simulated using the measured data are shown in figures 4.8 to 4.10.

The difficulties foreseen in accurately drilling a hole into the stator teeth prevented measurements for this component; the high slot fill of the windings also prevented insertion of the platinum resistance probes into the stator slot sections so that there was no data available for transient thermal model simulations for these components. However, tests

which had previously been performed by the manufacturer, on the same motor, facilitated a steady state comparison for most of the major thermal model components, including the rotor winding and rotor iron which had been recorded via sliprings mounted upon the rotor shaft. These steady state results are shown in table 4.8 alongside the simulations performed using the transient model; the simulated temperatures were computed by applying the recorded input current to the model, for a period equal to the actual duration of the manufacturer's test. As there were 115 temperatures recorded during this test, it proved possible to average the data to give an indication of the mean temperature for some of the components.

The four $^{rotor}_{\Lambda}$thermocouples occupied positions at the extreme axial ends of the winding and iron; the average of the two thermocouple measurements are presented in table 4.8. However, the rotor will be subject to a similar, asymmetric axial temperature distribution, caused by the external cooling fan, as the stator winding, and for that component it was observed that the drive end temperatures gave the best approximation to the mean. Applying the same principle to the rotor winding brings the simulated temperature to within 12% of that measured. It might be argued that the error could also be caused by a overestimation of the rotor iron loss component - the iron loss is split evenly between the stator and rotor. However, adjusting this loss in favour of the stator, whilst it might improve the rotor temperature correlation, degrades the stator temperature correlation as the simulated endwinding temperatures drop. Thus, as the main criterion for the motor protection application is that the stator endwinding temperatures stay within agreed limits, the present assumptions stand. As no rotor temperature data was

available from the other motors it must be presumed that any error in the rotor winding predictions will be of the same order as that identified here.

The stator winding hot spot temperature was taken as the hottest of 12 thermocouples embedded both in the drive-end, and non drive-end endwindings. The agreement with the simulated hot spot temperature is good.

Again using the steady state frame temperature to give an indication of the motor losses, still within the constraints noted for the BCP motor in the previous sub-section, indicates that they might be slightly high. The correlation between the measured temperature drop from the average frame to the average core temperature and the simulated frame/core temperature drop provides some evidence that the theoretical contact resistance, found for this motor from the extrapolated curve of Brunot and Buckland [31] shown in Chapter 2, was of the correct order of magnitude.

The transient model results from the varying load tests for the three nodes accessible to the prototyping system thermometers reinforce the observations from the steady state results of table 4.8 and further show that the thermal time constants, which also depend upon the thermal capacitances, accurately match those of the motor. The fact the motor was switched off, restarted and switched off again, near the end of the varying load test presented no difficulties in the thermal model simulation.

4.5.3 THE GEC 5.5 KW MOTOR.

The varying load test results for this motor are shown in figures 4.11 to 4.15.

Again the correlation between the measured and simulated endwinding hot spot temperatures, of primary importance in the motor protection application, was good. The difference between the frame and stator back iron temperatures was small and the corresponding simulated temperatures matched well, justifying the choice of the experimental value of frame/core contact resistance. Should the theoretical value have been used then the estimated increase in the simulated winding temperatures, at full load, would be 7°C; a percentage increase of 3%.

It would appear that the extrapolated contact resistance curve is not universally applicable; the value of this resistance is dependent upon factors other than the contact pressure, not least of these factors being the roughness of the contact surfaces. Any future solution to this problem will rely upon the availability of more data relating the microroughness of laminated materials to the thermal contact resistance over a wide range of contact pressures.

Another problem which must be considered with respect to the application of the same thermal model to motors of identical design is that of manufacturing tolerance. The components of the thermal model which would be most affected by slight differences in some dimensions are the frame, in that the frame/core contact resistance is critically dependent upon the outside core minus the inside frame measurement, and the airgap

in which the convective heat transfer coefficient is directly proportional to the gap width, and is also susceptible to manufacturing tolerances. Mainframe computer simulations, using different values of these critical dimensions, show that a 100% increase in the outside core minus the inside frame dimension leads to a 5% increase in the simulated endwinding hot spot temperature at full load steady state whilst a 50% increase in the airgap leads to a 7% increase in the endwinding simulation. These figures are considered reasonable enough to justify the use of a single model for motors of identical design, without having to resort to 'on-site' testing of each individual motor.

The effect of environmental factors upon the cooling of the motor must not be overlooked either. Dust or dirt blocking or partially blocking, the cowl air intake for instance, could lead to overheating as the volume flow rate of the cooling air is reduced. Again performing computer simulations for different values of the frame to ambient thermal resistance reveals that a 20% increase in this resistance results in a 10% endwinding temperature rise under full load conditions. Realistically, factors such as these can only be protected against by direct measurement of the winding temperatures. However, a possible compromise which would still allow a protection device based upon the thermal model, to be retro-fitted to existing machines would be to provide for measurement of the easily accessible frame temperature and to use this as the model offset, instead of the ambient. This would however, undermine the usability of the proposed device in addition to making it more expensive.

4.6 BALANCED MODEL PERFORMANCE - ON-LINE PREDICTIONS.

Within the constraints noted at the end of the previous section, it is evident from the results, including the steady state data, that the model is indeed suitable for use in the protection of small and medium sized, TEFC induction motors. The effectiveness of the proposed protection device, however, relies upon the performance of the model when computed upon a microprocessor in real time. Tests performed on the BCP 5.5 kW motor, using the microprocessor based on-line predictor, detailed in Chapter 3, provided a means by which this performance could be assessed.

The tests took a similar form to the varying load tests outlined in the previous section. The prototyping systems recorded both the measured temperatures and those predicted from the real time solution, performed every second by the systems own microprocessor. Although a complete set of measurements and predictions were made every second, to restrict the volume of data, only those valid for the first second in every minute were punched onto the paper tape. The resulting comparisons between the temperatures predicted and measured during the first on-line, varying load test are shown in figures 4.16 to 4.20.

The performance of the on-line predictor is excellent until two hours into the stationary cooling period at the end of the test, the predictor appears to fail. This failure has been previously noted and discussed in Chapter 3 in relation to the development of the on-line predictor software and its resolution. There it was reported that the failure was due to an insufficient resolution in the microprocessor calcu-

lations and data storage, and was not a hardware breakdown. This was confirmed by heating the motor up on full load, and then allowing it to cool with the on-line predictor running continuously - figure 4.21.

An immediate solution to this problem was implemented by re-formulating the constant matrices used in the stationary model solution for a longer time step of 60 seconds. Though this now gave excellent thermal tracking over a long cooling period, shown by repeating the previous test with the re-formulated matrices (figure 4.22), problems were anticipated for supply interruptions of only a few seconds. With this in mind, a further varying load test was performed, with the new stationary matrices, which included a period in which the motor was switched off for two seconds and then re-energized. The resulting comparisons between predicted and measured temperatures are shown in figure 4.23 to 4.27.

Concentrating upon the results for the endwinding component, this short de-energized period is shown at 48 minutes. It can be seen that the measured temperatures drop by 5°C over the relevant one minute recording cycle, whilst those simulated drop by 15°C. However, the model recovers and shows a very satisfactory agreement with the measured temperatures over the remainder of the test which also includes an additional 22 minute stationary cooling period before the motor is finally shut down at 280 minutes.

The slight discrepancies that exist between the on-line predictions and the computer simulations for the same motor (figures 4.2 to 4.6), are due to model corrections which were undertaken after the on-line

tests had been performed. While the corrections improve the model performance they do not detract from the relevance of the on-line predictor results which, should the model corrections have been carried out for the microprocessor model, would mirror the mainframe computer predictions.

	BCP 5.5kW	GEC 75kW	GEC 5.5kW
Frame Size	132S	250M	132S
Power Rating (kW)	5.5	75	5.5
Voltage Rating (v)	415	415	415
Current Rating (A)	10.9	133	11.2
Connection	Δ	Δ	Δ
Poles	4	4	4
Insulation Class	F	F	F

Table 4·1 Nameplate Details

	Locked Rotor Results				No-Load Results				F+W
	V_{sc} (V)	I_{sc} (A)	W_{sc} (W)	T_{wndg} (°C)	V_{oc} (V)	I_{oc} (A)	W_{oc} (W)	T_{wndg} (°C)	W_{fw} (W)
BCP 5.5kW	49.0	6.7	302	21	424	5.23	350	-	60
GEC 75kW	31.8	59.4	1380	83.1	415	59.6	2644	-	600
GEC 5.5kW	91.4	9.3	652	21	427	5.97	535	36	75

Table 4·2 Locked Rotor and No-load Test Results

	R_2	X_2
BCP 5.5kW	1.10	0.80
GEC 75kW	3.08	3.08
GEC 5.5kW	1.70	1.70

units-Ohms

Table 4·3 Rotor Parameter Frequency Correction Factors

	Locked Rotor		Load Test	
	c^2R_{20}	c^2X_2	c^2R_{20}	c^2X_2
GEC 5.5kW	3.973	7.37	4.02	7.72
GEC 75kW	.0537	.2127	.0498	.2251

units-Ohms

Table 4·4 Comparison Between Rotor Parameters from Frequency Corrected Locked Rotor and Separation of Losses

	Electrical Equivalent Circuit Parameters					
	cR_m	cX_m	c *	R_{10}	c^2R_{20}	c^2X_{sc}
BCP 5.5kW	1685.4	141.0	1.038	3.465	3.329	12.87
GEC 75kW	248.2	12.08	1.019	.0628	.0537	.4491
GEC 5.5kW	1102.0	124.9	1.052	2.838	3.973	13.96

units-Ohms
*dimensionless

Table 4·5 Electrical Equivalent Circuit Parameters

	Contact Coefficient ($W/m^2{}^\circ C$)	
	Measured	Theoretical
BCP 5.5kW	206.7	-
GEC 5.5kW	1497.7	666.7

Table 4·6 Frame/Core Contact Coefficient

Contact Pressure $N/m^2 x10^6$	Surface Finish (microroughness)			
	149.5 μm		75 μm	
	h ($W/m^2°C$)	T_d(°C)	h ($W/m^2°C$)	T_d(°C)
3.21	887.3	5.34	1250.0	3.80
1.95	666.7	7.13	1020.0	4.65
0.80	490.2	9.70	833.3	5.70

Table 4-7 The Effect of Surface Roughness and Contact Pressure on Contact Coefficient and Full Load Temperature Drop

COMPONENT	MEASURED TEMP (°C)	SIMULATED TEMP (°C)
FRAME	52.6 (av. of 36)	55.5
STATOR IRON	64.0 (av. of 11)	70.4
STATOR TEETH	-	80.4
SLOT WINDING	84.8 (av. of 24)	90.4
ENDWINDING	103.5 (hottest)	102.1
ROTOR WINDING	149.0 (av. of 2)	168.0
ROTOR IRON	141.7 (av. of 2)	166.5
SHAFT	-	109.8

Table 4-8 Comparison of Full Load Steady State Temperatures for GEC 75kW motor and Manufacturer's Test Results

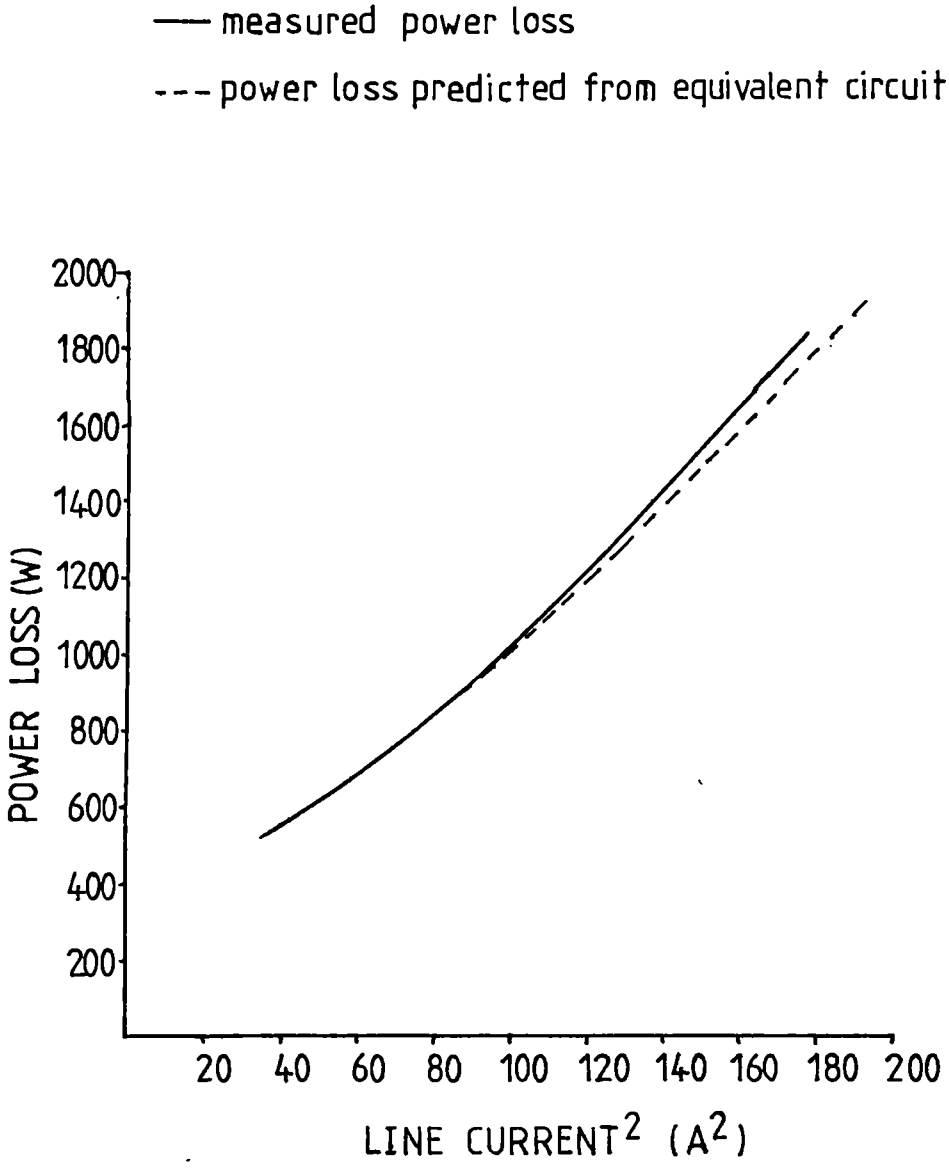

Figure 4·1 Measured and Predicted Losses for GEC 5·5kW

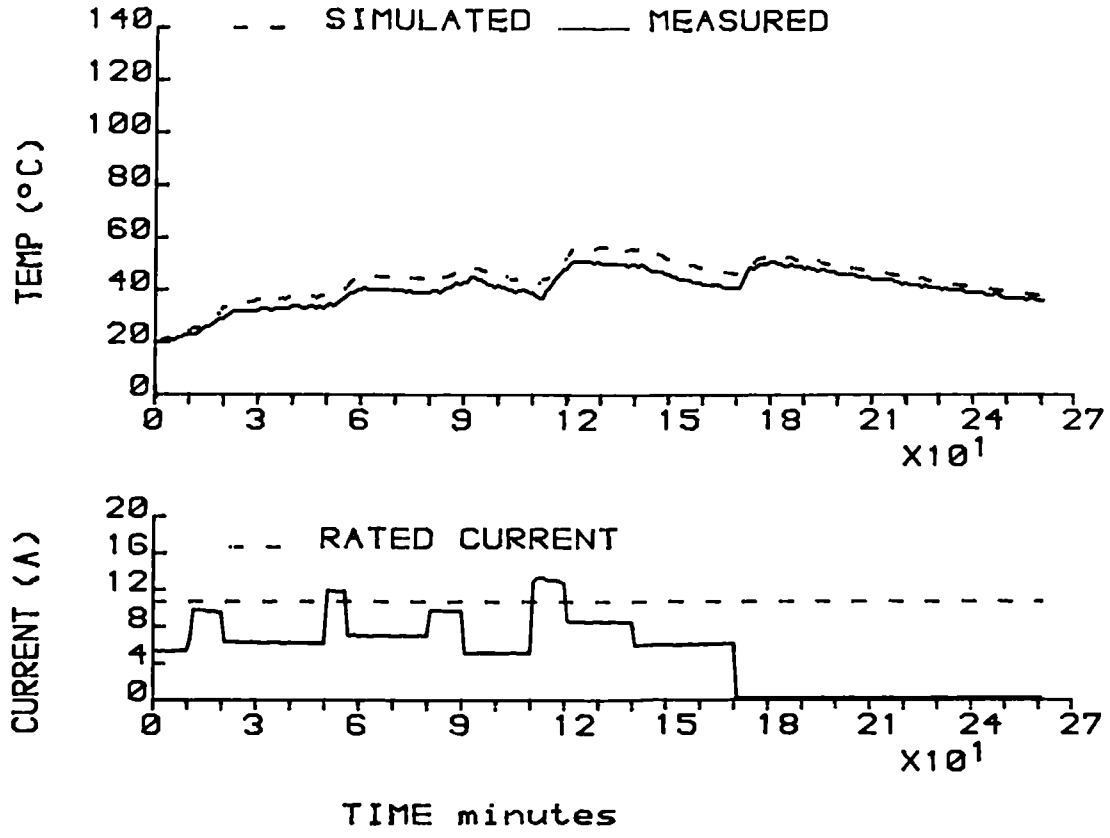

Figure 4·2 BCP 5·5 kW Frame

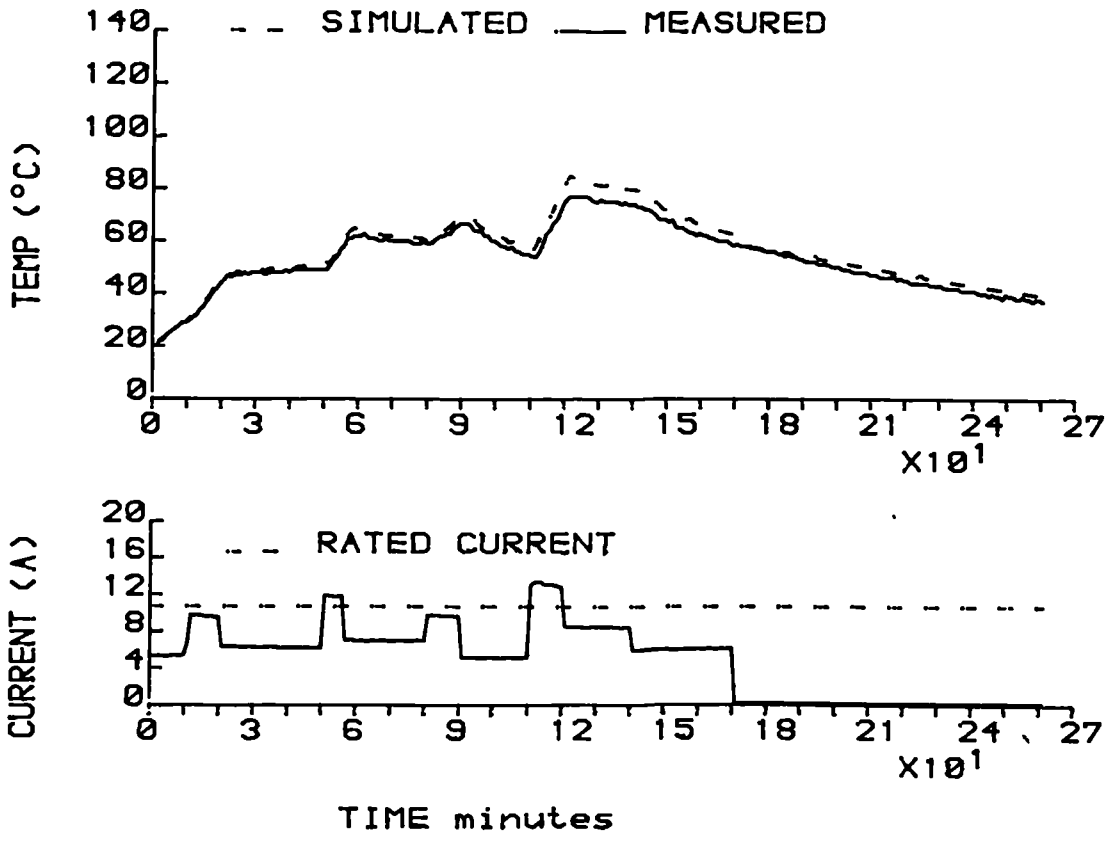

Figure 4·3 BCP 5·5 kW Stator Back Iron

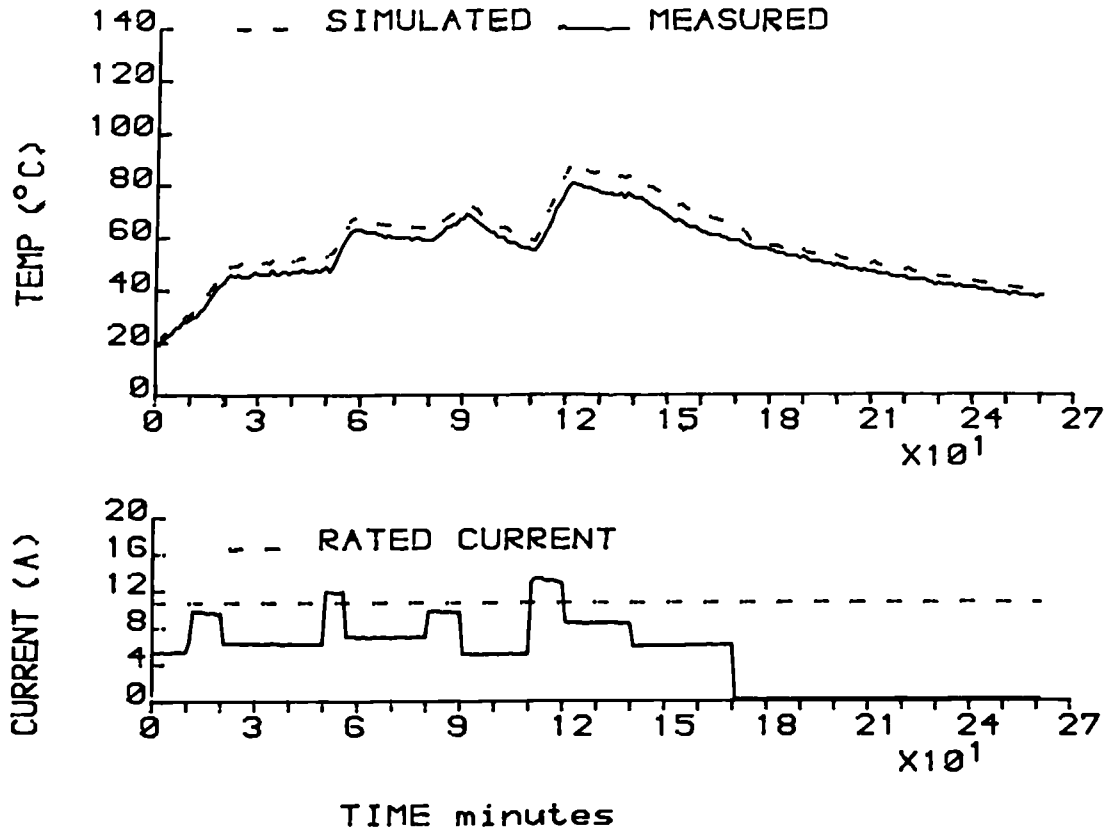

Figure 4·4 BCP 5·5kW Stator Teeth

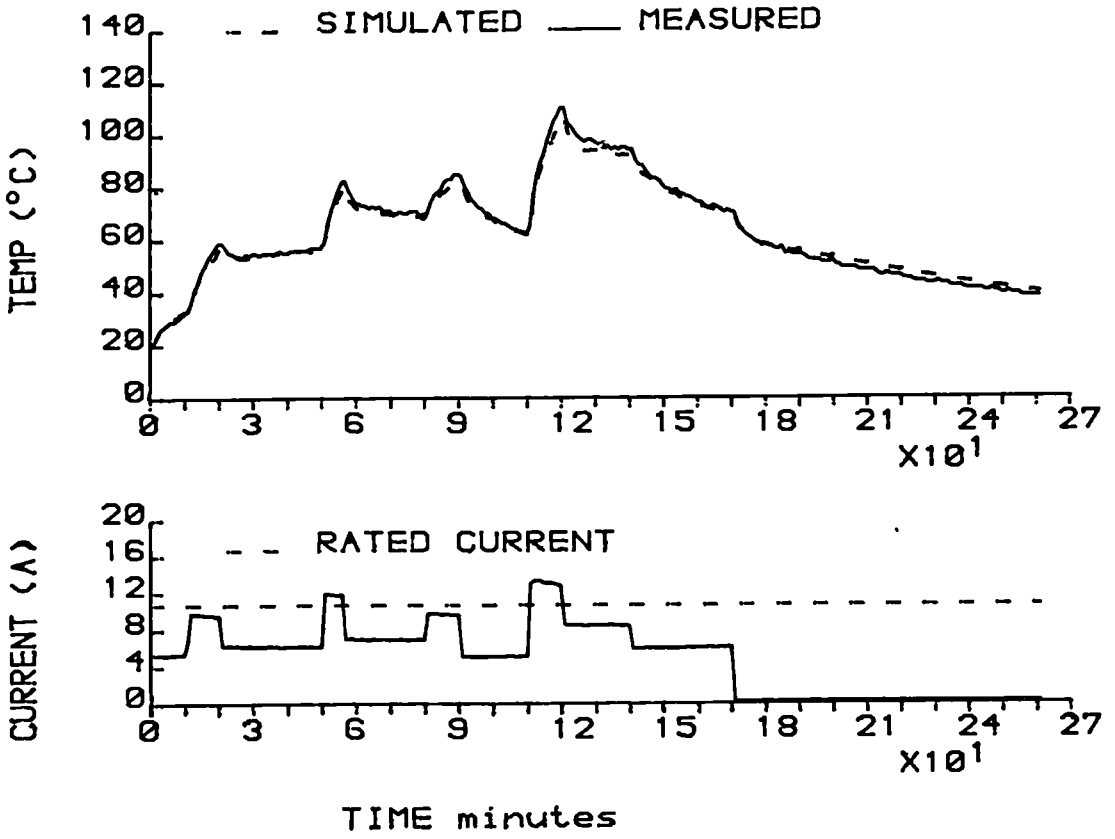

Figure 4·5 BCP 5·5 kW Stator Slot Winding

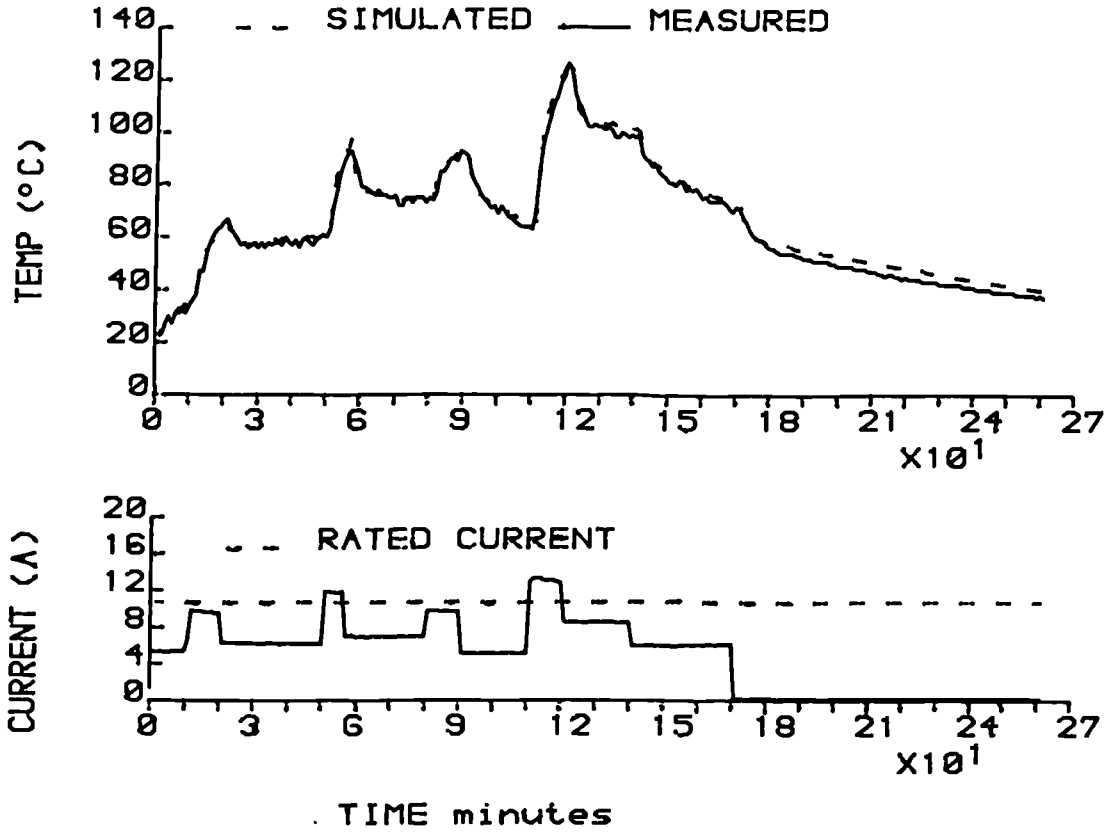

Figure 4·6 BCP 5·5kW Endwinding

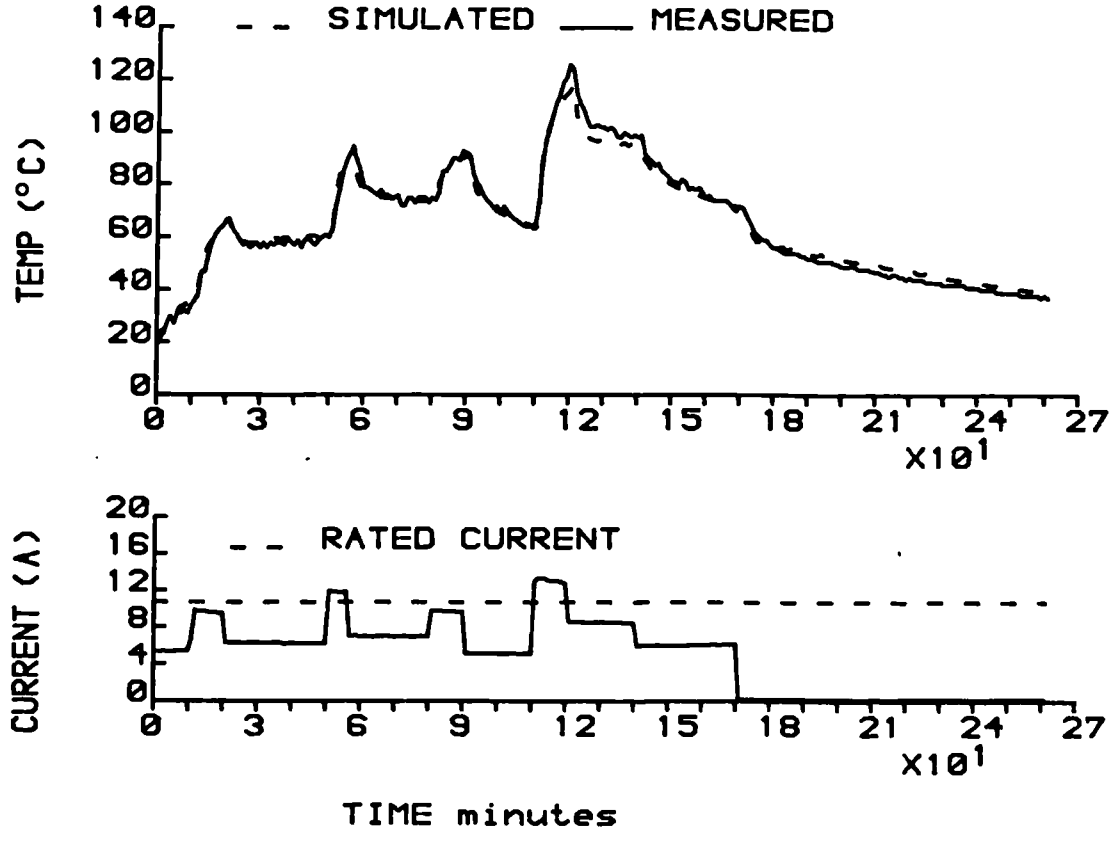

Figure 4·7 BCP 5·5 kW Endwinding without Generation Temperature Dependence

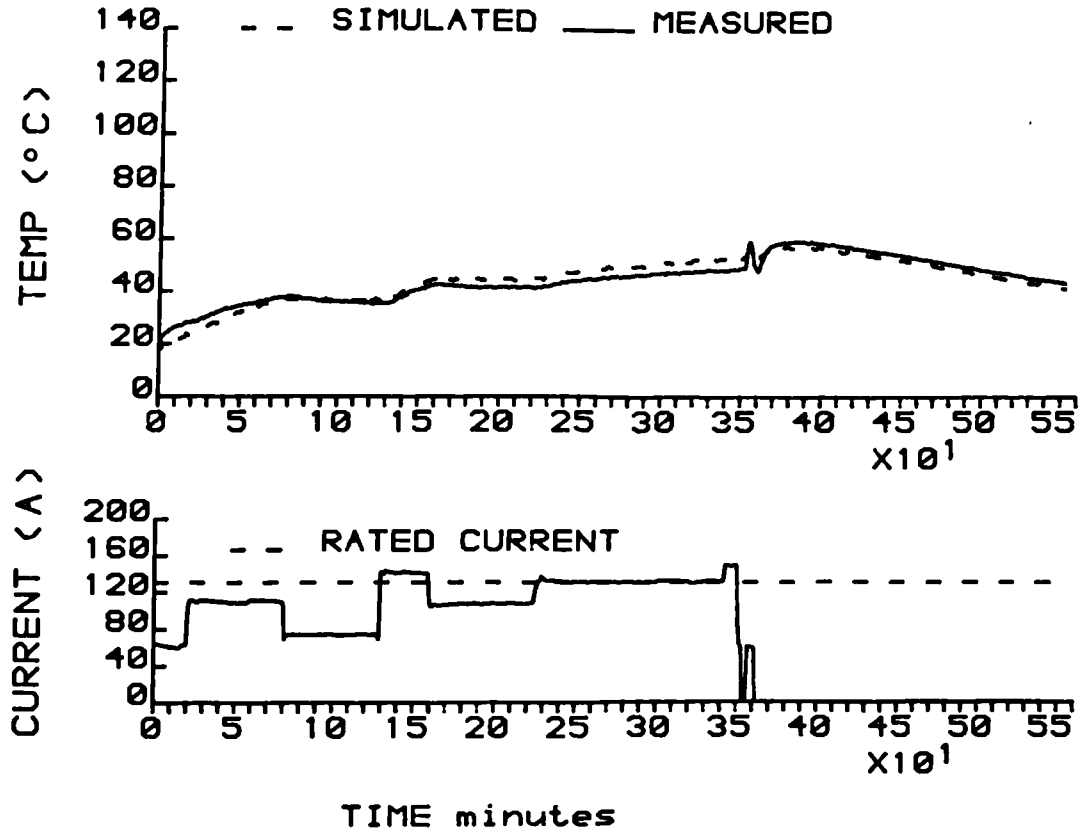

Figure 4·8 GEC 75kW Frame

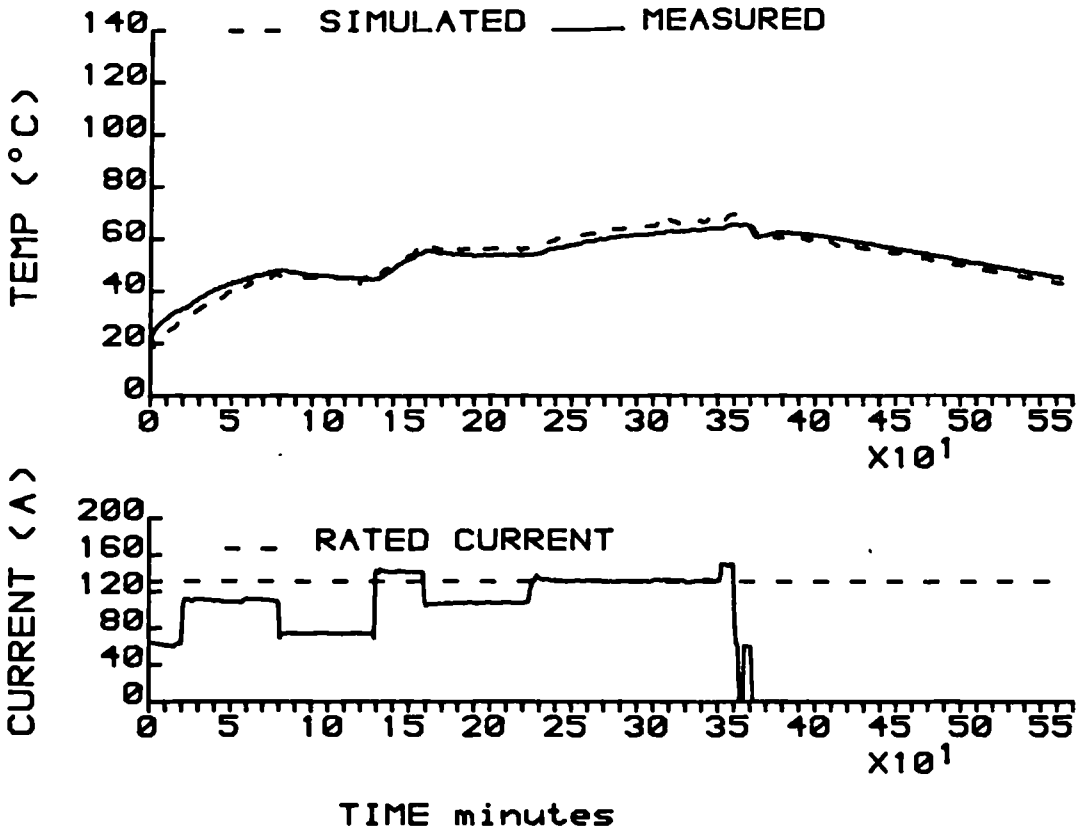

Figure 4·9 GEC 75 kW Stator Back Iron

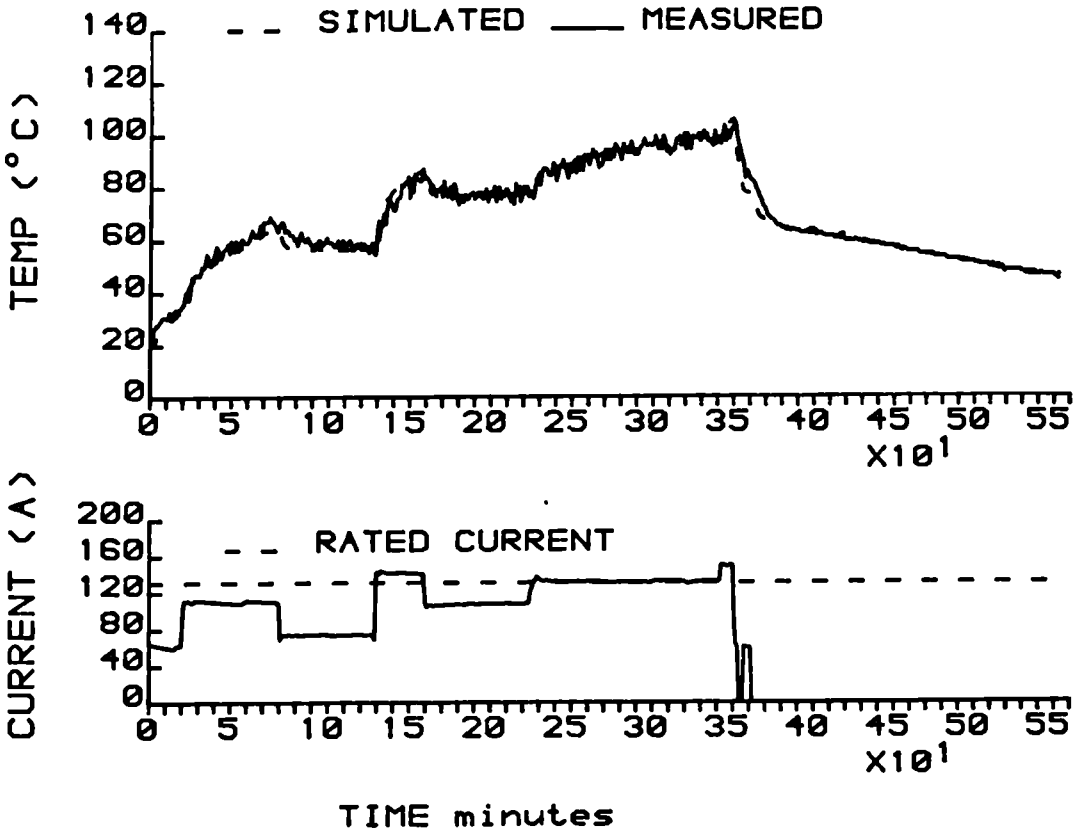

Figure 4·10 GEC 75kW Endwinding

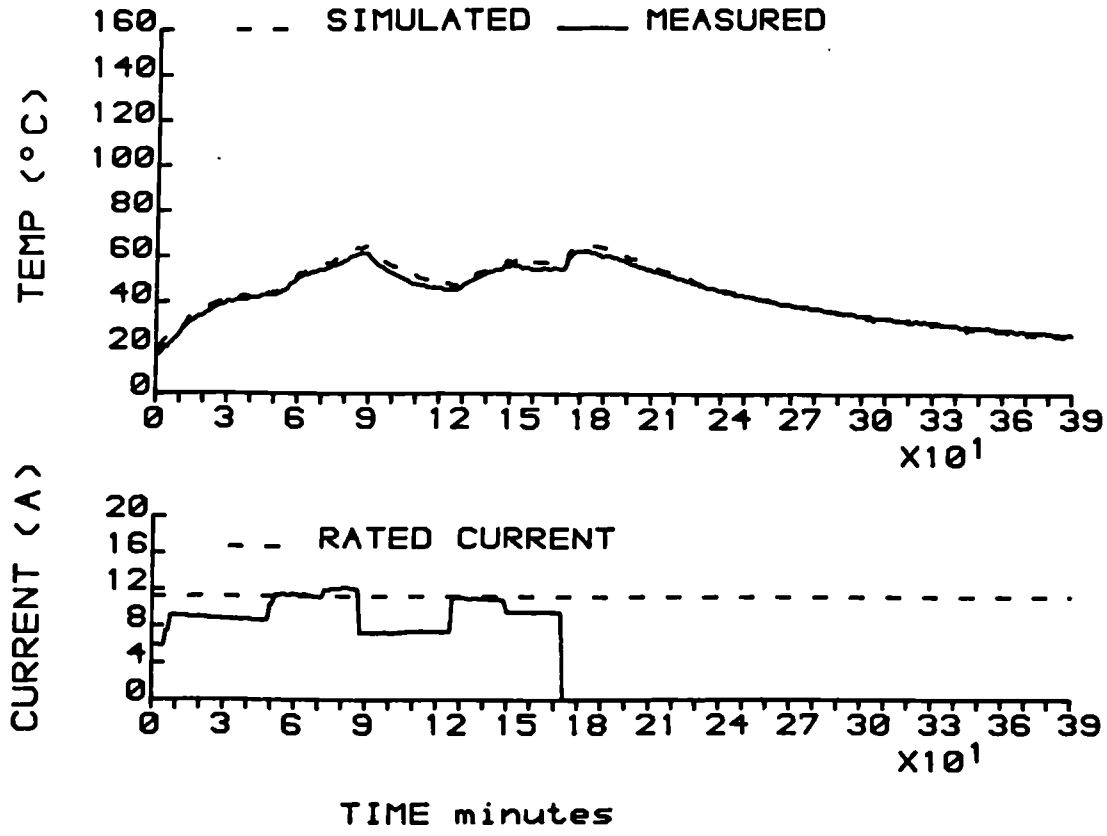

Figure 4·11 GEC 5·5 kW Frame

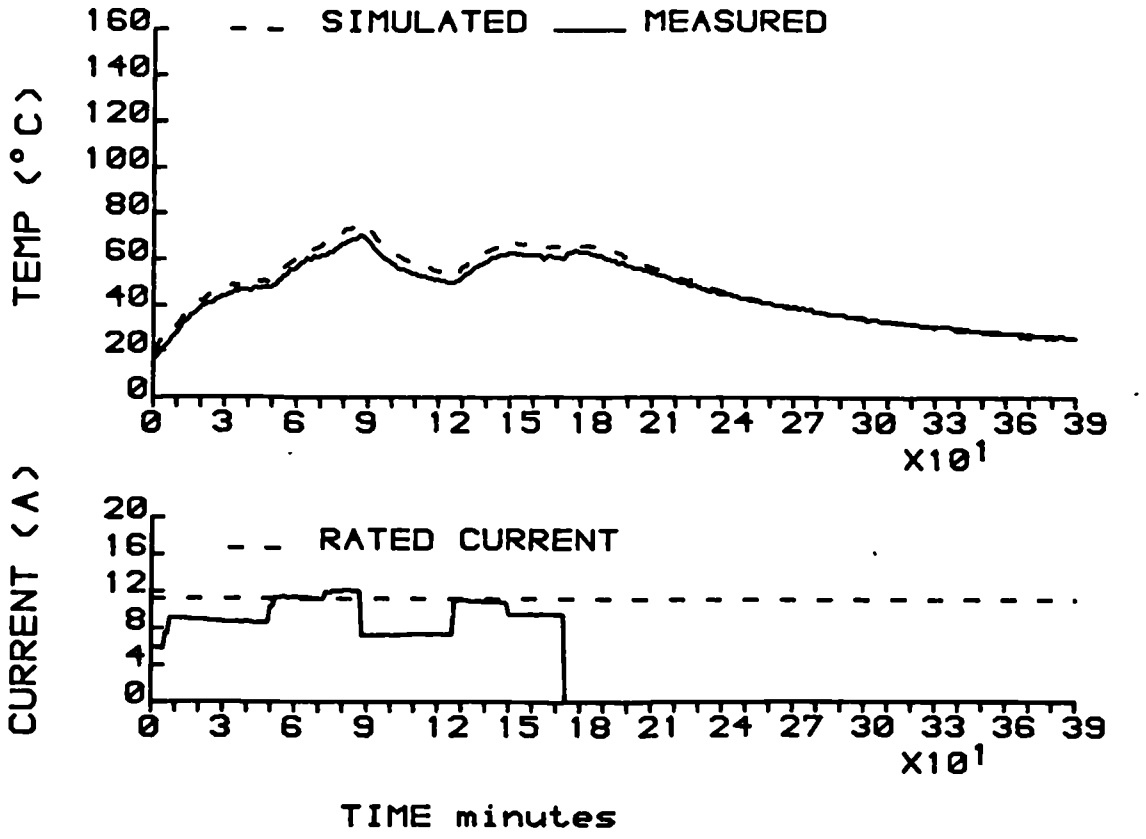

Figure 4·12 GEC 5·5 kW Stator Back Iron

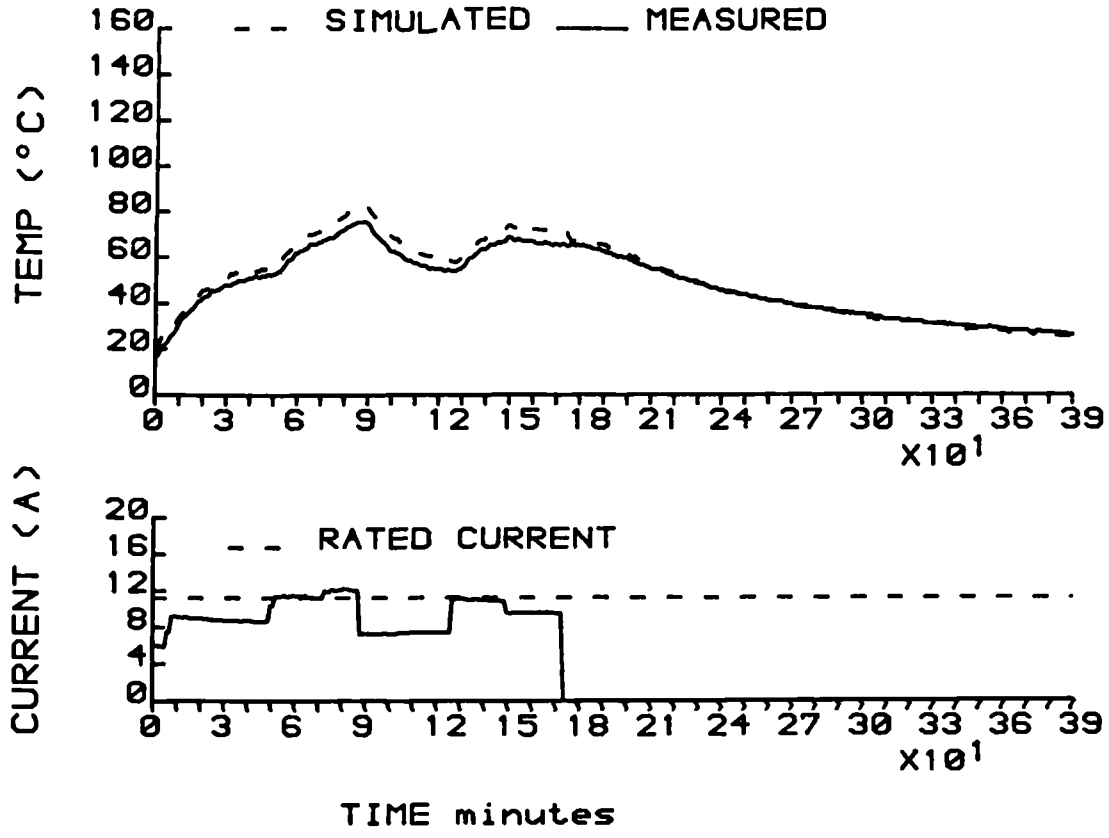

Figure 4·13 GEC 5·5 kW Stator Teeth

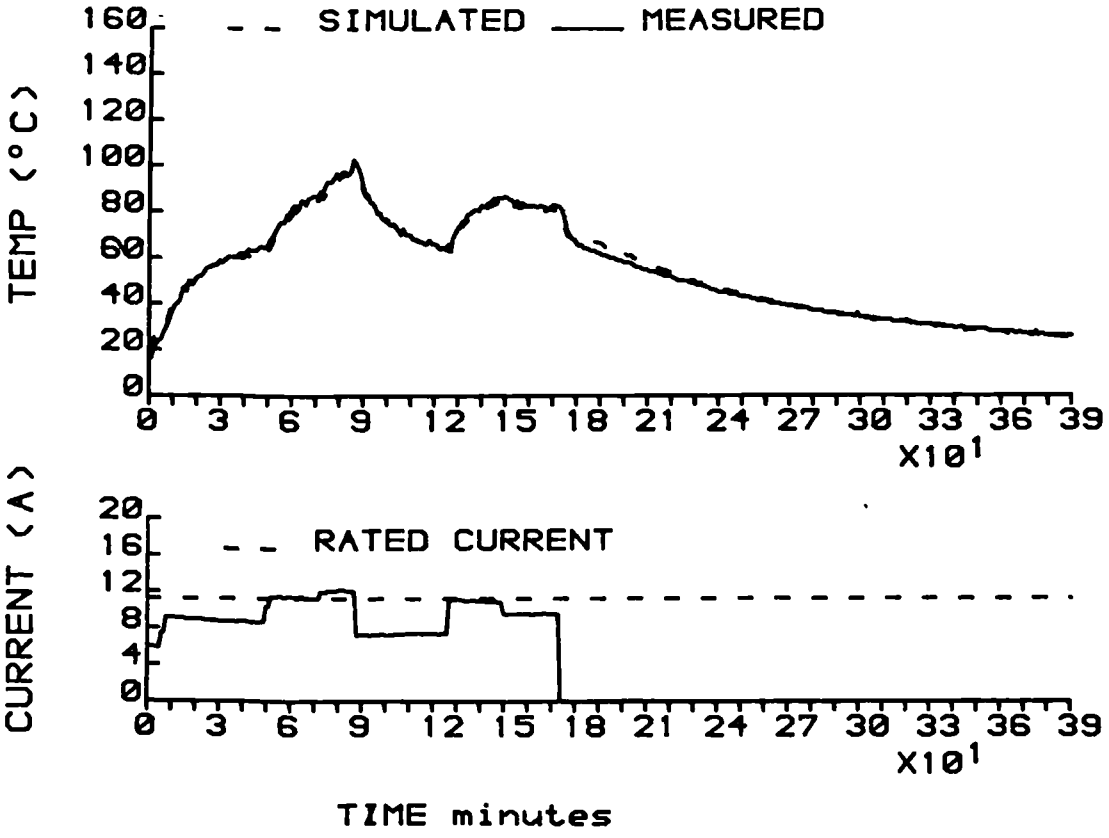

Figure 4·14 GEC 5·5 kW Stator Slot Winding

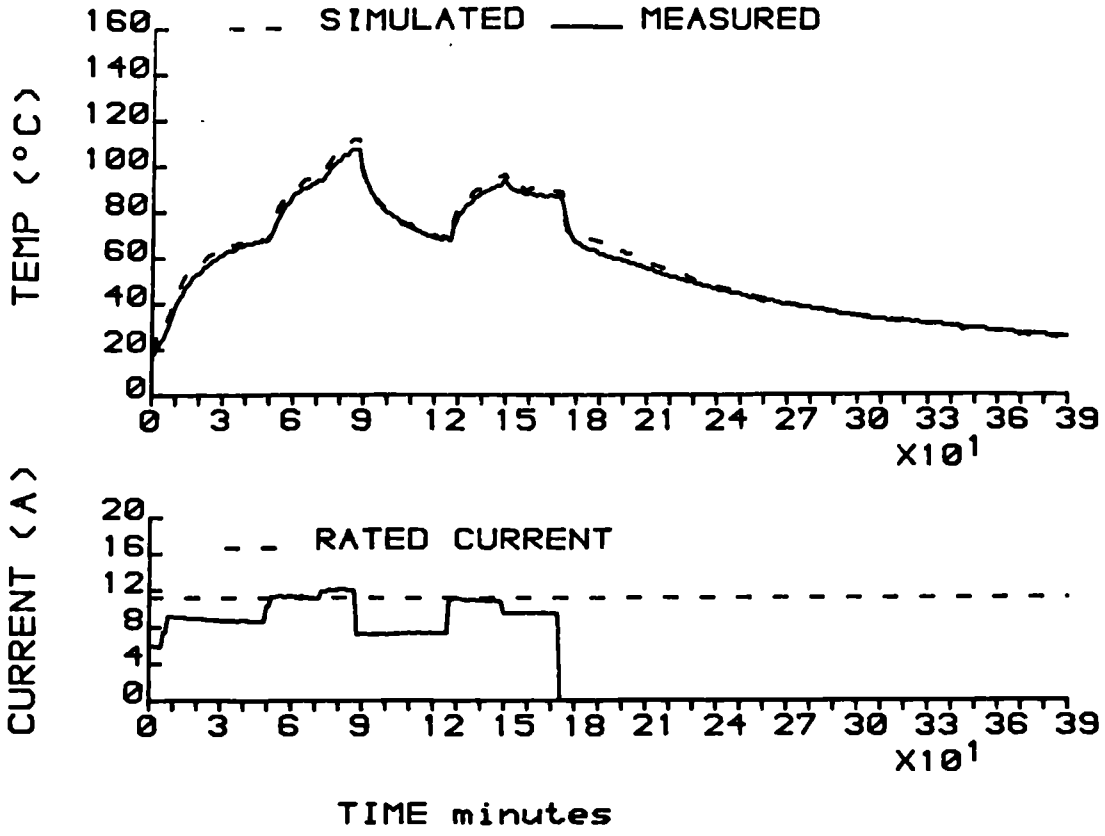

Figure 4·15 GEC 5·5 kW Endwinding

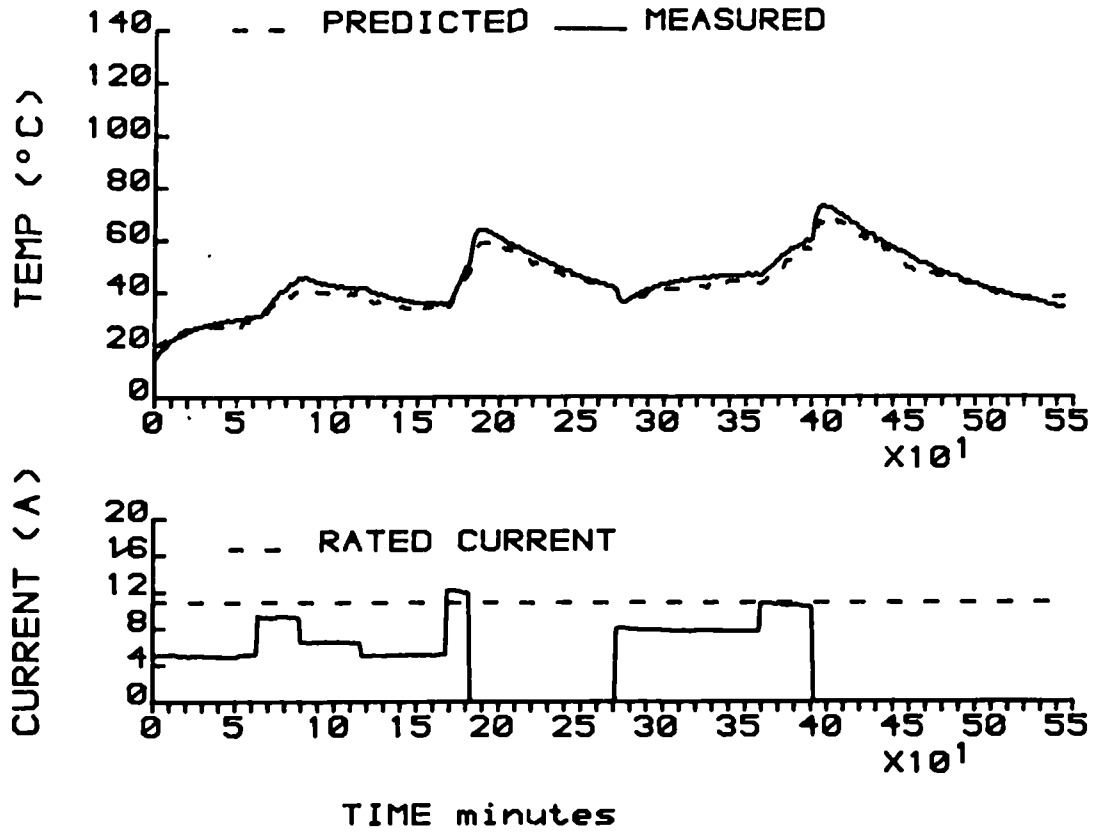

Figure 4·16 On-line Prediction BCP 5·5kW Frame

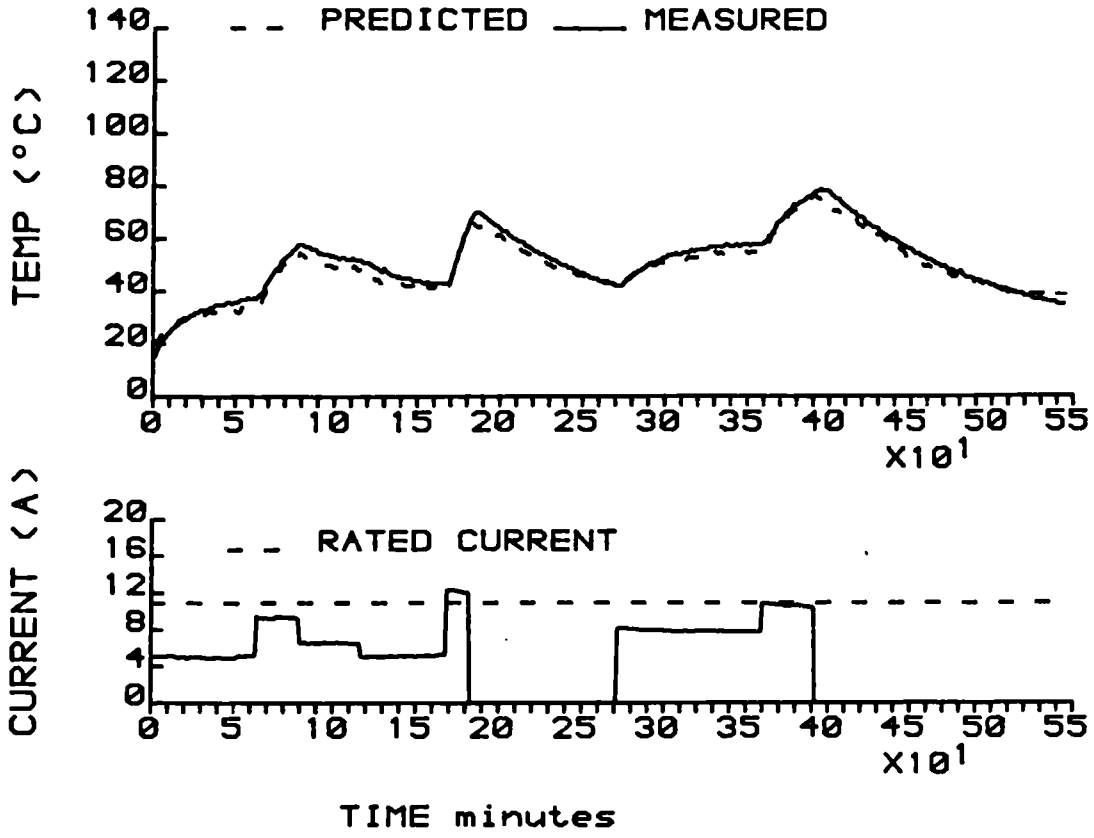

Figure 4·17 On-line Prediction BCP 5·5kW Stator Back Iron

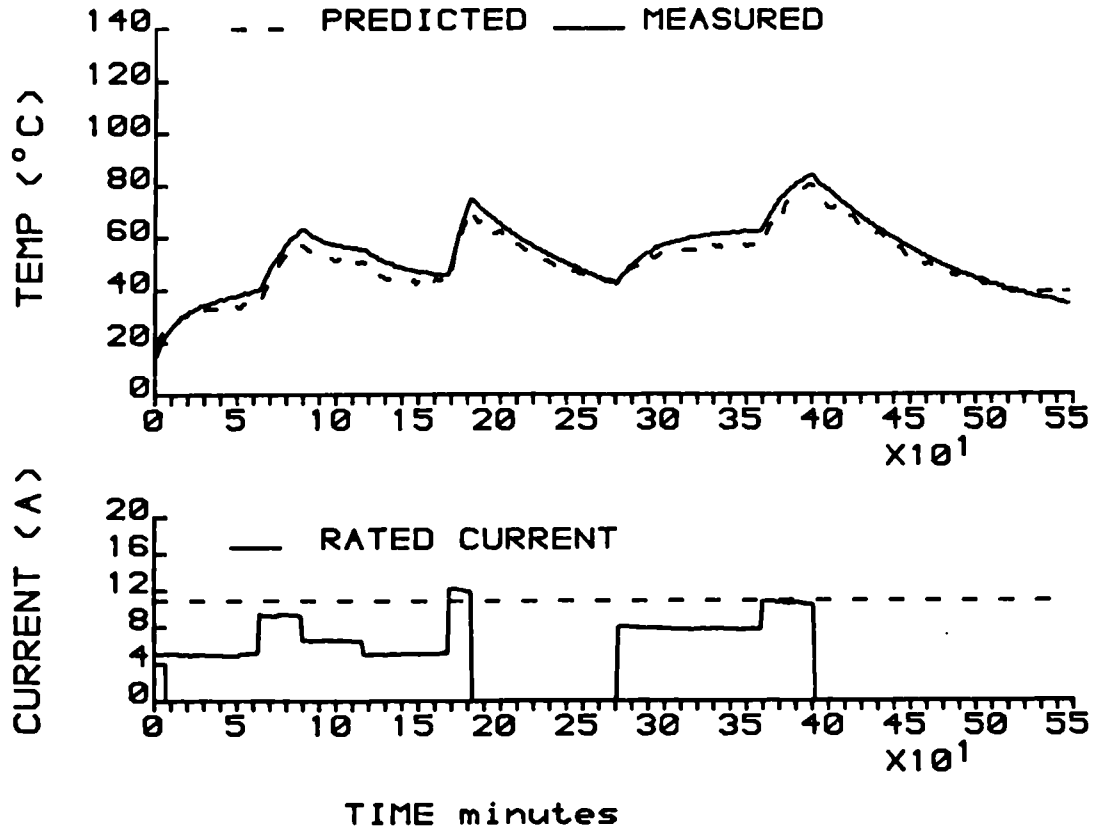

Figure 4·18 On-line Prediction BCP 5·5 kW Stator Teeth

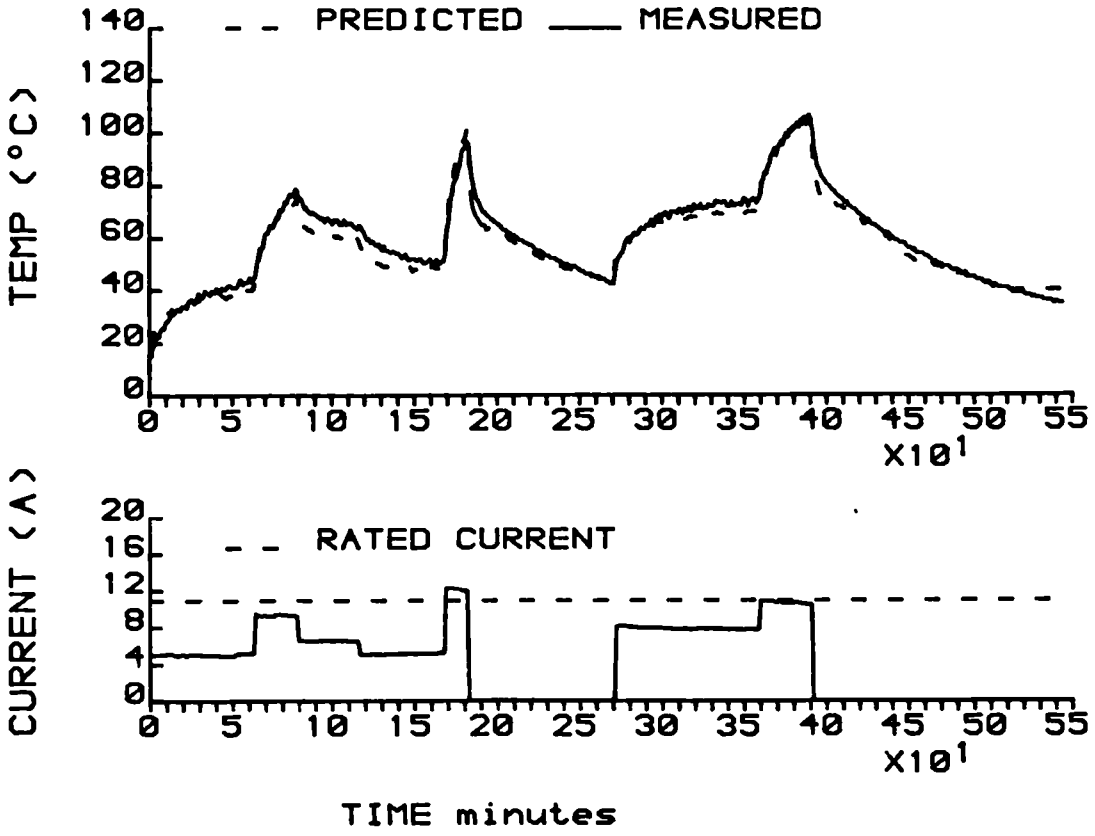

Figure 4·19 On-line Prediction BCP 5·5kW Stator Slot Winding

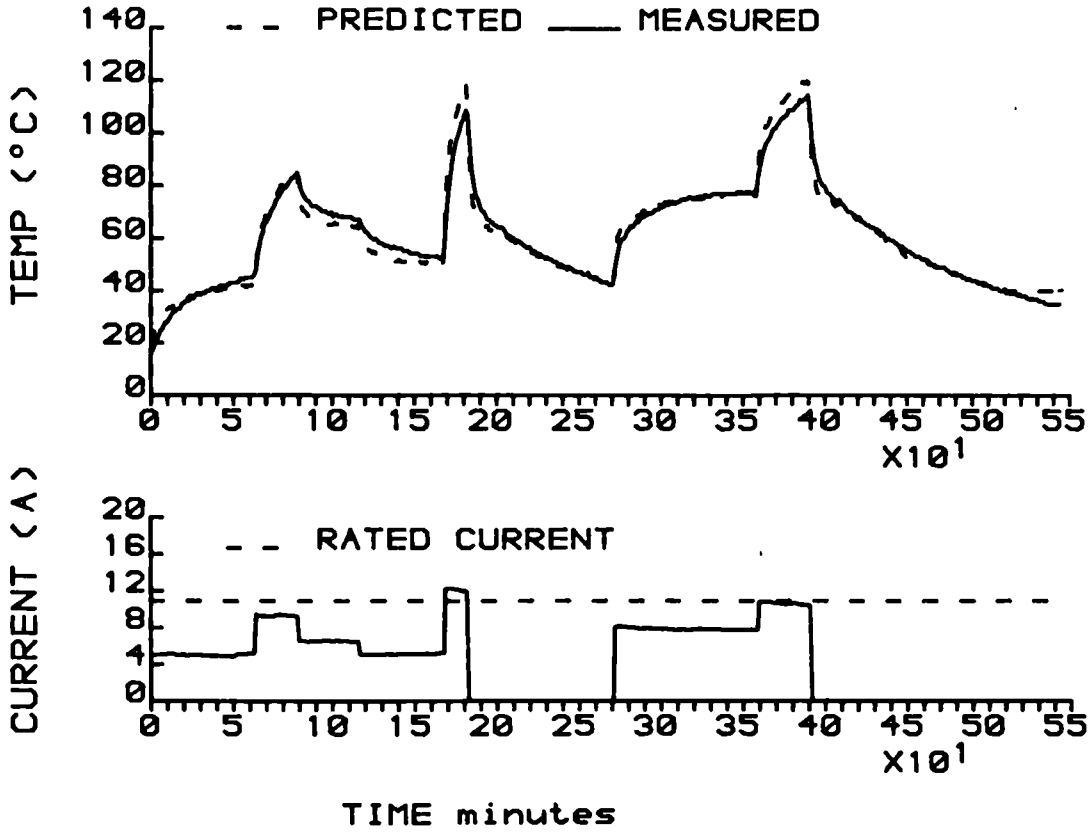

Figure 4·20 On-line Prediction BCP 5·5 kW Endwinding

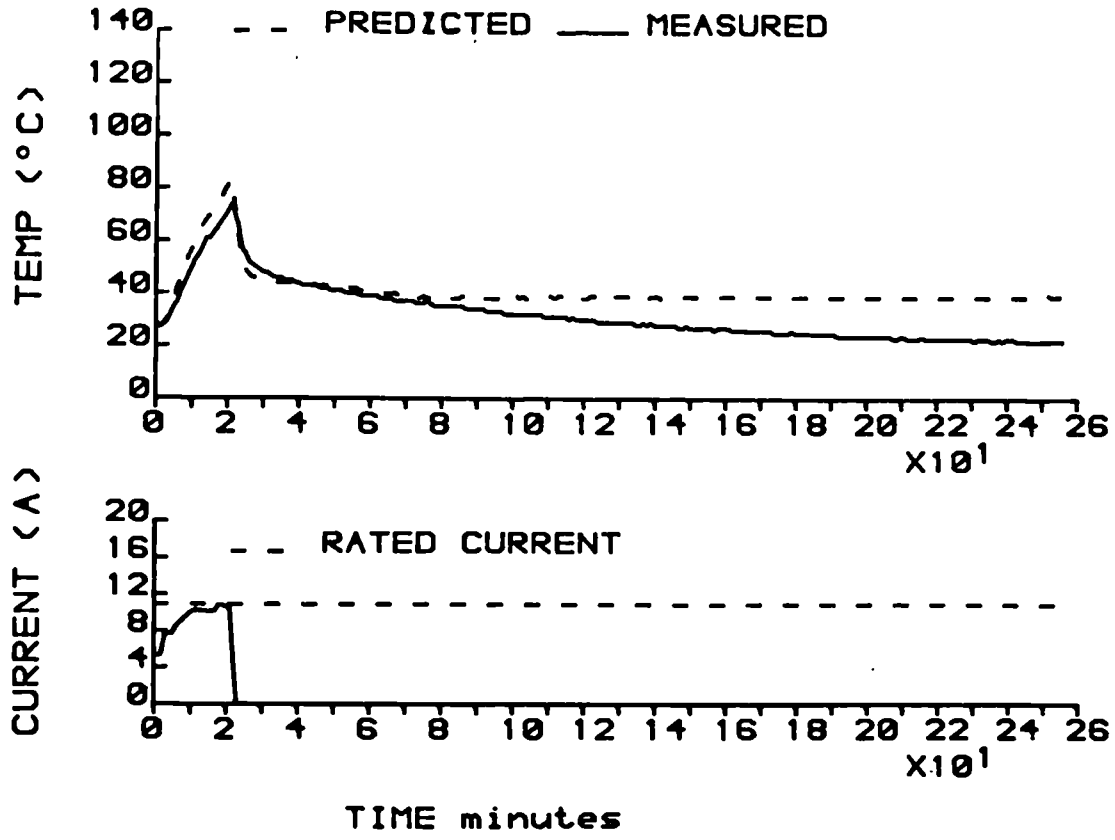

Figure 4·21 On-line Prediction BCP 5·5 kW Endwinding for Stationary $\Delta t = 1$ second

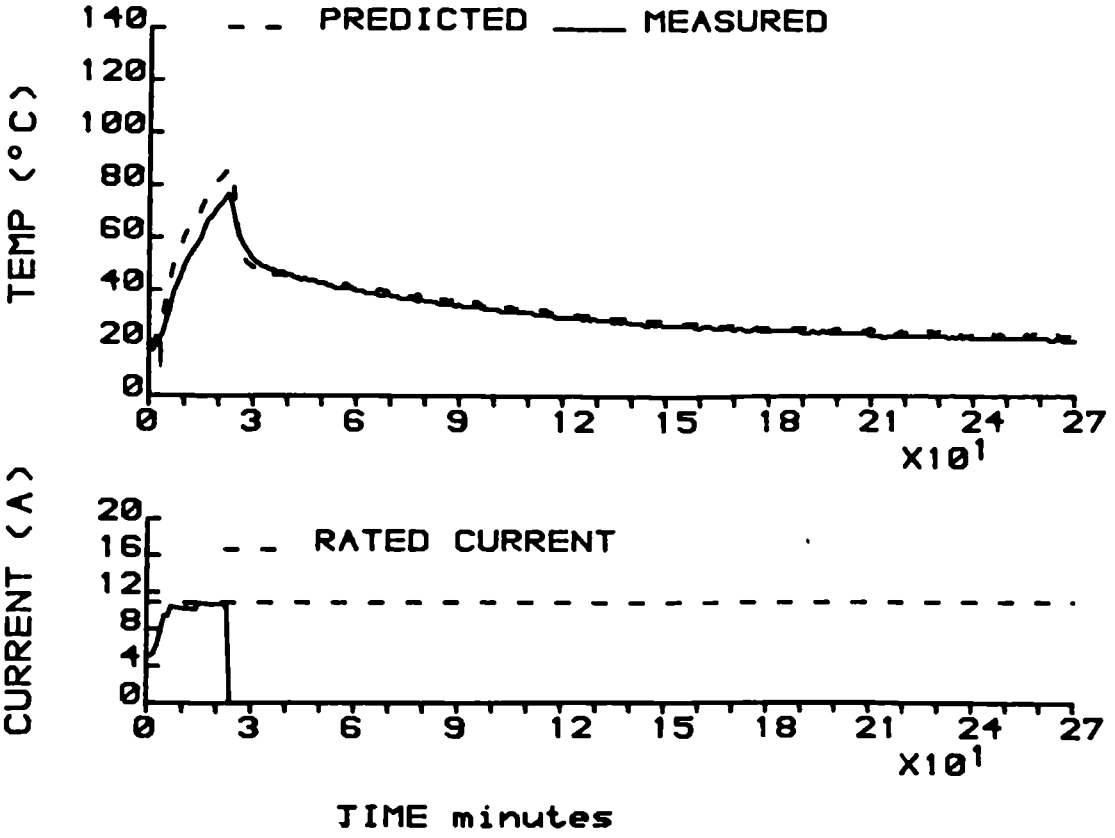

Figure 4·22 On-line Prediction BCP 5·5 kW Endwinding for Stationary $\Delta t = 60$ seconds

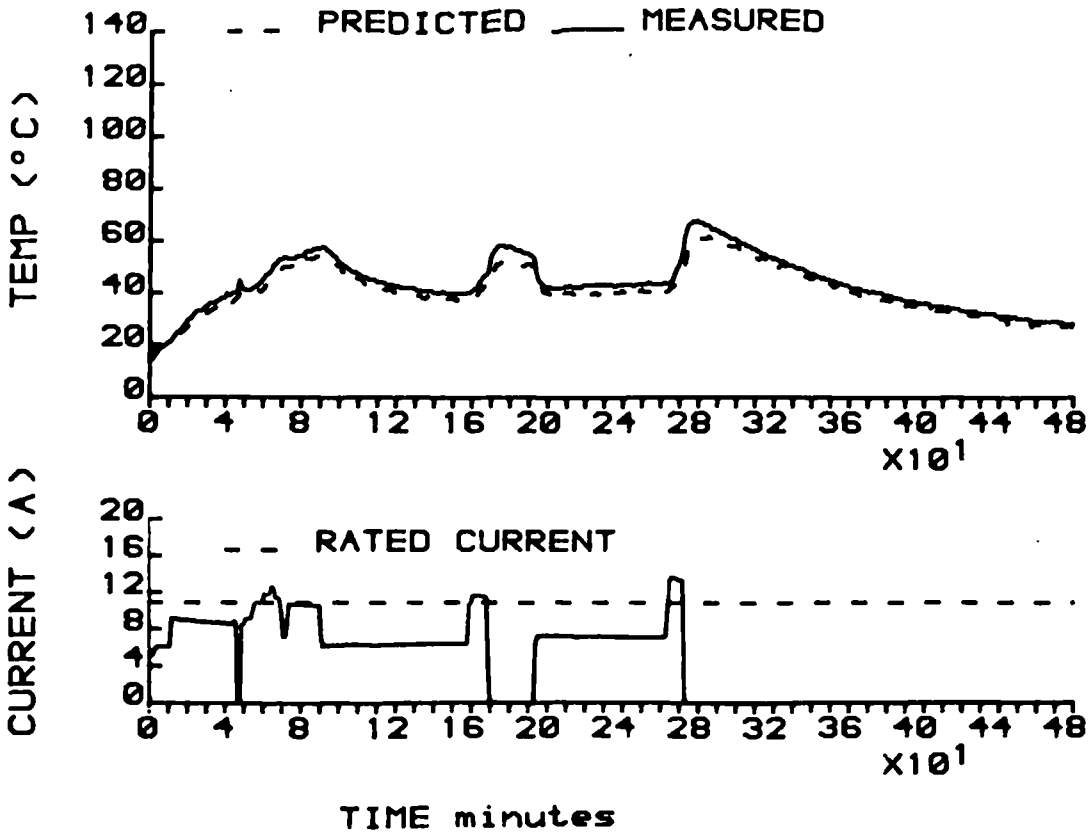

Figure 4·23 On-line Prediction BCP 5·5kW Frame with Stationary $\Delta t = 60$ seconds

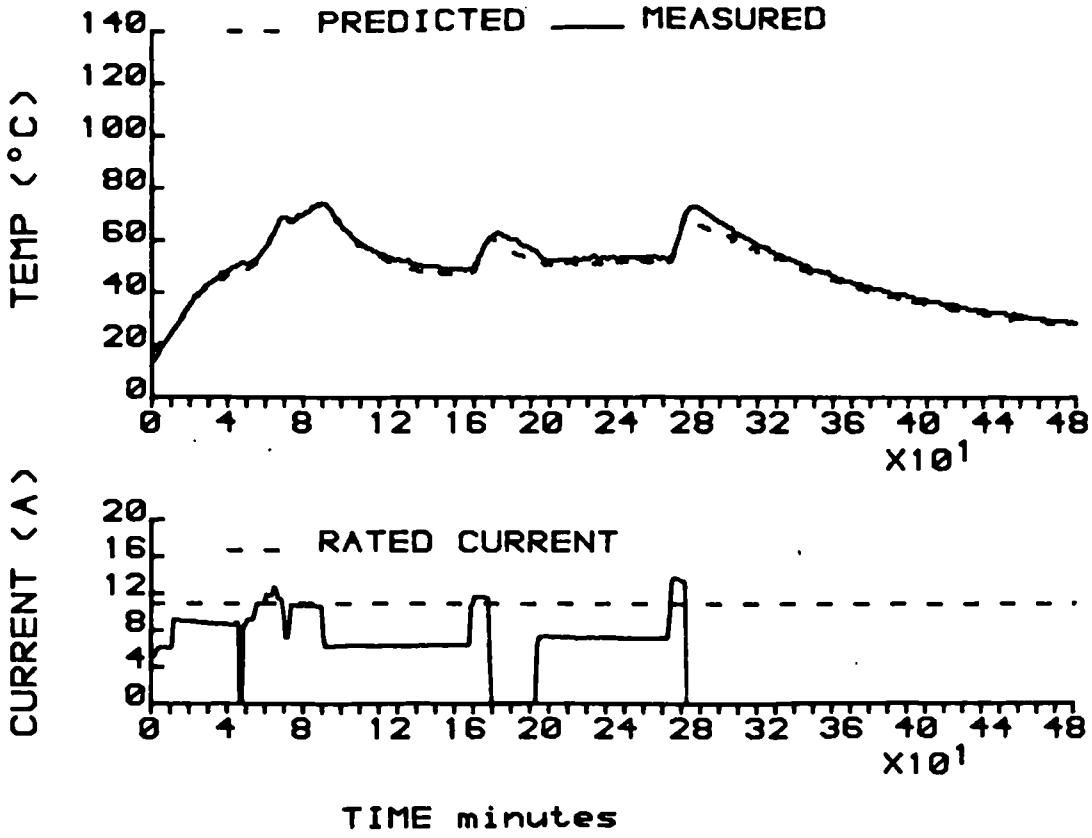

Figure 4·24 On-line Prediction BCP 5·5kW Stator Back Iron with Stationary $\Delta t = 60$ seconds

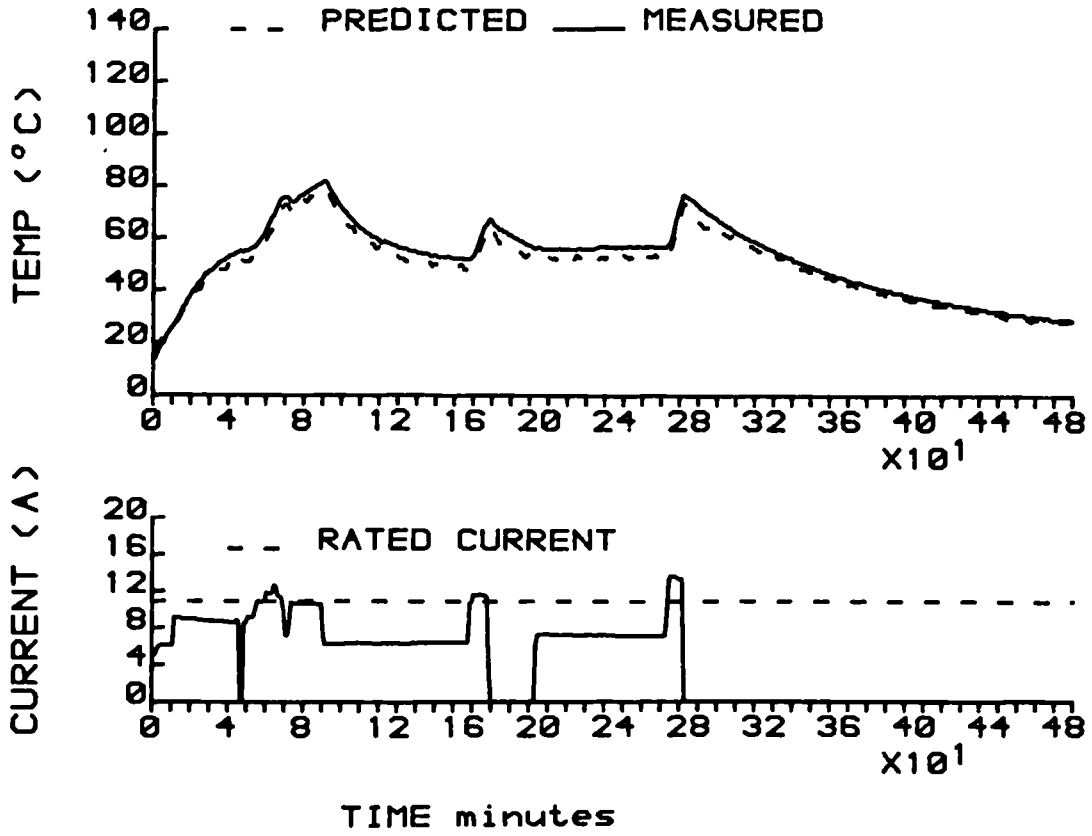

Figure 4·25 On-line Prediction BCP 5·5 kW Stator Teeth with Stationary $\Delta t = 60$ seconds

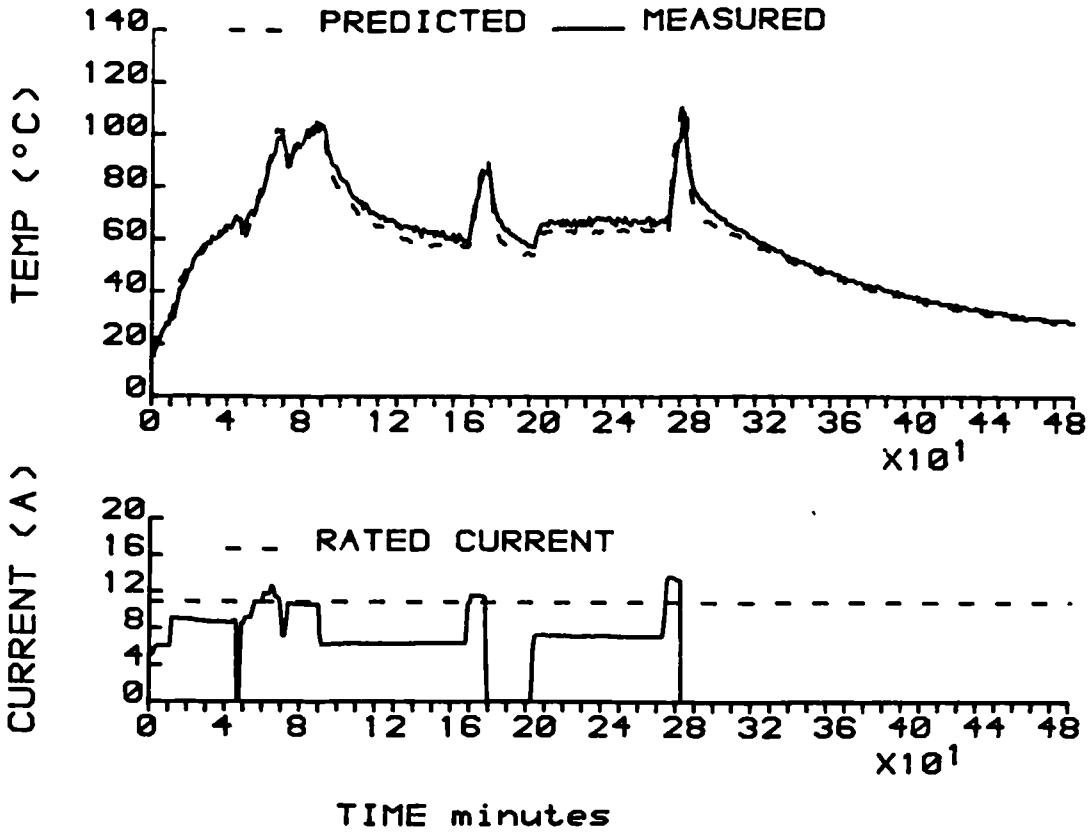

Figure 4·26 On-line Prediction BCP 5·5 kW Stator Slot Winding with Stationary $\Delta t = 60$ seconds

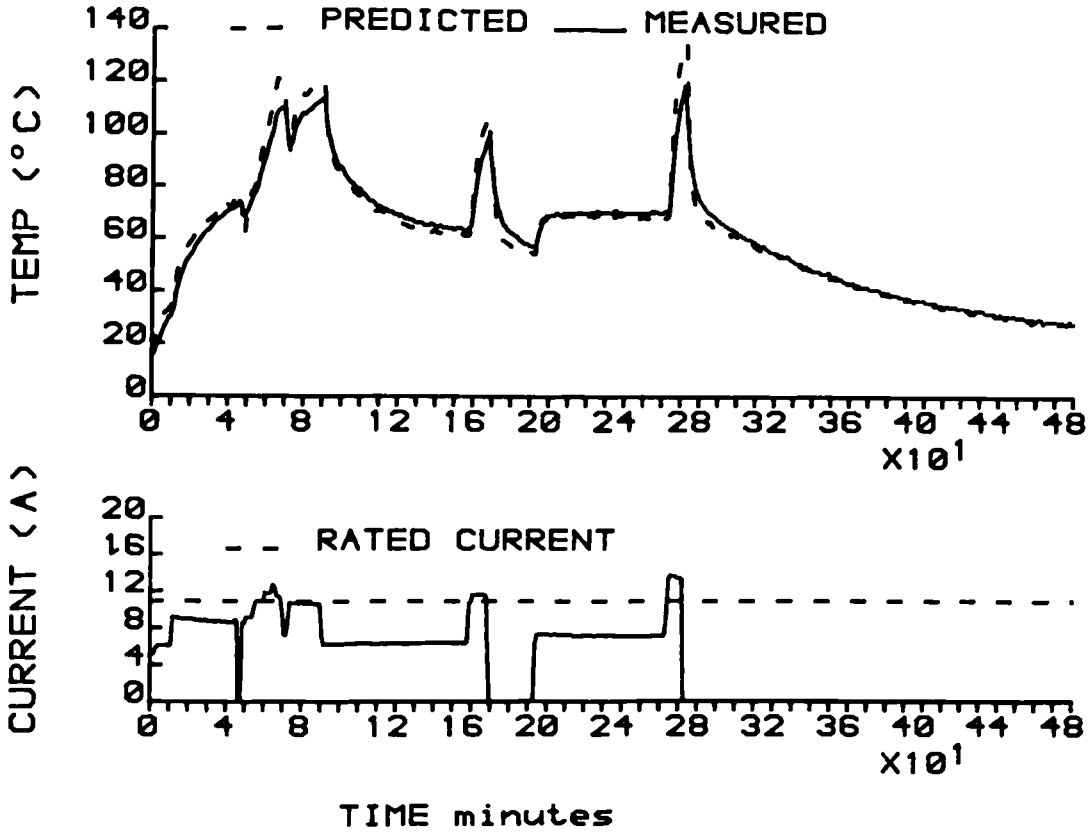

Figure 4-27 On-line Prediction BCP 5·5 kW Endwinding with Stationary $\Delta t = 60$ seconds

CHAPTER 5. THE UNBALANCED SUPPLY THERMAL MODEL.

5.1 INTRODUCTION.

Unbalanced three phase voltages are a common occurrence most frequently caused by an uneven distribution of single phase loads upon the incoming three phase supply. Generally, the unbalance is small and as such is often ignored. Even a small degree of unbalance, however, can have an adverse effect upon the performance of a three phase induction motor. The NEMA Standard [51], which applies to electrical apparatus manufactured in North America, does not recommend operation of three phase induction motors above a 5% voltage unbalance whilst Woll [26] points out that a serious loss of insulation life due to overheating could result from operation of motors from supplies with as little as a 2% unbalance. In fact, the NEMA recommendations are for motors with a 1.15 service factor thus clearly illustrating the need for sensitive protection of the new generation of smaller motors which do not possess this margin of tolerance to even small overloads.

Previous protection strategies have been to define the maximum allowable current unbalance, a method which is necessarily approximate, sometimes misleading and does not allow for the motor temperature at the onset of the fault condition. Gafford [28] translated the problem by advocating a multiplier ($k>1$) to simulate the additional heating effect of a negative sequence current over a positive sequence component of the same magnitude. This method was also adopted later by Westinghouse in their microprocessor based IQ 2000 device. Another device utilizes a

search coil, placed close to the motor shaft, which is tuned to particular harmonic frequencies imposed upon the magnetic leakage flux during unbalanced operation [1].

None of these devices use both the additional losses and their distribution to model the actual stator and rotor winding temperatures - a strategy which must ultimately afford more precise protection under unbalanced conditions.

The additional heating effects in three phase induction motors due to supply voltage unbalance have been investigated by several authors [24-28]. In their analyses they use the theory of symmetric components to translate the unbalanced system to a set of three balanced systems - the positive, negative and zero sequence components. For three wire systems, of which induction motors with no neutral connections are a subset, there is no zero sequence component and thus the system reduces to the positive and negative sequence components which can be treated separately and the effects of each superimposed to predict the overall performance of the motor. The positive sequence component is a balanced three phase system that produces a forward rotating magnetic field; the negative sequence component has the opposite phase sequence, thus producing a braking torque and also inducing high frequency currents in the forward rotating rotor. Under balanced conditions the negative sequence component reduces to zero.

The presence of a negative sequence current has a two-fold effect; firstly, for a given load, a larger positive sequence current is required to overcome the negative sequence braking torque and secondly, the high

frequency rotor currents cause disproportionately large rotor copper losses, particularly in rotors with a deep bar construction. As an example of this latter effect, it is estimated that for the 75 kW motor modelled during this work, the presence of a negative sequence current just one quarter of the positive sequence, not extraordinary even for voltage unbalance below the recommended 5%, would effectively double the rotor copper losses. Thus the net result of unbalanced operation is an increase in the motor losses for a given load accompanied by an increase in the motor temperatures.

In addition to the higher average temperatures, the concentration of the stator copper losses in the phase carrying the largest current, causes a more pronounced departure of the stator winding hot spot from the average winding temperature. This localisation of the stator losses was commented upon by Williams [27] who also calculated that for one particular motor, an 11% voltage unbalance caused 59% of the stator copper loss to occur in one phase; similar calculations based upon measurements taken during tests on the GEC 5.5 kW motor tested in this work indicate the same degree of loss concentration with as little as 3.2% supply unbalance.

In developing the thermal model then, it was necessary not only to include the additional losses, but also to model the spatial distribution of those losses around the stator winding. The former was implemented by using the sequence currents in the solution of the thermal generators whilst the latter required the re-evaluation of some of the components of the balanced thermal model of Chapter 2.

The use of sequence currents in the model solution led to the development of a sequence current measuring system using the prototyping system previously described in Chapter 3, and designed to be compatible with the on-line predictor software also outlined in Chapter 3. Time constraints prevented the eventual integration of the two systems though it was felt that the microprocessor implementation of the unbalanced model would mirror the predictions performed upon the mainframe computer, using data recorded using the sequence current measuring system, in the same way as the on-line predictions under balanced conditions agreed with the mainframe simulations (Chapter 4).

The distribution of the stator copper losses between the phases in the stator slot and endwinding sections required that further attention be given to the modelling of these components in order to predict the winding hot spot temperature. As the model seeks to determine the mean temperature of the slot winding and since the thermal conductance through the teeth and iron between the phase belts is relatively high [24], then it was assumed that the effects of the distributed losses could be assumed small and the balanced model for the slot component retained. For the endwinding component the dependence upon the endcap air temperature which is raised by the high rotor losses, the low inter-phase thermal conductivity particularly in single layer windings, plus the requirement for hot spot predictions all combine to advocate the remodelling of this component if it is to remain valid under unbalanced supply conditions. The remodelling was accomplished with minimum disturbance to the balanced model configuration presented in Chapter 2.

The stator teeth and iron components will also exhibit some temperature redistribution between the phase belts though, as the circumferential temperature gradients will be small in comparison with the windings, their models remain unchanged. It is acknowledged that all these small effects will add up to cause a larger endwinding temperature differential between the phases than will be predicted if they are neglected, however, in order to retain the simplicity of the thermal model, it is assumed that the majority of effects due to the uneven loss distribution will occur in the endwinding.

The model was tested by performing varying load tests on the two 5.5 kW motors supplied via three single phase variacs, the outputs of which could be varied to simulate different degrees of supply unbalance. The sequence current measuring system was incorporated into the prototyping system data logger and the combined system used to record the line currents, the sequence currents and the measured motor temperatures during these tests. The line and sequence currents were used to compute the unbalanced thermal model on the mainframe computer; the results of the unbalanced model predictions are shown in comparison with the measured temperatures in figures 5.16 to 5.28 and discussed in section 5.4.

5.2 THE REMODELLED ENDWINDING.

The endwinding component of the bulk component thermal model used for predicting the hot spot temperatures under balanced conditions, is modelled by the 'toroid with legs', a section of which is shown in figure 2.11 in Chapter 2; the complete component representation is shown in

figure 5.1. In order that this might be adapted to model the heat flow from the hottest phase to the cooler ones, it is split into three equal segments; one for each phase (figure 5.2). This can be represented in terms of a steady state thermal network, consisting of the thermal resistances of each segment to the component boundaries (R_1, R_2), the thermal resistance between the phases (R_3) and the thermal generators in each of the phases (G_1,G_2,G_3), by the circuit shown in figure 5.3.

Each of the nodes, T_1, T_2, T_3, represent the hottest temperatures in their respective phases and are modelled in accordance with the balanced endwinding component equations of figure 2.11. However, as each phase is considered separately the resistances R_1 and R_2, are three times their equivalents in Chapter 2. The boundaries with the slot winding and the endcap air, T_4 and T_5 respectively, are assumed to be at a constant temperature so that any difference in the hot spot temperatures can be formulated simply in terms of the per-phase generators and the thermal resistances shown.

The matrix equation which describes figure 5.3 is given below:

$$\begin{bmatrix} G_1 \\ G_2 \\ G_3 \end{bmatrix} = \begin{bmatrix} Y_t & -Y_3 & -Y_3 & -Y_1 & -Y_2 \\ -Y_3 & Y_t & -Y_3 & -Y_1 & -Y_2 \\ -Y_3 & -Y_3 & Y_t & -Y_1 & -Y_2 \end{bmatrix} \begin{bmatrix} T_1 \\ T_2 \\ T_3 \\ T_4 \\ T_5 \end{bmatrix} \qquad (5.1)$$

where,

Y_1 = thermal admittance to boundary with stator slot winding

Y_2 = thermal admittance to boundary with endcap air

Y_3 = inter-phase thermal admittance

$Y_t = Y_1 + Y_2 + 2.Y_3$

Assuming that node 1 represents the hottest phase, i.e. $G_1 > G_2$ and G_3, then the overall winding hot spot will be represented by T_1. The variables T_2 and T_3 can therefore be eliminated to leave an equation which describes a reduced, three node thermal network with a central node representing the endwinding hotspot.

$$\frac{1}{Y_t}\left[(Y_1+Y_2+Y_3).G_1 + Y_3.G_2 + Y_3.G_3\right] = (Y_1+Y_2).T_1 - Y_1.T_4 - Y_2.T_5 \qquad (5.2)$$

Multiplying equation 5.2 by 3, results in an equivalent circuit in which the thermal resistances compare exactly with the balanced endwinding model of Chapter 2. The thermal generator, G, required to give the hot spot temperature in this circuit is a function of the individual phase generators and the endwinding thermal resistances.

$$G = \frac{3}{Y_t}\left[(Y_1+Y_2+Y_3).G_1 + Y_3.G_2 + Y_3.G_3\right] \qquad (5.3)$$

Predictably, if the condition for balanced operation, $G_1 = G_2 = G_3$, is satisfied, then the above equation gives the total endwinding losses under balanced conditions and G is equivalent to that introduced at the balanced model node. Under unbalanced conditions, however, the generator described by the above equation exceeds the actual endwinding losses. Whilst this has the expected effect of raising the endwinding

hot spot prediction above that during balanced operation, it also affects the other model temperatures as these spurious losses find their way to the ambient air. Therefore, in order to ensure that the losses introduced into the model are the true endwinding losses and yet model the higher hot spot temperatures expected under unbalanced conditions without increasing the complexity of the thermal model, the equivalent circuit of figure 5.4 can be split into two components; figures 5.5(i) and (ii).

Figure 5.5(i) is exactly the same as the balanced model of Chapter 2; under conditions of unbalance this models the average of the hot spot temperatures for each phase, T_1'. The temperature rise above this for the hot spot of the hottest phase, T_a, is then given by the product of G_a with R_a from the additional equivalent circuit of figure 5.5(ii). The additional circuit parameters are derived as follows.

The average of the hot spot temperatures of each of the three phases, T_1', is given by reference to figure 5.5(i) as,

$$T_1' = \frac{1}{3(Y_1+Y_2)}\left[G_1 + G_2 + G_3 + 3.Y_1.T_4 + 3.Y_2.T_5\right] \qquad (5.4)$$

The hot spot temperature of the hottest phase endwinding can be found similarly from figure 5.4 as,

$$T_1 = \frac{1}{3(Y_1+Y_2)}\left[G_1 + G_2 + G_3 + \frac{2(Y_1+Y_2)G_1-(Y_1+Y_2)G_2-(Y_1+Y_2)G_3}{Y_t} + 3.Y_1.T_4 + 3.Y_2.T_5\right] \qquad (5.5)$$

Subtracting T_1' from T_1 for T_a gives,

$$T_a = R_t \left[G_1 - \frac{G_1+G_2+G_3}{3} \right] \tag{5.6}$$

Therefore, by analogy with the additional circuit of figure 5.5(ii), G_a and R_a are given by,

$$G_a = G_1 - \frac{G_1+G_2+G_3}{3} \tag{5.7}$$

$$R_a = \frac{1}{Y_1+Y_2+3.Y_3} \tag{5.8}$$

Modelling the effects of unbalanced operation on the endwindings in this way leaves the thermal model basically unchanged. The calculation of T_a is performed aside from the main thermal model calculations so that the extra, spurious losses, given by G_a, are not introduced into the model. From equation 5.6, it can be noted that the additional temperature rise, T_a, is a function of the difference between the hottest phase generator and the average phase generator and the endwinding thermal resistances.

In order that the model can be applied under transient load conditions, a thermal capacitance equal to that of figure 2.11 is added at the main node of figure 5.5(i) so that with respect to the balanced model the endwinding node is in no way changed. There will also be a thermal time constant associated with the additional equivalent circuit of figure

5.5(ii). For simplicity, and because of the relatively small temperature rises involved, this is ignored so that the additional temperature rise, T_a, is always a steady state value. This approximation under rising temperature conditions will over estimate the endwinding hot spot temperature which is considered to be a favourable condition with respect to its application in a protection device.

5.2.1 THE INTER-PHASE THERMAL RESISTANCE.

The inter-phase thermal resistance, R_3, is modelled as the resistance between the centres of two adjoining cylindrical rods separated by a strip of insulator (figure 5.6). The area of contact between the phases will be considerably larger than that indicated by figure 5.6 and can be approximated, for a single layer winding by,

$$A_f = \frac{2r.2\pi R}{3} \qquad (5.9)$$

where,

r = endwinding toroid cross section radius.

R = endwinding toroid radius.

For a double layer winding, this area will increase by a factor of 3 as the phases are in continuous contact around the whole of the toroid's circumference.

5.3 UNBALANCED MODEL THERMAL GENERATORS.

The losses due to the positive and negative sequence components

can be determined from their respective electrical equivalent circuits, shown in figure 5.7; the overall losses are found by summing the losses in both circuits. It should be noted that during normal motor operation (small slip), the negative sequence impedance is very much smaller than the corresponding positive sequence impedance and thus the shunting effect of the magnetizing branch can be ignored in the negative sequence circuit. It should also be noted that during motoring ($0<s<1$), the negative sequence mechanical output power, represented by $I_2^2 R_{r2}((s-1)/(2-s))$, is negative and thus reduces the power available at the motor shaft.

The losses calculated from the positive sequence equivalent circuit are those already formulated in Chapter 2 for the balanced model, using equivalent circuit parameters calculated from tests upon the motor under balanced supply conditions.

The stator parameters of the negative sequence equivalent circuit, R_{s2} and X_{s2}, are equal to their positive sequence equivalents R_{s1} and X_{s1} though due to the high frequency of the induced negative sequence currents, the rotor parameters differ. The ratios of R_{r2} and X_{r2} to R_{r1} and X_{r1} depend upon the motor supply frequency and the depth and physical properties of the rotor conductors. These ratios can be found from the theoretical curve of Swann and Salmon [41], referred to previously in Chapter 4. The previously determined positive sequence rotor quantities were calculated assuming an operating frequency of 0 Hz, therefore the factor by which these values must be multiplied to give the negative sequence rotor parameters can be found directly from the curves

assuming a negative sequence rotor current frequency of twice the supply frequency (100 Hz).

5.3.1 THE STATOR COPPER LOSS

The stator copper losses per phase P_{SC} are given by,

$$P_{SC} = I_{1p}^2 R_{s1} + I_{2p}^2 R_{s2} \tag{5.10}$$

The subscript 'p' denotes a phase quantity.
As the frequency of the positive and negative sequence stator currents are equal then,

$$R_{s2} = R_{s1} \tag{5.11}$$

and

$$P_{SC} = (I_{1p}^2 + I_{2p}^2)\, R_{s1} \tag{5.12}$$

As in Chapter 2, this loss is split between the slot and endwinding sections in the ratio of their respective volumes. Thus converting the phase currents into the line quantities which will be measured by the sequence current measuring system (the equivalent circuit parameters were calculated for a delta wound motor), and multiplying the per phase losses by three, leaves the slot and endwinding copper losses for the complete motor as,

$$P_{sw} = (I_1^2 + I_2^2).R_{s1}.f \tag{5.13}$$

$$P_{ew} = (I_1^2 + I_2^2).R_{s1}.(1-f) \tag{5.14}$$

These must further be divided by two as, due to the assumed axial symmetry, only half the motor is modelled.

The stator winding resistance is still temperature dependent of the form,

$$R_{s1} = (1 + \alpha_{cu} T_{sw}).R_{s10} \qquad (5.15)$$

where,

R_{s10} = stator winding resistance at 0°C

Also associated with the endwinding node in the unbalanced model is the additional circuit generator, G_a, given by equation 5.7; annotating the phase currents as I_{ap}, I_{bp} and I_{cp}, equation 5.7 can be rewritten as,

$$G_a = (I_{max}^2 - \frac{(I_{ap}^2+I_{bp}^2+I_{cp}^2)}{3}).R_{s1}(1-f) \qquad (5.16)$$

In a star wound motor, G_a, is given simply by determining the largest of the measured line currents and substituting accordingly in equation 5.16. For a delta wound motor however, whilst it is simple to find the average phase current squared in terms of the measured line currents (equation 5.17), there is no simple relationship between the maximum phase current , I_{max}, and the line currents.

$$\frac{(I_{ap}^2+I_{bp}^2+I_{cp}^2)}{3} = \frac{1}{3} \quad \frac{(I_a^2+I_b^2+I_c^2)}{3} \qquad (5.17)$$

For the three phase system shown in figure 5.8, providing that there is no zero sequence$_{\wedge}^{phase}$ component, it can be shown that the phase and line quantities are related by the phasor equations 5.18 to 5.20.

$$\bar{I}_{ap} = \frac{\bar{I}_a - \bar{I}_b}{3} \tag{5.18}$$

$$\bar{I}_{bp} = \frac{\bar{I}_b - \bar{I}_c}{3} \tag{5.19}$$

$$\bar{I}_{cp} = \frac{\bar{I}_c - \bar{I}_a}{3} \tag{5.20}$$

Applying the cosine rule to the angle between I_a and I_c in the triangle described by equation 5.20 (figure 5.9) gives,

$$9I_{cp}^{\ 2} = I_a^{\ 2} + I_c^{\ 2} - 2I_aI_c\cos\theta \tag{5.21}$$

As the line current phasors form a closed triangle, figure 5.10, it can also be shown that,

$$\theta = 180 - \phi \tag{5.22}$$

Where,

ϕ is the angle between $\bar{I}_a$ and $\bar{I}_c$, thus,

$$\cos\theta = -\cos\phi \tag{5.23}$$

Cos θ can be expressed in terms of the line currents as,

$$\cos\theta = \frac{I_b^{\ 2} - I_a^{\ 2} - I_c^{\ 2}}{2.I_a.I_c} \tag{5.24}$$

Making the substitution for $\cos\theta$, from equation 5.24, in equation 5.21 gives,

$$9.I_{cp}^{\,2} = 2I_a^{\,2} + 2I_c^{\,2} - I_b^{\,2} \qquad (5.25)$$

A similar treatment of I_{bp} and I_{ap} gives,

$$9.I_{bp}^{\,2} = 2I_c^{\,2} + 2I_b^{\,2} - I_a^{\,2} \qquad (5.26)$$

$$9.I_{ap}^{\,2} = 2I_b^{\,2} + 2I_a^{\,2} - I_c^{\,2} \qquad (5.27)$$

Hence, the largest phase current squared is given by twice the sum of the largest$^{\text{square}}_{\wedge}$line currents, minus the smallest line current squared. Assuming that I_a and I_c are larger than I_b causes I_{cp} to represent the largest phase current therefore, substituting I_{cp} from equation 5.25 for I_{max} in equation 5.16 gives,

$$G_a = \frac{(I_a^{\,2} + I_c^{\,2} - 2I_b^{\,2}).R_{s1}(1-f)}{9} \qquad (5.28)$$

Thus, the difference between the maximum and average phase current squared is given by sum of the largest$^{\text{square}}_{\wedge}$line currents minus twice the smallest line current squared. In common with the thermal generator equations derived previously, this must be divided by two to conform with the convention used in the thermal model. The calculation of the additional circuit generator, G_a, requires that all three line currents be known; the measurement of these quantities is therefore included in the sequence current measuring scheme.

5.3.2 THE ROTOR COPPER LOSS.

The rotor copper loss per phase, P_{RC}, is given by,

$$P_{RC} = (I'_{1p}/c)^2 c^2 R_{r1} + I_{2p}^2 R_{r2} \qquad (5.29)$$

Where (I'_{1p}/c) is equivalent to (I_2/c) of Chapter 2; they both represent the positive sequence referred rotor current.
The expression for $(I_2/c)^2$ and hence $(I'_{1p}/c)^2$ is given in Chapter 2 by equation 2.42.

$$(I'_{1p}/c)^2 = \frac{cX_m}{cX_m+2cX_{1sc}} \cdot I_{1p}^2 - \frac{1}{cX_m(cX_m+2cX_{1sc})} \cdot V_{1p}^2 \qquad (5.30)$$

giving the rotor copper losses per phase as,

$$P_{RC} = \frac{cX_m.c^2R_{r1}}{cX_m+2cX_{1sc}} \cdot I_{1p}^2 - \frac{c^2R_{r1} \cdot V_{1p}^2}{cX_m(cX_m+2cX_{1sc})} - I_{2p}^2.R_{r2} \qquad (5.31)$$

In this case, due to the high frequency of the negative sequence rotor currents, the negative sequence rotor resistance, R_{r2}, is likely to be greater than R_{r1}. Translating equation 5.31 from per-phase to line values gives the rotor copper loss for the whole motor as,

$$P_{RC} = \frac{cX_m.c^2R_{r1}}{cX_m+2cX_{1sc}} \cdot I_1^2 - \frac{3.c^2R_{r1} \cdot V_1^2}{cX_m(cX_m+2cX_{1sc})} - I_2^2.R_{r2} \qquad (5.32)$$

5.3.3 THE IRON LOSS.

Gafford [24] noted that the change in the iron loss, for quite substantial voltage unbalance, is small; he calculated the change to be 3.6% for a negative sequence voltage of 15%. In relation to the changes in the other losses, particularly the rotor copper loss, this can be considered negligible. In Chapter 2 the iron loss is calculated by subtracting the stator and rotor copper losses from the total equivalent circuit predicted losses. The same strategy is applied here giving the iron losses, P_I, in terms of the line sequence quantities, for the whole machine, as

$$P_I = \frac{3.V_1^2}{cR_m} - \frac{3.cR_{s1}V_1^2}{cX_m(cX_m+2cX_{1sc})} + \frac{((c-1)cX_m-2.cX_{1sc}).R_{s1}.I_1^2}{cX_m+2cX_{1sc}} \qquad (5.33)$$

5.4 THE SEQUENCE CURRENT MEASURING SYSTEM.

In order that the effects of unbalanced operation can be represented, the model requires input information on the magnitude of the positive and negative sequence currents plus the magnitude of each of the three line currents. The measuring system required to give this information must also conform to the following criteria:

1) That the time taken to measure and compute the information is sufficiently short to still allow the thermal model calculations to be performed within the same time period; chosen as one second in this case.

2) That the calculations of the currents should be sufficiently accurate for input into the thermal model.

3) That the measuring scheme should allow for the measurement of non-sinusoidal waveforms, particularly those typically found in induction motors.

The system chosen to fit these requirements sampled the magnitude of each of the line currents, digitally, a number of times during a single cycle of the current waveform; the line and sequence currents were computed subsequently from the compiled information. The system was developed upon the prototyping system described previously though some extra hardware was necessary to implement and control the sampling.

5.4.1 THE DIGITAL SAMPLING SCHEME.

Any unbalanced three phase system can be resolved into three balanced systems; the positive, negative and zero sequences. For three wire systems there is no zero sequence component and the unbalanced system can be represented as the superposition of the balanced positive and negative sequence components; such a system of unbalanced line currents is shown in figure 5.11.

The positive and negative sequence currents are defined, for the unbalanced system shown in figure 5.11(ii), by the equations below.

$$\bar{I}_1 = (1/3)(\bar{I}_a + a\bar{I}_b + a^2\bar{I}_c) \qquad (5.34)$$

$$\bar{I}_2 = (1/3)(\bar{I}_a + a^2\bar{I}_b + a\bar{I}_c) \qquad (5.35)$$

'a' is an operator which rotates the phasor upon which it acts through 120° while its magnitude remains fixed.

In order to calculate the sequence components, the respective waveforms must be shifted by 0°, 120° or 240° and the resulting waveforms added to give a wave of similar shape which is the positive or negative sequence component. To accomplish this digitally requires the simultaneous sampling of all three line currents a number of times, over a period which is an integer multiple of the period of the waveform. The more samples per period there are, the greater the resolution of the gathered data and accuracy of the solution. However, the calculation time required for assimilation of the measured data increases in proportion to the number of samples, as does the memory required for its storage.

A digital representation of the positive or negative sequence current can be constructed by adding the current samples from one waveform with those of the other waveforms displaced by the number of sampling periods equivalent to a time representing 120° or 240° intervals.

In this application 30 samples of each waveform were taken over a 20ms period representing just one cycle of a 50Hz line current; this was judged to fulfil the requirements noted earlier in this section without exceeding the time and memory reserved for the task of computing the currents.

The samples, are used to construct the sequence currents at 12° intervals. The positive sequence component is constructed as follows:

$$I_{1\ 0} = (1/3)(I_{a0} + I_{b120} + I_{c240}) \qquad (5.36)$$

$$I_{1\ 12} = (1/3)(I_{a12} + I_{b132} + I_{c252})$$

.

.

etc

The last number in the subscript, an integer multiple of 12°, refers to the magnitude of the current (I_a, I_b or I_c) at a time corresponding to the number of degrees shown, on a 50 Hz waveform, after the first sampling instant.

It is assumed that consecutive waveforms are identical so that it is not necessary to initiate the sampling at a predetermined reference point, that is, the first sample, although it is labelled 0°, is not necessarily at a zero crossing on the current waveform.

As it is the RMS current squared which will be used in the computation of the thermal generators, then each of the values $I_{1\ 0}$ to $I_{1\ 348}$ can be squared and added into an accumulator thus obviating the need to distinguish between the positive or negative values of $I_{1\ n}$.

The RMS positive sequence current squared is hence given by,

$$I_1^2 = \frac{1}{30} \sum_{n=0}^{29} I_{1\ n12}^2 \qquad (5.37)$$

Similarly for the negative sequence current with the distinction that:

$$I_{2\ 0} = (1/3)(I_{a0} + I_{b240} + I_{c120}) \tag{5.38}$$

$$I_{2\ 12} = (1/3)(I_{a12} + I_{b252} + I_{c132})$$

.

.

etc

and,

$$I_2^2 = \frac{1}{30} \sum_{n=0}^{29} I_{2\ n12}^2 \tag{5.39}$$

The RMS line currents squared can be found in a similar way by summing the squares of the measured values associated with the particular line current. I_a^2 for example, is calculated thus,

$$I_a^2 = \frac{1}{30} \sum_{n=0}^{29} I_{a\ n12}^2 \tag{5.40}$$

5.4.2 MEASURING SYSTEM HARDWARE.

In addition to the hardware afforded by the prototyping system, described in Chapter 3, some additional hardware was required to implement the sequence current measuring system; this is shown in block form in figure 5.12.

The line currents are interfaced via current transformers and a shunt resistance. Two operations are performed upon the signal at the

shunt; one, the signal is rectified and scaled for input to a monopolar analogue to digital converter and two, the unrectified signal is fed to a comparitor which generates a square wave of 5 Volts (logic 1) amplitude during the signal negative half cycle and zero during the positive half cycle. In this way, all eight bits of the analogue to digital converter can be used to represent the magnitude of the input signal thus doubling the accuracy of the current measurements; the sign bit, which in bipolar operation, would reduce the digital representation of the currents magnitude to seven bits, is generated separately.

All three analogue to digital converters and the sign bit latch share a common start signal so that all the samples are taken simultaneously; the output tristates are enabled separately after a delay to allow for the device conversion times, and the digital data transferred to the prototyping system memory via the system bus. Some local control, necessary to allow for the rather long tristate settling time of the converters used, was provided by a monostable, connected to the RDY input of the 8085A processor, which suspended the reading of the data bus for 700ns. The address decode circuit is shown in figure 5.13.

It is recognised that, in a minimum system, only two currents need to be measured, the third can be deduced as the instantaneous sum of the currents in a three wire system is zero. Furthermore, using the analogue to digital converters in bipolar mode would remove the need for the rectifying and sign bit generating hardware though at the expense of halving the resolution of the measurement. In this prototyping system, however, the described hardware was chosen for its accuracy and ease

of calibration, both important criteria with respect to the application of the system in testing the unbalanced model performance.

5.4.3 MEASURING SYSTEM SOFTWARE.

The software used to calculate the positive and negative sequence currents and the three line currents was designed to be easily integrated into the existing thermal model software described in Chapter 3. As such, the measurements and calculations of the currents were performed every second, to conform with the thermal solution time step, using the existing subroutines developed to perform the arithmetic in the thermal model solution described in Chapter 3. The complete current measurement can be divided into two stages - the data logging stage and the calculation stage. The first stage is dedicated solely to the task of sampling each of the currents 30 times over one complete cycle. In this stage the timing control is critical; it is provided by interrupts from the 8155 programmable timer/counter which are counted and stored by an interrupt routine. A start conversion pulse is sent to each of the analogue to digital converters and sign bit latch every 0.666 ms, equivalent to a 12° interval on a 50 Hz waveform. After a delay to allow for the conversion times the devices are polled in turn, in the expected order of phase sequence (i.e. I_a, I_b, I_c), followed by the sign indicator word (S). The data is stored in an orderly fashion in the prototyping system memory, figure 5.14.

Subsequent to issuing the start conversion signal for the penultimate (29^{th}) sample, the timer is reprogrammed to give a square wave of 5ms period, the nearest convenient integer divisor to the

maximum count capability of 5.33 ms. Reversion to the 5ms count, used previously in the software control for the on-line predictor of Chapter 3, ensures that the following sequence current calculations are not subjected to unnecessary stoppages to service the interrupt routine. A schematic of the timing control is shown in figure 5.15.

The entire data logging stage takes 20ms, equivalent to a complete cycle of the line current waveforms at 50 Hz, after which the sequence current calculations can proceed.

The scheme for computing the RMS line and sequence currents squared, described previously in section 5.4.1, is implemented by use of a loop counter; that is, a count which starts at the address of the first data byte of figure 5.14, I_{a0}, and moves through the data by successive increments until the address of the last data byte, S_{348} - an increment further to this address reverts the count back to the address of the first data byte and so on. It can be noted, from figure 5.14, that a loop count of 41 fulfils the requirements of the positive sequence calculations (equation 5.36), whilst a count of 81 is consistent with the requirements of the negative sequence calculation (equation 5.38).

The absolute value of the sum of every set of 3 data items, separated by the respective loop count, is squared and added into a 24 bit accumulator. The process repeats itself 30 times until the accumulator contains a number which is directly proportional to the RMS positive or negative sequence current squared. These values can be scaled and used directly in computing the thermal generators for an on-line solution which would follow in a real time implementation of the unbalanced model for a

protection device. In this case, however, the quantities so calculated were punched onto paper tape, transferred to the mainframe computer along with measurements of the motor temperatures recorded simultaneously during unbalanced varying load tests and used to produce the comparisons between measured and mainframe simulated temperatures shown in figures 5.16 to 5.28. The RMS line currents squared are calculated simply by summing the squares of each sample of the relevant current waveform, in this case the required loop count is 4.

5.4.4 MEASURING SYSTEM PERFORMANCE

To prove the accuracy of the sequence current and line current calculations, the sample data for the unbalanced system shown in figure 5.11, was compiled on the mainframe computer and entered, in the form of figure 5.14, into the prototyping system memory. A sinusoidal waveform was assumed with the first sample taken at a randomly chosen value of 5° on I_a. The mainframe computer was also used to calculate the exact solution from the magnitudes of the line currents. The errors between the exact solution and that produced by the sequence current measuring software using the prototyping system microprocessor were 0.05% and 2% for the positive and negative sequence currents respectively.

The sequence current measuring system as a whole was tested, after being calibrated, by accurately measuring the individual motor line currents, using conventional instruments, while the measuring system was running. The agreement between the sequence currents calculated manually and those predicted by the measuring system was again good,

giving errors no greater than 1% for both sequence currents and the line currents.

Because the software timing is fixed, based upon a 50Hz current waveform, any supply frequency variations about 50Hz will lead to errors in the sequence current measurements. To check that this approximation would not lead to significant errors, a mainframe simulation of the digital sampling scheme was performed, again on the unbalanced system shown in figure 5.11, for frequencies between 49.5 and 50.5Hz - these being the maximum expected excursions of the supply frequency. The results showed a maximum error in the negative sequence measurement over that at 50Hz of 3%; the corresponding error in the positive sequence current measurement was just 0.1%. The combined error in the calculation of the thermal generators was estimated at 0.3%.

An interesting property of the sequence current measuring system is its ability to deal with conditions of extreme unbalance such as that imposed by reducing the phase to neutral voltage in one phase to zero which created the most severely unbalanced condition included in the varying load tests described in the following section. An example of this condition is shown at 188 minutes in the results of the tests on the GEC 5.5kW motor (figures 5.20 to 5.23) where the negative sequence current exceeds the positive sequence current by a factor of 3; this actually implies a reversal of the line current phase sequence though it must be noted that the phase sequence of the supply voltage has not changed. The condition described results in a 50% negative sequence voltage and as the impedance of the motor at normal operating slips is much lower to the negative sequence than to the positive sequence (factor of 6 in

this case), it is not surprising that the negative sequence current exceeds the positive. The fact that the apparent phase sequence of the line currents had reversed was confirmed by plotting the sampled data, recorded during the data logging stage of the sequence current measurement, for a balanced and for an extremely unbalanced condition similar to that described above.

It is also worth mentioning that during the unbalanced condition shown at 188 minutes in the results for the GEC motor, the line currents themselves, while large, represent only a 35% unbalance; in contrast, those at 20 minutes in the same test, resulting in quite small temperature rises and actually delivering more torque than at 188 minutes, represent a 38% current unbalanced. It is evident therefore, that percentage current unbalance alone is not a sufficient criterion for protection.

5.5 UNBALANCED MODEL TESTS, RESULTS AND DISCUSSION.

Varying load tests, similar to those described in the previous Chapter, were executed on each of the 5.5 kW motors. Three single phase variacs, connected between line and neutral of the balanced laboratory supply, were used to simulate varying degrees of supply unbalance.

For the GEC 5.5kW motor the resistance thermometers were retained in exactly the same positions as for the balanced model tests of Chapter 4, thus only two endwinding temperatures were measured, one at each axial end. Since the drive end was invariably the hottest, this left only one endwinding hot spot measurement. Therefore, to ensure compatibility

with the simulated data from the unbalanced model solution, the phase winding which housed the drive end endwinding thermometer was maintained as the hottest phase throughout the test, regardless of the degree of unbalance. The stator slot winding thermometers were located in the cooler phases so were likely to measure lower than the component mean temperature; the same was true for the thermometer mounted in the stator teeth which was located in the vicinity of one of the cooler phases. After the test had been completed it was noticed that the stator back iron thermometer had become displaced from its position making the measurements for this node invalid; the comparisons between the measured and simulated data for this node were therefore excluded from the results.

Before the unbalanced varying load tests were performed on the BCP 5.5kW motor, thermometers were placed in similar locations on each of the endwinding and slot winding phases at the drive end of the motor thus providing additional information upon the temperature distributions between the phases and an enabling an estimate to be made of the mean phase temperatures for the slot and endwinding components for comparison with the predictions. During the tests the supply voltages were monitored manually; an average value was calculated and used in the thermal model solution.

The results for both the motors tested are presented as graphical comparisons between the measured data and that simulated by the unbalanced model using the sequence and line current measurements recorded during the tests. An indication of the degree of unbalance at any time is given by the magnitudes of the measured positive and negative sequence currents plotted beneath the temperature curves, using the

same time axis. The results for the GEC 5.5kW motor are shown in figures 5.16 to 5.24 and those for the BCP 5.5kW motor in figures 5.25 to 5.28.

5.5.1 THE GEC 5.5KW MOTOR.

Figure 5.16 to 5.19 show the measured temperatures from the unbalanced load test plotted against those predicted from the unbalanced thermal model for the GEC 5.5kW motor, using the average of the three line currents as the model input. These simulations include neither the additional losses caused by the sequence currents nor the compensations for the spatial distribution of the losses, as such they serve to demonstrate the importance of including these effects in the unbalanced model.

The frame and teeth nodes show similar agreement with those of figure 4.11 and 4.13 of the balanced model tests for this motor. However, it must be noted that the measured stator tooth temperature is likely to be a little lower than the component mean as it is mounted near to one of the cooler phases. The same is true for the stator slot winding temperature measurement; the apparent correlation with the simulated temperatures for this node imply that this too is less than the true component mean. The major discrepancy, as expected, occurred in the endwinding comparison where the simulated hot spot temperatures fall below the measured values over most of the curve. Since the measured values are likely to be slightly below the actual endwinding hotspot, the actual error in the simulation will be larger than shown. So it is apparent that the effects of unbalance cannot be ignored, at least when modelling the

endwinding hot spot temperature and that the average motor current for anything but mild supply unbalance is not an adequate model input.

The corresponding results using the unbalanced model with the sequence currents as inputs are shown in figures 5.20 to 5.23. The simulated frame temperatures, this time, exceed those measured which, using the calorimetric property of the frame measurements, indicates that the simulated motor losses were higher than the actual losses, particularly in the middle (130 mins) and near the end (195 mins) of the test. These periods, however, also correspond to the maximum cooling gradients, especially large for the rotor winding node simulation figure 5.24. As two thirds of the heat loss from the rotor winding node (calculated from thermal model data) is either transferred to the endcap air, or conducted via the shaft and bearings to the endcaps, then it is probable that a redistribution of the frame temperature from the centre to the axial extremities occurs. As the major heat flow paths now bypass the centrally positioned frame thermometer, its representation of the frame temperature must be doubted.

The difference between the simulated and measured stator teeth temperatures is not of great importance and can be attributed partly to the measurements being between the cooler slots and partly to model and measurement inaccuracies which were also apparent in the balanced model tests (figure 4.13). The stator iron losses which are introduced at this node, do not change significantly [24] and are not thought to be a major contributor to this discrepancy.

The stator slot and endwinding comparisons show clearly the advantages of compensating for the additional losses in the unbalanced model. The stator slot winding simulated temperatures are generally high as anticipated, the measured data being for one of the cooler phases. The success of the model in tracking the endwinding temperature in the hottest phase is shown in figure 5.23. The simulated curve includes the additional circuit temperature, T_a, designed to model the distribution of the losses between the endwinding phases. Comments upon the effect that introducing T_a has upon the unbalanced model performance are left until the next subsection where it can be compared with the experimental measurements of the differences between the endwinding phase temperatures. The simulated temperatures at the peaks (127 and 190 minutes) are 6% and 9% higher than the measured data; these values are in reasonable agreement with results for the balanced model for this node.

The pronounced effect that the presence of a negative sequence current has upon the rotor heating is illustrated in figure 5.24. As measured data was not available, the temperatures simulated using the unbalanced model and sequence currents are shown in comparison with those simulated using the average squared line current as the model input. The average squared line current, which is slightly larger than the average line current squared used in the simulations for figures 5.16 to 5.19, was chosen as it represents exactly the motor heating conditions if the frequency dependence of the rotor winding resistance is ignored. The difference between the curves is therefore due entirely to the additional losses associated with the high frequency negative sequence rotor currents and the secondary effect of the rotor winding resistance temperature dependence which further amplifies the difference. If the model

predictions are correct then the danger of rotor failure under conditions of extreme unbalance can plainly be seen; the rotor winding temperature rises by 112°C in just three minutes at the maximum unbalanced condition at 188 minutes and reaches a substantial 236°C, even though the sensitivity of this particular motor to rotor frequency changes is relatively modest. For deep bar motors, the effects shown here would be greatly exaggerated and it is these motors in particular which will suffer the greatest risk of rotor failure during unbalanced operation.

5.5.2 THE BCP 5.5KW MOTOR.

During the tests on this motor, temperatures were measured for each of phases of the stator endwinding and slot winding. The data thus obtained allows the average endwinding temperature and the difference between the average and hottest endwinding temperature to be found.

Using the sequence currents to calculate the thermal generators but excluding the additional circuit calculation, should simulate the average endwinding phase hot spot temperature. However the simulation, when compared with the average of the temperatures measured in each of the endwinding phases (figure 5.25), does not give the expected correlation; the simulated temperatures are 5%-10% higher.

In a separate test performed to investigate this apparent failure, measurements of the endwinding, slot winding and endcap air temperatures were taken at thermal equilibrium under an arbitrary condition of unbalance. These measurements were later compared with the results of a steady state simulation using the unreduced, 15 node model.

It was found that the simulated endcap air temperature was considerably higher than that measured, whilst the endwinding and slot winding simulations gave a similar degree of correlation with the measured values as the comparisons shown in the varying load test results (figure 5.25 and 5.28). The discrepancy in the endcap air temperatures was consistent with that which would cause an endwinding temperature rise of the order of the difference between the measured and simulated average endwinding temperatures.

The endcap air temperature becomes important during unbalanced conditionsas it provides one of the major heat transfer paths from the rotor which, under these conditions experiences a large increase in it s losses in proportion to the other nodes. So it would appear that the heat transfer from the endcap air to the cooler surfaces of the frame is under estimated though this only becomes apparent when the heat dissipated into the endcap air is large.

As thermometers were mounted in all three phases of this motor, it was possible to alter the phase with the largest losses and yet still monitor the hottest temperature. A comparison between the hottest measured endwinding temperature and the predicted average endwinding hot spot temperature (figure 5.26) shows that the latter in fact matches the hottest endwinding temperature quite closely. However, over much of the curve, and particularly at the peaks, the temperatures simulated using just the losses calculated from the sequence currents but not including the additional circuit calculation fall below those measured. As the measured temperatures are likely to be lower than the true hot spot temperatures, the inclusion of the additional circuit temperatures

can still be justified. Figure 5.27 shows the comparison between the hottest measured endwinding temperature and the endwinding simulations with the additional circuit calculations of temperature rise of the hottest phase over the average endwinding phase hot spot included; the agreement is good.

Analysis of the temperatures measured in each phase of the endwinding, at the peak unbalanced condition at 123 minutes showed that the actual difference between the hottest and average phase temperature measurements was 27°C while the additional circuit calculation predicted a difference of only 6°C. In one sense this is fortuitous as the combined errors in the additional circuit calculation and the average endwinding temperature simulation give a net hot spot simulation which agrees well with the measured data (figure 5.27).

The error in the additional circuit calculation occurs mainly as a result of the assumptions made in its derivation, particularly the assumption that the temperature at the boundary of each endwinding phase with the slot winding and endcap air is uniform. Observation of the measured slot winding temperatures at 123 minutes showed that there was in fact an 8°C difference between the hottest and average measured mean slot winding temperatures; the error is likely to be even greater at the boundaries and greater still at the boundary of the endwinding phases with the endcap air. However, accounting for the differing boundary temperatures would require the separate modelling of all three phases which would add another two nodes to the thermal model effectively increasing the solution time and memory requirements by 25%. The benefits which might be gained using this approach cannot be justified particularly

as the assumption that the slot winding mean temperatures are the same in each phase would still be required.

Figure 2.28 shows the good agreement between the average of the stator slot winding thermometer measurements and the temperatures simulated for that node by the unbalanced thermal model.

The results show clearly the need to include the effects of the negative sequence current and the spatial distribution of the stator copper losses if the heating conditions that occur during unbalanced operation are to be modelled effectively. The model has proved successful in tracking the hottest endwinding in both the motors tested with some reservations about the assumption of uniform temperatures at the endwinding component boundaries. Realistically, such assumptions are necessary if the simple structure of the model is to be retained. The similarity of the unbalanced model to the balanced model which has already been tested in a real time situation, suggests that implementing an 'on-line' unbalanced model should not be difficult; the system developed to measure the symmetrical components of the motor input currents was specifically designed to be easily integrated with the microprocessor software. The resulting system would form the basis of the proposed protection device which would provide the closest possible protection during both balanced and unbalanced operation. The other protection functions which might be implemented in the proposed protection device have been discussed previously in Chapter 3.

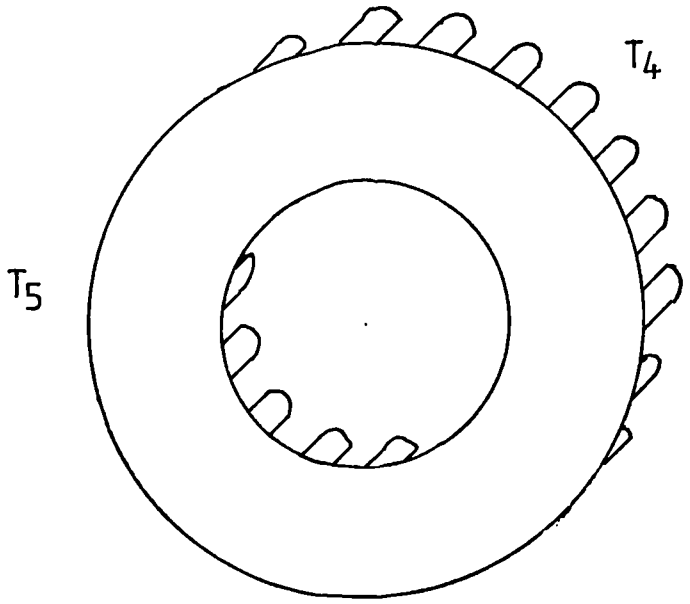

T_4 = slot winding boundary temperature
T_5 = endcap air boundary temperature

Figure 5·1 Complete Endwinding Component Representation

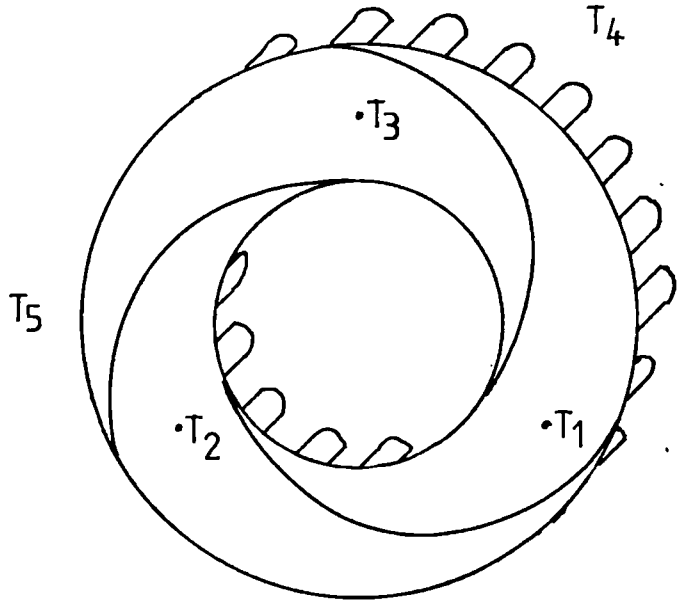

Figure 5·2 Unbalanced Model Endwinding Representation

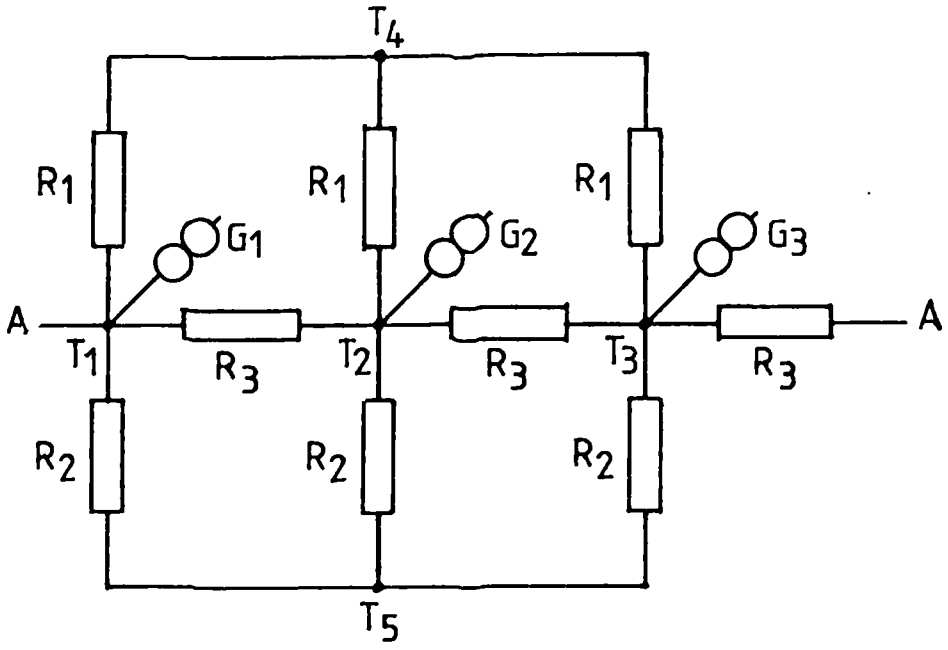

Figure 5·3 Endwinding Thermal Equivalent Circuit

$$G = \frac{3}{Y_t}\left[(Y_1+Y_2+Y_3).G_1+Y_3.G_2+Y_3.G_3\right]$$

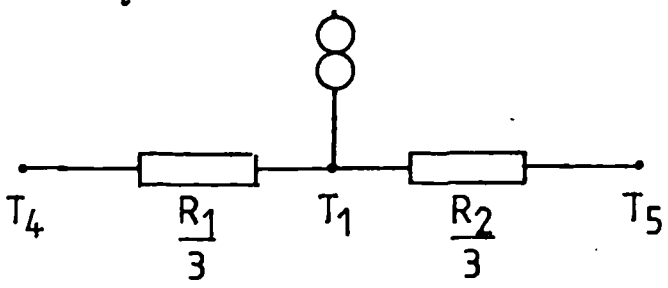

Figure 5·4 Reduced 'Hot Spot' Equivalent Circuit

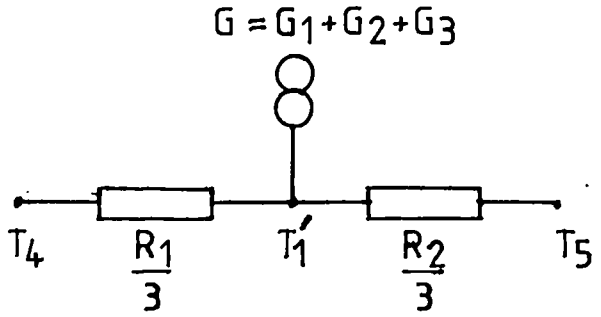

Figure 5·5 (i) Balanced Endwinding Model

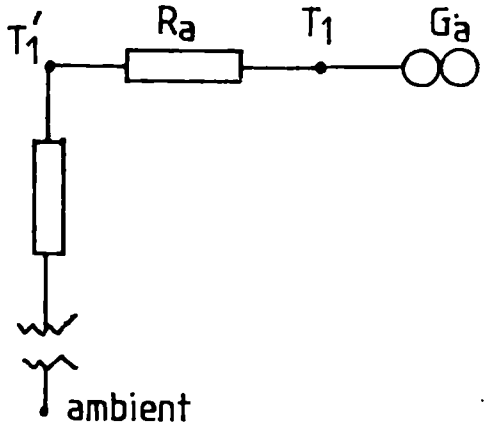

Figure 5·5 (ii) Additional Thermal Equivalent Circuit

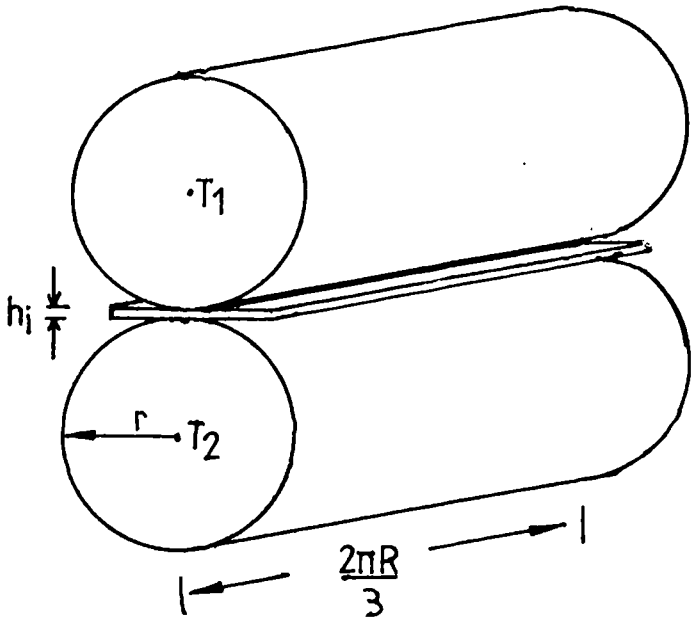

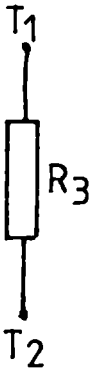

$$R_3 = \frac{3w}{8\pi^2 F k_v R} + \frac{3h_i}{4\pi k_i r_1 R}$$

R = endwinding toroid outer radius
r_1 = endwinding toroid inner radius
h_i = phase separator thickness
w = surface to hot spot : surface to mean temperature ratio
k_i = insulation conductivity
k_v = varnish conductivity
F = radial conductivity factor

Figure 5·6 Inter-phase Thermal Resistance

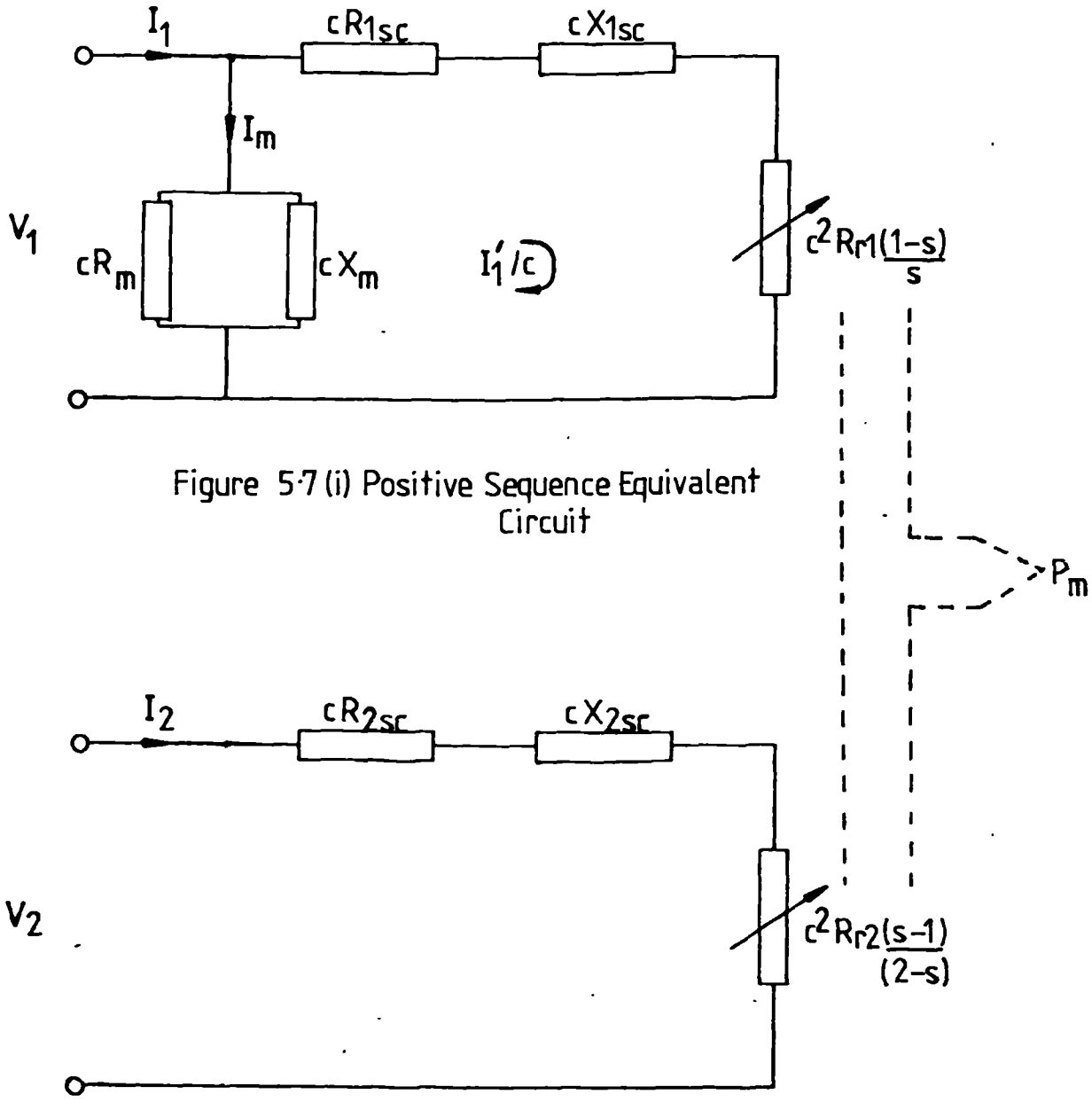

Figure 5·7 (i) Positive Sequence Equivalent Circuit

Figure 5·7 (ii) Negative Sequence Equivalent Circuit

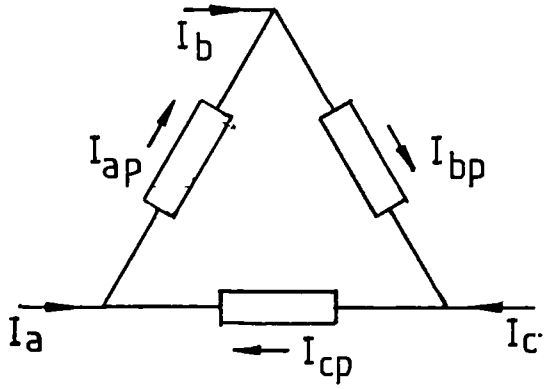

Figure 5·8 Delta Wound Line and Phase Currents

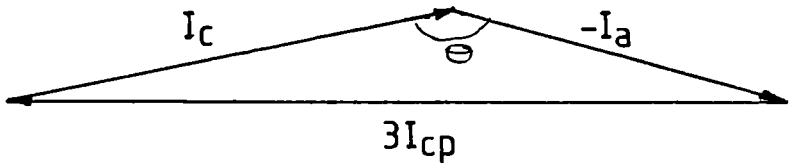

Figure 5·9 Phase and Line Current Phasor Diagram

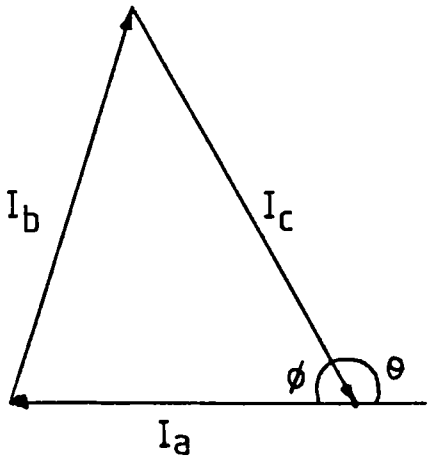

Figure 5·10 Line Current Phasors

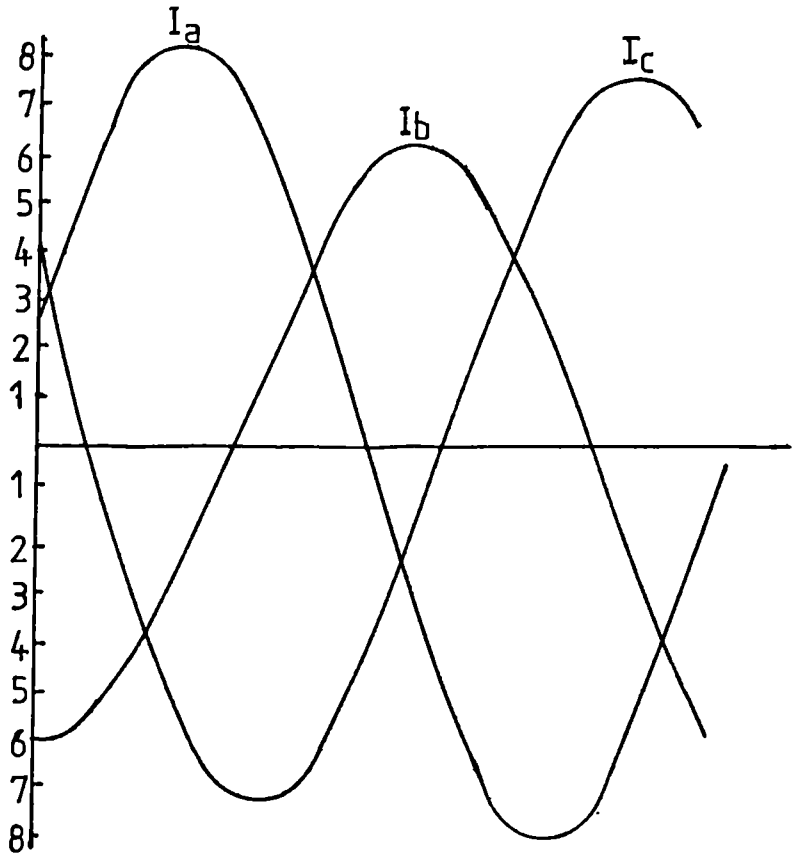

Figure 5·11(i) Unbalanced 3-Phase Line Currents

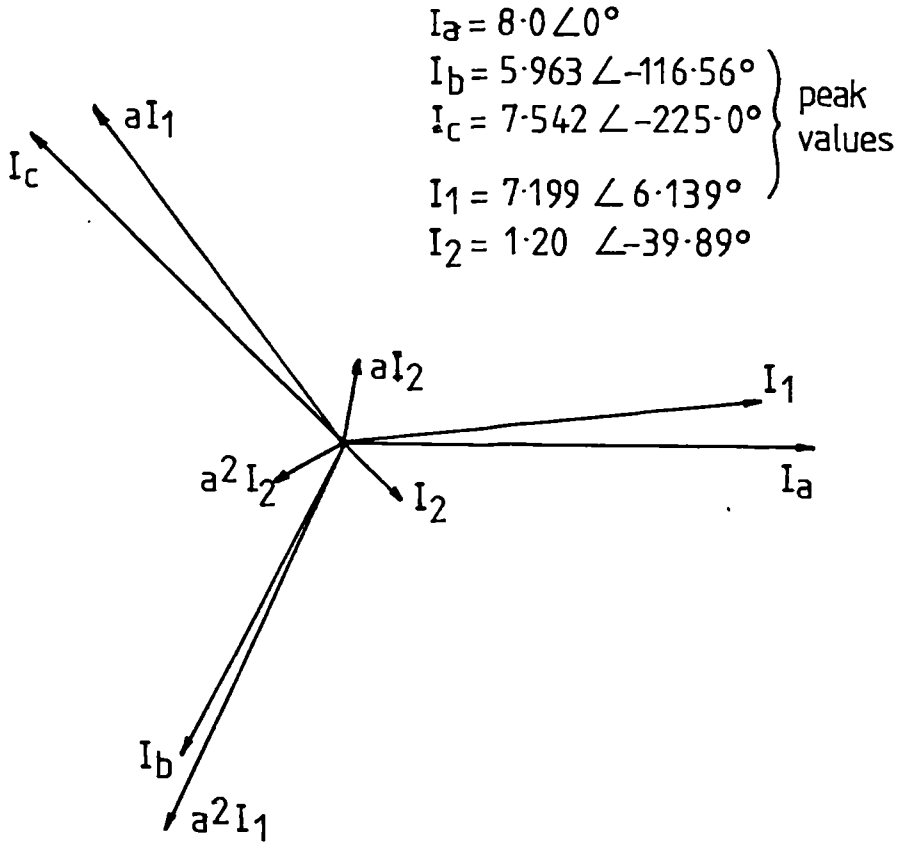

Figure 5·11(ii) Positive and Negative Sequence Current Vectors

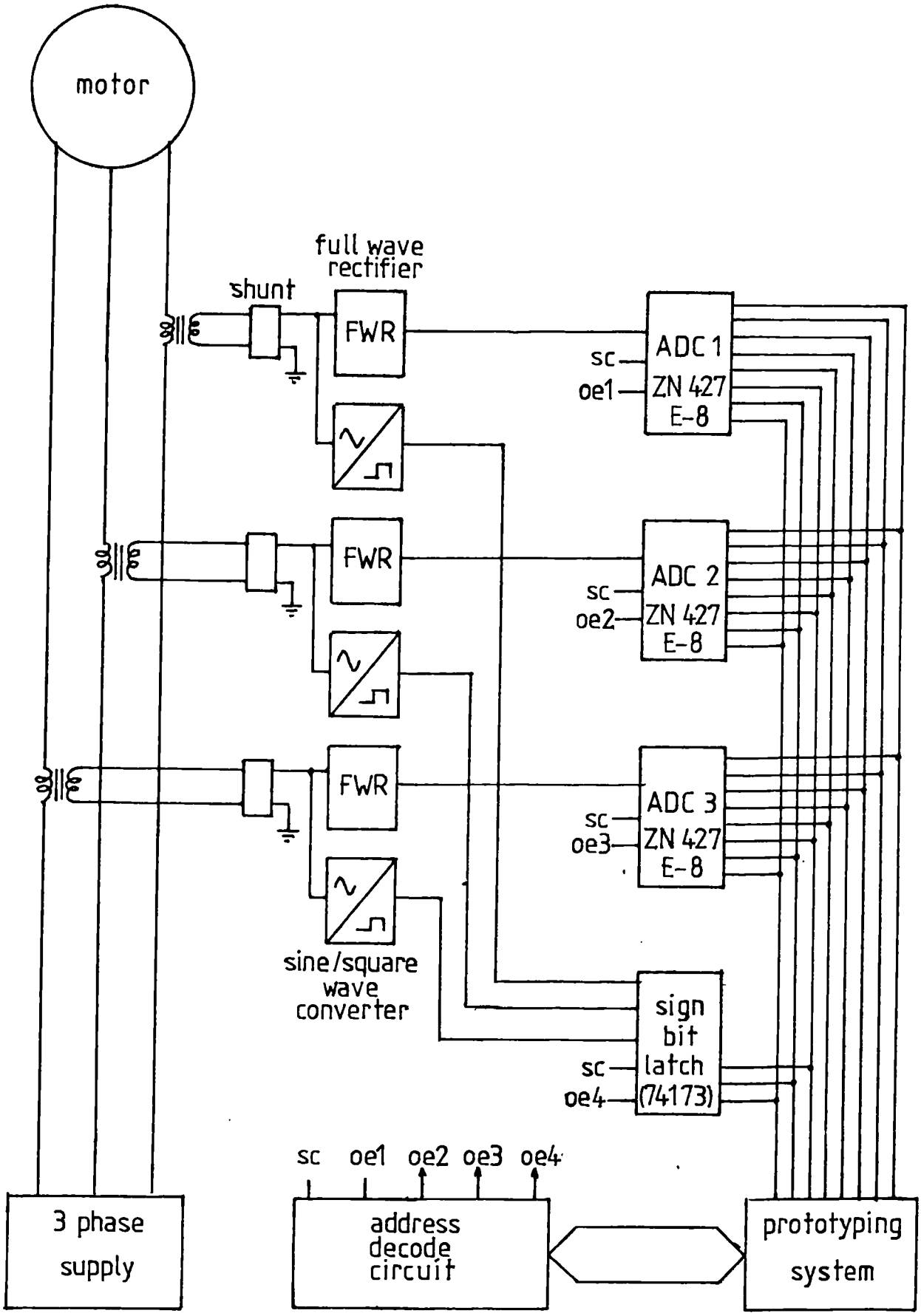

Figure 5·12 Block Diagram of Sequence Current Measuring System

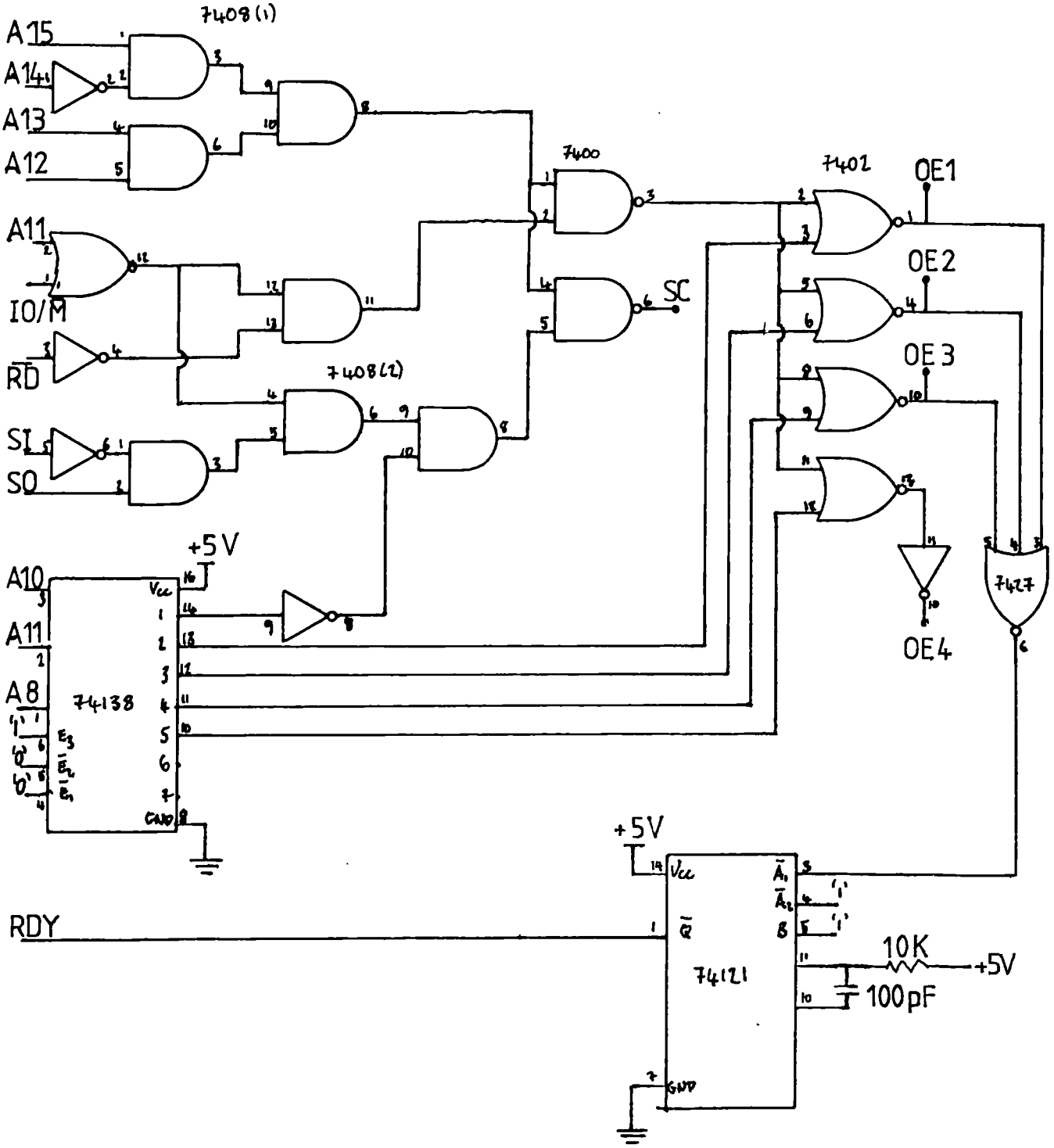

SC start conversion for all 3 ADC's and sign bit latch
OE1 output enable for ADC 1
OE2 output enable for ADC 2
OE3 output enable for ADC 3
OE4 output enable for sign bit latch

Figure 5·13 Address Decode Circuit for Sequence Current Measuring System

I_{a0}	I_{b0}	I_{c0}	S_0	I_{a12}	I_{b12}	I_{c12}	S_{12}	I_{a24}	I_{b24}	I_{c24}	S_{24}	I_{a36}	I_{b36}	I_{c36}	S_{36}
I_{a48}	I_{b48}	I_{c48}	S_{48}	I_{a60}	I_{b60}	I_{c60}	S_{60}	I_{a72}	I_{b72}	I_{c72}	S_{72}	I_{a84}	I_{b84}	I_{c84}	S_{84}
I_{a96}	I_{b96}	I_{c96}	S_{96}	I_{a108}	I_{b108}	I_{c108}	S_{108}	I_{a120}	I_{b120}	I_{c120}	S_{120}	I_{a132}	I_{b132}	I_{c132}	S_{132}
I_{a144}	I_{b144}	I_{c144}	S_{144}	I_{a156}	I_{b156}	I_{c156}	S_{156}	I_{a168}	I_{b168}	I_{c168}	S_{168}	I_{a180}	I_{b180}	I_{c180}	S_{180}
I_{a192}	I_{b192}	I_{c192}	S_{192}	I_{a204}	I_{b204}	I_{c204}	S_{204}	I_{a216}	I_{b216}	I_{c216}	S_{216}	I_{a228}	I_{b228}	I_{c228}	S_{228}
I_{a240}	I_{b240}	I_{c240}	S_{240}	I_{a252}	I_{b252}	I_{c252}	S_{252}	I_{a264}	I_{b264}	I_{c264}	S_{264}	I_{a276}	I_{b276}	I_{c276}	S_{276}
I_{a288}	I_{b288}	I_{c288}	S_{288}	I_{a300}	I_{b300}	I_{c300}	S_{312}	I_{a312}	I_{b312}	I_{c312}	S_{312}	I_{a324}	I_{b324}	I_{c324}	S_{324}
I_{a336}	I_{b336}	I_{c336}	S_{336}	I_{a348}	I_{b348}	I_{c348}	S_{348}								

Figure 5·14 Sampled Data Format

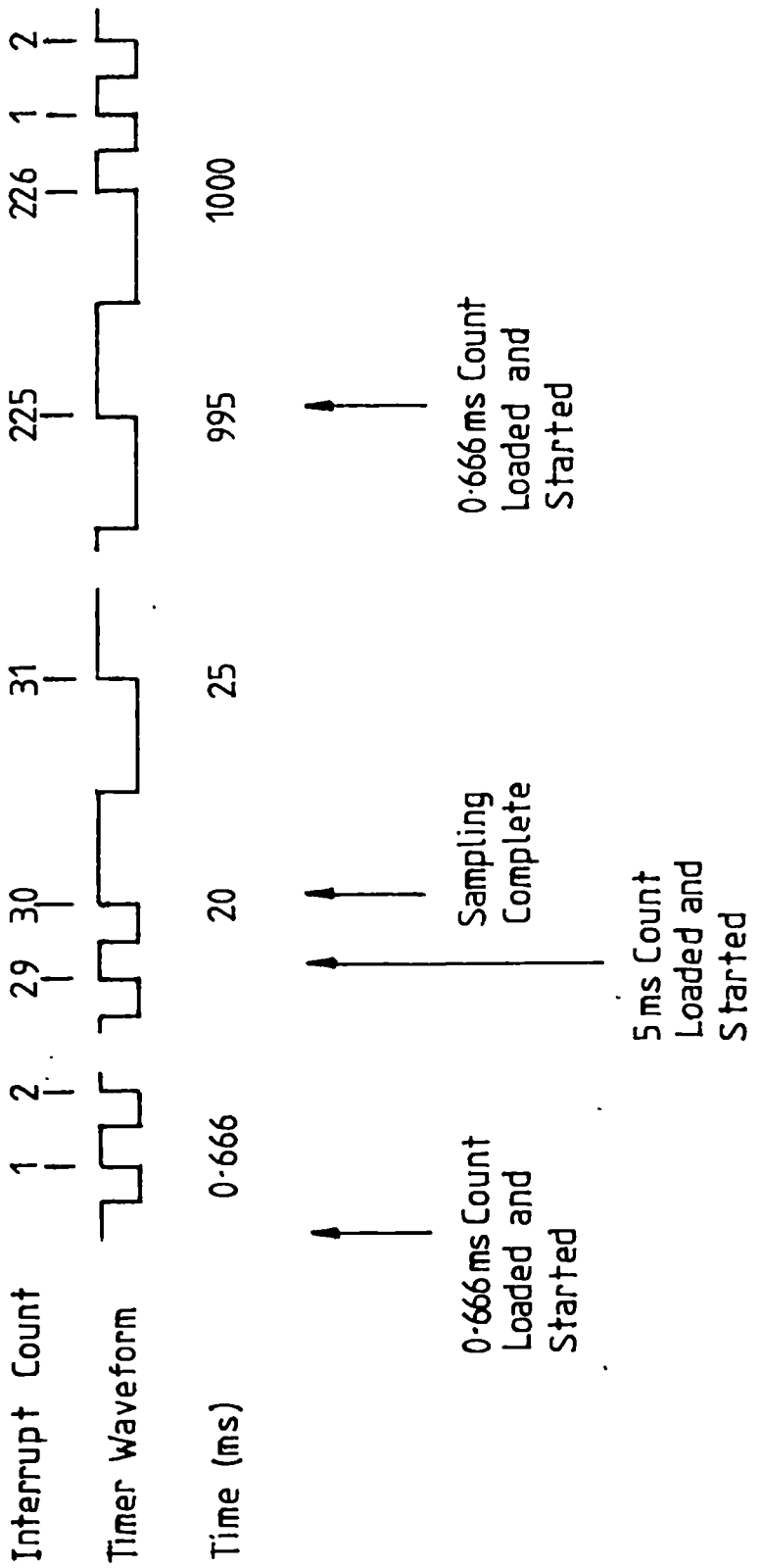

Figure 5·15 Sequence Current Measuring System Timing Schematic

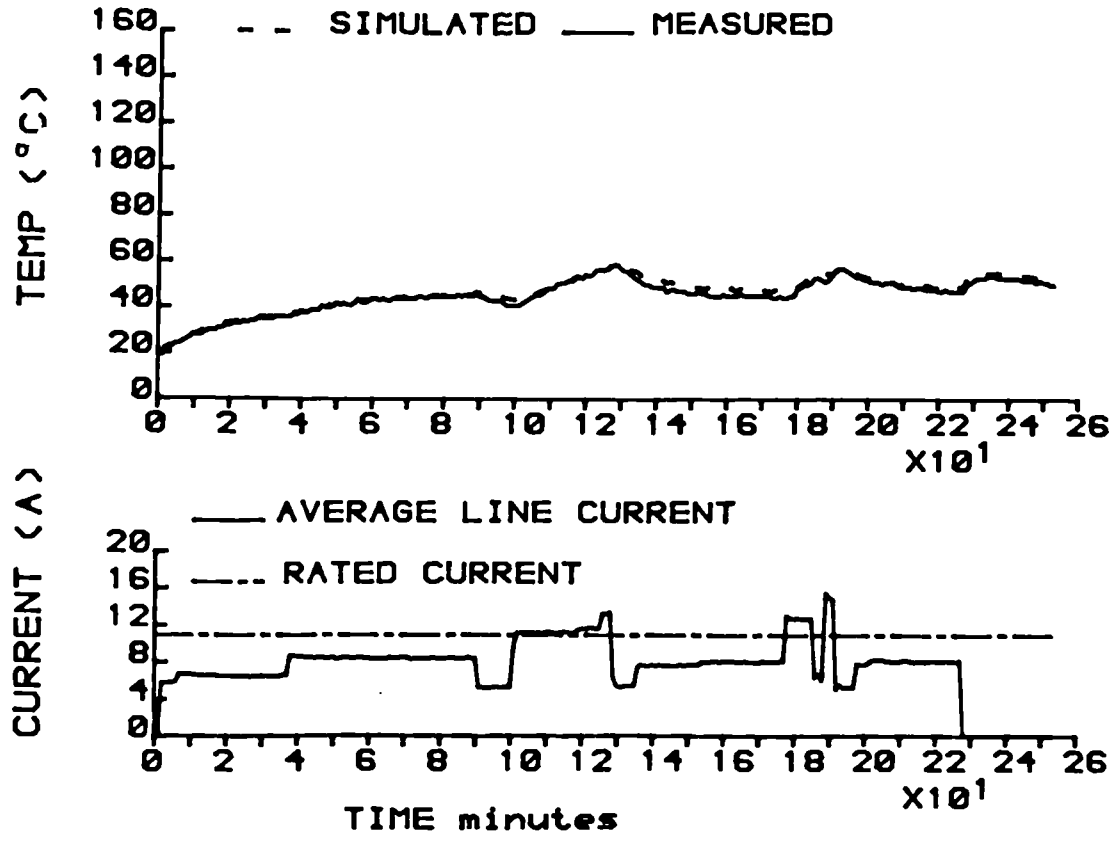

Figure 5·16 GEC 5·5 kW Frame using Average Current as Model Input

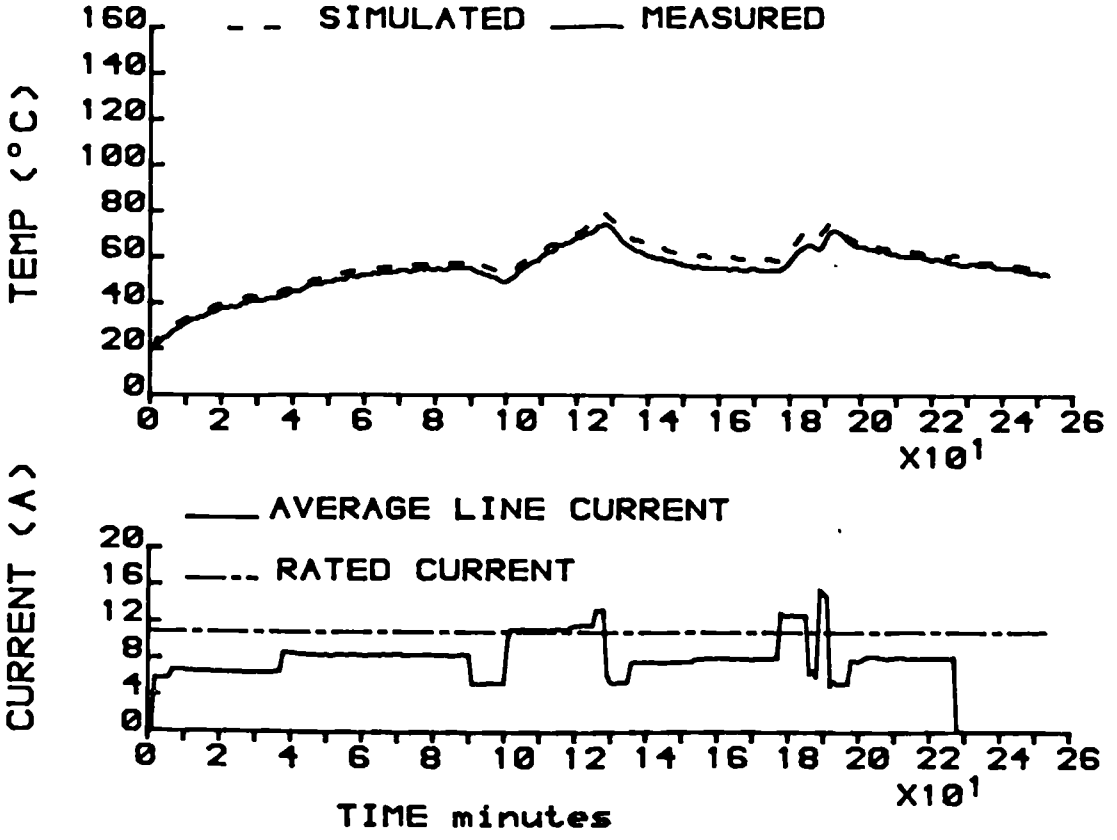

Figure 5·17 GEC 5·5 kW Stator Teeth using Average Current as Model Input

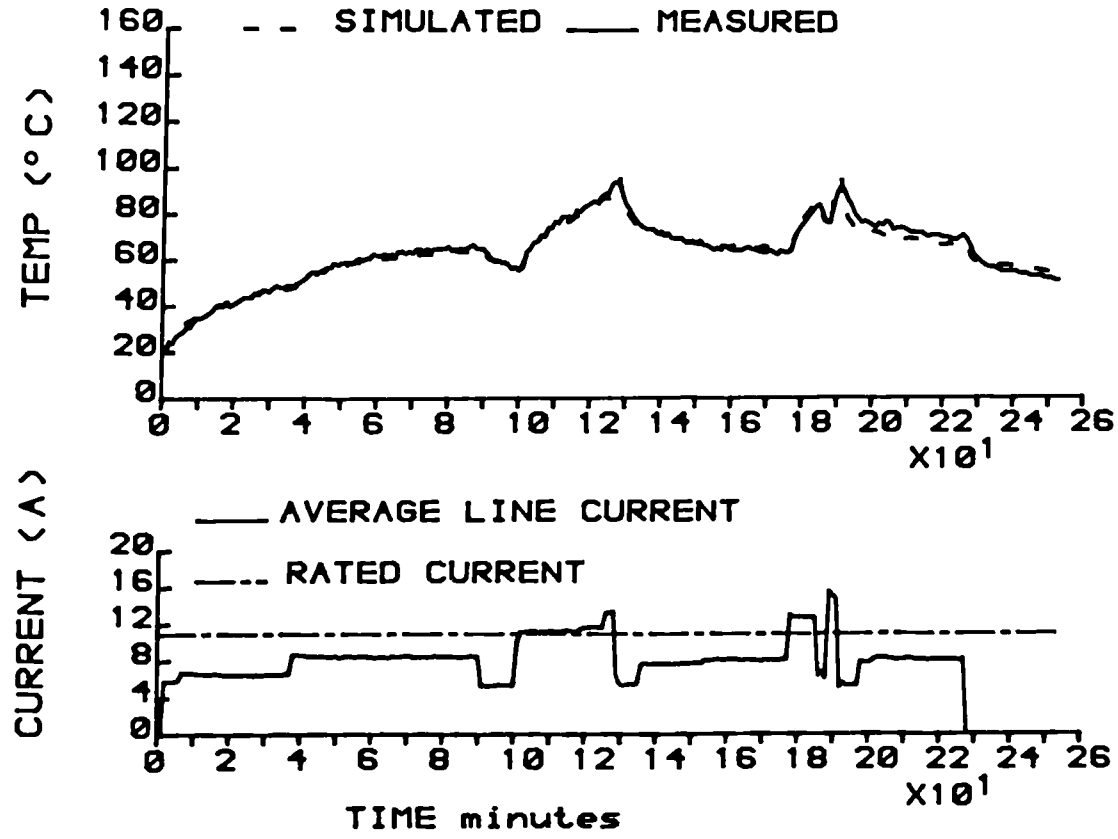

Figure 5·18 GEC 5·5 kW Slot Winding using Average Current as Model Input

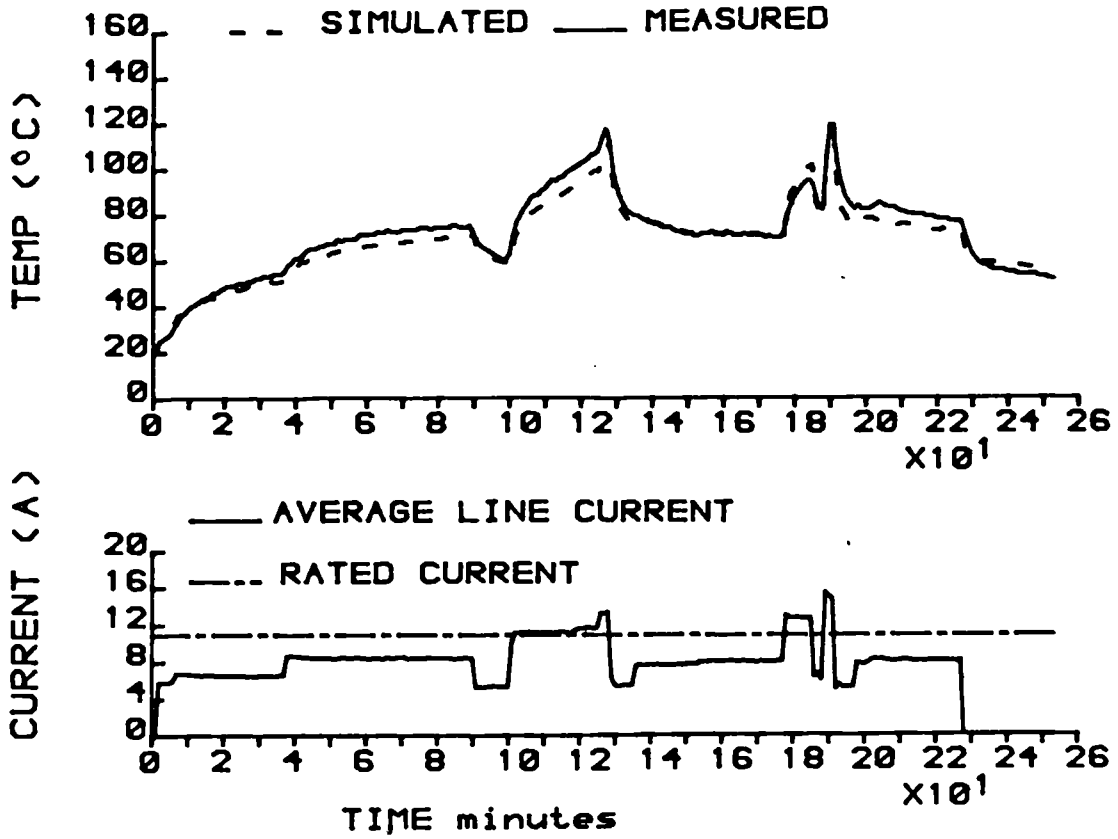

Figure 5·19 GEC 5·5 kW Endwinding using Average Current as Model Input

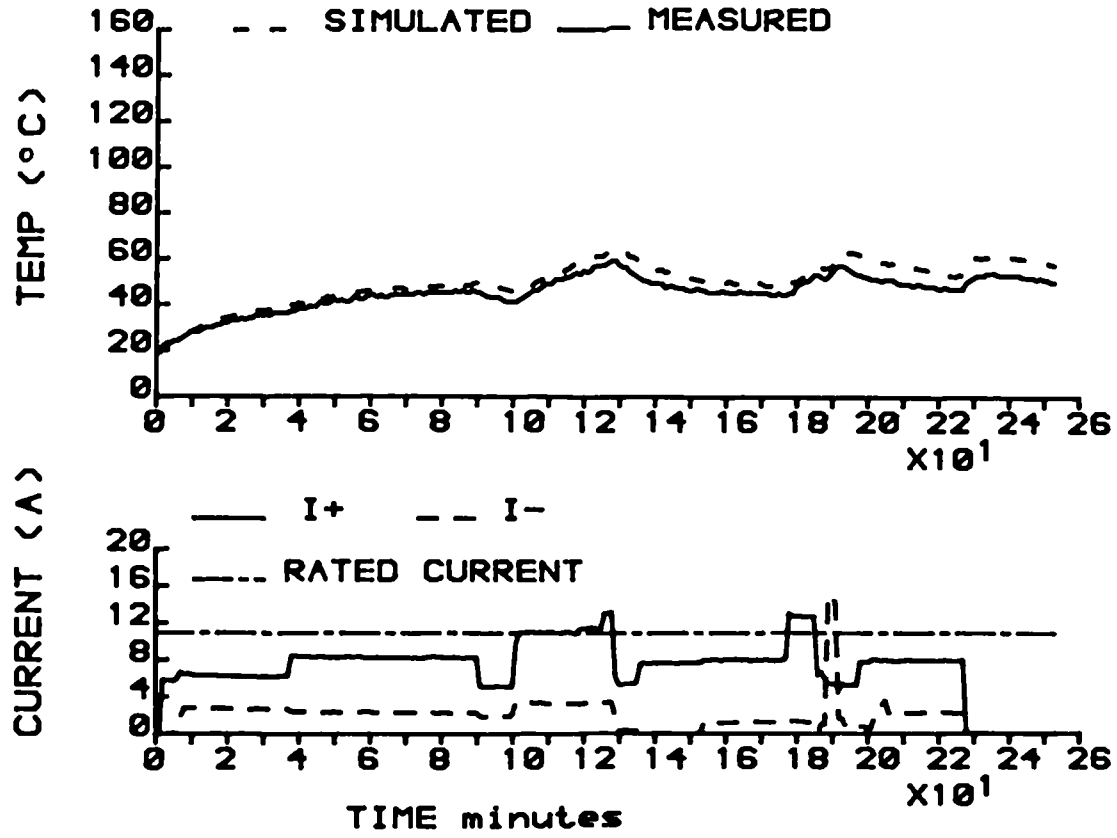

Figure 5·20 GEC 5·5kW Frame using Sequence Currents as Model Inputs

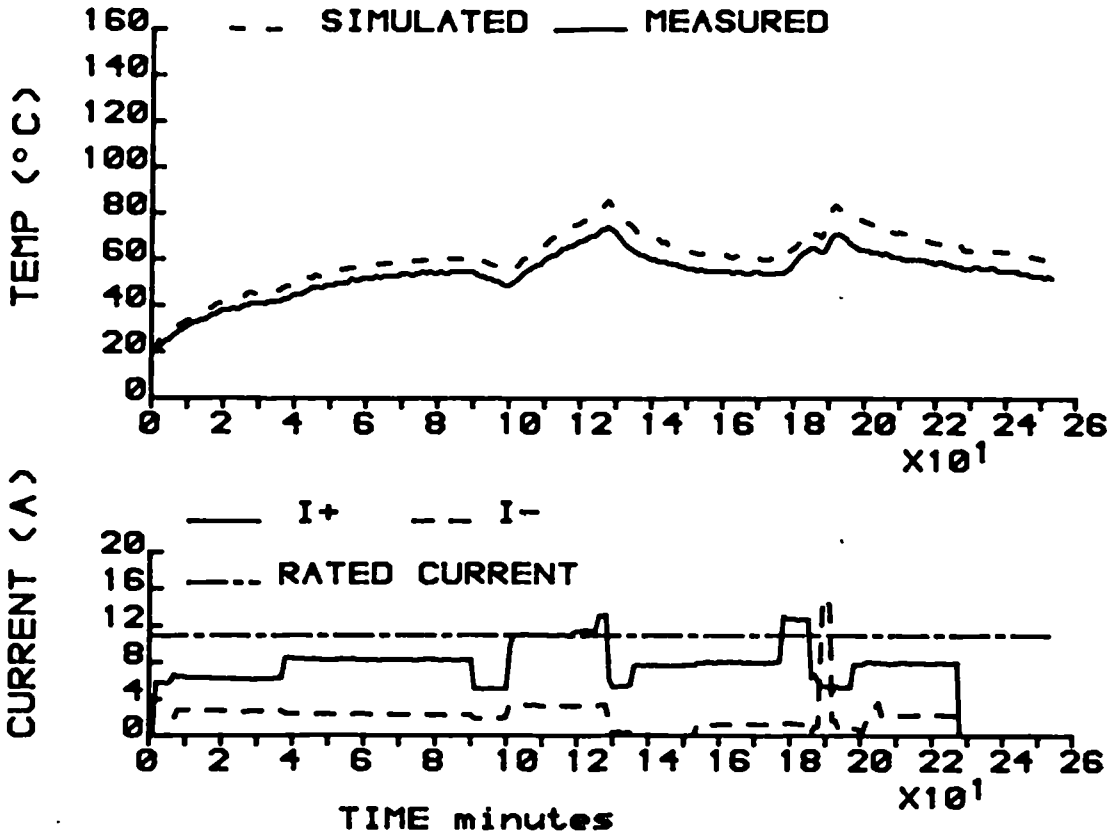

Figure 5·21 GEC 55kW Stator Teeth using Sequence Currents as Model Inputs

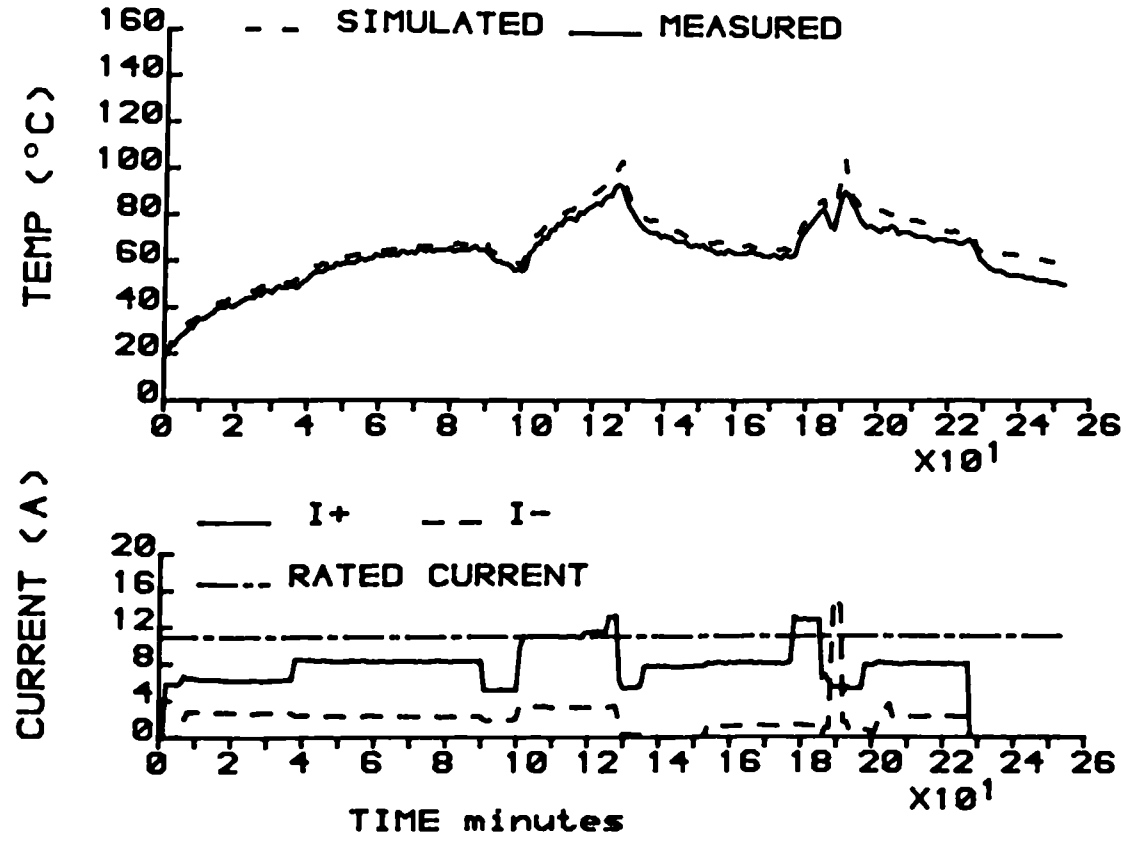

Figure 5·22 GEC 5·5kW Slot Winding using Sequence Currents as Model Inputs

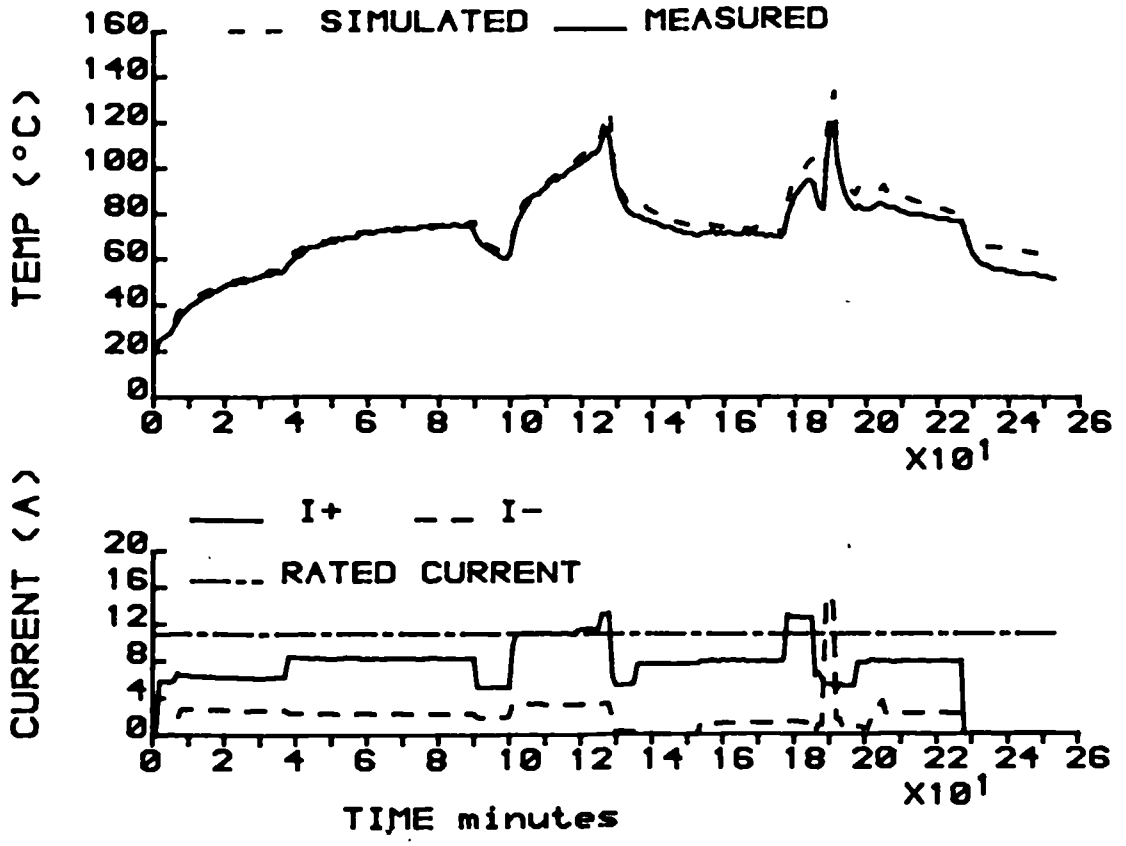

Figure 5·23 GEC 5·5kW Endwinding using Sequence Currents as Model Inputs

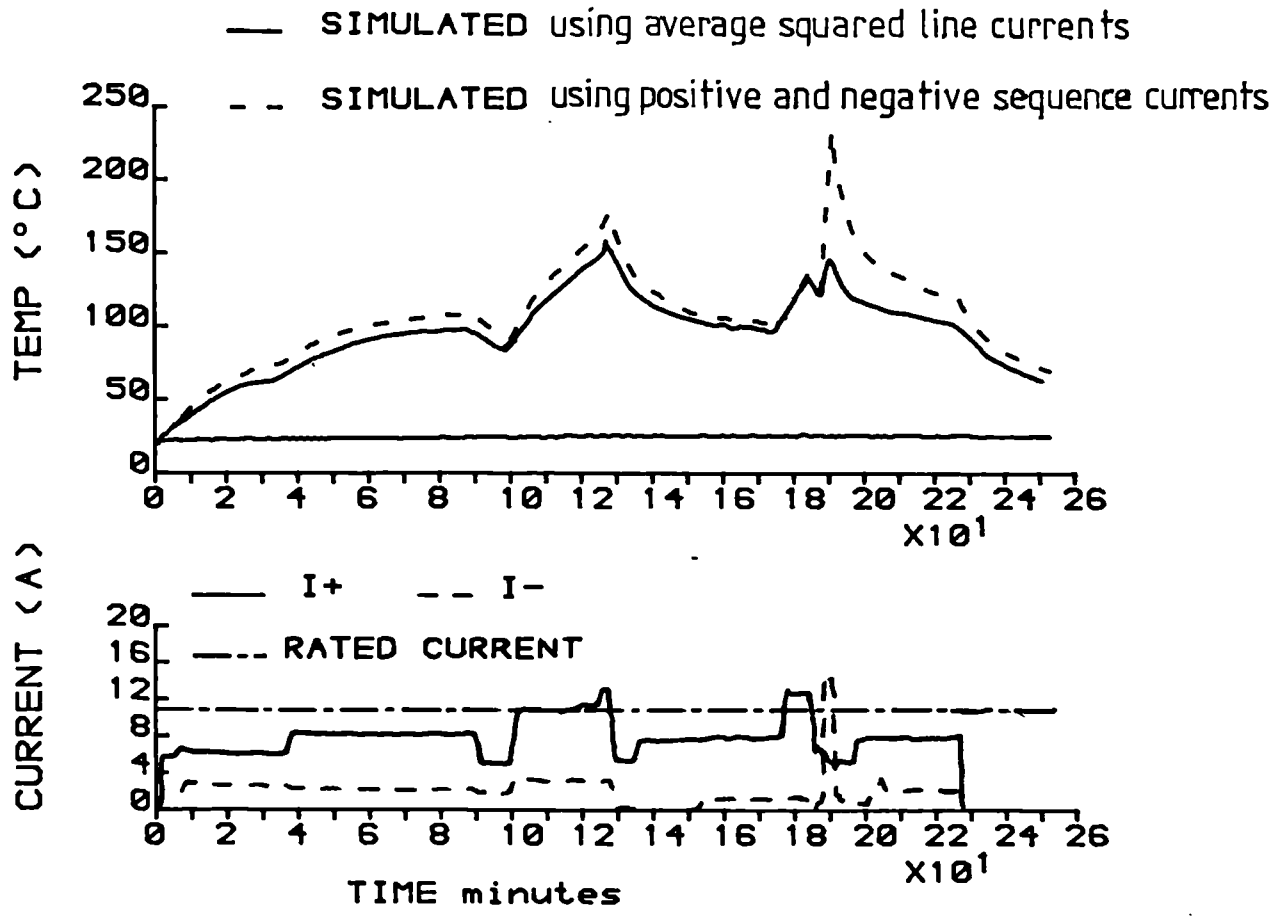

Figure 5·24 Rotor Winding Simulations for GEC 5·5kW

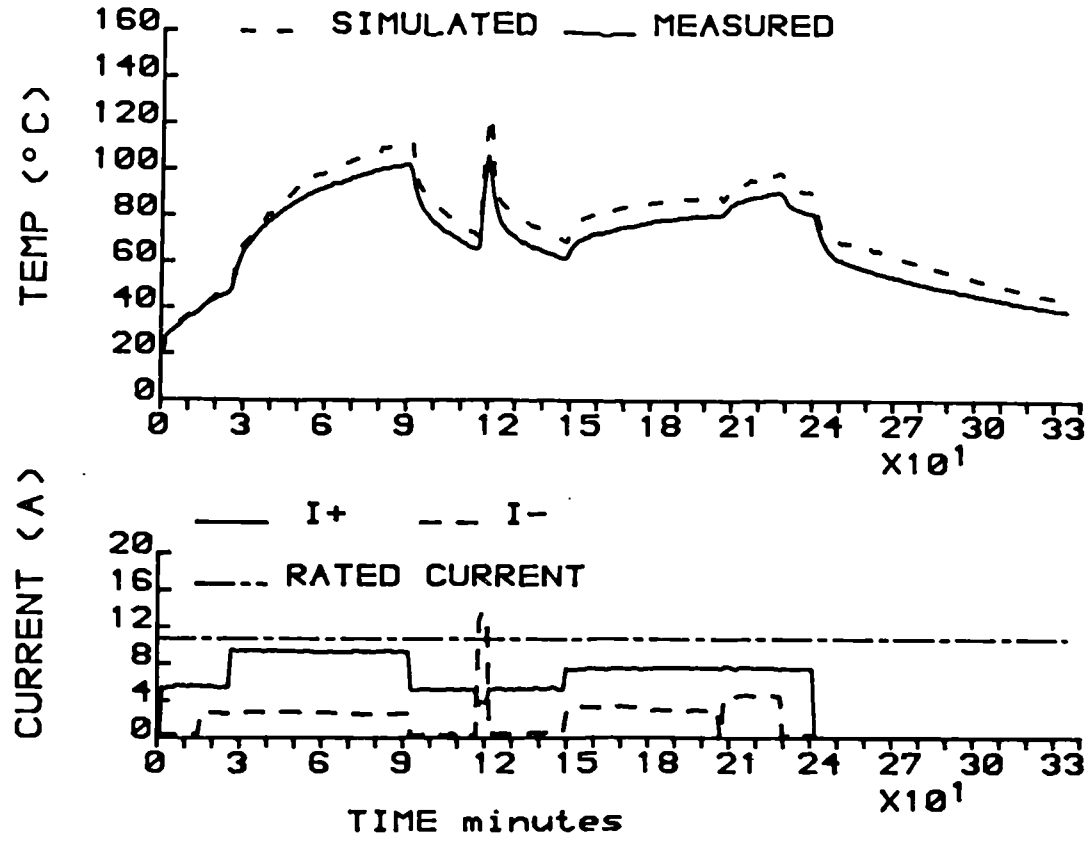

Figure 5·25 BCP 5·5kW Measured Average Endwinding Temperature against Simulated Average Phase Hotspot

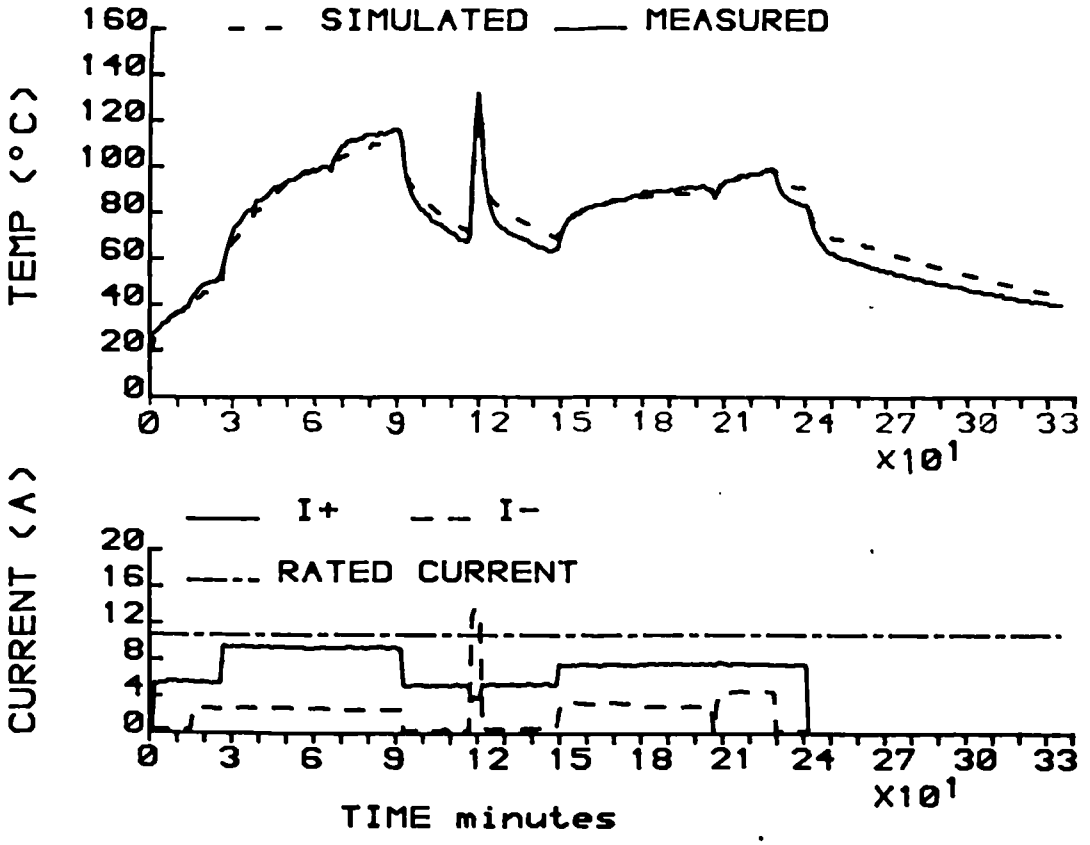

Figure 5·26 BCP 5·5kW Hottest Measured Endwinding Temperature against Simulated Average Phase Hotspot

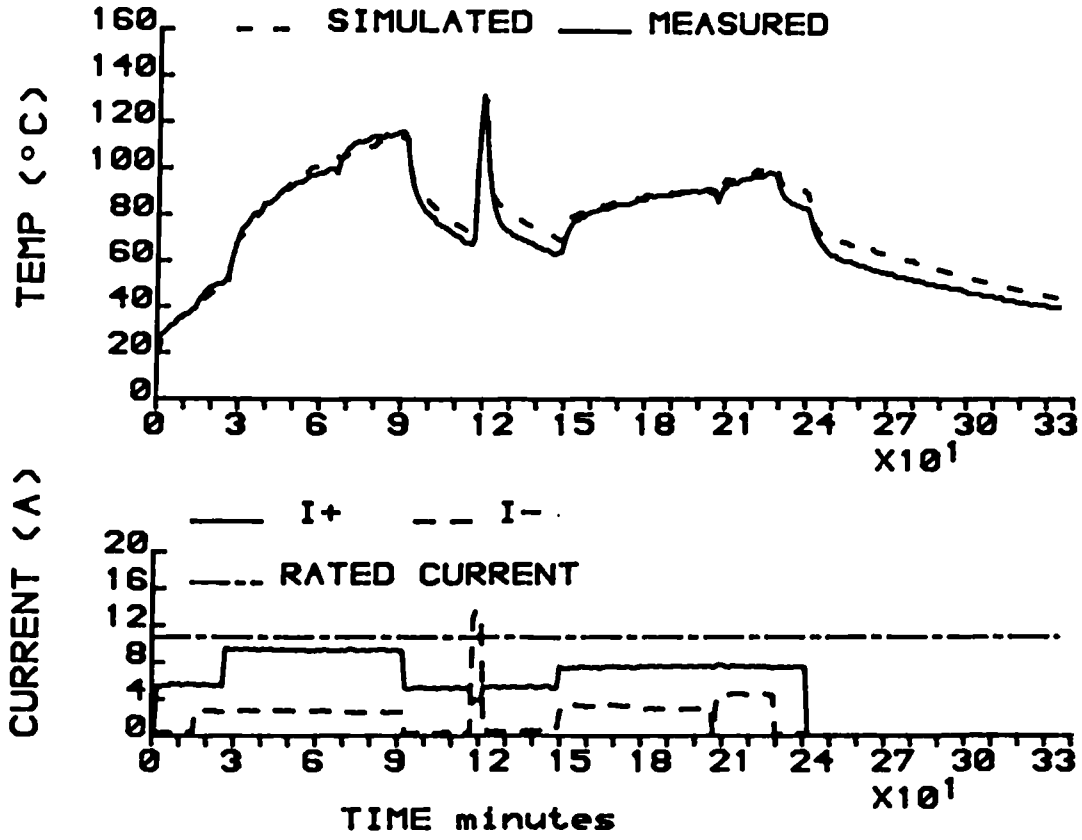

Figure 5·27 BCP 5·5kW Hottest Measured Endwinding Temperature against Simulated Hottest Phase Hotspot

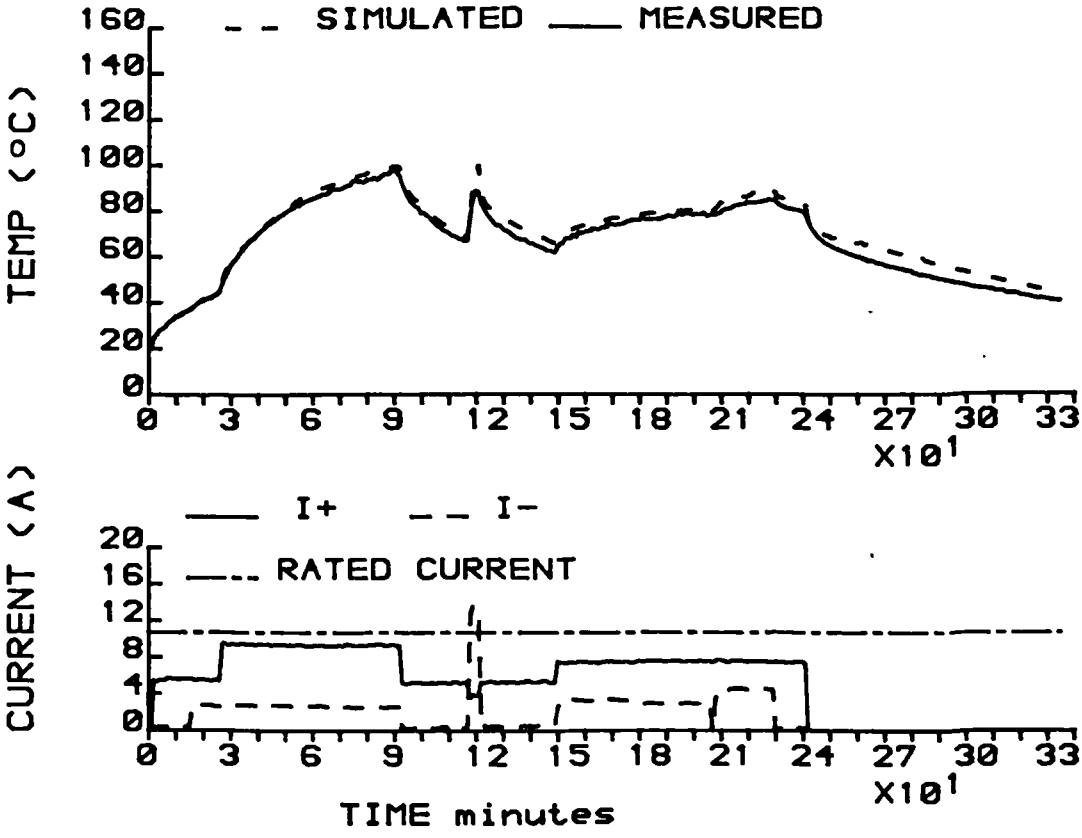

Figure 5·28 BCP 5·5kW Average Measured Slot Winding Temperature against Simulated Average

CHAPTER 6. DUTY CYCLE TEMPERATURE CALCULATIONS.

6.1 INTRODUCTION.

As a sideline to the work on the motor protection device and in response to a proposal put forward by GEC Small Machines plc., the thermal model was incorporated into a thermal prediction system, developed on the mainframe computer, aimed at providing motor temperature information relating to a prespecified duty cycle. In one sense this is also a motor protection application in that a motor which has been incorrectly specified and is operating on a more arduous duty than it is capable of, ignoring environmental hazards and assuming that the duty is rigidly enforced, may well have a reduced lifetime. On the other hand, a motor which is not being used to its full capability constitutes a possibly unnecessary cost on the part of the purchaser.

Normally, it is the responsibility of the applications department of a motor manufacturer, in conjunction with the purchaser, to choose the motor most suitable for a given application. The choice is aided by the designation of a duty cycle rating [29] to each motor, by the manufacturer, which indicates the kind of duties for which the motor is suitable. The purchaser declares the power rating and the duty cycle for the function for which the motor is required: the manufacturer can then provide a suitable motor; this may involve simply choosing a motor in current production or even making a novel modification to an existing motor.

The criterion which establishes the correct motor for the specified duty cycle is that it must be capable of operating the duty cycle, delivering the required power output, or starting and braking against the inertia of the load, without exceeding its insulation class temperature rating and hence reducing its lifetime. It is relatively easy to show that a motor will operate, within these limits, at a given output power, running continuously; the problem for the applications department comes when the machine is being subjected to a periodic duty of starting, running, braking and periods of cooling at standstill. The transient nature of the temperature changes in the windings under these conditions, make the determination of the correct machine difficult.

One way to specify a motor is that it should remain within its power rating. However, for duties which contain long periods of partial loading, it might be quite acceptable to use a smaller frame size and subject the motor to overloads when required. The difficulty comes in quantifying the expected lifetime of the motor.

The use of a thermal model, in conjunction with the theory on insulation aging by Dakin [30], and others [45-47], can provide a means of determining the aging and maximum temperature rises for a particular duty cycle. Such a system is investigated in this Chapter.

The bulk component thermal model of an induction motor has been shown to give good correlations with temperatures measured during transient conditions (Chapter 4). It is adapted in this Chapter to estimate the motor losses from power output information rather than the current input; the losses during starting and braking are also treated.

The resulting model is incorporated into a system implemented on the mainframe computer, which allows interactive specification of a duty cycle and computes the maximum mean stator winding temperature rise, the maximum stator winding hot spot temperature, the maximum rotor winding temperature and the aging of the motor relative to continuous operation at rated load. In the final section, two fictional case studies are presented which are used to demonstrate some of the properties of the thermal calculation system. The first case study in particular serves to underline the importance of compensating for the frequency dependence of the rotor equivalent circuit parameters during the analysis of duties which involve the starting and braking of high inertia loads.

6.2 SPECIFICATION OF DUTY CYCLE.

A purchaser of an electric motor will specify the required duty cycle in one of two ways:

1) In the form of one of the British Standard duty cycles S1-S8 [29].

2) In the form of a time sequence graph, showing the required duties, their duration and the order in which they will be performed.

The British Standard duty cycles, S1-S8, are listed in table 6.1. The cycles S1, S2, S3 and S6, are reasonably easy to translate in terms of the existing thermal model as they contain only periods of running and stationary cooling already covered in Chapters 2 and 4. The only difference is that the losses to be introduced into the model must be found in terms of the required motor power output as opposed to the current

input. The losses during starting and braking also have to be considered before the thermal model can be applied to the duty cycles described by S4, S5 and S7. These duties are of importance when the motor must drive a high inertia load; under these conditions the losses may be large, particularly the rotor losses during electric braking, and could lead to substantial winding temperature rises [11]. A thermal analysis of a motor operating on the final duty cycle, S8, which contains operating speed changes, would require a set of thermal models each formulated for the differing ventilation conditions. Whilst this is possible, it is not particularly practical to implement in a desk top system such as that envisaged to eventually support the duty cycle thermal calculation system and hence is not dealt with here.

In addition to these British Standard duty cycles, provision must be made for the specification of the unique duty cycles presented as time sequence graphs. Again speed changes must be excluded.

6.3 MOTOR LOSSES DURING CONTINUOUS RUNNING.

The motor losses, formulated in terms of the power output and supply voltage, can be calculated from the electrical equivalent circuit presented previously in Chapter 2 (figure 2.20).

Considering the real and reactive power, per phase, to the right of the magnetizing branch of the equivalent circuit gives,

$$V_1^2.(I_2/c)^2 = ((I_2/c)^2.cR_{sc}+(W/3))^2 + ((I_2/c)^2.cX_{sc})^2 \qquad (6.1)$$

Expanded, this gives a quadratic in $(I_2/c)^2$, the solution of which is a function of the equivalent circuit constants and the power output.

$$(I_2/c)^2 = \frac{V_1^2 - 2cR_{sc}.W/3 - (V_1^4 - 4cR_{sc}.W.V_1^2/3 - 4cX_{sc}^2.W^2/9)^{\frac{1}{2}}}{2.(cX_{sc}^2 + cR_{sc}^2)} \qquad (6.2)$$

The stator current squared I_1^2, corresponding to this value of $(I_2/c)^2$ can be found from equation 6.3 which is derived from the equation originally formulated to give $(I_2/c)^2$ in terms of I_1^2 in Chapter 2.

$$I_1^2 = \frac{V_1^2}{cX_m^2} + (I_2/c)^2\frac{(cX_m+2cX_{sc})}{cX_m} \qquad (6.3)$$

Once I_1^2 and $(I_2/c)^2$ have been found, the stator and rotor copper losses can be determined from equations 6.4 and 6.5 respectively.

$$P_{SC} = 3.I_1^2.R_1 \qquad (6.4)$$

$$P_{RC} = 3.(I_2/c)^2.c^2R_2 \qquad (6.5)$$

Finally, the iron losses, which include an internal friction and windage component, are found by subtracting P_{SC} and P_{RC} from the total equivalent circuit power loss to give,

$$P_I = \frac{3.V_1^2}{cR_m} + 3.(I_2/c)^2.cR_1 - 3.I_1^2R_1 \qquad (6.6)$$

The losses are distributed between the model nodes, in accordance with the criteria established in Chapter 2, to give the generator matrix for input into the thermal model. The temperature dependence of the parameters is included in the duty cycle thermal calculations.

Apart from the calculation of the thermal generators, the thermal model solution remains unchanged. Therefore the model performance can be described by the results of Chapter 4, provided that the losses calculated from the power output can be equated with those calculated from the input current. The comparison can be shown by plotting the predicted losses calculated from the power output and those measured during a load test on the GEC 5.5kW motor, during which measurements of power output were recorded (figure 6.1). The test was originally designed to compare the measured losses with those predicted from line current measurements in Chapter 4.

6.4 MOTOR LOSSES DURING STARTING AND BRAKING.

The motor losses during starting and braking cannot be found from the equivalent circuit parameters alone; they depend also upon the properties of the load namely, its inertia and its torque/speed relationship. Only direct on line starting and AC braking (plugging) are treated as these represent the most arduous starting and braking duties.

Plugging is performed by interchanging the connections to two phases thus creating a magnetic field rotating in the opposite direction to the rotor motion. The initial effect upon the motor can be likened to supplying it from a negative sequence voltage supply; i.e. large

currents are induced in the rotor conductors at approximately twice the supply frequency. Under these conditions, the effect of the frequency dependence of the rotor winding parameters cannot be ignored. The braking torque will bring the motor to a standstill when all the kinetic energy of the moving parts of both the rotor and the stator have been 'absorbed' as heat dissipated in the rotor or work done by the load. The latter is dependent upon the mean load torque as it slows from rated speed to standstill. This load torque might act in the same direction as the braking torque, for example in a duty where the motor is driving a fan, or against the braking torque such as for a lift on a downward journey. The large currents drawn from the supply cause substantial stator and rotor copper losses, the latter are further increased due to the frequency dependence of the rotor winding resistance.

During direct on line starting the initial currents drawn by the motor are again large and again the frequency dependence of the rotor winding resistance has to be considered, though in this case the rotor frequency varies between the supply frequency, at standstill, and near 0Hz when the acceleration is complete.

During both starting and braking the iron losses will normally be small in comparison with the copper losses and can be neglected without serious error. For instance, it is estimated that the energy dissipated as heat in the stator and rotor iron of the GEC 5.5 kW motor amounts to less than 5% of the energy dissipated as heat in the windings when starting a small, pure inertia load of 0.4 kg-m^2. For higher inertia loads and for braking the percentage will be even lower.

The calculation of the losses during starting and braking involves finding the motor's mean starting torque, to determine the time needed for starting and braking, and the mean rotor and stator currents squared which give the power losses to be introduced over the starting or braking period. The mean referred rotor current squared, per phase, for starting and braking, $(I_2/c)^2_{av}$, can be found by integrating equation 6.7 between the limits for the motor slip of $s_1=1$, $s_2=0$ and $s_1=2$, $s_1=1$ respectively.

$$(I_2/c)^2_{av} = \int_{s_1}^{s_2} \frac{V_1^2}{cX_{sc}^2+cR_1^2} \left[\frac{s^2}{\frac{(c^2R_2)^2}{cX_{sc}^2+cR_1^2} + \frac{2cR_1.c^2R_2.s}{cX_{sc}^2+cR_1^2} + s^2} \right] ds \qquad (6.7)$$

The analytic solutions of equation 6.7, for starting and braking, are given by equations 6.8 and 6.9 respectively.

$$(I_2/c)^2_{av} = k - \frac{k.b.}{2}\left(\ln\frac{a+b+1}{a}\right) - k(a-(b/2)^2)^{\frac{1}{2}} \left[\tan^{-1}\left(\frac{1+(b/2)}{(a-(b/2)^2)^{\frac{1}{2}}} \right) - \tan^{-1}\left(\frac{(b/2)}{(a-(b/2)^2)^{\frac{1}{2}}} \right) \right] \qquad (6.8)$$

$$(I_2/c)^2_{av} = k - \frac{k.b.}{2}\left(\ln\frac{a+2b+4}{a+b+1}\right) - k(a-(b/2)^2)^{\frac{1}{2}} \left[\tan^{-1}\left(\frac{2+(b/2)}{(a-(b/2)^2)^{\frac{1}{2}}} \right) - \tan^{-1}\left(\frac{1+(b/2)}{(a-(b/2)^2)^{\frac{1}{2}}} \right) \right] \qquad (6.9)$$

Where,

$$a = \frac{c^2 R_2}{cX_{sc}^{\ 2} + cR_1^{\ 2}}$$

$$b = \frac{2cR_1 . c^2 R_2}{cX_{sc}^{\ 2} + cR_1^{\ 2}}$$

$$k = \frac{V_1^{\ 2}}{cX_{sc}^{\ 2} + cR_1^{\ 2}}$$

The average starting and braking torques, T_{av}, are given by solving equation 6.10 for motor slips between the limits defined previously for the average referred rotor current squared to give equations 6.11 and 6.12.

$$T_{av} = \frac{1}{\omega_s} \int_{s_1}^{s_2} \frac{V_1^{\ 2}}{cX_{sc}^{\ 2} + cR_1^{\ 2}} \left[\frac{s}{\frac{(c^2 R_2)^2}{cX_{sc}^{\ 2} + cR_1^{\ 2}} + \frac{2cR_1 . c^2 R_2 . s}{cX_{sc}^{\ 2} + cR_1^{\ 2}} + s^2} \right] ds \qquad (6.10)$$

Where ω_s = the motor synchronous speed (rads/s)

Using the symbols a, b and k defined previously, the average starting and braking torque are given by,

$$T_{av} = \frac{k . c^2 R_2}{2\omega_s} \left(\ln \frac{(a+b+1)}{a} \right) - \frac{k . c^2 R_2 . b}{2\omega_s (a-(b/2)^2)^{\frac{1}{2}}} \left[\tan^{-1} \left(\frac{1+(b/2)}{(a-(b/2)^2)^{\frac{1}{2}}} \right) - \tan^{-1} \left(\frac{(b/2)}{(a-(b/2)^2)^{\frac{1}{2}}} \right) \right] \qquad (6.11)$$

$$T_{av} = \frac{k.c^2R_2}{2\omega_s}\left(\ln\frac{(a+2b+4)}{a+b+1}\right) - \frac{k.c^2R_2.b}{2\omega_s(a-(b/2)^2)^{\frac{1}{2}}}\left[\tan^{-1}\left(\frac{2+(b/2)}{(a-(b/2)^2)^{\frac{1}{2}}}\right) - \tan^{-1}\left(\frac{1+(b/2)}{(a-(b/2)^2)^{\frac{1}{2}}}\right)\right] \quad (6.12)$$

Both the winding resistances, R_1 and R_2, are temperature dependent and each is corrected at each stage in the duty cycle thermal calculations. The rotor parameters R_2 and X_2 are also frequency dependent. The values of these parameters vary linearly with frequency and hence slip, over a large range of frequencies [41] though rather than attempt an analytic solution of equations 6.7 and 6.10 with this frequency dependence included, a frequency compensation factor, based on the mean slip during starting and braking, was applied to c^2R_2 and c^2X_2 in equations 6.8, 6.9, 6.11 and 6.12. The calculation of the mean slip during starting and braking is confounded by the fact that their values depend not only on the torque/speed properties of the motor but also of the load it is driving. The mean slip during starting and braking was calculated by solving the slip/time equations for various types of load, using a numerical Runge-Kutta method. As these equations, shown for the loads simulated in Appendix E, are straightforward functions of c^2R_2 and other parameters which are independent of frequency, it is not difficult to include the linear frequency dependence into the numerical solution. The results of the simulations are shown for starting in table 6.2 and braking in table 6.3. They show that whilst a linear approximation holds true for braking, the mean slip being approximately 1.5, it does not hold true for starting in which case a better approximation is a mean slip of 0.25. As the loads simulated span a wide range of induction motor applications, it is considered that the above approxi-

mations to the mean slip can be adopted generally; the corresponding rotor parameter frequency correction factors for the GEC 5.5kW motor are shown in table 6.4.

As the currents, I_1 and (I_2/c), are large during both starting and braking, the shunting effect of the magnetizing branch of the equivalent circuit can be neglected without serious error; therefore,

$$I_1^2 = (I_2/c)^2 \qquad (6.13)$$

Thus the stator and rotor copper losses during starting and braking, for the whole motor, can be found from equations 6.4 and 6.5 though this time I_1 and I_2/c are the mean values computed from equation 6.8 or 6.9 and equation 6.13. The iron losses, considered small in comparison with the above copper losses, are neglected.

Ultimately it is the energy, not the power, which gives the correct model input to predict the temperature rise so it does not suffice to simply apply the above losses for an arbitrary period of time such as the thermal model time step. This is illustrated in table 6.5 which shows the predicted temperature rise for the eight, reduced model nodes, for the GEC 5.5kW motor, as a function of the time over which the estimated energy dissipated as heat in the motor, during starting and braking, is introduced to the model. The motor is assumed to be driving a pure inertia load so that the energy dissipated in the rotor during starting will be equal to the kinetic energy of the moving parts of both the motor and load; during AC braking (plugging) the energy dissipated will be three times this value [52]. The stator winding energy loss is assumed

to be related to that in the rotor by the ratio of the stator and rotor winding resistances. As can be seen, there was only a 7% change in the predicted endwinding temperature for a ten fold increase in the time period over which this energy was introduced in the model solution; the longer time periods allow more heat transfer to the cooler components. It is also worth noting here that a threefold increase in the energy applied in the model between the simulation for starting and braking, led to a proportionate increase in the temperature rise for the smaller time periods.

On the above evidence, it can be reasonably assumed that, so long as an accurate estimate of the energy to be input into the model is established, then the time over which that energy is applied to the model is only of secondary importance.

The starting and braking time, t, is a function of the load torque, T_l, the combined motor and load inertia, J, and the average starting or braking torque of the motor, T_{av}.

$$t = \frac{\Delta\omega . J}{T_{av} - T_l} \qquad (6.14)$$

Where,

$\Delta\omega$ = change in angular velocity (rads/s)

The average load torque, T_l, can be either positive or negative depending upon whether it acts to oppose or reinforce the motor starting or braking torque, T_{av}.

The starting and braking times also have an influence upon the choice of the time step to be used in formulating the thermal model matrices as this must be governed, ultimately, by the shortest duty cycle period and this is likely to occur during either starting or braking.

6.5 MOTOR AGING CALCULATIONS.

The final decision whether or not a particular motor is suitable for a given duty cycle must be based upon whether or not the motor will have a satisfactory lifetime; this is assuming that the critical temperatures at which the insulation material becomes ineffective or the rotor winding material becomes too ductile, are not exceeded. Work by Dakin [30], based upon the Arrhenius chemical rate equation, gives insulation lifetime as an exponential function of the absolute insulation temperature in Kelvin.

$$L_T = \text{Exp}((b/T) - a) \tag{6.15}$$

where,

L_T = insulation lifetime (hrs)

T = Absolute insulation temperature (K)

a,b = insulation constants.

A more useful concept for comparing the effect of various loading cycles on the deterioration of insulation is that of relative aging [16,45,46]. This gives the lifetime for a particular load cycle, L_T, as a function of a reference lifetime, L_{Tref}, normally based on continuous operation at the maximum insulation temperature under rated conditions; for electric machines the maximum insulation temperature can be equated to the

stator winding hot spot temperature. In defining these conditions, Whitman [45,46] chose the permitted insulation temperature assuming an average ambient temperature, over a 24 hour cycle, of 30°C.

$$R = \frac{L_{Tref}}{L_T} \tag{6.16}$$

A relative aging which is greater than unity indicates that the insulation is deteriorating more quickly than it would be during continuous operation under rated conditions, over the same period of time. Under transient temperature conditions the insulation aging rates are continuously changing so to determine the effective relative aging for a given duty cycle, equation 6.16 must be integrated over the total duty cycle duration.

$$R = \frac{1}{t_1 - t_0} \int_{t_0}^{t_1} \text{Exp}\left(b.\left(\frac{1}{T_{ref}} - \frac{1}{T(t)}\right)\right) dt \tag{6.17}$$

Where,

t_0, t_1 = duty cycle start and end times.

The solution of equation 6.17 requires the temperature/time profile of the stator winding hot spot temperature T(t); information which is readily available from the solution of the thermal model. In order to incorporate this calculation into the thermal calculations, a stepwise approximation to equation 6.17, must be established which can be applied over the same time steps that are used in the model solution. The simplest approximation can be made by assuming that the change in R over the time step, Δt, is small; however, this is not generally the case as R is sensitive to

even small temperature changes. A second, better approximation is made by assuming a linear temperature change over the time step Δt, giving the relative aging, R, as a function of the temperatures at the k^{th} and $(k-1)^{th}$ time steps.

$$R = \frac{1}{t_1 - t_0} \sum_{k=1}^{n} \text{Exp}\left(b.\left(\frac{1}{T_{ref}} - \frac{2}{T(k\Delta t)+T((k-1)\Delta t)}\right)\right) \Delta t \qquad (6.18)$$

Whitman [46] used this approximation to estimate the relative aging during an exponential temperature cycle of 4 hours duration and found that it gave only a 10% error over the exact solution. In his analysis he approximated the whole 4 hour exponential by a single linear approximation so it is envisaged that the same method applied over a much shorter time period, equal to one thermal model time step, would give rather more accurate results.

6.6 INTERACTIVE DUTY CYCLE THERMAL CALCULATIONS.

The interactive system used to perform the duty cycle thermal equations is structured in three parts.

1) Duty cycle specification.

2) Thermal Calculations.

3) Graphical presentation of results.

Transfer between the three parts was controlled by a command programme illustrated in the flowchart of figure 6.2. In part 1 (figure 6.3) the data required to compute the thermal model is compiled - this consists of the nature of the duty, that is, starting, continuous running etc, followed by the data relevant for that duty. During starting and braking the required data is the load inertia and the average load torque; both these quantities must be known prior to entering the programme. For systems in which the inertia of the motor itself is significant, the value entered must be sum of the motor and load inertias. A positive average load torque denotes that the load acts to oppose starting and to aid braking. For the other duties, the required power output and the duty duration are entered: as stationary cooling is signified by zero output power then running on no-load must be represented by an arbitrary output power of 1W.

In this system the duty duration is restricted to integer multiples of one minute, chosen as the time step used in formulating the 'continuous running' matrices for the thermal model solution in order to give a modest execution time for most duty cycles but retain a reasonable degree of resolution. If greater resolution is required, a second set of matrices formulated using a much smaller time step, could be used in a separately defined period following the one minute calculations.

The programme can be applied to both the standard duty cycles and others; a facility to store the duty cycle specification was included so that the same data could be applied to a number of motors to provide a comparison.

Before control is transferred to the thermal calculation programme, figure 6.4, the particular motor to be tested against the duty cycle is chosen. It is assumed that the thermal model matrices and electrical equivalent data for the motor already exist; the latter must also include the multiplication factors for the frequency dependent rotor parameters which are critical in the calculation of the motor temperatures during starting and braking. The thermal calculation programme is based upon the thermal model software already covered in Chapters 2 and 3; the calculation of the motor losses, hence thermal generators are, however, unique to this Chapter.

A separate time step of 0.5 seconds was chosen in formulating the thermal model matrices to be used in calculating the starting and braking temperature rises. For starting, the motor is initially at rest and finally rotating at rated speed, and vice versa for braking, thus at first sight neither the stationary nor the rotating model are applicable since both assume constant speed. However, as the stationary model represents the more onerous condition, it was chosen in preference to the rotating model; the short starting and braking times ensure that any errors resulting from this assumption will be small.

The calculation of starting and braking time from equation 6.14 cannot be guaranteed to yield an integer multiple of 0.5 seconds. However, recalling that it is the energy which is of prime importance in computing the temperature rises, the nearest integer multiple of 0.5 seconds was chosen as the time period and the losses, introduced at each time step, were compensated so that the overall energy input remained

the same. The resistances R_1 and R_2 were adjusted for temperature changes at each time step.

The relative aging calculation was performed for each time step though, as the total duty cycle period is unknown prior to the calculations, due to uncertainties regarding the starting and braking times, the final calculation is performed after all the thermal calculations have been completed. The reference temperature, T_{ref}, used in the aging calculations was chosen to be the thermal model predicted steady state winding hot spot temperature, in kelvin, for the motor continuously delivering rated output, assuming an average ambient temperature over 24 hours of 30°C [45,46]. In this way, any absolute errors that there might be in the thermal model estimations of the hot spot temperatures are minimized in the relative aging calculation. There is no reason why the average ambient temperature expected over the duration of the specified duty cycle could not be entered interactively with the other duty cycle data though, if this were adopted, it would also be sensible to adjust T_{ref} to the new ambient conditions.

Although all the nodal temperatures are calculated, only the following are made explicitly available for output:

1) Average stator winding temperature rise above ambient.
2) Maximum stator winding 'hot spot' temperature rise.
3) Maximum mean rotor winding temperature rise.

The average stator winding temperature was calculated as the weighted combination of the slot winding mean and the endwinding hot spot temperatures in accordance with equation 2.55 used in the calculation of the

stator winding temperature dependence in Chapter 2. All three of the above are easily converted to the absolute temperatures by the addition of the chosen ambient. A plot of these temperatures as a function of time, over the duration of the duty cycle, is also output to indicate when the temperature profile had settled into a steady state condition; this information was useful in excluding the 'pre-steady state' temperatures in the aging calculation for a duty cycle of indefinite period.

All the thermal calculations assume that the motor will be operating from a balanced three phase supply, as will normally be the case. Extending the system to include unbalanced operation would require an algorithm which related the motor losses to the power output and degree of voltage unbalance, the temperatures could then be computed using the unbalanced model; this could prove useful in choosing a motor to replace one which it is suspected failed because of the effects of unbalanced heating.

6.7 CASE STUDIES.

6.7.1 CASE STUDY 1 (S7).

A motor is required to drive a fan rated at 4125W running at approximately 1500 rpm. The inertia of the fan is rather large (5kg-m^2), and is near to the maximum rating (5.5 kg-m^2) of the GEC D132S 5.5 kW motor which has been suggested for this duty; the inertia rating is more than twice that of the next frame size down- the 4 kW D112M. Although the continuous running power rating is only 75% of the rated load of the D132S, it is by no means certain that the motor will be capable of

operating under the arduous conditions of the proposed duty which specifies that the fan is started, run continuously for 40 minutes and then brought rapidly to standstill by means of electric braking before repeating the cycle again on an indefinite basis.

The torque required to drive the fan is proportional to the square of its speed and is described by equation 6.33 below,

$$T_L = \frac{P_o(1-s)^2}{\omega_s}$$

Where,

P_o = rated fan power (4125W).

ω_s = motor synchronous speed.

s = slip.

The mean fan torque during starting and braking is found by integrating the above equation between the limits s=1, s=0 and s=2, s=1: for both cases the solution is,

$$T_L = \frac{P_o}{3\omega_s}$$

Substituting the values for the rated fan output and motor synchronous speed gives a torque of 8.75 N-m; this torque will oppose the motor starting torque but aid the braking action.

The duty cycle is specified as follows;

Number of cycles	Indefinite.
Stage 1	Direct-on-line starting.
Stage 2	Continuous at 4125W for 40 mins.
Stage 3	Plugging to standstill.

The results of the thermal analysis performed for the GEC 5.5 kW motor are as follows:

Maximum stator winding temperature rise (mean)	124.6°C
Maximum stator winding temperature rise (hot-spot)	140.8°C
Maximum rotor temperature rise (mean)	162.1°C
Relative aging (over 8 cycles)	0.798

The stator winding temperature rise profile for the first eight cycles is shown in figure 6.5.

The rated temperature rise for class F insulation (assuming a 40°C ambient) is 115°C [52]; it can be observed that this temperature is exceeded quite significantly by the maximum recorded hot spot temperature. However, the aging analysis over the first eight cycles, shows an estimated relative aging of 0.798; this suggests that if the expected lifetime of the insulation under continuous operation at full load is 30,000 hours then running indefinitely on the above duty cycle would result in an extended lifetime of 37,600 hours. However, averaging the relative aging over the first eight cycles in this way can be misleading as it also includes the lower temperatures before the system settles upon its periodic temperature cycle (figure 6.5). Performing the aging analysis over the subsequent eight cycles gives a better approximation to the

relative aging of 0.983; the expected lifetime now being reduced to 30,500 hours.

The above analysis included the frequency compensation for the rotor parameters based on the mean rotor current frequency during starting and braking. If these compensations are ignored, the resulting analysis, over the first eight cycles, gives the following data:

Maximum stator winding temperature rise (mean)	171.6°C
Maximum stator winding temperature rise (hot-spot)	197.8°C
Maximum rotor temperature rise (mean)	168.0°C
Relative aging (over 8 cycles)	45.8

The apparent relative aging is now much greater, reflecting the higher stator temperatures. The rotor temperatures, on the other hand, are much the same indicating that the total energy expended in the rotor has not changed significantly; this is to be expected as the total kinetic energy of the system and the work done by the load will be equal in both cases.

The greatest error when ignoring the rotor parameter frequency dependence arises in the calculation of the stator copper losses. If the frequency dependence is ignored, both the mean stator winding current and rotor winding current increase as the overall motor impedance is reduced; in addition, there is an overall reduction in the motor starting and braking torque which leads to an increase in the calculated starting and braking time. In the calculation of the rotor energy loss, the combined effects of the higher current and the longer starting and

braking periods are balanced by the reduction in the rotor winding resistance. However, the calculated stator energy loss experiences a significant increase resulting in the exaggerated temperatures shown above. For duties, such as this, which involve starting and braking high inertia loads, the rotor frequency effects cannot be ignored.

6.7.2 CASE STUDY 2 (S3).

A motor is required to drive a load of insignificant inertia on a duty cycle similar to S3 in the British standards [29]. The load of 6.5 kW is to be driven for 20 minutes in every hour, the remaining 40 minutes are to be spent at rest and de-energized. The purchaser is reluctant to buy a 7.5kW D132M if it can be shown that a D132S, the next frame size down, rated at 5.5kW, would suffice. The duty cycle specification is as follows:

Number of cycles	Indefinite.
Stage 1	Continuous at 6500W for 20 mins
Stage 2	Stationary cooling for 40 mins.

An eight cycle thermal profile for the GEC 5.5kW D132S is shown in figure 6.6. The thermal analysis over the same eight cycle period gave the following information:

Maximum stator winding temperature rise (mean)	93.0°C
Maximum stator winding temperature rise (hot-spot)	99.1°C
Maximum rotor temperature rise (mean)	153.4°C
Relative aging (over 8 cycles)	0.688

So even though the motor is being subjected to output power overloads of 20%, it is operating well within its insulation class limits. Again the relative aging calculation includes the 'pre-steady state' temperatures; the correct relative aging for indefinite operation upon the steady state cycle was 0.92.

The slight temperature rise that can be observed in figure 6.6, shortly after the beginning of the de-energized periods, is caused by the heat transfer from the hotter rotor across the airgap and into the endcap air; it can be seen to occur to some extent in the measurements under similar conditions in the varying load tests.

S1 Continuous running duty-type

S2 Short-time duty-type

S3 Intermittent periodic duty-type

S4 Intermittent periodic duty-type with starting

S5 Intermittent periodic duty-type with starting and electric braking

S6 Continuous operation at varying loads duty-type

S7 Continuous operation duty-type with starting and electric braking

S8 Continuous operation duty-type with related load/speed changes

Table 6·1 Duty Types and Designation

load	inertia ($kg\text{-}m^2$)	output power (W)	mean slip
A	5.0	0	0.21
B	5.0	5500	0.26
C	5.0	5500	0.31

load A pure inertia

load B fan-type load

load C constant load opposing starting torque

Table 6·2 Mean Slip during Starting

load	inertia ($kg\text{-}m^2$)	output power (W)	mean slip
A	5.0	0	1.53
B	5.0	5500	1.47
C	5.0	5500	1.63
D	5.0	5500	1.51

load A pure inertia

load B fan-type load

load C constant load opposing braking torque

load D constant load aiding braking torque

Table 6·3 Mean Slip during Braking

	c^2R_2	c^2X_2
starting	1.1	0.55
braking	2.07	2.07

units-Ohms

Table 6·4 GEC 5·5kW Motor Rotor Parameter Frequency Factors

Component	Temperature rise °C								
	starting period (s)					braking period (s)			
	1	3	5	10		1	3	5	10
frame	0.0	0.0	0.0	0.0		0.0	0.0	0.0	0.0
back iron	0.0	0.0	0.0	0.0		0.0	0.0	0.0	0.1
teeth	0.0	0.0	0.1	0.1		0.0	0.1	0.2	0.3
slot wndg	2.2	2.1	2.1	1.9		6.7	6.4	6.2	5.7
endwinding	3.4	3.3	3.3	3.1		10.1	10.0	9.8	9.4
rotor wndg	4.6	3.9	3.4	2.7		13.7	11.8	10.4	8.0
rotor iron	0.1	0.3	0.4	0.6		0.3	0.8	1.2	1.9
shaft	0.0	0.0	0.0	0.0		0.0	0.0	0.0	0.0

Table 6·5 GEC 5·5kW Motor Starting and Braking Pure Inertia Load of 0·4kg-m^2

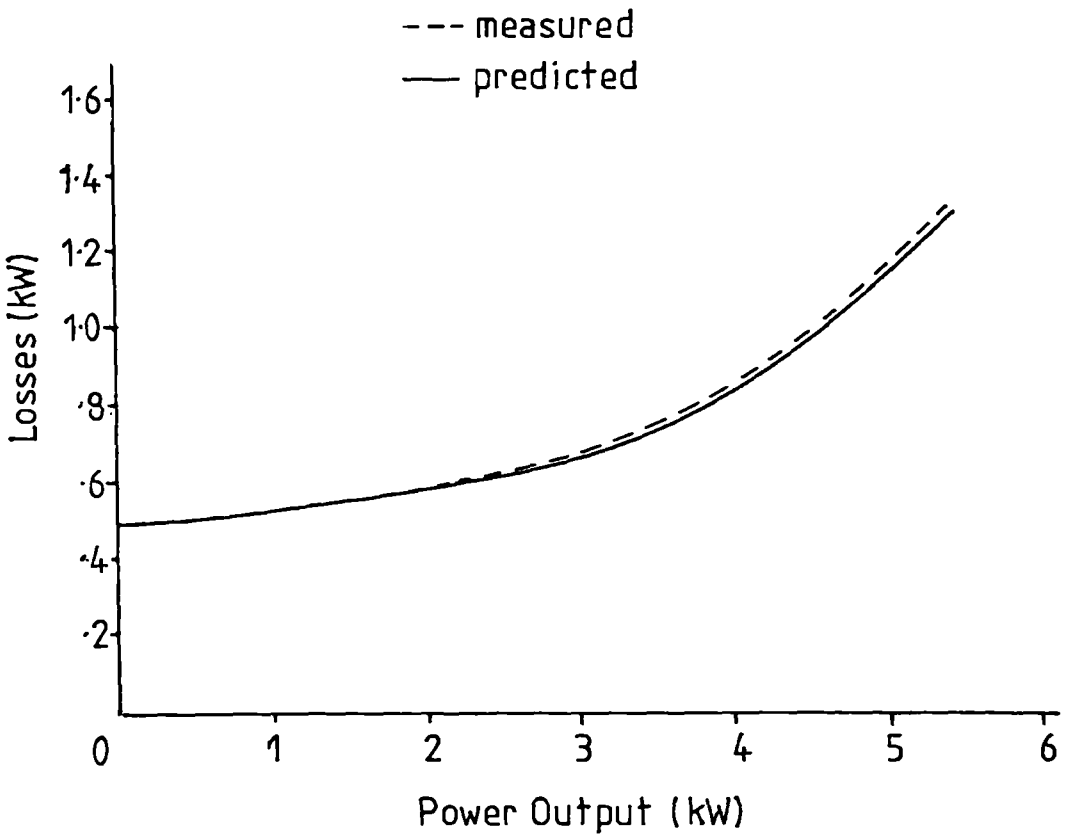

Figure 6-1 GEC 5·5kW Motor Losses versus Power Output

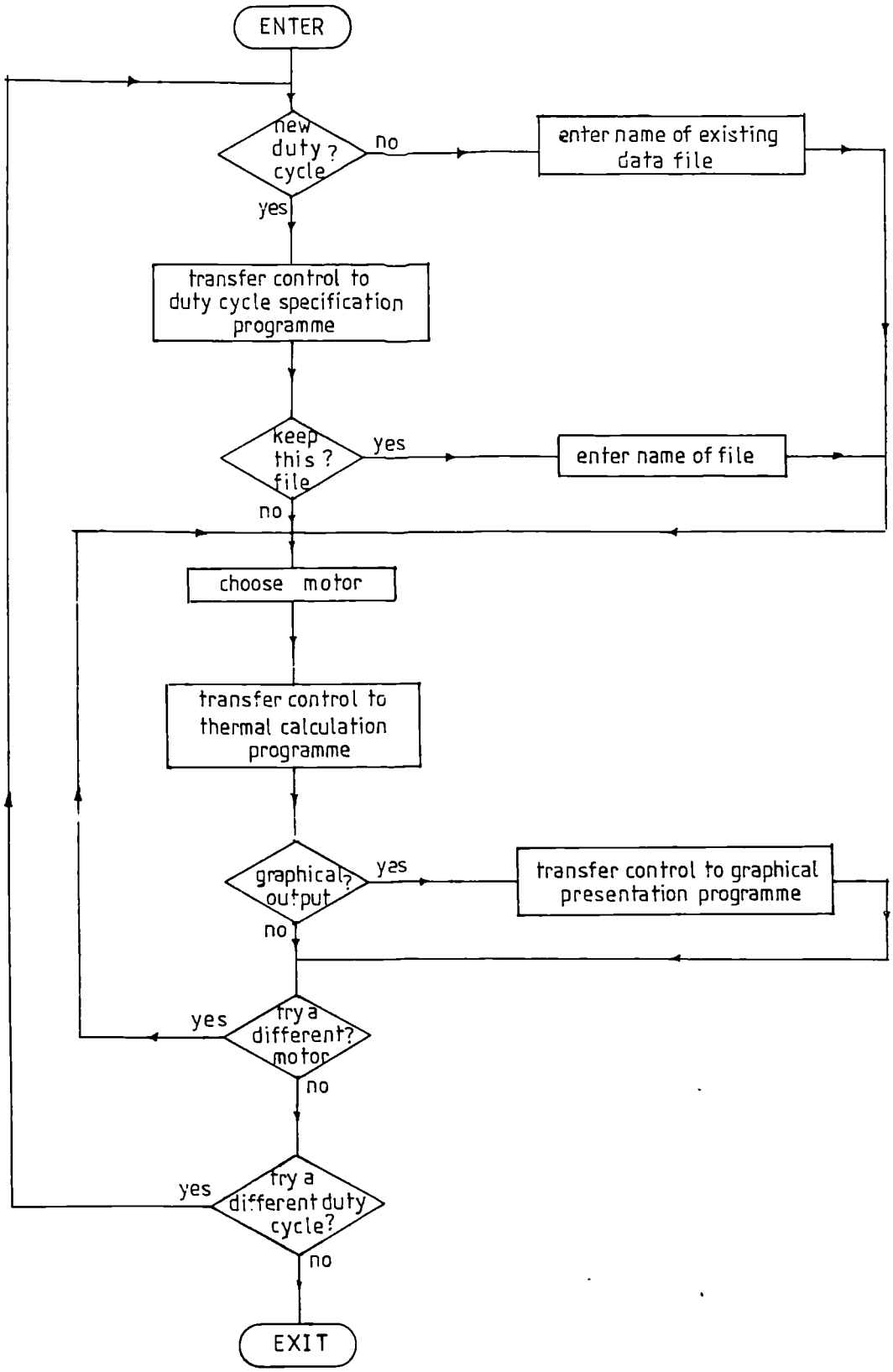

Figure 6·2 Command Programme Flowchart

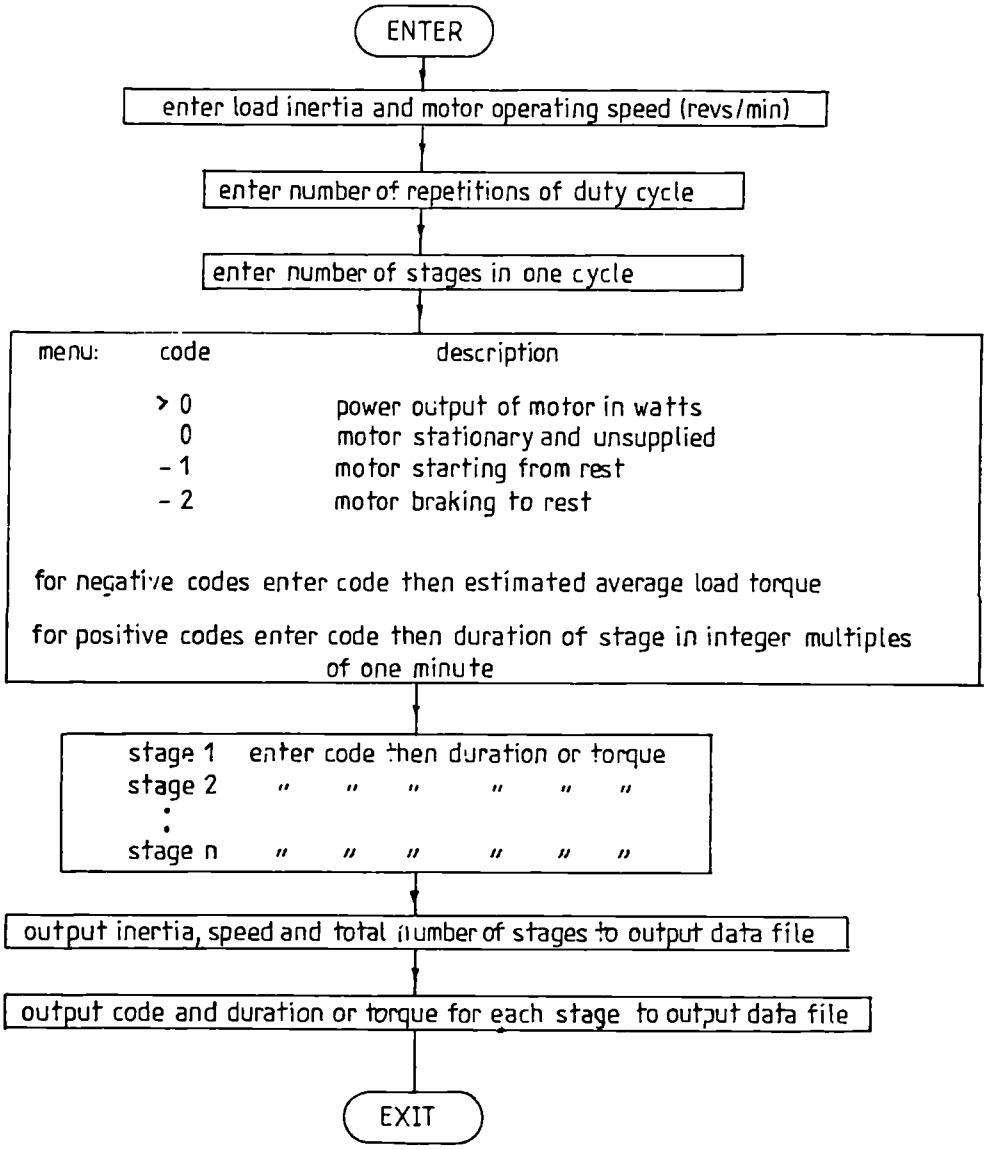

Figure 6·3 Duty Cycle Specification Flowchart

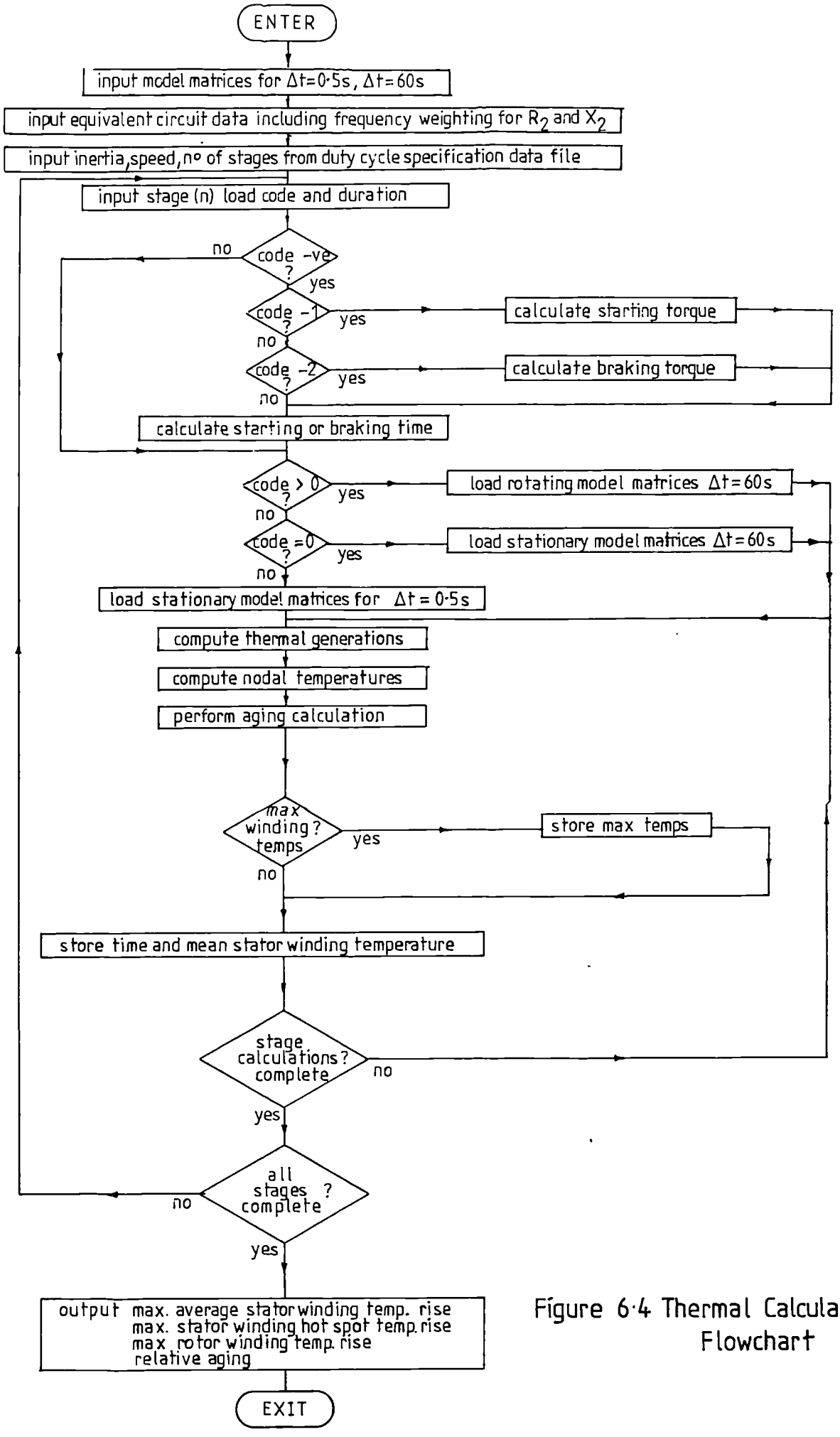

Figure 6·4 Thermal Calculation Flowchart

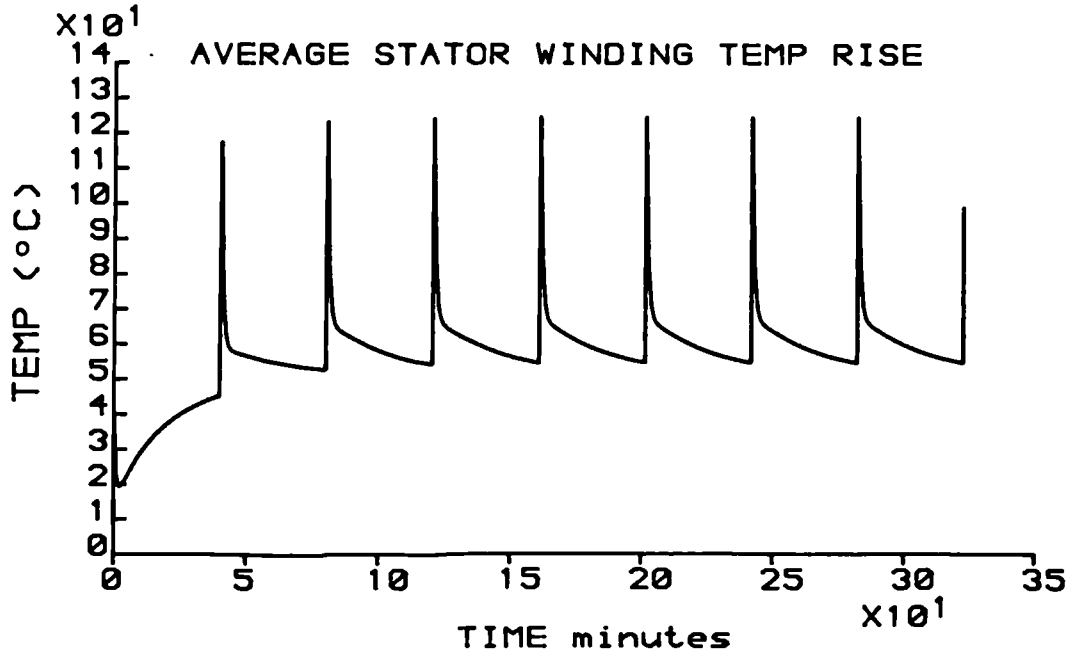

Figure 6·5 Temperature Profile for First Eight Cycles of Case Study 1 (S7)

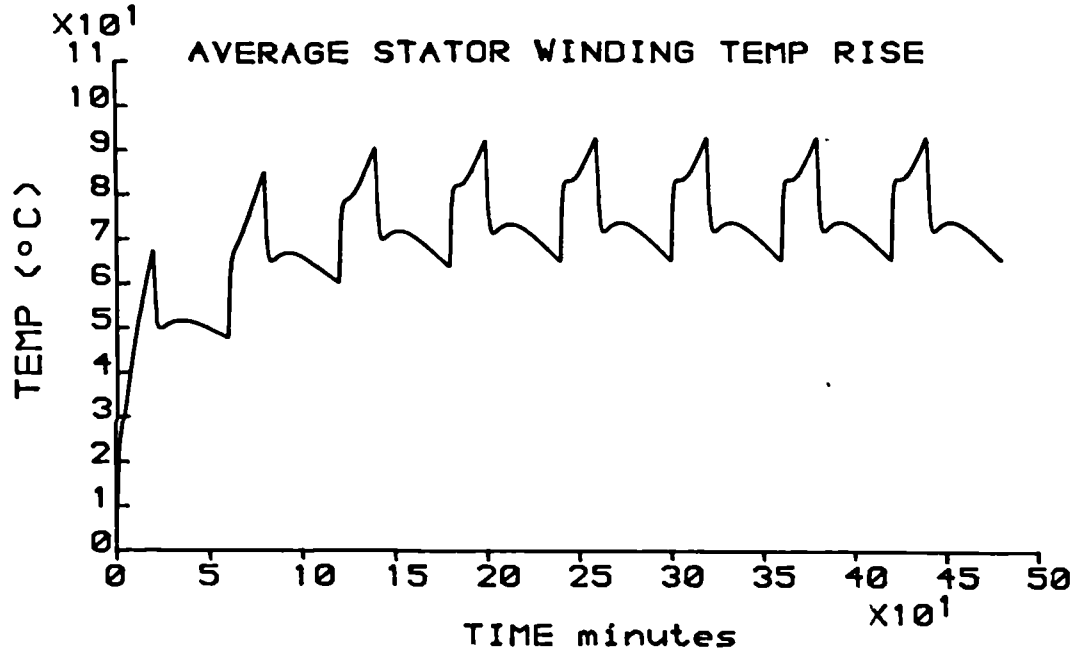

Figure 6·6 Temperature Profile for First Eight Cycles of Case Study 2 (S3)

CHAPTER 7. SUMMARY AND CONCLUSIONS.

If the new generation of smaller cheaper motors are to be used, confidently, to the limits of their capability, a new generation of protection devices will be required which are able to model the important motor temperatures accurately over the complete spectrum of operating conditions. The trend in protection devices has already begun, with the move from single node models such as the bi-metal strip and more recent solid state relays, to more complicated two node models. The growing recognition of the dangers involved when operating motors from unbalanced three phase supplies is illustrated by the increasing number of devices which now offer protection against phase unbalance in addition to the extreme case of single phasing. It is fair to say however, that no single device, currently available, models both the additional unbalanced losses and their spatial distribution between the stator winding phases, a model which as it represents the true heating conditions inside the motor must afford the closest protection. Further advances in motor protection devices will rely upon the application of more accurate thermal models and, as this necessarily entails detailed dimensional knowledge of each motor, will require close cooperation between motor and relay manufacturers.

A fifteen node, bulk component thermal model of a totally enclosed fan cooled (TEFC) induction motor has been proposed as being suitable for application to motor protection. The model is unique in that it seeks to model the heating conditions in the motor from, as far as possible,

purely dimensional data, physical constants and published heat transfer characteristics and does not rely on 'tuning' to fit measured motor temperatures. In this work, temperature dependence is included in the motor loss calculations to account for the changes in the stator and rotor winding resistances; the rotor winding resistance, for instance, could change by over 60% between start-up and running at full load. Implementing temperature dependence is important in helping to protect against the thermal runaway condition where high winding temperatures cause greater losses which further raise the winding temperatures and so on. Three four-pole TEFC induction motors are modelled and tested to prove that the model can be applied generally to motors of this kind.

In the model presented in this work, special attention was paid to the modelling of the frame/core contact resistance. Though much work has been done on the subject of thermal contact resistance, little seems applicable to the nature of the materials and surfaces in contact at the frame/core boundary of an electrical machine. This is surprising as the position of the contact on the main heat flow path from the stator windings to the ambient means that it has a direct influence on the winding temperatures. As electrical motor manufacturers in general are attempting to reduce the material volume, hence cost, of their motors, the lack of data regarding a possible mechanism by which this could be achieved is hard to understand. Detailed work on this problem is a substantial piece of research in itself and is outside the scope of this thesis, however some useful pointers were identified.

Tests performed on each of the motors showed that the model was able to predict the important endwinding temperatures very accurately

during varying load conditions that included periods of overload and extended periods of stationary cooling. The approximations employed in modelling the smaller motors held when applied to the larger 75kW motor suggesting that the model could be applied generally to four-pole TEFC induction motors. More work will be required to determine whether or not the theoretical and experimental data used to find the internal convective heat transfer coefficients would translate effectively to the operating speeds of two, six and eight-pole motors.

The model data for the two 5.5kW motors was markedly different despite their outside dimensions being identical; the differences were most marked in the airgap and rotor where the large airgap and the rotor cooling holes in the Brook Crompton Parkinson motor kept the rotor winding relatively cool and less susceptible to thermal runaway. This is significant as it is likely that conventional thermal protection devices would share common settings to protect what have been shown to be, thermally, two quite different machines. Evidence of the satisfactory prediction of rotor winding temperatures was gained by comparing a full load, steady state simulation of the temperatures in the 75kW motor, with measurements of the rotor winding temperatures recorded, via sliprings mounted on the shaft, by the motor manufacturer.

To investigate the feasibility of using the thermal model in a motor protection unit, the model was programmed into a system incorporating an eight bit microprocessor of the same kind as used in the other contemporary microprocessor based devices. Tests conducted using this system showed that the proposed device was indeed feasible and in fact would give a thermal tracking ability unequalled by any currently

available device. The ability of the model to predict both endwinding hotspot and rotor winding temperatures explicitly is unique, as is the property of future temperature prediction implicit in the thermal model solution. The latter property could be used to advantage in several situations; in a stand alone protection device it could be used to trigger an alarm so that the fault causing the overload might be identified and cleared before a shutdown was necessary, or as a remote unit in a larger system it could relay data to a master controller which might use the data to control the switching limits in a parallel machine drive based on a fore-knowledge of the future load requirements.

Several points regarding the solution of the model on a microprocessor were raised during testing. Not least of these was the question of the thermal model resolution which is governed by the number of bits used to store and calculate the thermal model constants and variables. It was found that the model would fail in instances where the change in temperature over the one second time step suggested, was less than one bit of the binary number used to store the motor temperatures. Although this was successfully overcome by substituting the model solution for a longer time step during stationary cooling it is thought, especially for larger motors which have relatively long thermal time constants, that a move from sixteen bit to twenty-four bit resolution would be a sensible progression. Though this move would involve a greater initial effort in producing the more complicated software, the effort would only be necessary once, the additional memory required would not be prohibitive and the extra computation time could be recovered by moving to a faster system clock than that used in the system adopted here.

The thermal model was modified to allow for the additional heating effects and the spatial distribution of the stator copper losses which occur as the result of operating induction motors from unbalanced three phase supplies. Protecting motors against these effects will become increasingly important if the trend toward smaller motors continues and although an increasing number of devices are including some means of protection, as yet, no single device has attempted to model both the additional losses and the effects of the concentration of the stator copper losses in the phase carrying the largest current. In this work, the induction motor losses during unbalanced operation were found by measuring the symmetrical components of the input currents and computing the losses associated with the positive and negative sequence components separately. The rotor resistance used in the calculation of the negative sequence rotor copper loss was weighted to allow for the increased resistance of the rotor winding to these currents which are induced at approximately twice the supply frequency; this becomes increasingly significant for rotors of deep bar construction. The use of the sequence currents in the unbalanced model led to the development of a digital sequence current measuring system which computed the square of the positive and negative sequence currents, along with the square of each line current, in a form compatible with the thermal generator calculations performed on the microprocessor. Although the measuring system was based on line current samples taken at fixed timing intervals which were consistent with a 50Hz waveform, it was shown that the errors involved in taking measurements from waveforms within the expected range of frequencies, from 49.5Hz to 50.5Hz, were negligible.

The endwinding component was remodelled to provide a means of representing the spatial distribution of the stator copper losses. The remodelling had a minimal effect upon the original form of the thermal model as it proved possible to resolve the resulting endwinding thermal equivalent circuit into that originally developed for balanced operation plus a simple additional circuit. The additional circuit modelled the extra endwinding hot-spot temperature rise of the hottest phase over the average hot-spot temperature rise of the three phases and was computed outside the main thermal model calculations which, apart from the use of the sequence components in the calculation of the thermal generators, remained unchanged. Comparisons of measured and simulated temperatures during varying load tests in which the three phase supply was purposefully subjected to varying degrees of unbalance, gave satisfactory evidence of the validity of both the restructured model and the measuring system. Furthermore, the tests illustrated the need to include the negative sequence current in the thermal calculations and suggested that the possibility of damage to some designs of rotor, during severe supply unbalance could not be discounted. It was also shown that percentage unbalance, adopted in many protection devices, is not a reliable protection criterion.

The integration of the sequence current measuring system and the unbalanced model, programmed on the microprocessor system, remains to be performed and further work will be required to translate the resulting experimental system into a viable, robust commercial product. A possible development of the device might be the creation of a hybrid device which would possess both the security of protection found in devices based upon direct measurement of stator winding temperatures and the desirable

properties of the thermal model. Instead of referencing the thermal calculations to a preprogrammed ambient temperature, the easily accessible frame temperature could be measured directly and the thermal calculations referenced to this. In this way hazards which might not previously have been detected because they were not reflected in the motor supply conditions could be protected against; a broken cooling fan or a blocked or partially blocked cowl are plausible examples of this kind of fault. Such a hybrid device might find an application in environments where dirt and dust could not be prevented from coming into contact with the motors.

The success of the thermal model relies upon the individual modelling of each type of motor and it is true that the quantity of data generated in each individual case does not readily lend itself to programming the device with the required data 'on-site'. However, a data library consisting of the electronic memory devices used to store the model data could overcome this problem; the data for a range of motors could be stored on one device which could then be supplied with the protection relay in accordance with it's application.

The compilation of the thermal model data requires a detailed knowledge of the motor design data, the cooperation of the motor manufacturers would therefore be imperative if the device was to receive widespread application. The thermal model data could, however, be of immediate use to the motor manufacturer in its own right and this itself might justify the effort, on the part of the manufacturer, of including the calculation of the thermal model parameters at the design stage of a motor. An obvious application of the thermal model for motor manufacturers in

general, is in the preliminary investigations of the effect of design modifications on motor temperatures; this is consistent with the current trend toward computer aided tools in the mechanical design of electrical machines. The results of the model simulations could be used to indicate whether it would be worthwhile proceeding with the construction of prototype machines. One less obvious but important application was suggested by a motor manufacturer who saw that the model could be used as a useful tool in aiding the staff whose responsibility it is to suggest the motor most compatible with a particular customers needs. Following his suggestion, a duty cycle thermal calculation system was developed to calculate the winding temperatures in a given motor during a pre-specified duty cycle thus giving valuable information about the compatibility of the duty cycle and motor. It is felt that the system could be used to particular advantage in the analysis of multi-stage duty cycles where the estimation of the likely motor temperatures would be difficult without resorting to expensive and time consuming tests.

The particular features that were included in the system were illustrated in two fictional case studies which were based on the British Standard duty cycles S3 and S7. In the analyses the motor losses were computed from the power output information included in a duty cycle specification. The losses during starting and braking were also treated as these become significant in duties which involve the acceleration and deceleration of high inertia loads. Allowing for the frequency dependence of the rotor impedance proved critical in the calculation of the starting and braking losses as ignoring this phenomenon caused an over-estimation of the acceleration and deceleration times which in turn led to excessive stator winding losses and temperature rises. The frequency dependence

was implemented by applying multiplication factors based upon the mean slip, hence rotor frequency, during starting and braking; slips of 0.25 and 1.5 respectively were found to give the best approximations for a range of load types. An aging analysis was included with the duty cycle temperature calculations to provide another useful parameter on which the most sensible choice of motor could be made. The aging of the stator winding insulation during a given duty cycle was calculated relative to the aging over the same period of continuous operation at rated load. Further work will be required to find an algorithm to correlate the motor losses to a given power output and voltage unbalance so that some guidelines could be given to customers on the maximum safe limits of supply unbalance.

It has been shown that the thermal model performs well for the motors tested under both balanced and unbalanced operating conditions. It has also been shown that the model can track motor temperatures in real time in a protection role and a means by which this can be extended to include protection during unbalanced conditions has been identified. Further work will be required to model two, six and eight pole motors and those that operate from 60Hz supplies. If the model performs satisfactorily for these motors then the work could be extended to variable speed, inverter fed motors, either by having a data base of the thermal model data for a number of different speeds or by recomputing the thermal model parameters and matrices at each stage; the latter would require considerable computing power and would not be compatible with real time applications. This application would also require an analysis of the harmonic losses associated with the non-sinusoidal output of inverters so that these could be included in the thermal generator calculations.

REFERENCES

[1] K. Goodchild, P. Rayner, 'Nearer the Brink'. Electronics and Power, February 1976.

[2] P.G.A. Wilson, 'Complete Protection of Motors Under Variable Load Conditions'. Second European Conference on Drives/Motors/Controls, Harrogate 1983, pp 172-178.

[3] "Motormaster", a Descriptive Bulletin by GEC Measurements.

[4] "OLE Electronic Overload Relay", a Descriptive Bulletin by Simplex GE.

[5] "Electronic Motor Protection Unit CET-3", a Descriptive Bulletin by Sprecher and Schuh.

[6] E.B. Turner, H.M. Willey, "Microprocessor Based Universal Motor Protection System". IEEE Trans. on Ind. Appl., vol 1A-17, 1981, pp 58-62.

[7] "IPS Intelligent Protection System", a Descriptive Bulletin by Kraus and Naimer.

[8] "IQ 2000" a Descriptive Bulletin by Westinghouse.

[9] "Motor Protection Device", UK Patent GB 2066597B.

[10] "Motor Control Apparatus", UK Patent GB 2114390A.

[11] A.N. Eliasen, "The Protection of High Inertia Drive Motors". IEEE Trans. on Power Apparatus and Systems, vol PAS 99 No.4 1980.

[12] E.L. Wilson, R.E. Nickell, "Application of the Finite Element Method to Heat Conduction Analysis". Nuclear Engineering Design 4 1966, pp 276-286.

[13] T.J. Roberts, "The Solution of the Heat Flow Equations in Large Electrical Machines". Proc. IME, vol 184 pt 3E 1969, pp 70-83.

[14] S.B. Preston, M.A. Thomas, G.A. Pennington, "Non Steady State Thermal Performance of Electrical Machines". Proc. IME, vol 184 pt 3E 1969, pp 9-14.

[15] P.H. Mellor, D.R. Turner, D. Roberts, "Microprocessor Based Thermal Protection". Proc. Second Int. EMDA conf. IEE Sept 1985, pp 16-19.

[16] P.H. Mellor, "Improvements in the Efficiency and Thermal Aging of Single and Parallel Machine Drives". Ph. D. Thesis, Univ. of Liverpool 1983.

[17] V.K. Screenivasan, D.P. Sengupta, "Thermal Design of a Totally Enclosed Fan Cooled Induction Motor". IEEE PES Winter Meeting Paper A 77 97-9, 1977.

[18] R.L. Kotnik, "An Equivalent Thermal Circuit for Non Ventilated Induction Motors". Trans. AIEE vol 73 pt 3A 1954, pp 1604-1609.

[19] L. Imre, Z. Jagasits, J. Barcza, "Computer Simulation of the Transient Warming of Rotary Electrical Machines". Proc. Second Int. Conf. on Numerical Methods in Thermal Problems, Venice July 1981, pp 685-696.

[20] D.R. Boothman, E.C. Elgar, R.H. Rehder, R.J. Wooddall, "Thermal Tracking - A Rational Approach to Motor Protection". IEEE PES Winter Meeting, Jan. 1974.

[21] D.I. Sannikov, N.I. Yakovenko, V.D. Shapkin, "Recalculation of Permissible Heat Operating Conditions for Induction Motors". Elektromekh., No 1 1984, pp 44-49.

[22] I.J. Perez, J.G. Kassakian, "A stationary Thermal Model for Smooth Air Gap Rotating Electrical Machines". Elec. Machines and Electromechanics, vol 3 No 3-4 1979, pp 285-303.

[23] N.R. Namburi, "Thermal Modelling of an Induction Motor". IEEE Trans. Power Apparatus and Systems, vol pas 102 No 8 Aug. 1983, pp 2636-2639.

[24] B.N. Gafford, W.C. Duesterhoeft, C.C. Mosher, "Heating of Induction Motors on Unbalanced Voltages". Trans. AIEE, vol 78 pt 3A June 1959, pp 282-288.

[25] R.F. Woll, "Effect of Unbalanced Voltage on the Operation of Polyphase Induction Motors". IEEE Trans. on Ind. Appl. vol 1A-11 No 1 Jan/Feb 1975.

[26] W.T. Martiny, R.M. McCoy, H.B. Margolis, "Thermal Relationships in an Induction Motor under Normal and Abnormal Operation". Trans. AIEE vol 80 pt 3 April 1961, pp 66-78.

[27] J.E. Williams, "Operation of 3-Phase Induction Motors on Unbalanced Voltages". AIEE Trans. PAS, vol 73 pt 3A April 1954, pp 459-467.

[28] B.N. Gafford, "Thermal-Synthesis Relay is Best Replica of Motor Heating". Trans. AIEE vol 78 pt 3A June 1959, pp 288-295.

[29] "Duty and Rating", British Standards, BS 4999 pt 30 1972.

[30] T.W. Dakin,"Electrical Insulation Deterioration treated as a Chemical Rate Phenomenon". AIEE Trans. vol. 67 1948, pp 113-122.

[31] I.W. Brunot, F.F. Buckland, "Thermal Contact Resistance of Laminated and Machined Joints". Trans. ASME April 1950, pp 253-257.

[32] "Heat Transfer and Fluid Flow Data Book". General Electric 1969.

[33] G.I. Taylor, "Distribution of Velocity and Temperature Between Concentric Cylinders". Proc Royal Society vol. 159 A 1935, pp 546-578.

[34] C. Gazley, "Heat Transfer Characteristics of Rotational and Axial Flow Between Concentric Cylinders". Trans. ASME Jan 1958, pp 79-89

[35] G.E. Luke, "The Cooling of Electric Machines". Trans. AIEE vol 45 1923, pp 1278-1288.

[36] Y. Mori, W. Nakayami, "Forced Convective Heat Transfer in a Straight Pipe Rotating Around a Parallel Axis". Int. J. Heat Transfer vol 10, pp 1179-1194.

[37] Yu.P. Shlykov, Ye.A Ganin, "Thermal Resistance of Metallic Contacts". Int. J. Heat Mass Transfer vol 7 1964, pp 921-929

[38] M.G. Say, "Alternating Current Machines". Pitman 1976.

[39] S.C. Lennox, M. Chadwick, "Mathematics for Engineers and Applied Scientists". Heinemann 1977.

[40] B. Noble, "Applications of Undergraduate Mathematics in Engineering". Collier Macmillan 1967.

[41] S.A. Swann, J.W. Salmon, "Effective Resistance and Reactance of a Rectangular Conductor Placed in a Semi-Closed Slot". Proc. IEE vol 110 No9 Sept 1963.

[42] "MDS 85 Users Manual". Intel Corporation 1978.

[43] "SDK 85 Users Manual". Intel Corporation 1978.

[44] P.G. Cummings, W.D. Bowers, W.J. Martiny, "Induction Motor Efficiency Test Methods". IEEE Trans on Ind. Appl. vol. 1A-17 No3 May/June 1981.

[45] L.C. Whitman, "Simplified Methods of Calculating Insulation Life Characteristics". AIEE Trans. PAS Oct. 1961, pp 683-685.

[46] L.C. Whitman, W.W. Whitman, "Mathematics of Insulation aging". AIEE Trans. vol 78 Sept 1959, pp 308-318.

[47] K. Micheal, "The Thermal Behaviour of Insulation in Electrical Machines". Brown Boveri Review vol. 49 No 11-12 1962, pp 630-639.

[48] NAG Fortran Library Manual, Mark 11.

[49] GINO-F Graphics User Manual, Issue 2.7A October 1983.

[50] "Losses and Efficiency", British Standards, BS 4999 pt 33.

[51] NEMA Standards, pt 14 June 1980, pp 6.

[52] T. Wildi, "Electrical Power Technology". Wiley 1980.

APPENDIX A. GENERAL EQUATIONS FOR THE RADIAL AND AXIAL MEAN TEMPERATURES OF A CYLINDRICAL ELEMENT.

Expressions for the radial and axial mean temperatures can be derived from the equation for heat storage (H_s) in the cylindrical element, figure A1.

$$H_s = \rho.V.c_p.T_m \tag{A1}$$

ρ = material density (kg/m^3)

V = cylinder volume (m^3)

c_p = specific heat capacity at constant pressure ($J/kg°C$)

T_m = mean temperature of cylinder (°C)

$$H_s = \rho.c_p.T_m.\pi(r_2^2-r_1^2).L \tag{A2}$$

Defining an elemental volume in cylindrical co-ordinates, v_e, small enough to be considered at a uniform temperature, T, then the elemental heat stored, H_{se}, is given by equation A4.

$$v_e = r.d\theta.dl.dr \tag{A3}$$

$$H_{se} = \rho.c_p.T.r.d\theta.dl.dr \tag{A4}$$

The volume integral of equation A4 can be equated to the total heat stored given by equation A2.

$$\rho.c_p.T.r.d\theta.dl.dr. = \rho.c_p.T_m.\pi(r_2^2-r_1^2).L \qquad (A5)$$

The radial mean temperature is therefore defined by,

$$T_m = \frac{2}{r_2^2-r_1^2}\int_{r_1}^{r_2} T_r.r.dr \qquad (A6)$$

The axial mean temperature is given similarly by,

$$T_m = \frac{1}{L}\int_0^L T_l.dl \qquad (A7)$$

where,

T_r = radial temperature profile.

T_l = axial temperature profile.

The one dimensional equation which describes heat flow by conduction in the radial direction is,

$$\frac{\partial^2 T}{\partial r^2} + \frac{1}{r}.\frac{\partial T}{\partial r} + \frac{g}{k} = 0 \qquad (A8)$$

g = heat generated per unit volume (W/m^3)

k = thermal conductivity in the radial direction ($W/m°C$)

The general solution to equation A7 gives the radial temperature profile,

$$T_r = a.\ln r + \frac{g.r^2}{4k} + b \qquad (A9)$$

a,b are arbitrary constants

The constant 'a' may be found by substituting in the boundary conditions $T_r = T_1$ at $r = r_1$ and $T_r = T_2$ at $r = r_2$ and subtracting.

$$a = \frac{1}{\ln(r_2/r_1)}\left[T_2 - T_1 + \frac{g.(r_2^2 - r_1^2)}{4k}\right] \qquad \text{(A10)}$$

Substituting equation A9 into equation A6 for T_m gives,

$$T_m = \frac{2}{r_2^2 - r_1^2}\int_{r_1}^{r_2} \frac{(a.\ln r + g.r^2 + b).r.dr}{4k} \qquad \text{(A11)}$$

Performing the integration and substituting for 'a' gives the general solution for the mean temperature of a cylindrical element in the radial direction as,

$$T_m = T_2\left[\frac{r_2^2}{(r_2^2 - r_1^2)} - \frac{1}{2\ln(r_2/r_1)}\right] + T_1\left[\frac{1}{2\ln(r_2/r_1)} - \frac{r_1^2}{(r_2^2 - r_1^2)}\right] + \frac{g.(r_1^2 + r_2^2)}{8k} - \frac{g.(r_2^2 - r_1^2)}{8k.(\ln(r_2/r_1))} \qquad \text{(A12)}$$

In the axial direction, conductive heat flow is described by equation A13.

$$\frac{\partial^2 T}{\partial l^2} + \frac{g}{k} = 0 \qquad \text{(A13)}$$

In this instance, k is the axial conductivity of the cylinder.

The equation is parabolic and has the solution,

$$T_l = \frac{-g.l^2}{2k} + A.l + B \qquad \text{(A14)}$$

The constants are found by substituting the boundary conditions $T_l = T_3$ at $l = 0$ and $T_l = T_4$ at $l = L$.

$$A = \frac{1}{L}\left[T_4 - T_3 + \frac{g.L^2}{2k}\right] \qquad \text{(A15)}$$

$$B = T_3 \qquad \text{(A16)}$$

Solving equation A7 with T_l given from equation A14 yields the general equation for the axial mean temperature.

$$T_m = \frac{T_3 + T_4}{2} + \frac{g.L^2}{12k} \qquad \text{(A17)}$$

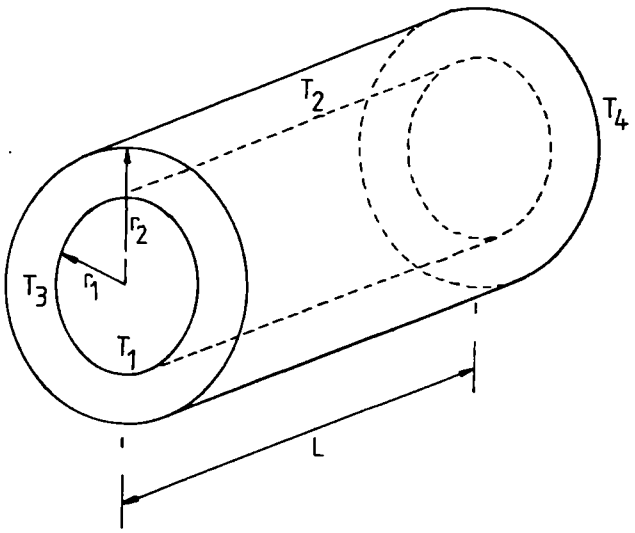

Figure A1 Two Dimensional Cylindrical Element

BCP 5.5KW DYNAMIC MODEL CAPACITANCES AND ADMITTANCES

C1=	0.3874540E+04	C2=	0.2512413E+04	C3=	0.1145940E+04	C4=	0.3160736E+03		
C5=	0.3309883E+03	C6=	0.4743613E+03	C7=	0.1901172E+04	C8=	0.7682674E+03		
YA=	0.1300000E+02	YB=	0.2606300E+01	YC=	0.9997972E+01	YD=	-0.4902265E+03	YE=	0.3033941E+00
YF=	0.1521533E+03	YG=	0.6448443E+02	YH=	0.5850364E+01	YI=	0.1369494E+00	YJ=	-0.2124622E+03
YK=	0.1156912E+02	YL=	0.8267672E+01	YM=	0.2364685E+01	YN=	0.9047966E+00	YO=	0.6406020E+00
YP=	0.1607860E+01	YQ=	-0.5689841E+04	YR=	0.8003118E+00	YS=	0.4513813E+02	YT=	-0.1088194E+03
YU=	0.2659949E+00	YV=	0.1301890E+01	YW=	0.1373682E+01				

BCP 5.5KW STATIONARY MODEL CAPACITANCES AND ADMITTANCES

C1=	0.3874540E+04	C2=	0.2512413E+04	C3=	0.1145940E+04	C4=	0.3160736E+03		
C5=	0.3309883E+03	C6=	0.4743613E+03	C7=	0.1901172E+04	C8=	0.7682674E+03		
YA=	0.2350000E+01	YB=	0.1038500E+01	YC=	0.9997972E+01	YD=	-0.4902265E+03	YE=	0.1458466E+00
YF=	0.1521533E+03	YG=	0.6448443E+02	YH=	0.5850364E+01	YI=	0.6569347E-01	YJ=	-0.2124622E+03
YK=	0.1156912E+02	YL=	0.8267672E+01	YM=	0.1070424E+01	YN=	0.8243825E+00	YO=	0.5888441E+00
YP=	0.1463522E+01	YQ=	-0.5689841E+04	YR=	0.3282741E+00	YS=	0.4513813E+02	YT=	-0.1088194E+03
YU=	0.1933127E+00	YV=	0.1301890E+01	YW=	0.1373682E+01				

GEC 5.5KW DYNAMIC MODEL CAPACITANCES AND ADMITTANCES

C1=	0.3002634E+04	C2=	0.2447138E+04	C3=	0.1252816E+04	C4=	0.3000200E+03		
C5=	0.3154982E+03	C6=	0.5213712E+03	C7=	0.1887732E+04	C8=	0.1092735E+04		
YA=	0.1700000E+02	YB=	0.4130200E+01	YC=	0.4076837E+02	YD=	-0.4484785E+03	YE=	0.3148276E+00
YF=	0.1388275E+03	YG=	0.7528420E+02	YH=	0.5887556E+01	YI=	0.1610975E+00	YJ=	-0.2473756E+03
YK=	0.1160262E+02	YL=	0.1042186E+02	YM=	0.2170182E+01	YN=	0.3227846E+01	YO=	0.1288439E+01
YP=	0.4960851E+01	YQ=	-0.5413172E+04	YR=	0.8458079E+00	YS=	0.4960769E+02	YT=	-0.1225591E+03
YU=	0.2428649E+00	YV=	0.1369105E+01	YW=	0.1435898E+01				

GEC 5.5KW STATIONARY MODEL CAPACITANCES AND ADMITTANCES

C1=	0.3002634E+04	C2=	0.2447138E+04	C3=	0.1252816E+04	C4=	0.3000200E+03		
C5=	0.3154982E+03	C6=	0.5213712E+03	C7=	0.1887732E+04	C8=	0.1092735E+04		
YA=	0.2600000E+01	YB=	0.1658500E+01	YC=	0.4076837E+02	YD=	-0.4484785E+03	YE=	0.1509751E+00
YF=	0.1388275E+03	YG=	0.7528420E+02	YH=	0.5887556E+01	YI=	0.7724671E-01	YJ=	-0.2473756E+03
YK=	0.1160262E+02	YL=	0.1042186E+02	YM=	0.1020467E+01	YN=	0.2944459E+01	YO=	0.1195214E+01
YP=	0.4511577E+01	YQ=	-0.5413172E+04	YR=	0.3489961E+00	YS=	0.4960769E+02	YT=	-0.1225591E+03
YU=	0.1164660E+00	YV=	0.1369105E+01	YW=	0.1435898E+01				

GEC 75KW DYNAMIC MODEL CAPACITANCES AND ADMITTANCES

C1=	0.5633550E+05	C2=	0.2203063E+05	C3=	0.8374464E+04	C4=	0.3273240E+04
C5=	0.2510030E+04	C6=	0.4296290E+04	C7=	0.2401159E+05	C8=	0.7185354E+04
YA=	0.5850000E+02	YB=	0.1946490E+02	YC=	0.1134908E+03	YD=	-0.1172168E+04
YE=	0.1054561E+01	YF=	0.3646254E+03	YG=	0.1801143E+03	YH=	0.2548596E+02
YI=	0.3889613E+00	YJ=	-0.5821505E+03	YK=	0.5025772E+02	YL=	0.2729411E+02
YM=	0.9400340E+01	YN=	0.6251073E+01	YO=	0.4617704E+01	YP=	0.1197107E+02
YQ=	-0.3018612E+05	YR=	0.5277541E+01	YS=	0.1083357E+03	YT=	-0.2536636E+03
YU=	0.1148331E+01	YV=	0.2025741E+01	YW=	0.2102023E+01		

GEC 75KW STATIONARY MODEL CAPACITANCES AND ADMITTANCES

C1=	0.5633550E+05	C2=	0.2203063E+05	C3=	0.8374464E+04	C4=	0.3273240E+04
C5=	0.2510030E+04	C6=	0.4296290E+04	C7=	0.2401159E+05	C8=	0.7185354E+04
YA=	0.1170000E+02	YB=	0.4634500E+01	YC=	0.1134908E+03	YD=	-0.1172168E+04
YE=	0.4669956E+00	YF=	0.3646254E+03	YG=	0.1801143E+03	YH=	0.2548596E+02
YI=	0.1679554E+00	YJ=	-0.5821505E+03	YK=	0.5025772E+02	YL=	0.2729411E+02
YM=	0.3810580E+01	YN=	0.3406125E+01	YO=	0.2708104E+01	YP=	0.6435489E+01
YQ=	-0.3018612E+05	YR=	0.1649064E+01	YS=	0.1083357E+03	YT=	-0.2536636E+03
YU=	0.5081192E+00	YV=	0.2025741E+01	YW=	0.2102023E+01		

APPENDIX C. THE PROTOTYPING SYSTEM HARDWARE.

The system was based upon an Intel SDK 85 single board microprocessor system. In addition to the basic SDK 85 kit another 8155 Random Access Memory and input/output port chip was added primarily for the use of its programmable timer; the timer on the original 8155 was used by the system monitor software stored in the 8755 Read Only Memory. Two two kilobyte ROM (2716) devices were added externally, figure C1, to store the data logging and/or thermal prediction software and the thermal model data. An extra one kilobyte of RAM (6116) was also added to supplement the 512 bytes already available in the 8155's.

The platinum resistance motor temperature measuring circuit is shown in figure C2. The potential drop across any of the thermometers is multiplexed to an operational amplifier (725) by ten pairs of analogue switches which are activated on the specific output of the address decode circuitry during a memory write cycle of the 8085 processor. The 725 amplifier provides the initial scaling; a second amplifier (741) connected in the differential mode, outputs a signal which is directly proportional to the specified thermometer temperature in celcius. This is converted to digital form (ADC 0804) ready to be transferred to the system memory during a memory read cycle. The constant current source delivers a current of approximately 1mA which is small enough to discount any self-heating effects in the resistance thermometers.

The line current measuring circuit is shown in figure C3. A current transformer provides a voltage, proportional to the line current, across a 5A/.2V current shunt in it's secondary circuit. The amplified voltage is fed to a true RMS to DC converter (AD 426A) which in turn provides the input to an Analogue to Digital converter (ZN 427 E-8). The eight bit digital output is input into the processor, when required, via port 29H of the second 8155. The circuit was calibrated so that 15A and 150A gave the maximum (FF(hex)) output for the 5.5kW and 75kW motors respectively.

The hardware required to interface the Facit Paper Punch, used as the medium of data transfer between the prototyping system and the mainframe computer, is shown in figure C4. Data is transferred via port 21H of the first 8155 by a handshaking mechanism controlled from the least significant bits of ports 22H and 23H of the same 8155.

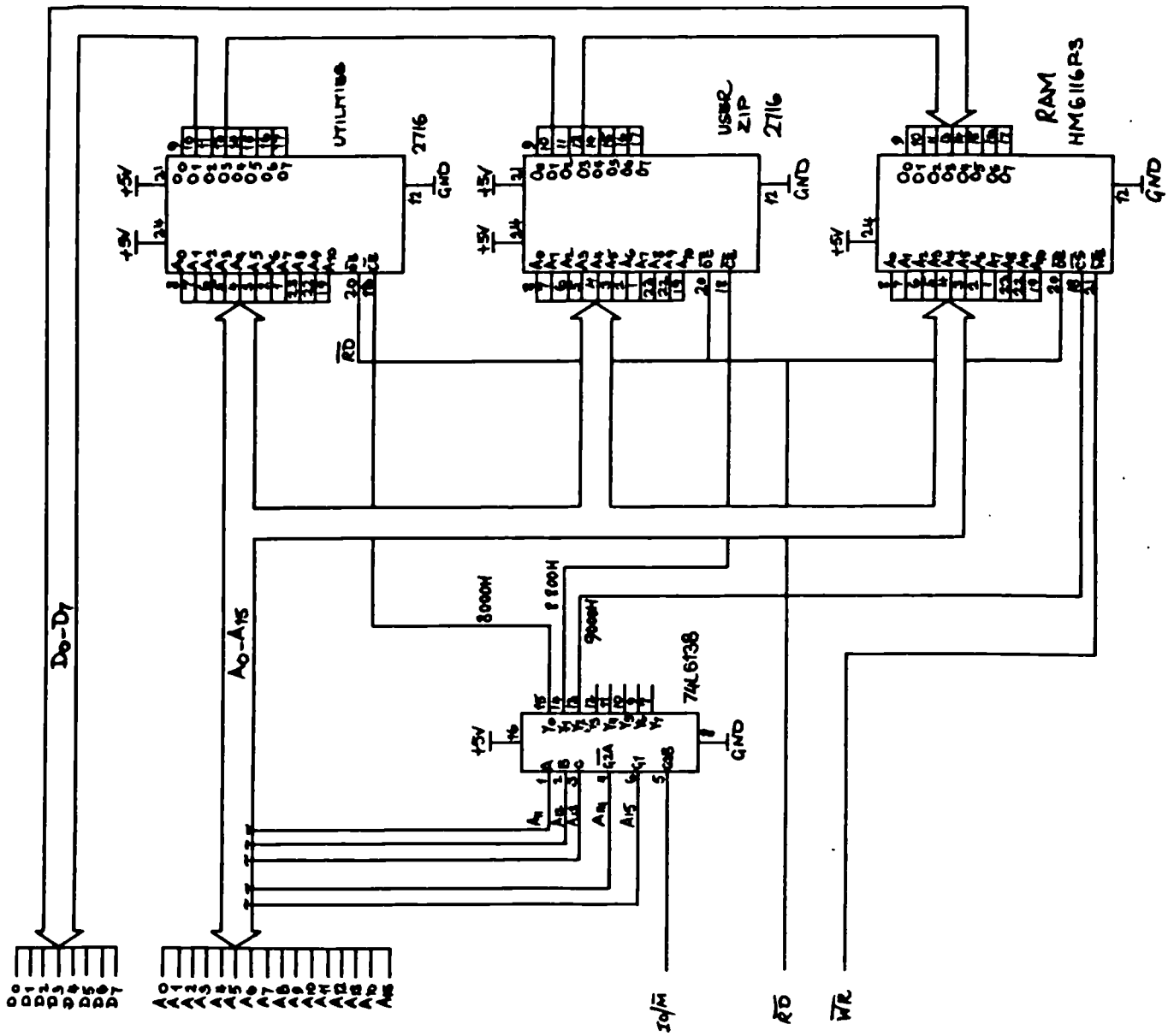

Figure C1 Additional Memory

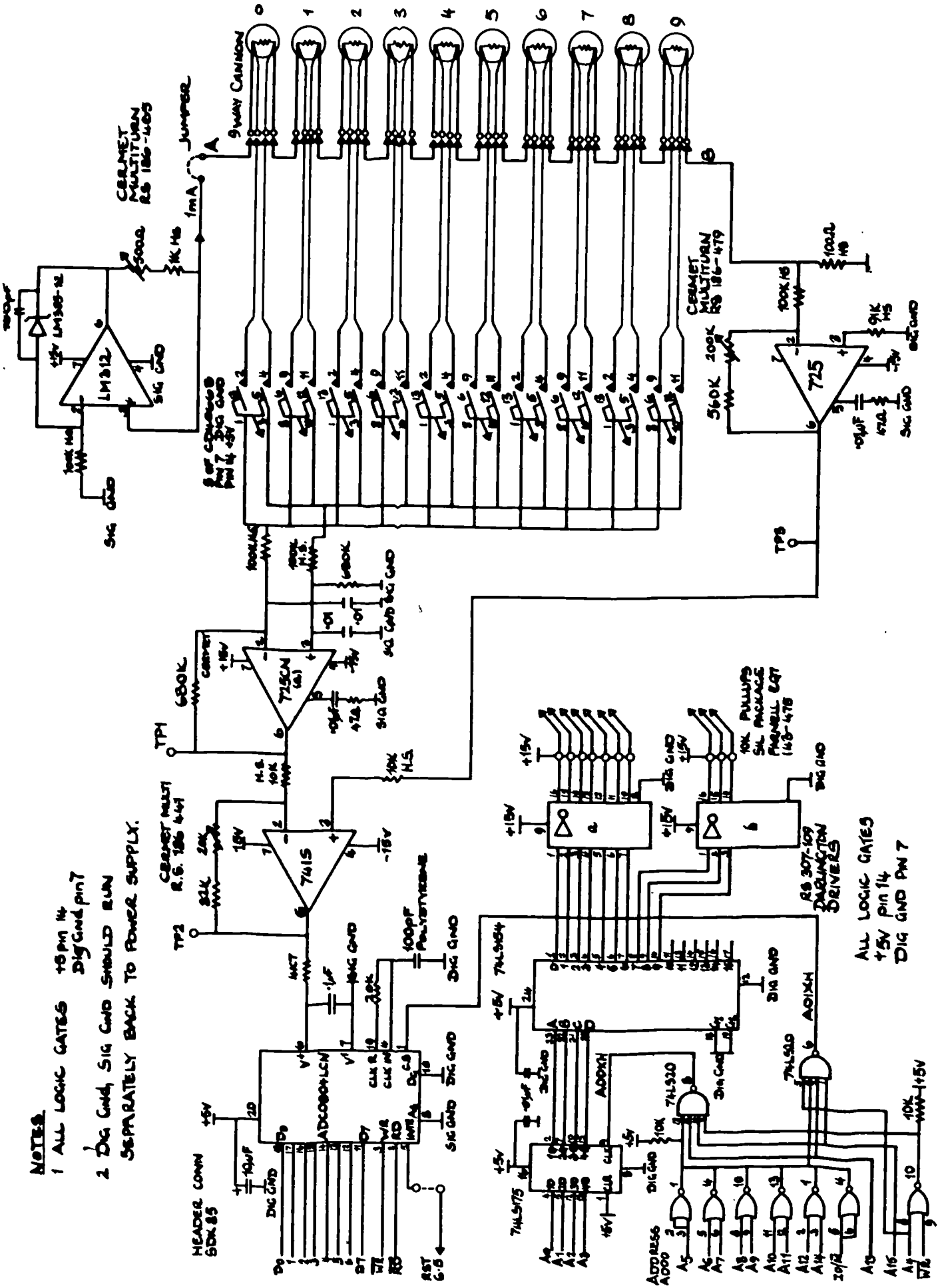

Figure C2 Temperature Measuring Circuit

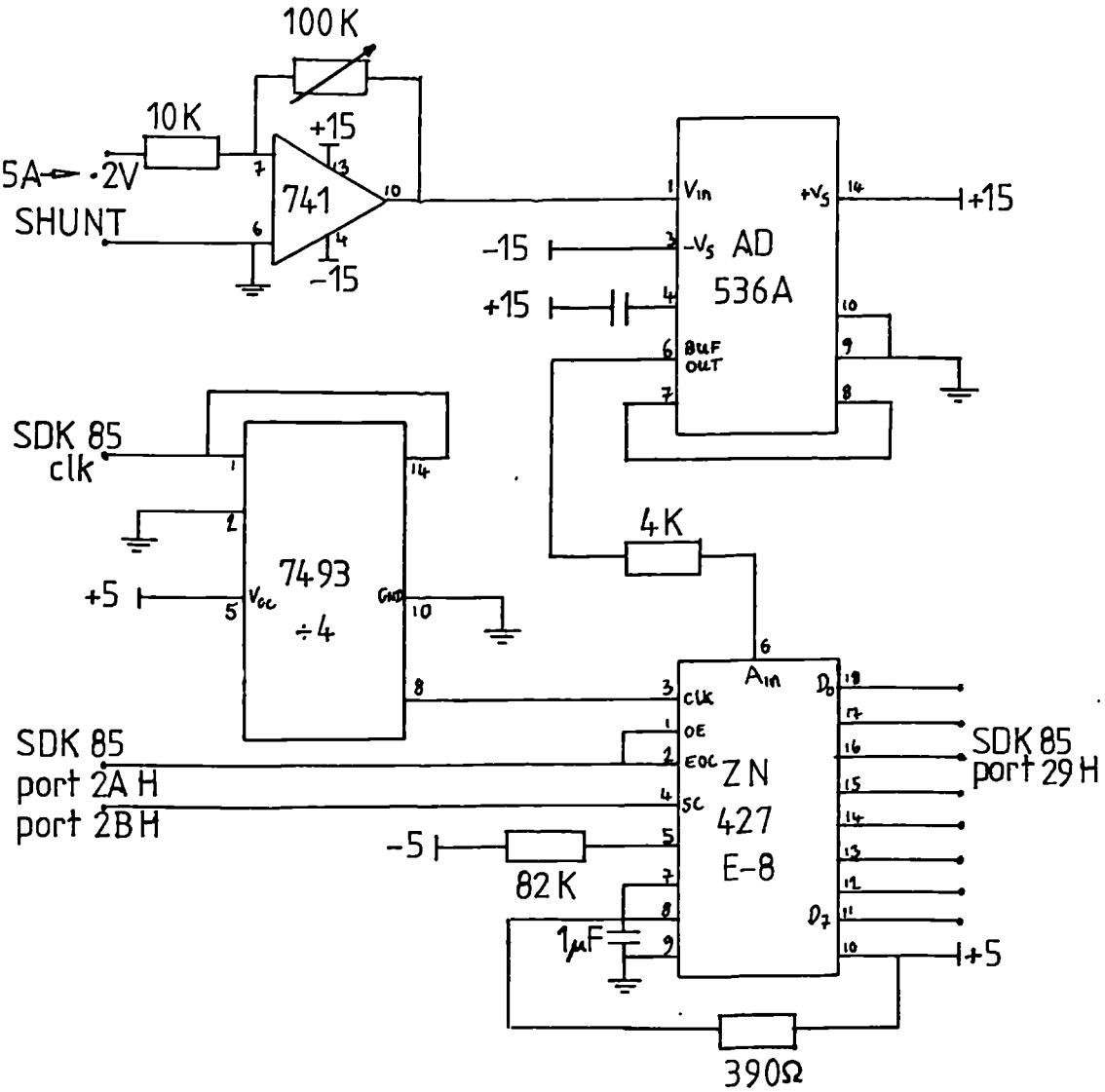

Figure C3 Balanced Supply Current Measuring Circuit

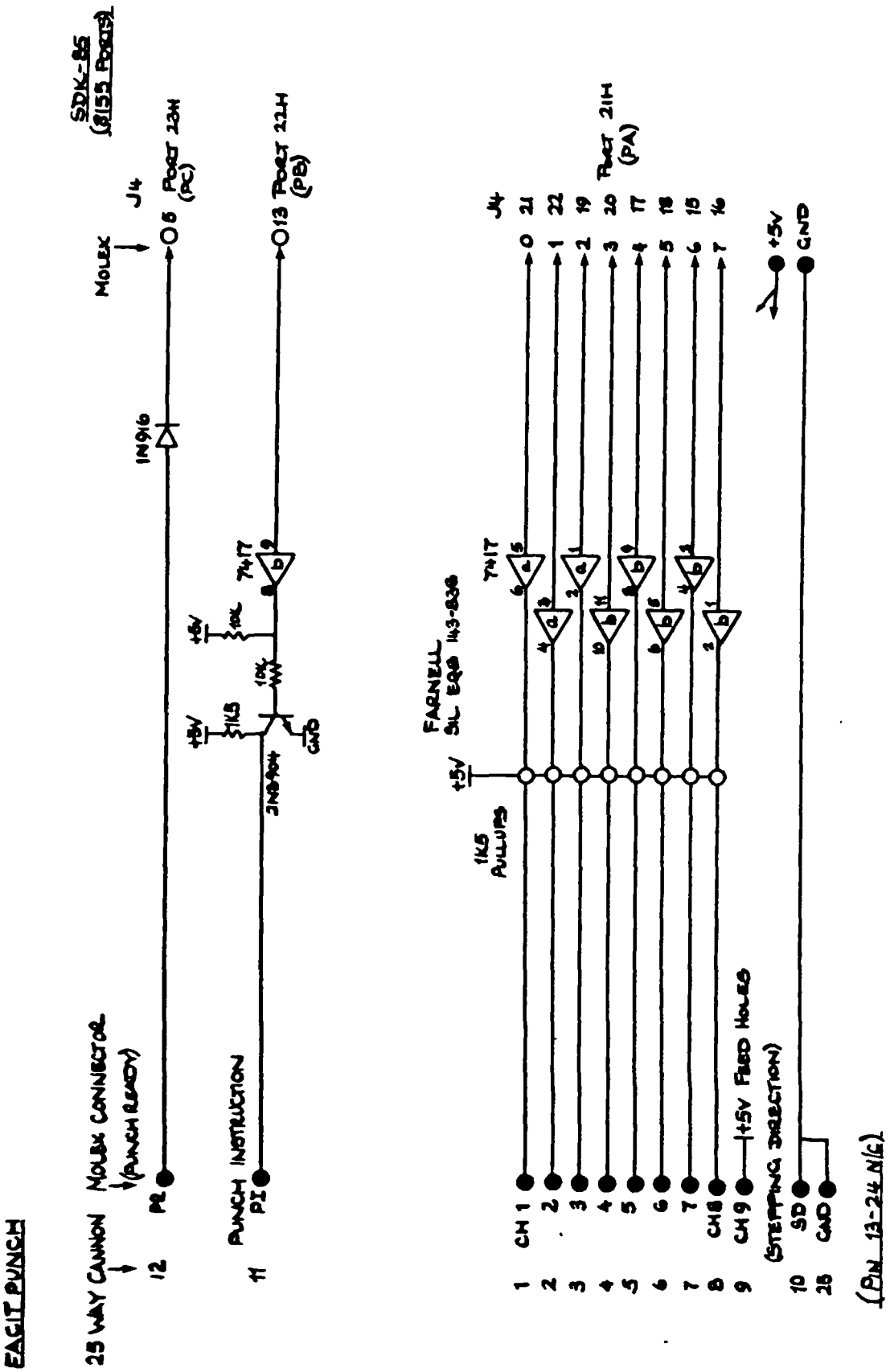

Figure C4 Facit Paper Punch Interface

APPENDIX D. THERMAL PREDICTOR/DATA LOGGER SOFTWARE

The software developed for the on-line predictor was written in Intel 8085 Assembler Language and developed upon an Intel MDS Development System and Emulator (ICE 85). A copy of the programme listing has been left with the supervisor of this project, Mr D.R. Turner, at the University of Liverpool.

The thermal predictions were performed at intervals of one second so the thermal model data constant matrices were formulated accordingly. The model constants were scaled to fit within 15 bits, the 16^{th} being reserved as a sign bit. To implement the timing control, a real time clock was created by connecting the output of a programmable timer/counter to the RST 7.5 interrupt pin of the 8085 microprocessor. The timer was programmed to give a square wave of 5ms period, this being the closest convenient integer divisor of one second to the maximum count capability of 5.33ms. The interrupt routine updated counts representing the number of five milliseconds, seconds, minutes and hours that had elapsed since the programme was started.

The multiplication of two sixteen bit numbers was performed by a subroutine designed to give the result correct to 24 bits; the least significant 8 bits were rounded off during the calculation. The result was added or subtracted from a 24 bit accumulator depending upon the state of a flag set to indicate the expected sign of the outcome, any sign bits having been masked out before the multiplication. The use of the accu-

mulator facilitated the implementation of the matrix multiplications which required 8 such multiplications for every row calculation. When the multiplication was complete the 24 bit accumulator was divided by an integer power of two to give the final 16 bit result.

The software is initialised by setting the programme variables to their initial values. The initial temperature matrix is set to zero as are the clock counts. The programmable timer is programmed with a count length corresponding to 5ms for the 3.072 MHz clock frequency of the SDK 85, and started. Once initialisation is complete the programme enters a loop in which it remains until a reset is issued from the SDK 85 keypad.

A measurement cycle follows in which the thermometer temperatures are recorded along with the line current which is squared and interrogated; a flag is set if the current is zero. This flag is used subsequently to indicate a stationary unsupplied machine; if this is the case then the stationary model is solved.

$$[T_n] = [D_{1s}][T_{n-1}]$$

Otherwise the first part of the rotating model equation is solved and stored in anticipation of the calculation of the generator matrix.

$$[T_n] = [D_{1r}][T_{n-1}]$$

To implement the generator matrix calculations, the temperature weightings to be applied to those components of the motor losses which are dependent upon the stator and rotor resistances, R_1 and R_2, must

be found. The generator matrix calculation continues with the temperature weighted parameters being multiplied by the line current squared; the line voltage squared is set to the average value expected in the laboratory (427V) and is implicit in the thermal model parameters. The column generator matrix, $[G_n]$, is then made up by distributing the calculated motor losses between the motor nodes in accordance with the criteria established in Chapter 2. The second rotating model calculation ($[D_{2r}][G_n]$) follows and the result is added to the first giving the rotating model predicted nodal temperature rise above the ambient temperature. The measured ambient temperature is added, in preference to a constant, assumed value, to enable a direct comparison with the measured temperatures.

Although the calculations, and measurements, took place every second, for the purpose of plotting graphical comparisons, data was punched onto paper tape only once every minute. To avoid the data to be punched being overwritten by the subsequent thermal calculations, only the data valid for the first second of every minute was formatted in ASCII, Binary Coded Decimal digits and transferred to an area of memory reserved for the punching subroutine. The ASCII, Binary Coded Decimal format was required to give an ordered data file upon the subsequent transfer of the information to the mainframe computer.

Because of the relatively slow tape punching mechanism the time required to punch all the data exceeded one second so the data was punched in three separate blocks during consecutive one second cycles at the start of each one minute interval. After the data has been punched, or if there is no data to be punched in that particular cycle,

the programme enters a wait loop and continually polls the real time clock until the start of the next one second cycle is indicated.

APPENDIX E. MEAN SLIP DURING STARTING AND BRAKING DUTIES.

The slip/time equations for some common induction motor loads are shown below.

Pure inertia load

$$\frac{ds}{dt} = \frac{-3c^2R_2.V^2}{J.\omega_s^2}\left[\frac{s}{(c^2R_2)^2 + 2.s.R_1.c^2R_2 + s^2.R_1^2}\right]$$

Fan-type load

$$\frac{ds}{dt} = \frac{-3c^2R_2.V^2}{J.\omega_s^2}\left[\frac{s}{(c^2R_2)^2 + 2.s.R_1.c^2R_2 + s^2.R_1^2}\right] + \frac{T_{max}(1-s)^2}{\omega_s.J}$$

Constant load acting against motor torque

$$\frac{ds}{dt} = \frac{-3c^2R_2.V^2}{J.\omega_s^2}\left[\frac{s}{(c^2R_2)^2 + 2.s.R_1.c^2R_2 + s^2.R_1^2}\right] + \frac{T_l}{\omega_s.J}$$

Constant load acting with motor torque

$$\frac{ds}{dt} = \frac{-3c^2R_2.V^2}{J.\omega_s^2}\left[\frac{s}{(c^2R_2)^2 + 2.s.R_1.c^2R_2 + s^2.R_1^2}\right] - \frac{T_l}{\omega_s.J}$$

In the above equations,

J = inertia of motor and load ($kg\text{-}m^2$

V = motor phase voltage (V)

ω_s = motor synchronous speed (rads/s)

T_{max} = fan load torque at rated speed (N-m)

T_1 = constant load torque (N-m)

The equations are solved numerically using a Runge-Kutta method. As the referred rotor winding resistance, R_2, is linearly dependent upon the frequency, it is represented in the above equations by,

$$R_2(s) = \left(\frac{(a-1).s}{2} + 1\right).R_2(0)$$

a = rotor frequency correction factor at twice supply frequency

$R_2(0)$ = rotor winding resistance at zero hertz.

Arbitrary stator and rotor winding temperatures of 70°C and 100°C were used to compute the values of R_1 and R_2 in the analysis for the GEC 5.5kW motor in Chapter 6.

MICROPROCESSOR BASED INDUCTION MOTOR THERMAL PROTECTION

P.H. Mellor, D.R. Turner, D. Roberts

Department of Electrical Engineering and Electronics, The University of Liverpool.

INTRODUCTION

Today higher demands are being made of modern induction motor protection devices. Machines are now running closer to their thermal limits in order to acheive higher specific outputs, and users require a finer degree of protection to avoid unneccessary shutdowns and loss production.

Induction motors may fail because of mechanical stresses or environmental factors, however the majority of failures are still a result of supply and loading faults that cause excessive insulation temperatures. The latter include phase unbalance, phase loss, overloads and stall. They can be guarded by stand alone relays that monitor the machines supply and provide an estimate of the insulation temperatures, thereby avoiding the difficult and costly installment of temperature detectors in the motor's windings. However accurate estimation of peak winding temperatures during transient loads is essential if such relays are to be used with confidence.

The motor protection relays that are now available protect against most electrical failures. The majority use an I^2t characteristic to model the induction motors thermal performance. Some use an electrical R-C analogue to simulate the heating conditions, Wilson(1) discusses one that uses two time constants to simulate both the iron and copper temperatures and allows for the loss of ventilation during standstill. Digital circuits and microprocessors have been employed to perform the protection function in a similar manner to the analogue devices. In addition they have been used to measure inbalance in terms of sequence components and use this to correct the effective heat input to the trip characteristic. The presently available protection devices are designed to be applicable to a wide range of machine ratings, and facilities are provided to match the protection characteristic to the installed machine. The matching process and the simple thermal equivalents can only result in an approximation to the winding temperatures.

The paper describes a microprocessor based thermal protection device(2,3) that utilises a more complex thermal model of an induction motor to provide a better assessment of the insulation temperature rise. The model provides estimates of both the peak stator and rotor winding temperatures. It is derived from dimensional information and the electrical equivalent circuit of the induction motor and applies to range of small to medium sized, mush would machines.

A prototype device is described for a 5.5kW machine. It is based upon a low cost 8 bit microprocessor system, which solves the thermal model in real time from inputs of the machines supply. Results are also given for a medium size 75kW induction motor.

THERMAL MODEL

Thermal models of electrical machines are well established in the literature. In this application the design of the thermal model is dominated by the requirements of the microprocessor protection device. The amount of real time computation needs to be restricted, whilst acheiving good accuracy by modelling all the major components of the machine. In addition, the model should be applicable to a range of machine sizes and not tailored to a particular machine.

A bulk conduction and storage model was found to meet both the accuracy and simplicity requirements. Here, a machine is divided into a number of lumped components, which are interconnected through a linear mesh of thermal impedances. The induction motor was modelled as the ten components shown in Figure 1, with symmetry assumed about the shaft and a radial plane through the centre of the machine.

Basic Components

Perez and Kassakian(4) have shown that a general rectangular component can be represented by a point source approximating to its mean temperature, with internal heat generation acting as an input at that node. A similar general component was used to model each section of the induction motor, in this case evaluated in cylindrical co-ordinates as these were more appropriate to small machines. The mean temperature of the component was approximated from a superposition of independent theoretical solutions to the heat conditions in the radial and axial directions. The thermal component was then described by a network of thermal impedances derived from the dimensions. To model the transient, thermal storage was included as an additional heat transfer at the point of mean temperature.

The endwinding, for example, was modelled from the basic cylindrical form as a toriod with 'legs' illustrated together with the thermal network in Figure 2.

Heat Generation

The heat generations within the machine are a result of electrical and internal mechanical losses, which can be subdivided into voltage dependant no load losses, such as iron and mechanical losses, and current dependent copper and stray load losses. By assuming balanced conditions, the heat generations, u, were shown(3) to be related to the supply phase voltage, v, and current, i, by functions of the form:

$$u = u_v v^2 + u_I i^2 \qquad (1)$$

where the constants, u_v, u_I, could be determined from the parameters of the induction motors's electrical equivalent circuit. They were distributed amongst the iron and copper thermal components in accordance with accepted practice, with the majority of heat loss occuring in the stator slot and endwindings, stator teeth and rotor periphery.

Complete Structure

The separate components are interconnected directly or were appropriate through additional convective heat transfers across the air paths within the motor. The magnitudes of the latter heat transfers were obtained from the analytical and emperical work of a number of authors on similar geometries to those found in induction motors. Only the frame to ambient film coefficient was found directly from measurements of the motor surface temperature on load. The resultant mesh of thermal resistances, capacitances and heat sources for

the induction motor is given in Figure 3.

A number of specific features were included to give a more accurate representation of the machines thermal performance and to improve the protection aspects of the model.

i) The heat generations were derived from the equivalent circuit applied over the normal working range. Care was taken to ensure that stray load loss and deep bar effects were included.

ii) The variation in stator and rotor winding resistances with temperatures was taken into account by making the appropriate generation constants temperature dependant.

iii) The endwinding temperature was estimated as a maximum 'hot spot' value as apposed to the mean. This was achieved, without interfering with the basic assumptions of the model, by weighting the values of thermal impedances by the factor, w, shown in Figure 2. The magnitude of the factor was found by assuming a parabolic temperature distribution over the endwinding cross-section.

Model Equations

The network in Figure 3 used a total of fifteen nodes to model the ten thermal components, and was described by fifteen heat balance equations. Seven of the nodes, however, had negligable thermal capacitance and could be elimated from the network using standard mathematical techniques. The system was thus reduced to eight linear differential equations, expressed in matrix from as:

$$C \frac{d\Theta}{dt} = Y_r\Theta + (u_v v^2 + u_I i^2) \qquad (2)$$

where C = matrix of thermal capacitances
Θ = matrix of eight component temperatures
Y_r = matrix of inter-nodal thermal conductances
u_v = voltage dependant generations
u_I = current dependant generations

The above equations applied to the induction motor when it was rotating. At standstill the convective elements of the branch thermal impedances would vary because the cooling fans are no longer effective, and a separate conductance matrix Y_s was needed to describe the machine. The standstill equation becomes:

$$C \frac{d\Theta}{dt} = Y_s\Theta \qquad (3)$$

The solutions of equations (2), (3) in real time was based upon a discrete approximation to the system, where the load on the machine was assumed to remain constant over short time intervals. The differential equations were then solved by using eigenvector techniques to provide a discrete solutions over the kth time interval of the form:

$$\Theta_{k+1} = A_r\Theta_k + (B_r v^2 + B_I i^2) \qquad (4)$$

$$\Theta_{k+1} = A_s\Theta_k \qquad (5)$$

The stationary solution (5) is exact, whereas the running solution assumes constant phase current and voltage over the time interval. Both equations are referred to the ambient temperature, which must be added as an offset to obtain the absolute motor temperatures.

Allowance for the variation of winding resistances with temperature was made by recalculating the generation factors at each time step. The running temperatures were then found from:

$$\Theta_{k+1} = A_r\Theta_k + (I + a\Theta_k)(B_v v^2 + B_I i^2) \qquad (6)$$

where the sparse matrix, a, described the dependance of each heat generator on the three winding components in the model.

MICROPROCESSOR IMPLEMENTATION

A prototype prediction device was developed for a 5.5W TEFC induction motor, that was operating under balanced conditions at constant supply voltage. The device would then only require the monitoring of a single phase current and the ambient temperature. The thermal calculations were performed at a time step of one second, a period which was short compared with the thermal time constants of the machine.

The hardware consisted of an 8 bit Intel 8085 microprocessor with the minimum support of an 8155 RAM and a 8755 EPROM. The rms phase current and ambient temperature were measured by a 12 bit, low cost, integrating analogue to digital converter, which was interfaced to the input ports on the 8155.

A flow chart of the microprocessor software is given in Figure 4. At the start of each cycle the motor phase current was read from the analogue to digital converter. From its value either the stationary or the more complex rotating matrix equations were evaluated. The previous predicted temperatures were then overwritten with the new calculations and the cycle repeated. To avoid wastage of the microprocessors time, the analogue to digital converter operated in parallel with the calculation procedure and was serviced through an interupt to the processor.

Integer arithmetic was used throughout the matrix equations to minimise execution time. This was achieved by a careful scaling of the matrix constants and temperatures, which were all stored as 16 bit, two byte, integers. The matrix equations were evaluated *a row at a time* with the intermediate totals held in a 24 bit accumulator. Each 16 bit multiplication was subdivided into four 8 bit multiplications, each calculated by the shift and add technique, with only the significant 24 bits added into the accumulator. A single multiplication and add operation was performed in approximately 600 μs, and the total rotational calculation in under 100 ms. It was found through simulation on a mainframe computer, that this method of calculation introduced no significant error when compared with floating point calculations at the mainframe's full 32 bit accuracy.

DEVICE PERFORMANCE

Small resistance themometers were placed in the test machine at positions which corresponded, as far as possible, to the nodes of the thermal models. They were embedded in the stator slot and endwindings and placed in bore holes drilled to the centre of the stator teeth and back iron. Their temperatures were recorded by the prototype microprocessor and printed together with the predicted values on a punch tape for later analysis. Rotor temperatures were checked as soon as the machine was brought to a halt.

The comparison between the predicted and actual measured temperatures was good throughout the motor, when tested over a number of varying load cycles. Figure 5 shows the results obtained for the peak endwinding temperature over a load that included regions of standstill and overload. The weighting of the endwinding to obtain a peak value was effective at high loads, where the predicted temperatures exceeded those of the thermometers.

Results are also presented in Figure 6 for a larger 75kW machine, where the calculated temperatures were derived from a computer simulation of the prediction device performance. In both cases the thermal models were derived from only dimensional information of the induction motors and simple external tests, used to obtain the electrical equivalent circuit parameters and the frame film coefficients.

CONCLUSIONS

The protection device successfully estimated the insulation temperatures for a balanced varying load. Unbalanced operation would require measurements of the supply sequence components, from which heat generations could be derived using the appropriate electrical equivalent circuit. The model would also need to be extended to estimate the temperature variations in each phase winding. In the tests the induction motors were driving low inertia loads, during extended starts, however, the low slip electrical equivalent circuit may no longer apply and slip dependant heat generation would need to be introduced. The thermal model is capable of estimating rotor temperatures for protection in these conditions.

Although a thermal model is needed for each particular size and make of machine, it is easily formulated from basic tests and dimensions. Models can be interchanged in the protection device simply by replacing the memory integrated circuit.

The microprocessor used only ten per cent of the cycle time to perform the thermal calculations, the remainder is available for the other protection functions found on commercial devices. In addition the stored thermal model can be used to predict future temperatures of the induction motor from the past trends in the load. This additional facility would give forwarning of likely shutdowns or failures.

ACKNOWLEDGEMENTS

The authors would like to thank GEC Small Machines and the UK Science and Engineering Research Council for their support of this project.

REFERENCES

1) Wilson, P.G.A., 1983, 'Complete protection of motors under variable load conditions', Proc. Drives/Motors/Controls, 172-178.

2) UK Patent Appl. GB 8429434.

3) Mellor, P.H., 1983, 'Improvements in the efficiency and ageing of single and parallel machine drives', Ph.D. Thesis, University of Liverpool.

4) Perez, I.J., Kassakian, J.K., 1979, 'A stationary thermal model for smooth air gap rotating machines', Electric Machines and Electromechanics, 3, 285-303.

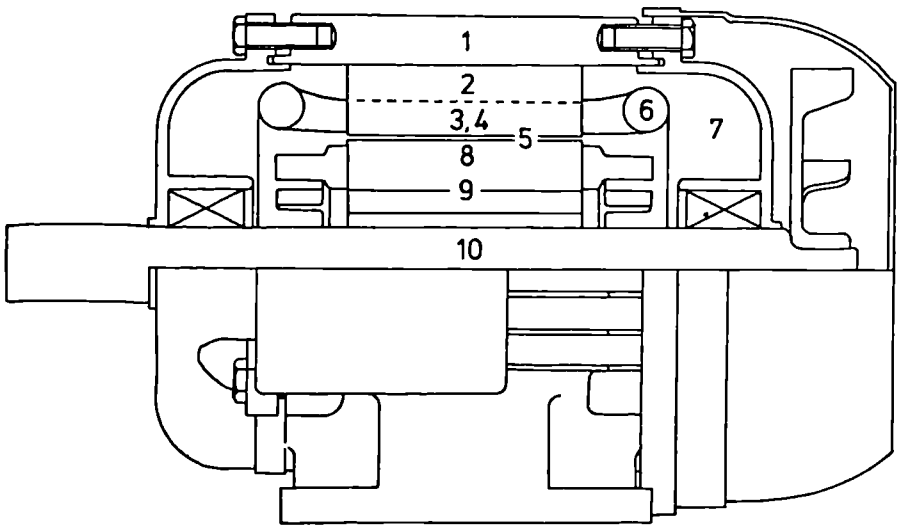

1 Frame
2 Stator Iron
3 Stator Teeth
4 Stator Winding
5 Air Gap
6 Endwinding
7 Encap Air
8 Rotor Winding
9 Rotor Iron
10 Shaft

FIGURE 1 INDUCTION MOTOR CONSTRUCTION

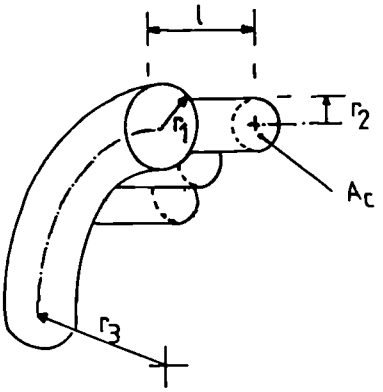

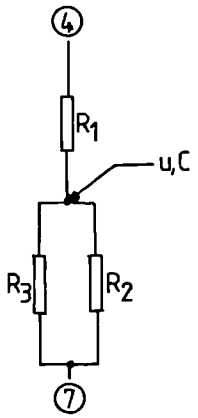

$$R_1 = \frac{lw}{nA_c k_c}$$

$$R_2 = \frac{r_1 w}{2\pi F k_i (r_1 4\pi r_3 - n r_2^2)}$$

$$R_3 = \frac{w}{2\pi F k_i l n}$$

$$C = \frac{\rho_c c_c A_c n(1-\alpha)L}{2w\alpha}$$

$$u = \frac{3}{2}(1-\alpha)u_{12}\,i^2$$

FIGURE 2 ENDWINDING MODEL

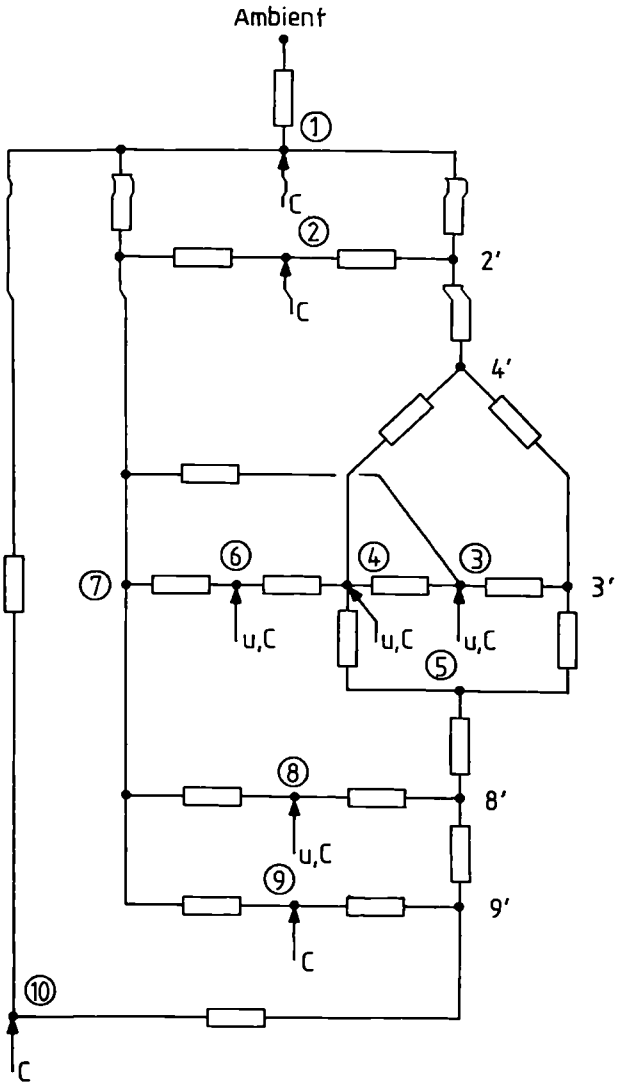

FIGURE 3 INDUCTION MOTOR THERMAL EQUIVALENT CIRCUIT

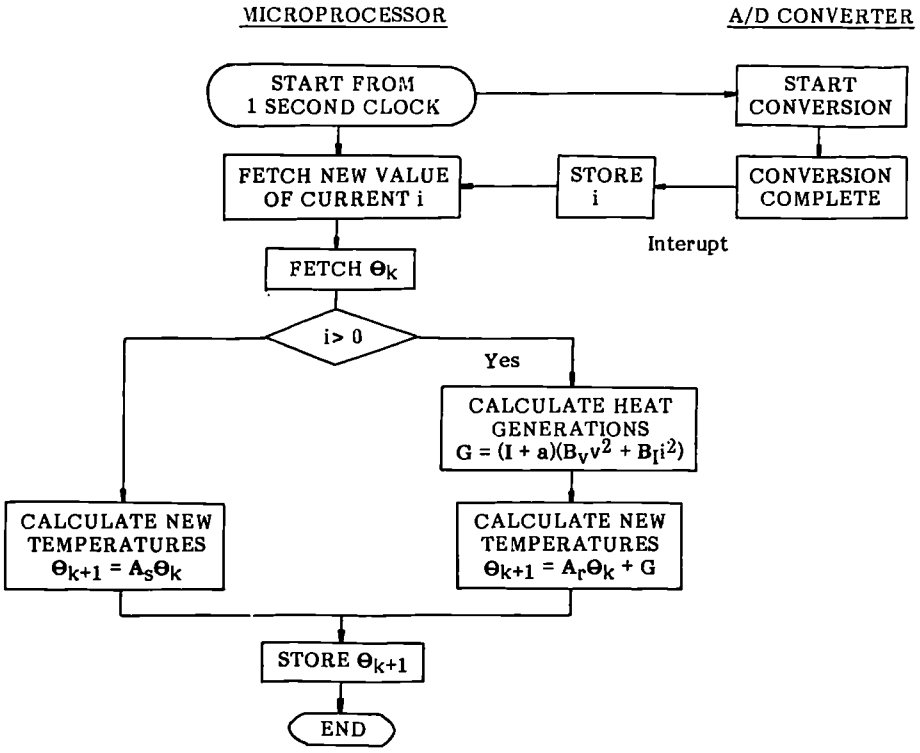

FIGURE 4 FLOWCHART OF MICROPROCESSOR CALCULATIONS

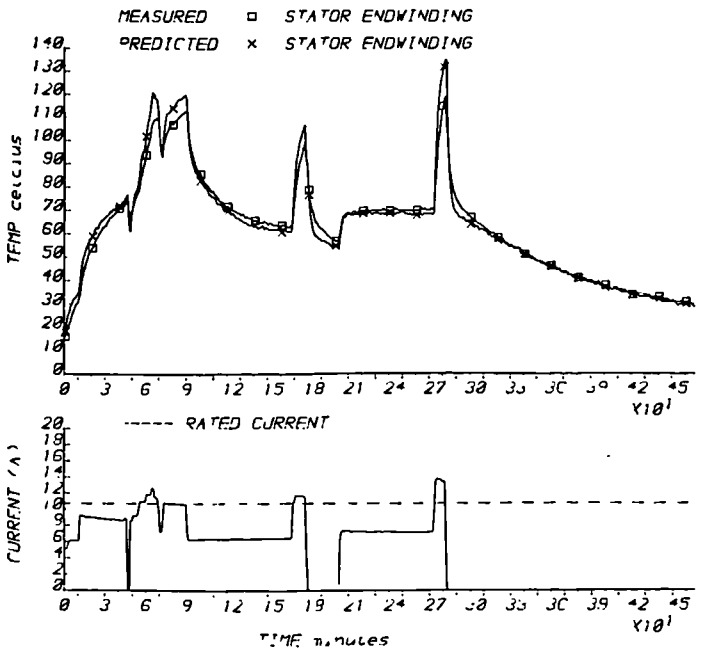

FIGURE 5 5.5kW INDUCTION MOTOR

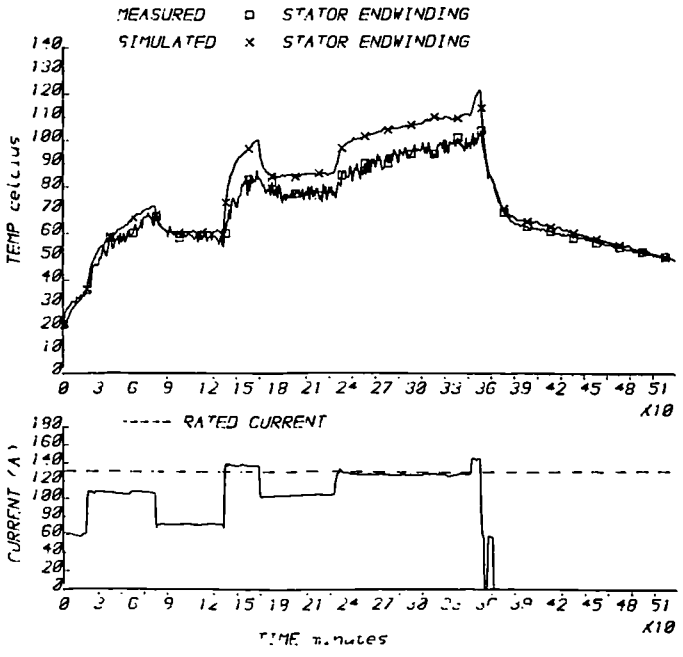

FIGURE 6 75kW INDUCTION MOTOR